ACS SYMPOSIUM SERIES 1040

Fuel Cell Chemistry and Operation

Anode
Cathode

EDITED BY
Andrew M. Herring, Thomas A. Zawodzinski Jr.,
and Steven J. Hamrock

Fuel Cell Chemistry and Operation

Downloaded by 89.163.35.42 on June 21, 2012 | http://pubs.acs.org
Publication Date (Web): April 30, 2010 | doi: 10.1021/bk-2010-1040.fw001

Downloaded by 89.163.35.42 on June 21, 2012 | http://pubs.acs.org
Publication Date (Web): April 30, 2010 | doi: 10.1021/bk-2010-1040.fw001

Downloaded by 89.163.35.42 on June 21, 2012 | http://pubs.acs.org
Publication Date (Web): April 30, 2010 | doi: 10.1021/bk-2010-1040.fw001

ACS SYMPOSIUM SERIES **1040**

Fuel Cell Chemistry and Operation

Andrew M. Herring, Editor
Colorado School of Mines

Thomas A. Zawodzinski Jr., Editor
University of Tennessee - Knoxville
Oak Ridge National Laboratory

Steven J. Hamrock, Editor
3M Company

Sponsored by the
ACS Division of Fuel Chemistry

American Chemical Society, Washington, DC

Library of Congress Cataloging-in-Publication Data

Fuel cell chemistry and operation / [edited by] Andrew M. Herring, Thomas A. Zawodzinski, Jr., Steven J. Hamrock ; sponsored by the ACS Division of Fuel Chemistry.
p. cm. -- (ACS symposium series ; 1040)
Includes bibliographical references and index.
ISBN 978-0-8412-2569-5 (alk. paper)
1. Proton exchange membrane fuel cells. 2. Fuel cells. I. Herring, Andrew M. II. Zawodzinski, Thomas A. III. Hamrock, Steven J. IV. American Chemical Society. Division of Fuel Chemistry.
TK2933.P76F84 2010
621.31'2429--dc22
2010012713

Downloaded by 89.163.35.42 on June 21, 2012 | http://pubs.acs.org
Publication Date (Web): April 30, 2010 | doi: 10.1021/bk-2010-1040.fw001

The paper used in this publication meets the minimum requirements of American National Standard for Information Sciences—Permanence of Paper for Printed Library Materials, ANSI Z39.48n1984.

Copyright © 2010 American Chemical Society

Distributed by Oxford University Press

All Rights Reserved. Reprographic copying beyond that permitted by Sections 107 or 108 of the U.S. Copyright Act is allowed for internal use only, provided that a per-chapter fee of $40.25 plus $0.75 per page is paid to the Copyright Clearance Center, Inc., 222 Rosewood Drive, Danvers, MA 01923, USA. Republication or reproduction for sale of pages in this book is permitted only under license from ACS. Direct these and other permission requests to ACS Copyright Office, Publications Division, 1155 16th Street, N.W., Washington, DC 20036.

The citation of trade names and/or names of manufacturers in this publication is not to be construed as an endorsement or as approval by ACS of the commercial products or services referenced herein; nor should the mere reference herein to any drawing, specification, chemical process, or other data be regarded as a license or as a conveyance of any right or permission to the holder, reader, or any other person or corporation, to manufacture, reproduce, use, or sell any patented invention or copyrighted work that may in any way be related thereto. Registered names, trademarks, etc., used in this publication, even without specific indication thereof, are not to be considered unprotected by law.

PRINTED IN THE UNITED STATES OF AMERICA

Downloaded by 89.163.35.42 on June 21, 2012 | http://pubs.acs.org
Publication Date (Web): April 30, 2010 | doi: 10.1021/bk-2010-1040.fw001

Foreword

The ACS Symposium Series was first published in 1974 to provide a mechanism for publishing symposia quickly in book form. The purpose of the series is to publish timely, comprehensive books developed from the ACS sponsored symposia based on current scientific research. Occasionally, books are developed from symposia sponsored by other organizations when the topic is of keen interest to the chemistry audience.

Before agreeing to publish a book, the proposed table of contents is reviewed for appropriate and comprehensive coverage and for interest to the audience. Some papers may be excluded to better focus the book; others may be added to provide comprehensiveness. When appropriate, overview or introductory chapters are added. Drafts of chapters are peer-reviewed prior to final acceptance or rejection, and manuscripts are prepared in camera-ready format.

As a rule, only original research papers and original review papers are included in the volumes. Verbatim reproductions of previous published papers are not accepted.

ACS Books Department

Downloaded by 89.163.35.42 on June 21, 2012 | http://pubs.acs.org
Publication Date (Web): April 30, 2010 | doi: 10.1021/bk-2010-1040.pr001

Preface

This volume arises from the latest symposium entitled Fuel Cell Chemistry and Operation in a series of ACS Fuel Division symposia, begun in 1999, held at the Philadelphia ACS meeting (Fall 2008). Several practically important themes were touched on in this meeting. These include fuel cell electro-catalysis and membrane development as well as durability of fuel cell components. In addition, several papers presented varying results and views on a fundamentally interesting method, broad-band dielectric spectroscopy. This was of particular interest to the organizers because of the high potential for insight arising from the method on the one hand coupled to radically different interpretations of data in the literature. Two contributions to this volume reflect this discussion. In short, the debate is over matters of interpretation of features in the data. Application of dielectric spectroscopy to the study of polymers has a long history. However, polymeric electrolytes with substantial conductivity present significant problems for traditional measurement techniques using low surface area electrodes. Significant interfacial polarization can arise in such cases, leading to spectral features that are spurious. We leave it to the reader to assess the approaches described herein.

Andrew M. Herring

Dept. of Chemical Engineering
Colorado School of Mines
Golden, CO

Thomas A. Zawodzinski Jr.

Dept. of Chemical and Biomolecular Engineering
University of Tennessee-Knoxville
Knoxville, TN

Physical Chemistry of Materials Group
Oak Ridge National Laboratory
Oak Ridge, TN

Steven J. Hamrock

3M Fuel Cell Components Program
3M Company
St. Paul, MN

Downloaded by 89.163.35.42 on June 21, 2012 | http://pubs.acs.org
Publication Date (Web): April 30, 2010 | doi: 10.1021/bk-2010-1040.ch001

Chapter 1

Status of Fuel Cells and the Challenges Facing Fuel Cell Technology Today

Kathi Epping Martin,[*,1] John P. Kopasz,[2] and Kevin W. McMurphy[3]

[1]Hydrogen, Fuel Cells and Infrastructure Technologies, U.S. Department of Energy, 1000 Independence Avenue SW, Washington, DC 20375-0121
[2]Argonne National Laboratory, 9700 South Cass Avenue, Argonne, IL 60439
[3]SENTECH, Inc., 7475 Wisconsin Avenue, Bethesda, MD 20854
[*]Kathi.Epping@ee.doe.gov

The Department of Energy (DOE) Hydrogen Program supports research and development that has substantially improved the state-of-the-art in fuel cell technology, especially with regard to the major technical hurdles to fuel cell commercialization - durability, performance, and cost of fuel cell components and systems. In particular, membrane and catalyst structure and composition have been found to be critical in obtaining improved performance and durability. For example, advancements in alloy catalysts, novel catalyst supports, and mechanically-stabilized membranes have led to single-cell membrane electrode assemblies (MEAs) with platinum metal group loadings approaching the DOE 2015 MEA target that have a lifetime of 7,300 hours under voltage cycling, showing the potential to meet the DOE 2010 automotive fuel cell stack target of 5,000 hours (equivalent to 150,000 miles). In addition, improvements in the performance of alloy catalysts and membranes have helped improve overall performance and reduce the modeled cost of an 80-kW direct hydrogen fuel cell system for transportation projected to a volume of 500,000 units per year to $73/kW. While component research enabled such advances, innovation in characterization and analysis techniques has improved researchers' understanding of the processes that affect fuel cell performance and durability. An improved understanding of these processes will be key to

In Fuel Cell Chemistry and Operation; Herring, A., et al.;
ACS Symposium Series; American Chemical Society: Washington, DC, 2010.

making further progress in eliminating cost, durability, and performance challenges that remain for fuel cell technology.

Introduction

Fuel cells offer benefits in transportation, stationary, and portable power applications. One of the major benefits is an increase in efficiency over conventional technology. Fuel cells are more than two times as efficient as internal combustion engines (ICEs), with the potential for greater than 80% efficiency in combined heat and power systems (*1*).

In addition to improving efficiency, fuel cells also can enhance energy security by reducing the nation's dependence on foreign oil. The United States (U.S.) imports 58% of its total petroleum, and transportation accounts for two-thirds of U.S. petroleum use (*2*). Projections indicate U.S. domestic oil production, even when considering biofuels and coal-to-liquids contributions, will continue to account for less than half the national demand. The U.S. Department of Energy (DOE) is investigating hydrogen and fuel cell technologies as one of a portfolio of options to reduce U.S. dependence on oil and to diminish this imbalance. In addition, fuel cell vehicles offer the potential for very low or zero emissions from the the vehicles. Emissions from the complete fuel cycle can also be substantially reduced compared to current vehicles. Recent estimates indicate a possible reduction in greenhouse gas emissions of more than a factor of two when the hydrogen is produced from natural gas reforming (*3*). Further reductions can be achieved when the hydrogen is made from renewable or nuclear energy.

Research has been focused on fuel cells as replacements for ICEs in light duty vehicles. For success in the marketplace, the fuel cell vehicles must offer value, performance, and benefits to the consumer that are comparable to the existing vehicles. DOE, with input from industry, has set targets for hydrogen and fuel cell technologies to achieve performance and cost comparable to competing alternatives. For example, the targets for automotive fuel cells include a cost target of $30/kW by 2015 ($45/kW by 2010), 5,000-hour durability (equivalent to 150,000 miles), and increased efficiency to 60% (*4*). The cost target is for production at manufacturing volumes of 500,000 systems per year.

In other potential applications for fuel cells, such as stationary power generation (distributed power), backup power, portable power, material handling, and other specialty applications, the life-cycle cost of the competing technology allows for a higher fuel cell cost. These applications are considered early markets for fuel cells. For example, for distributed power generation key targets include a fuel cell cost of $750/kW and a durability of 40,000 hours (*4*). The cost target for distributed power is significantly higher (less aggressive) than the automotive target in order to compete with other technology in the stationary sector. While the durability target appears to be much more aggressive for distributed power generation applications than that for automotive applications, the automotive duty cycle includes much more dynamic behavior with many more cycles in power demand than the distributed power duty cycle. The 40,000 hours under the

Downloaded by 89.163.35.42 on June 21, 2012 | http://pubs.acs.org
Publication Date (Web): April 30, 2010 | doi: 10.1021/bk-2010-1040.ch001

distributed power duty cycle, therefore, is believed to be less demanding than the 5,000 hours under automotive conditions. Fuel cells are now at the point where they can begin to compete in some of these early markets. Deployment of fuel cells in these markets will help develop the manufacturing and supplier base, increase production volumes to help lower fuel cell costs, and broaden public awareness of fuel cell technology (*5*).

Fuel Cell Challenges

DOE has been funding research to address the technical hurdles to fuel cell commercialization. Two of the major hurdles are the cost and durability of the polymer electrolyte membrane (PEM) fuel cell.

Downloaded by 89.163.35.42 on June 21, 2012 | http://pubs.acs.org
Publication Date (Web): April 30, 2010 | doi: 10.1021/bk-2010-1040.ch001

Cost

To be competitive with entrenched technology, such as the ICE, fuel cells must provide similar benefits at a comparable cost. Fuel cells are currently more expensive and costs need to be reduced. Recent estimates indicate that at high-volume production (500,000 units), the cost of an 80-kW direct hydrogen fuel cell system for transportation would be $73/kW (*6*). The DOE target for fuel cell system cost is $30/kW by 2015. A breakdown of the cost estimate indicates that the fuel cell stack accounts for slightly more than half of the cost. To achieve the necessary activity, conventional catalysts are composed of finely-dispersed platinum (Pt) particles. Due to the high cost of Pt, the catalyst ink accounts for slightly less than half of the fuel cell stack cost (47%) at high production volumes (*7*). At low production volumes (1,000 systems/year), however, the membrane becomes the major contributor to the fuel cell stack cost (*7*). In addition, the current PEMs require humidification and limit the maximum fuel cell temperature. Membranes that could operate at low relative humidity (RH) and higher operating temperatures would allow system simplification by reducing or eliminating the need for humidification and reducing the thermal management system.

Durability

Fuel cells, especially for automotive propulsion, must operate over a wide range of operating and cyclic conditions. The desired operating range encompasses temperatures from below the freezing point to well above the boiling point of water, humidity from ambient to saturated, and half-cell potentials from 0 to >1.5 volts. The severity in operating conditions is greatly exacerbated by the transient and cyclic nature of the operating conditions. Both cell and stack conditions cycle, sometimes quite rapidly, between high and low voltages, temperatures, humidities, and gas compositions. The cycling results in physical and chemical changes, sometimes with catastrophic results. Furthermore, the anode side of the cell may be exposed to both hydrogen and air simultaneously during start/stop cycles, leading to potentials of > 1.5 V.

DOE durability targets for stationary and transportation fuel cells are 40,000 hours and 5,000 hours, respectively, under realistic operating conditions including load cycling and start/stop. For transportation fuel cells, transient operation includes includes (*8*):

17,000 start/stop cycles
1,650 freeze cycles
1,200,000 load cycles.

The effects of the cycles are (*9*)

Up-transient – hydrogen starvation
Down-transient – differential pressure imbalance
Dynamic operation (load cycling) – enhanced corrosion and membrane mechanical stress
Low power – high voltage (corrosion of catalysts and/or supports)
Off – oxygen ingression to anode, support corrosion

In addition to the foregoing cycles associated with normal operation, there is the potential for unplanned cycles associated with system failure caused by non-stack components. Such system shutdowns reportedly account for 85-90% of system failures (*10*). Fuel cells must be able to withstand off-specification operating conditions caused by unplanned system malfunctions.

In particular, degradation due to start-up and shut-down is an issue. Under start-stop conditions local potentials can approach 1.5 V, a potential at which carbon supports readily corrode. Catalysts and supports that can withstand fuel starvation and the mixed potentials that can result from start-up/shut-down procedures are needed.

Downloaded by 89.163.35.42 on June 21, 2012 | http://pubs.acs.org
Publication Date (Web): April 30, 2010 | doi: 10.1021/bk-2010-1040.ch001

Recent Advances

Cost

A major focus of DOE supported efforts is directed toward reducing fuel cell costs to achieve market competitiveness. Cost estimates have determined that the major contribution to stack cost at high production volumes is the catalyst. DOE investigates four strategies to improve catalysts and decrease cost: 1) lowering Pt and Pt group metals (PGM) content through improved catalyst utilization and durability, 2) use of Pt and other PGM alloys to decrease PGM content and increase activity, 3) development of non-precious metal catalysts that maintain performance and durability compared to Pt at a reduced cost, and 4) use of novel support structures to decrease corrosion and increase durability.

PGM catalyst performance or activity has been increased while reducing the Pt content through the efforts of several groups investigating Pt alloys and structured nanoparticles. The importance of the catalyst structure has been previously described by Ross et al. (*11*). Studies have indicated an enhanced activity for specific crystal surfaces over that for Pt particles or Pt deposited on carbon (Pt/C). Combining control of surface structures with alloy composition, 3M has developed NSTF catalysts exhibiting transition metal alloy catalysts with an oxygen reduction reaction (ORR) rotating disc electrode (RDE) half-wave potential at least 50mV better than dispersed Pt/C, including a PtNiFe alloy having a half-wave potential ORR of 0.960 mV as measured at Argonne National Laboratory (ANL) (*12*). See Figure 1.

These catalysts have demonstrated 8x (PtCoMn) and 10x (PtNiFe) the activity of Pt/C. The PtCoMn catalyst has also demonstrated improved durability (*13*).

Other groups are investigating alternative structures to try to obtain improved activity and durability. UTC Power and Brookhaven National Laboratory (BNL) are developing core-shell structured Pt catalysts to reduce Pt content while increasing activity, while researchers at ANL are investigating core-shell structures with Pd. The catalysts consist of a core of base metal or base metal alloy, coated with a thin shell of Pt or PGM. The hopes are that by using a base metal core, the amount of PGM can be reduced. The base metal core also interacts electronically with the PGM shell, altering the d-band gap of the PGM shell, affecting reactivity. The PGM shell provides a less reactive covering, protecting the base. BNL and UTC Power have developed Pt-containing catalysts of this type with higher activity than Pt/C. Figure 2 compares the activity of Brookhaven's $PtAuNi_5$ core-shell catalyst with Pt/C on the basis of activity per milligram of Pt. The core-shell structure was determined by EDS. The $PtAuNi_5$ catalyst catalyst produced more than twice the current per gram of Pt for a given voltage at voltages of 0.8V or less, but the activity per cm^2 remains lower than Pt (*14*). ANL has been investigating Pd alloys and Pd core-shell systems. ANL has developed a Cu_3Pd catalyst with a higher activity on a surface area basis than that for Pt/C at 0.8V (*15*). Unfortunately, ANL has only been able to prepare this material with large particle sizes and achieve only ~ 75% of the mass activity of Pt/C per gram of PGM.

While these alloy and core-shell systems show promise, further improvements in activity are needed and durability of these systems still needs to be demonstrated.

Another strategy to reduce costs is to remove Pt and PGM altogether. Recent work at Los Alamos National Laboratory (LANL), University of South Carolina, and 3M has shown significant improvement in activity and durability of non-PGM catalysts. LANL and 3M have developed transition metal –N-C heterocyclic catalysts with impressive activity. Starting from various precursors containing C-N bonds, they have prepared active ORR catalysts, and demonstrated lifetimes on the order of hundreds to greater than 1000 hours (*15*, *16*). RDE experiments indicate that catalysts derived from polyaniline and Fe_3Co (PANI-Fe_3Co/C) trail Pt/C reference catalyst (E-TEK) by no more than 80 mV at E½. Peroxide generation in these catalysts is low, with H_2O_2 generation reduced to ~0.5%. MEA performance for the polypyrrole FeCo/C catalyst in oxygen is illustrated in Figure 3, below. The maximum power density was greater than 400 mW/cm^2 in oxygen.

The University of South Carolina has developed carbon-based metal-free catalysts and carbon composite catalysts for the ORR. Carbon catalysts have been known to catalyze peroxide production, however Popov et al. have been

Downloaded by 89.163.35.42 on June 21, 2012 | http://pubs.acs.org
Publication Date (Web): April 30, 2010 | doi: 10.1021/bk-2010-1040.ch001

Downloaded by 89.163.35.42 on June 21, 2012 | http://pubs.acs.org
Publication Date (Web): April 30, 2010 | doi: 10.1021/bk-2010-1040.ch001

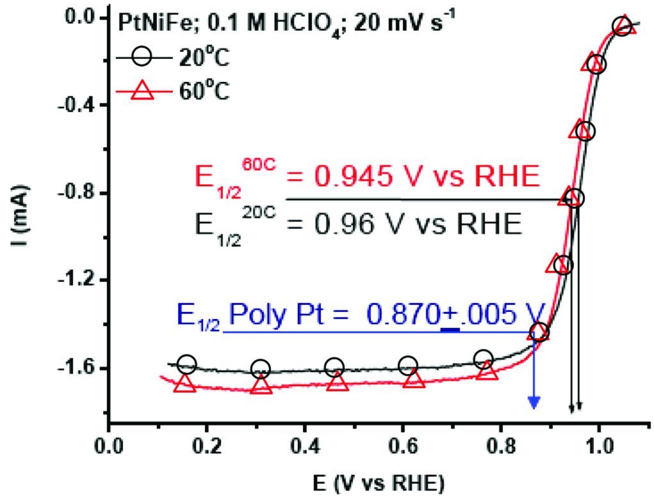

Figure 1. RDE results from ANL demonstrating >50 mV increase in ½ wave potential for the 3M PtNiFe alloy over polycrystalline Pt.

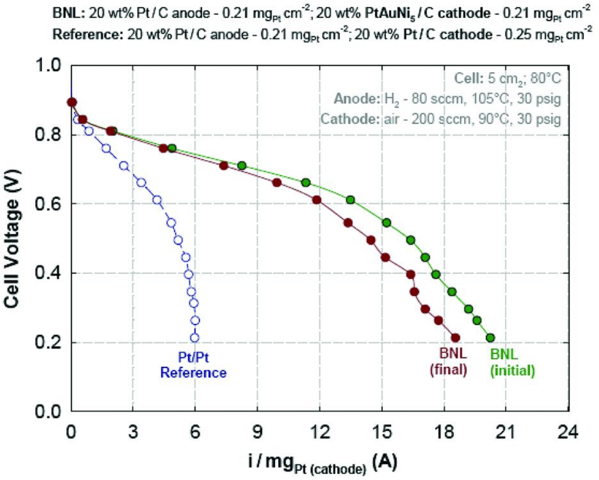

Figure 2. Comparison of $PtAuNi_5$ core-shell catalyst to Pt/C showing greater than twice the current per gram of Pt for the $PtAuNi_5$ core-shell catalyst.

able to suppress H_2O_2 formation and promote the 4 e- ORR in a catalyst with no metal present (*17*). Activity was increased further when the carbon-free catalyst was used as a support for a carbon composite catalyst formed from pyrolysis of a CoFe-C-N non-PGM catalyst. Activity increased further upon acid leaching of this catalyst (see Figure 4). No metal atoms or particles were observable on the surface, although metal atoms covered by several graphene layers were observed (*17*). Significant questions remain for the non-PGM catalysts, including questions regarding the identity of the active site and the role of the transition metals and

Downloaded by 89.163.35.42 on June 21, 2012 | http://pubs.acs.org
Publication Date (Web): April 30, 2010 | doi: 10.1021/bk-2010-1040.ch001

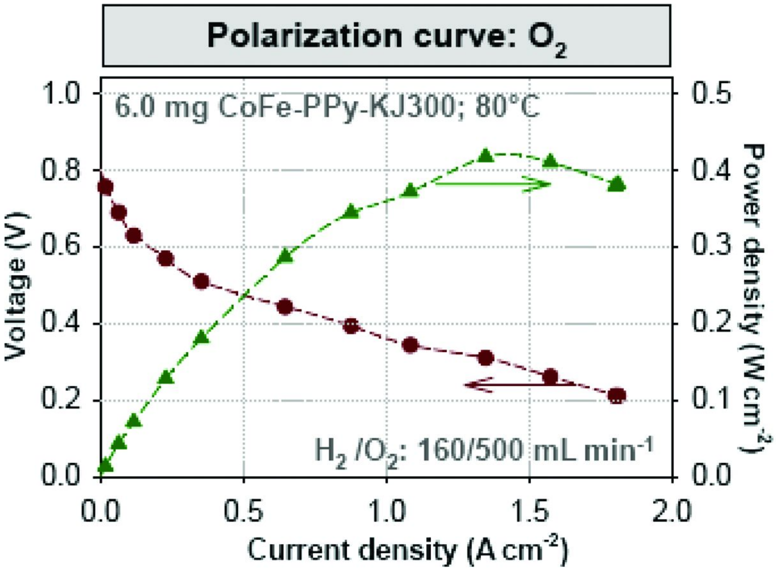

Figure 3. MEA performance of LANL FeCo/C-polypyrrole catalyst demonstrating power density of > 400 mW/cm².

nitrogen in the catalysts. The activity of non-PGM catalysts is still short of the targets.

Another area to reduce costs, especially at low manufacturing volumes, is membranes. In addition, improvements in membrane properties, particularly improved conductivity under low RH and at higher temperatures, can indirectly reduce system costs by reducing or eliminating the need for external humidifiers and reducing the size of the thermal management system. DOE has supported research to develop new membranes that can operate at high temperature (120°C) and low RH. Three main strategies and combinations of these strategies are being pursued: (1) control of polymer and membrane structure to control phase segregation and optimize the hydrophilic region where proton conduction takes place, while managing the hydrophobic region to obtain the mechanical properties needed; (2) utilizing materials such as inorganic oxides, heteropolyacids, or ionic liquids that which have potential for nonaqueous proton conduction, so the conduction mechanism does not rely on water at conditions where water may be scarce; and (3) use of hydrophilic additives to help retain water at high temperature so the water content in the membrane will be sufficient to conduct water at high temperature and low RH.

One approach for phase segregation utilizes sulfonated rigid rod liquid crystalline polymers. Bulky or angled comonomer units attached to the rigid backbone force the chains apart, creating pores lined with sulfonic acid groups. This structure creates a hydrophilic region (pores lined with sulfonic acid groups) with high concentrations of acid groups. The controlled architecture allows the polymer to hold water tightly in the regions between the hydrophobic backbones, generating high conductivity even at low RH. Case Western Reserve University

Downloaded by 89.163.35.42 on June 21, 2012 | http://pubs.acs.org
Publication Date (Web): April 30, 2010 | doi: 10.1021/bk-2010-1040.ch001

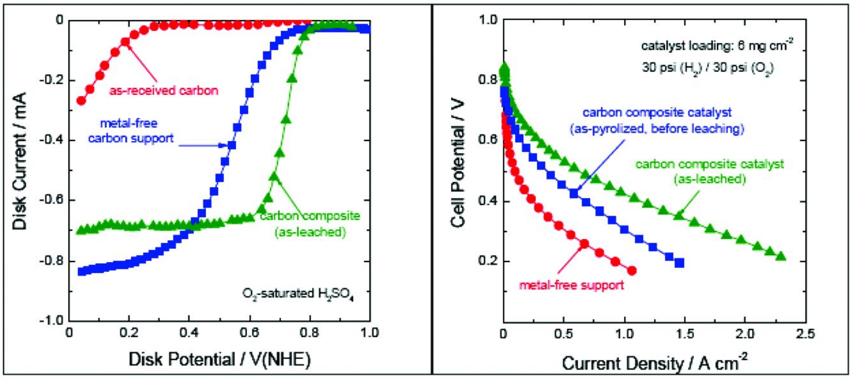

Figure 4. RDE and MEA demonstrating activity of University of South Carolina metal-free carbon and carbon composite catalyst.

achieved proton conductivity exceeding 0.1S/cm at 120°C and 50% RH using a graft copolymer of poly(p-biphenyldisulfonic acid) with di-t-butylphenol. See Figure 5 (*18*). However, the mechanical properties of these systems have been unsatisfactory to date.

Researchers have also developed composite membranes, which control phase segregation by providing proton conduction functionality by one polymer and the mechanical properties by another, with proton conductivity reaching ~ 0.1S/cm at 120°C and 50% RH. Examples of these membranes include two approaches: electrospun fibers of ionomer to form a conductive mat that is filled with an inert matrix for stability, and a porous inert matrix ((either 2D grids with patterned holes or 3D mesh) filled with ionomer (*19*, *20*). These approaches allow the use of lower equivalent weight PFSA materials with higher conductivity that would be unstable on their own. Using the dimensionally stabilized membrane, Giner achieved .093 S/cm at 120°C and 50% RH (*20*).

DOE has seen the most success using this first strategy (phase segregation control), but has made some progress using the second and third strategies. Colorado School of Mines (CSM) has seen some success using strategy 2, non-acqueous proton conduction. CSM's approach investigates membranes prepared by immobilizing heteropolyacids through crosslinking the heteropolyacids with organic linkers. CSM has successfully prepared new ionomers, dubbed polyPOMs, using this technique. Recent work has focused on using the lacunary heteropolyacid $H_8SiW_{11}O_{39}$. Using 80% of the heteropolyacid monomer and 20% of a comonomer, butyl acrylate, CSM has prepared a film with a conductivity of 0.1 S/cm at 120°C and 50% RH (as measured by both CSM and their partner 3M) (*21*), but this achievement has yet to be verified by independent testing.

The third strategy for conduction at high temperature and low RH utilizes hydrophilic additives that can provide some water for conduction at high temperature. Florida Solar Energy Center (FSEC) at the University of Central Florida has improved the conductivity of Nafion with a phosphotungstic acid (PTA) additive. FSEC has demonstrated a conductivity of 0.06S/cm at 120°C and 50% RH (*22*). FSEC also demonstrated improved durability with the PTA additive (*22*).

Durability

Research and technical validation projects have demonstrated membrane, stack, and fuel cell system durability approximately 50% greater than previously reported. Automotive fuel cell systems are being tested in vehicles under real-world driving conditions in the Technical Validation program. Fuel cell system lifetimes have been predicted based on measured performance degradation over time, and extrapolating the results to a point of 10% voltage drop for the stack output. The maximum stack lifetime projected through this program has increased to 1900 hours (*23*). In addition to the maximum projected lifetime, the maximum demonstrated lifetime, average lifetime, and average projected lifetime have all increased.

To increase system durability further, DOE-sponsored efforts have focused on improving the durability of the system components. Catalyst degradation is one of the main contributors to the observed degradation in fuel cell performance. Particle growth and sintering, catalyst dissolution, and corrosion of the carbon support all contribute to performance degradation. Potential cycling conditions accelerate catalyst sintering and dissolution. Pt alloys are being investigated for improved durability, as well as increased activity.

Recent advances in membrane and catalyst technology have led to improved durability while lowering PGM loading to 0.2 mg/cm^2. Figure 6 presents the durability improvement using these techniques over higher-loading and unstabilized MEAs. Traditional Pt/C catalysts with traditional membranes failed in 200-600 hours of testing under load cycling conditions. 3M improved catalyst durability using its NSTF PtCoMn catalysts while still using traditional PFSA membranes without chemical stabilization, increasing the MEA durability to ~ 3500 hours. 3M achieved further improvements in MEA durability by combining their PFSA ionomer with mechanical stabilization to decrease swelling and shrinking during cycling. With this approach, 3M increased the durability to beyond 7300 hours (*11*). This feat represents significant progress in MEA durability; however these improvements must still be demonstrated in a stack and under real-world driving conditions which include start-up/shut-down cycles.

In addition to demonstrated improvements in performance and durability, there have been significant advances in characterization techniques and the fundamental understanding of degradation mechanisms. At Oak Ridge National Laboratory (ORNL), researchers using Transmission Electron Microscopy (TEM) have quantified Pt and Pt alloy particle growth in operating fuel cells, a key cause of fuel cell performance degradation. Figure 7 shows the changes in particle size for a PtCo alloy under various cycling conditions (*24*). Using Z-contrast Scanning TEM they have observed Pt particle coalescence during heating of a Pt/C system. From their observations they concluded that Pt particle growth did not occur by dissolution/reprecipitation in this system, but by Pt particles moving across the C

Downloaded by 89.163.35.42 on June 21, 2012 | http://pubs.acs.org
Publication Date (Web): April 30, 2010 | doi: 10.1021/bk-2010-1040.ch001

Downloaded by 89.163.35.42 on June 21, 2012 | http://pubs.acs.org
Publication Date (Web): April 30, 2010 | doi: 10.1021/bk-2010-1040.ch001

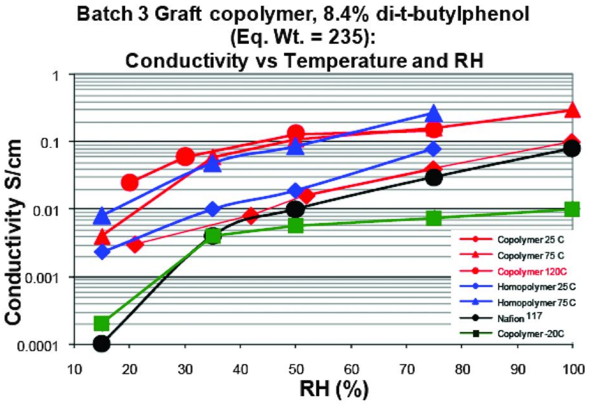

Figure 5. Conductivity of rigid rod liquid crystalline polymers at various relative humidities demonstrating high conductivity at low relative humidity.

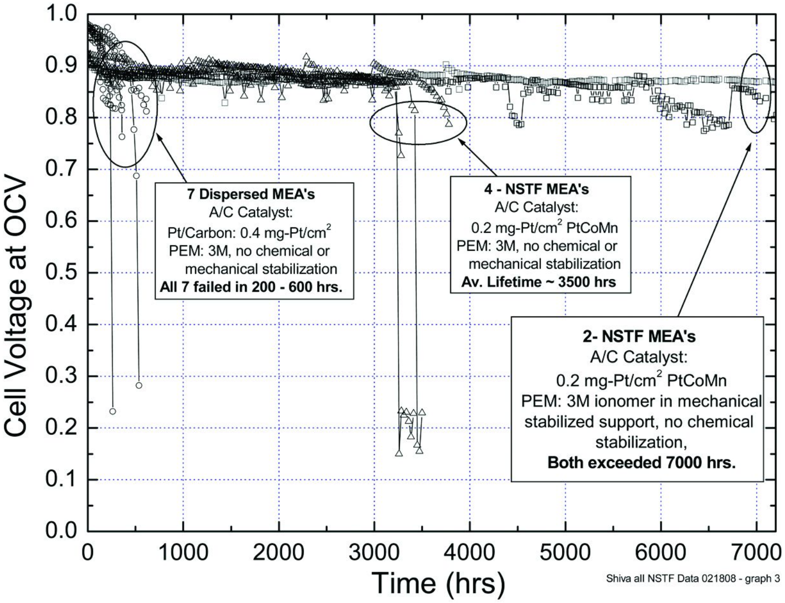

Figure 6. Accelerated durability test results demonstrating >7000 h durability under cycling conditions for 3M NSTF MEA.

surface and coalescing with nearby particles to form larger single crystal particles (*25*). This technique offers potential for new insight into catalyst degradation.

Using neutron imaging, researchers at Los Alamos National Laboratory (LANL) have elucidated potential pathways for fuel cell performance improvements through in situ studies of the effects of gas diffusion layer (GDL) design parameters on the water transport behavior of fuel cells (*26*). Neutron imaging and computational fluid dynamics (CFD) results show accumulation

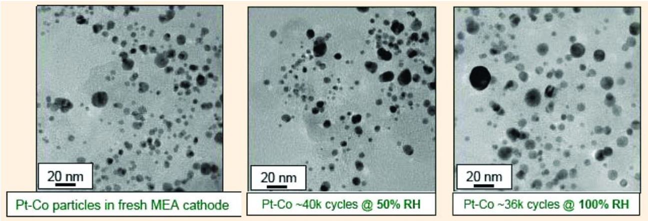
20 nm
Pt-Co particles in fresh MEA cathode
20 nm
Pt-Co ~40k cycles @ 50% RH
20 nm
Pt-Co ~36k cycles @ 100% RH

Figure 7. The effect of Relative Humidity (RH) on Pt particle size during potential cycling.

of water at the lands. Water content calculated by the CFD calculations closely matches the measured water via neutron imaging. In addition, this work has also revealed GDL degradation mechanisms.

Although the research at LANL has led to a greater understanding of material effects on water transport, more research is needed in this area to meet commercialization requirements. The stresses of freeze/thaw conditions and start-up and shut-down cycles continue to exacerbate degradation of fuel cell components (*27*). In addition, insufficient water transport can lead to performance degradation for MEAs. Therefore, the fuel cell research community requires a greater understanding of mass transport fundamentals, especially water transport, and new or improved MEA materials based on this fundamental understanding.

Conclusions

While recent advances have been impressive, cost, durability, and performance remain as key challenges to fuel cell technology. Catalysts remain the major cost factor at high production volumes.

At current Pt costs, the catalytic activity must be increased and Pt loading must be decreased to meet cost targets for automotive fuel cells. Recent work has been successful at reducing Pt loading using ternary alloys and by utilizing structured particles with an onion layer approach. Despite these advances, PGM loadings likely will have to be reduced further -- significantly below the current DOE targets -- if fuel cell cost targets are to be met. Consequently, future work should target ultra-low PGM or non –PGM catalysts. Recent work in the area of non-PGM catalysts at LANL, University of South Carolina and 3M has shown significant improvement in activity and durability. Further improvements are needed to make these systems viable in an automotive fuel cell.

Improvements in membrane performance, and in particular membrane performance at high temperature without external humidification, are key to reducing overall fuel cell system costs. Recent advances have improved conductivity at 120°C and reduced the humidification level needed, while still maintaining conductivity at low temperature. Several approaches exceed conductivities of 0.1S/cm at 120°C and relative humidities below 70% RH, showing potential for achieving DOE's ultimate goals. However, durability remains to be proven.

Downloaded by 89.163.35.42 on June 21, 2012 | http://pubs.acs.org
Publication Date (Web): April 30, 2010 | doi: 10.1021/bk-2010-1040.ch001

References

1. Vogel, J. U.S. DOE Hydrogen Program 2008 Annual Progress Report. http://www.hydrogen.energy.gov/pdfs/progress08/v_d_4_vogel.pdf.
2. *Transportation Energy Data Book*, 27th ed.; ORNL-6981; Oak Ridge National Laboratory: Oak Ridge, TN, 2008; pp 1−16.
3. Learning Demonstration Vehicle Greenhouse Gas Emissions. http://www.nrel.gov/hydrogen/docs/cdp/cdp_62.ppt#494,1,CDP#62.
4. Multi-Year Research, Development and Demonstration Plan, Hydrogen, Fuel Cells & Infrastructure Technologies Program, October 2007, Table 3.4.2.
5. Hydrogen and Fuel Cell Technical Advisory Committee to the Department of Energy, Hydrogen and Fuel Cell Technical Advisory Committee Biennial Report to the Secretary of Energy (September 2007), retrieved August 27, 2008, from http://www.hydrogen.energy.gov/pdfs/htac_letter_report_attach.pdf.
6. Garland, N.; Marcinkoski, J. DOE Hydrogen Program Record #8019. http://hydrogen.energy.gov/pdfs/8019_fuel_cell_system_cost.pdf.
7. Garland, N. 2008 Fuel Cell Seminar Paper GHT 33-1. http://www.fuelcellseminar.com/2008_presentations.
8. Motupally, S., UTC Power. Personal communication to Benjamin, T., Argonne National Laboratory. September 19, 2007.
9. Schneider, J.; Rigolo, M.; Knights, S.; Hicks, M.; Escobedo, G.; Nelson, E.; Collins, W.; Taha, E.; Iiyama, A. An Automotive Perspective on Durability Protocol Challenges from Single Cells to Fuel Cell Vehicle Systems. Durability & Performance Conference, Florida, 2007 Iiyama. http://www.usfcc.com/members/An%20Automotive%20Perspective%20on%20Durability%20Protocol%20Challenges%20from%20Single%20Cells%20to%20Fuel%20Cell%20Vehicle%20Systems_Final%20Release.pdf.
10. Wessel, S., Ballard Power Systems. Personal communication to Benjamin, T., Argonne National Laboratory. September 20, 2007.
11. Stamenkovic, V. R.; Fowler, B.; Mun, B. S.; Wang, G.; Ross, P.; Lucas, C. A.; Markovic, N. M. *Science* **2007**, *317*, 493–496.
12. Debe, M. U.S. Department of Energy Hydrogen Program 2008 Annual Merit Review Proceedings. http://www.hydrogen.energy.gov/pdfs/review08/fc_1_debe.pdf.
13. Adzic, R.; Atanassova, P.; Atanassov, P.; More, K.; Myers, D.; Wieckowski, A. ; Yan, Y.; Zelenay, P. U.S. Department of Energy Hydrogen Program 2008 Annual Merit Review Proceedings. http://www.hydrogen.energy.gov/pdfs/review08/fc_3_zelenay.pdf.
14. Myers, D. U.S. Department of Energy Hydrogen Program 2008 Annual Merit Review Proceedings. http://www.hydrogen.energy.gov/pdfs/review08/fc_2_myers.pdf.
15. Atanasoski, R. U.S. Department of Energy Hydrogen Program 2008 Annual Merit Review Proceedings. http://www.hydrogen.energy.gov/pdfs/review07/fc_4_atanasoski.pdf.

Downloaded by 89.163.35.42 on June 21, 2012 | http://pubs.acs.org
Publication Date (Web): April 30, 2010 | doi: 10.1021/bk-2010-1040.ch001

16. Zelenay, P. U.S. Department of Energy Hydrogen Program 2008 Annual Merit Review Proceedings. http://www.hydrogen.energy.gov/pdfs/review08/fc_3_zelenay.pdf.
17. Popov, B. U.S. Department of Energy Hydrogen Program 2008 Annual Merit Review Proceedings. http://www.hydrogen.energy.gov/pdfs/review08/fcp_15_popov.pdf.
18. Litt, M. U.S. Department of Energy Hydrogen Program 2008 Annual Merit Review Proceedings. http://www.hydrogen.energy.gov/pdfs/review08/fc_19_litt.pdf.
19. Pintauro, P. U.S. Department of Energy Hydrogen Program 2008 Annual Merit Review Proceedings. http://www.hydrogen.energy.gov/pdfs/review08/fc_20_pintauro.pdf.
20. Mittelsteadt, C. K.; Braff, W.; Chen, M.; VanBlarcom, S.; Liu, H.. U.S. Department of Energy Hydrogen Program 2008 Annual Merit Review Proceedings. http://www.hydrogen.energy.gov/pdfs/review08/fc_24_mittelsteadt.pdf.
21. Herring, A., CSM. Personal communication to Kopasz, J., Argonne National Laboratory. January 25, 2009.
22. Fenton, J. U.S. Department of Energy Hydrogen Program 2008 Annual Merit Review Proceedings. http://www.hydrogen.energy.gov/pdfs/review08/fc_15_fenton.pdf.
23. Wipke, K. 2008 Fuel Cell Seminar. http://www.fuelcellseminar.com/pdf/2008/wednesdayPM/02_Wipke_K_DEM33-3.ppt.pdf.
24. More, K. L.; Reeves, S.; Blom, D. U.S. DOE Hydrogen Program, 2007 Annual Merit Review Proceedings. http://www.hydrogen.energy.gov/pdfs/review07/fc_3_more.pdf.
25. More, K. L.; Allard, L.; Reeves, S. U.S. DOE Hydrogen Program, 2008 Annual Merit Review Proceedings. http://www.hydrogen.energy.gov/pdfs/review08/fc_9_more.pdf, 2008 AMR.
26. Borup, R.; Mukundan, R.; Davey, J.; Wood, D.; Springer, T.; Kim, Y. S.; Spendelow, J.; Rockward, T.; Pivovar, B.; Arif, M.; Jacobsen, D.; Hussey, D.; Chen, K.; More, K.; Wilde, P.; Zawodzinski, T.; Gurau, V.; Johnson, W.; Cleghorn, S. U.S. DOE Hydrogen Program 2007 Annual Progress Report. http://www.hydrogen.energy.gov/pdfs/progress07/v_r_3_borup.pdf.
27. Jarvi, T. DOE Fuel Cell pre-solicitation workshop, Jan. 23−24, 2008. http://www1.eere.energy.gov/hydrogenandfuelcells/pdfs/fuelcell_pre-solicitation_wkshop_jan08_jarvi.pdf.

Downloaded by 89.163.35.42 on June 21, 2012 | http://pubs.acs.org
Publication Date (Web): April 30, 2010 | doi: 10.1021/bk-2010-1040.ch001

Downloaded by UNIV OF DELAWARE MORRIS LIB on June 21, 2012 | http://pubs.acs.org
Publication Date (Web): April 30, 2010 | doi: 10.1021/bk-2010-1040.ch002

Chapter 2

Membranes for PEM Fuel Cells

3M Research Activities

Michael A. Yandrasits and Steven J. Hamrock*

3M Fuel Cell Components Program, 3M Center 201-1W-28, St. Paul, MN 55144, USA
***sjhamrock@mmm.com**

Proton exchange membrane fuel cells (PEMFC) are a promising technology for use in a variety of applications, including automotive, stationary and portable power systems. Although many technical advances have been made in the past few years, PEMFCs have still not found widespread use. Major barriers to PEMFC commercialization include the need for substantial external system humidification and careful temperature control. The absence of these controls can result in poor performance and durability. A key weak point in this regard is the polymer electrolyte membrane. For this reason, effort is being focused on the development of membranes with improved performance and durability under hotter, drier operating conditions. Work at 3M on methods of providing increased membrane conductivity and durability is discussed.

Introduction

Perfluorsulfonic acid (PFSA) membranes have found use in modern proton exchange membrane (PEM) fuel cells. These membranes have excellent proton conductivity, mechanical strength, and chemical stability. Fuel cell systems are commercially available based on these membranes in several markets including telecommunications back up power, stationary power generation, and microelectronic applications. Several hundred prototype vehicles have also been made and are in test at various locations around the United States (*1*). This work demonstrates the potential for fuel cell vehicles but the technology

In Fuel Cell Chemistry and Operation; Herring, A., et al.;
ACS Symposium Series; American Chemical Society: Washington, DC, 2010.

is yet to be commercialized for automobiles. One barrier, among many, to this commercialization is the requirement that PFSA membranes be hydrated or mostly hydrated for optimum performance. In addition, a practical limitation to humidifying the hydrogen and air streams has resulted in a temperature limit of about 80°C. Therefore a critical area of research is focused on developing membranes that can operate at conditions with little or no humidification and at temperatures up to 120°C. The following chapter will outline the issues associated with this research and give some examples of the approaches being used in 3M's Fuel Cell Components Program to develop new membranes that can meet the requirements of the automobile industry.

Downloaded by UNIV OF DELAWARE MORRIS LIB on June 21, 2012 | http://pubs.acs.org
Publication Date (Web): April 30, 2010 | doi: 10.1021/bk-2010-1040.ch002

The Problem

Proton exchange membranes serve three basic functions; 1) conduct protons from the anode to the cathode, 2) be electrically insulating, and 3) provide a barrier that prevents the reactant gases from mixing. Implicit in this list is the additional requirement that the membrane have suitably long lifetimes for the desired application. This usually means that the polymer have hydrolytic and oxidative stability and have good mechanically integrity.

In addition to these basic requirements modern PFSA membranes need to be humidified in order to achieve maximum performance and durability. This requirement has several drawbacks such as the additional expense of humidifiers and parasitic power losses from their operation, dilution of hydrogen and air with water vapor, and since the fuel cell itself produces water, the situation can exist where mass transport or "flooding" occurs at high current densities (liquid water begins to collect in catalyst layer and current collector and limits access of gases to catalyst). All of these issues result in increased system complexity.

Related to the water management requirements are temperature requirements. Because the current membranes need the incoming gases to be nearly 100% relative humidity, the fraction of water in these gases rapidly increases as the operating temperature approaches 100°C. This becomes a practical limit especially at low gas pressures.

If operating temperatures of 120° to 150°C could be achieved the system becomes simpler due to factors such as improved resistance of the catalyst to carbon monoxide and other poisons, improved heat rejection, and in some cases, increased efficiency as a result of combined heat and power.

For the reasons outlined above and others there is a significant need for membranes that depend less on water for conductivity, allowing hotter and drier operating conditions. The United States Department of Energy (DOE) working with input from the automobile industry and fuel cell component manufacturers have established performance targets of 100 mS/cm at 120°C and 20-40% relative humidity (*2*).

Downloaded by UNIV OF DELAWARE MORRIS LIB on June 21, 2012 | http://pubs.acs.org
Publication Date (Web): April 30, 2010 | doi: 10.1021/bk-2010-1040.ch002

3M's Approach

3M Ionomer Basics

Due to the success of PFSA based membranes, we have chosen this system to build upon to meet the new targets. Figure 1 shows the structure for the 3M ionomer and DuPont's widely used Nafion ™ ionomer.

The chemical structures are similar for these two polymers with the 3M ionomer having a lower monomer molecular weight. One consequence of using the shorter side chain is the slightly higher levels of TFE monomer that can be incorporated for the same equivalent weight. This relationship is shown in Figure 2 where the weight percent TFE is plotted against equivalent weight in g/mol. An arbitrary comparison is made at an EW of about 800 g/mol.

As expected, the overall crystallinity is higher for the 3M ionomer due to the higher TFE levels. Figure 3 shows the wide angle X-ray diffraction pattern for two ionomers that have an EW of about 1,000 g/mol. The 3M ionomer has a larger shoulder on the amorphous halo with a spacing of about 5 angstroms. This result is consistent with other researchers that have characterized ionomers such as Nafion™ as a function of EW (*3*).

Even though these polymers are generally very low in percent crystallinity, it is believed that the crystalline regions act as physical crosslinks. These domains are, in part, responsible for the physical integrity of the membranes when swollen in water at high humidity or in the presence of liquid water. The amount of crystallinity is dependant on equivalent weight where the lower EW polymers will necessarily have low crystallinity and, at some EW value, the crystallinity will disappear entirely (*4*).

The Low EW Path

One approach to increasing the conductivity of PEMs is to lower the equivalent weight (i.e. increase the acid content). Figure 4 shows the proton conductivity of a series of 3M ionomers with varying equivalent weights. The samples were held at a constant dew point of 80°C. The conductivity was then measured as a function of temperature while maintaining the dew point at the 80°C level. The bottom X-axis shows the cell temperature and the top axis the calculated relative humidity for this series.

The conductivity decreased for each membrane as the temperature increased and the relative humidity decreased in this experiment. It is expected that lower EW ionomers would have higher proton conductivity. For the data shown below, the 640 EW ionomer has a conductivity of nearly three times that of the 980 EW sample at the 120°C cell temperature and 80°C dew point.

A similar experiment was conducted on another series of these membranes where the conductivity was measured at a constant temperature of 30°C while the relative humidity was increased from 40 to 100% RH. Figure 5 shows the results of this experiment for the membranes with EWs between 650 and 1100 g/mol.

In Fuel Cell Chemistry and Operation; Herring, A., et al.;
ACS Symposium Series; American Chemical Society: Washington, DC, 2010.

Downloaded by UNIV OF DELAWARE MORRIS LIB on June 21, 2012 | http://pubs.acs.org
Publication Date (Web): April 30, 2010 | doi: 10.1021/bk-2010-1040.ch002

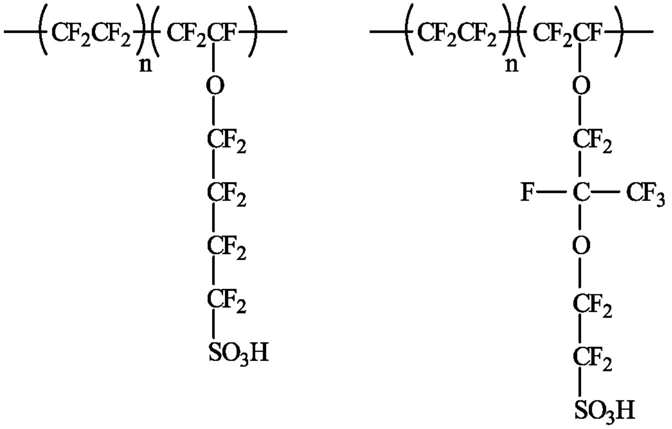

Figure 1. Chemical Structure for the 3M ionomer (left) and DuPont's Nafion™ ionomer (right)

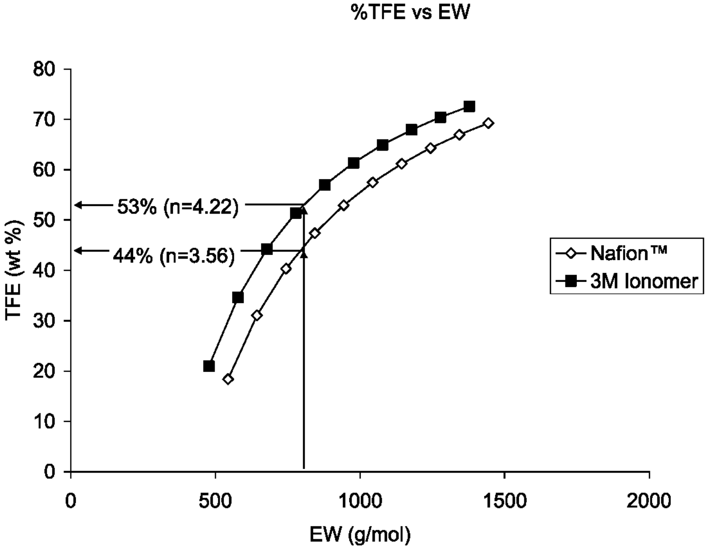

Figure 2. Weight percent TFE plotted against equivalent weight for 3M ionomer and Nafion™

Both experiments demonstrate the benefit of the lower EW ionomer in regard to increase proton conductivity at lower humidities.

The following graph was generated in order to fully appreciate the impact of these conductivity values on the performance of a fuel cell that is operated under conditions of low relative humidity. Figure 6 shows the loss in performance calculated from the measured conductivity data. At the lower temperatures where the cell temperature and the dew point are the same, 80°C, there is little difference between samples and the benefit of the low EW ionomers is nearly insignificant.

Downloaded by UNIV OF DELAWARE MORRIS LIB on June 21, 2012 | http://pubs.acs.org
Publication Date (Web): April 30, 2010 | doi: 10.1021/bk-2010-1040.ch002

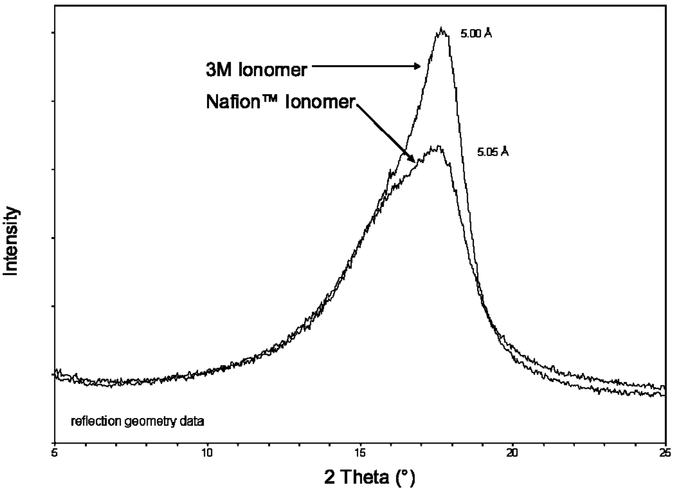

Figure 3. Wide angle X-ray diffraction for 3M ionomer and Nafion™ at 1,000 EW

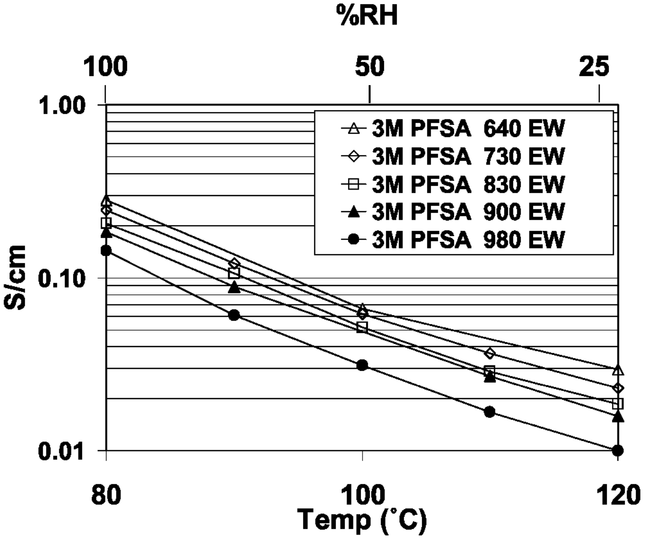

Figure 4. Conductivity as a function of temperature for a series of 3M ionomer membranes held at a constant dew point of 80°C

However, when the cell temperature is increased to 120°C the difference in performance between the 980 EW membrane and the 733 EW sample is about 100 mV.

The relationship in Figure 6 also shows that even the 733 EW ionomer membrane has a loss of performance of about 70 mV at the 120°C condition as compared to the 80°C fully saturated case. Additional work is needed in order to reduce or eliminate this performance loss.

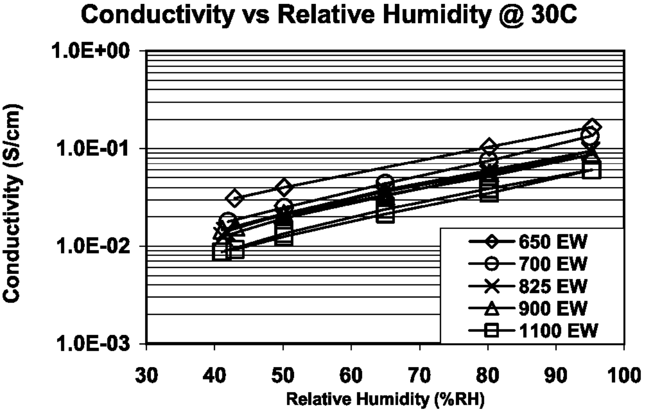

Figure 5. Conductivity as a function of relative humidity for a similar range of EW membranes at 30°C

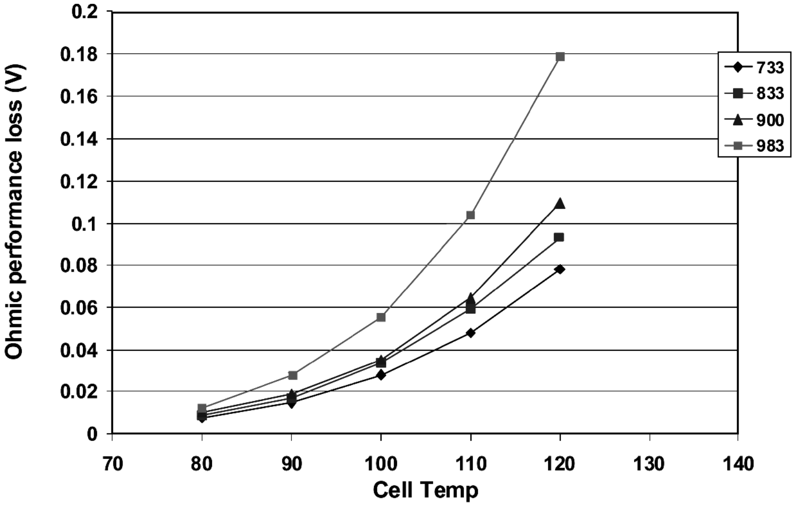

Figure 6. Loss in performance calculated for a series of 3M ionomer membranes (25 μm thick) of different EW as a function of cell temperature at a constant dew point (80°C).

Since the above data shows the dramatic improvements in conductivity and performance that are possible by making very low EW ionomers, it is logical to consider the EW necessary in order to achieve the targets set out by the DOE and the automobile industry. Figure 7 shows the conductivity as a function of equivalent weight for membranes measured at three different humidities.

By using PFSA ionomers with EWs below about 600 g/mol the DOE targets could, in principle, be met. However, equivalent weights much lower than this start to approach the molecular weight of the 3M monomer of 380g/mol. In reality, the vinyl ether monomer does not homopolymerize well and the perfectly

Downloaded by UNIV OF DELAWARE MORRIS LIB on June 21, 2012 | http://pubs.acs.org
Publication Date (Web): April 30, 2010 | doi: 10.1021/bk-2010-1040.ch002

Downloaded by UNIV OF DELAWARE MORRIS LIB on June 21, 2012 | http://pubs.acs.org
Publication Date (Web): April 30, 2010 | doi: 10.1021/bk-2010-1040.ch002

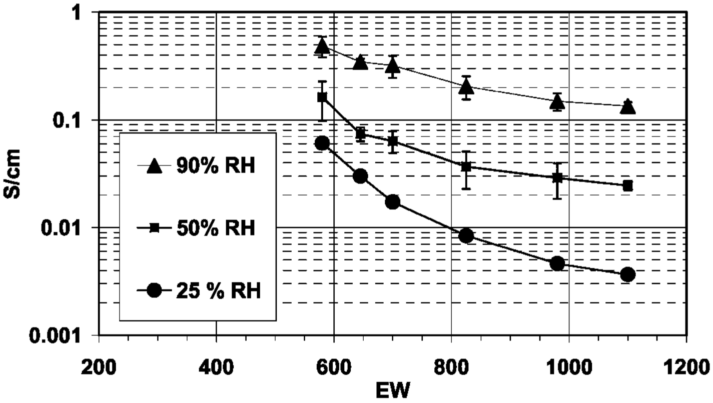

Figure 7. Conductivity at 80°C as a function of EW for membranes measured at 25%, 50%, and 90% relative humidities.

alternating polymer of the vinyl ether monomer and TFE is a more realistic lower limit of about 480 g/mol. It is interesting to note that the conductivity at low RH (25%) increases at a faster rate as the EW is lowered compared to the higher RH conditions (90%).

Ultra Low EW Polymers

Since the traditional PFSA chemistry has a lower limit in achievable equivalent weights we are looking for strategies that allow the incorporation of more acid groups per repeat unit. One way to accomplish this goal is to use the sulfonyl fluoride precursor as a reactive group for attaching additional acid functional groups. Figure 8 shows the structure of a sulfonimide made by reacting the sulfonyl fluoride form of the polymer with ammonia to make the sulfonamide followed by reacting with benzene sulfonyl chloride to make the sulfonimide.

The proton on the nitrogen is acidic making this polymer an ionomer by itself. The analogous polymer made with bis[(perfluoroalkyl)sulfonyl]imide-based ionomer has been well characterized as a fuel cell membrane (*5*).

In the case shown in Figure 8 it is expected that the proton on the nitrogen is less acidic that the bis-perfluoro imide. However, one could imagine additional acid functionality that can be attached to the benzene ring (R) thereby reducing the EW of the polymer to values lower than could be achieved by simply increasing the mole fraction of the sulfonic acid vinyl ether monomer.

This approach is not without challenges. Synthetic routes for high volumes have yet to be developed. And the thermal and oxidative stability of these compounds may not be suitable for the aggressive durability targets. Nonetheless, if these concerns can be addressed, polymers based on a PFSA precursor have the potential to be viable ultra low EW ionomers.

Downloaded by UNIV OF DELAWARE MORRIS LIB on June 21, 2012 | http://pubs.acs.org
Publication Date (Web): April 30, 2010 | doi: 10.1021/bk-2010-1040.ch002

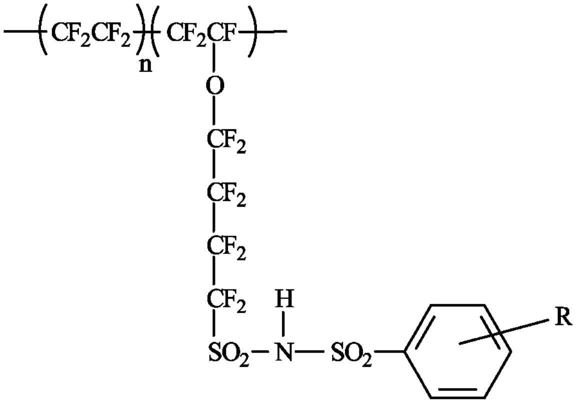

Figure 8. One example of a way to add additional acid groups (R) to an existing PFSA precursor polymer.

The Physical Side of Ultra Low EW Polymers

Increasing the total acid content (i.e. lowering the EW) is an effective strategy for increasing the proton conductivity in PFSA based ionomers. However, the membrane must also serve as a barrier that prevents the reactant gases from mixing. One consequence of the increased acid levels is an increase in the amount of water that the membrane absorbs when humidified. Figure 9 shows the length change versus time for a series of membranes held at 25°C and 50% RH for 4 hours followed by an increase in the humidity to 100% RH over the next 4 hours with a final 2 hour hold at 100% RH.

As expected, the change in length is greatest for the lowest EW membranes. In addition the membranes continue to swell even after the RH reaches 100%. This indicates that the time it takes for these samples to reach an equilibrium amount of water may also be greater. The relationship between water uptake and humidity is not linear. Figure 10 shows the change in length plotted as a function of EW for the data shown in Figure 9.

The data can be fit with a power function with a high degree of correlation. The implications of this data are that membranes with equivalent weights low enough to meet the automotive and DOE targets will likely swell to a very large extent.

This type of swelling presents another problem in the form of mechanical fatigue as the membranes cycle between wet and dry conditions. A quantitative analysis of this effect is difficult to describe but qualitatively one can understand that a membrane that is cycled between 0 and 15% length change is likely to experience more fatigue and failure compared to a similar polymer cycled between 0 and 5% length change.

In addition to the excessive swelling of low EW ionomers these polymers will become water soluble below some critical equivalent weight. Figure 11 shows the results of a water solubility experiment. In this study membranes were boiled in

Downloaded by UNIV OF DELAWARE MORRIS LIB on June 21, 2012 | http://pubs.acs.org
Publication Date (Web): April 30, 2010 | doi: 10.1021/bk-2010-1040.ch002

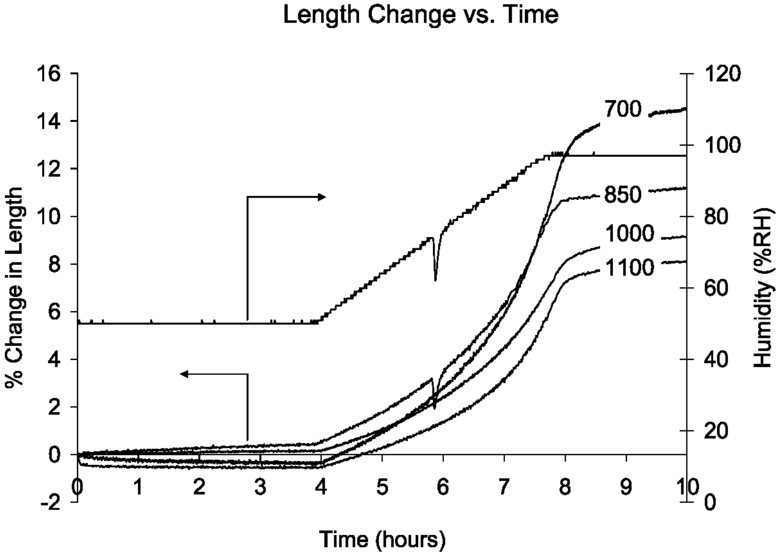

Figure 9. Change in length vs. time for a series of membranes of differing EW. The relative humidity is ramped from 50% to 100% between hours 4 and 8.

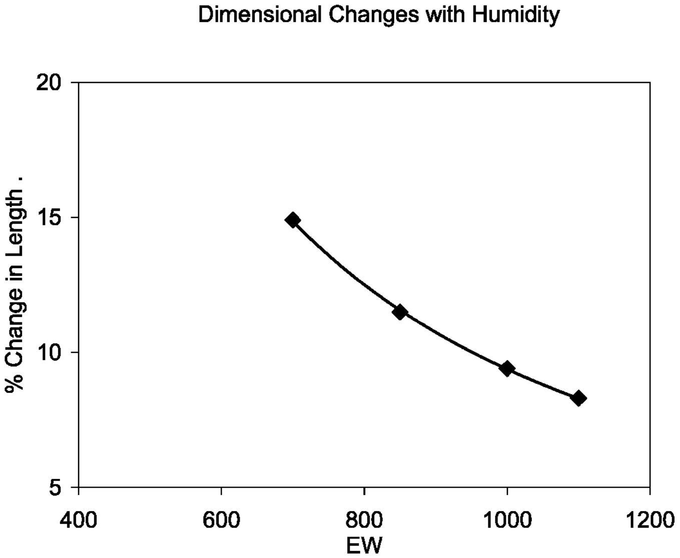

Figure 10. Dimensional changes in both length for a series of membranes measured between 50% ad 100% RH.

deionized water for 30 minutes. A coarse filter was used to remove the swollen membrane pieces from the liquid water. The solids content of the liquid was measured and used to calculate the soluble fraction of the membrane.

Downloaded by UNIV OF DELAWARE MORRIS LIB on June 21, 2012 | http://pubs.acs.org
Publication Date (Web): April 30, 2010 | doi: 10.1021/bk-2010-1040.ch002

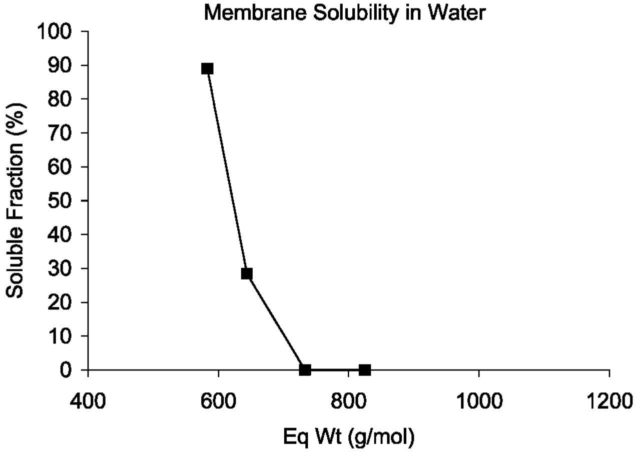

Figure 11. Water solubility of 3M Ionomer membranes in boiling water as a function of equivalent weight.

This experiment shows that membranes made from 3M ionomer have essentially no solubility in water when the EW is above about 700 g/mol. Below this value the soluble fraction rapidly increases and the polymer is almost completely soluble in hot water at EWs below about 550 g/mol.

While the performance targets are often considered to be relevant under hot and dry conditions, this result is significant since it is expected that liquid water will be present in the fuel cell at various operating conditions such as start up, shut down, or high current.

Crosslinking Strategies

The previous section outlined one of the main issues associated with ultra low equivalent weight ionomers. Namely that EWs low enough to meet the DOE and automotive targets will likely swell to an unacceptable extent or even dissolve in liquid water. One way to minimize these effects is to crosslink the ionomer after it has been formed into the membrane film. In addition to reduced swelling, crosslinking could also improve the membranes mechanical properties such as the alpha transition (*6*). There have been many publications and patents in this area (*7–10*) but to date there are no commercialized crosslinked PFSA ionomers.

In order for a crosslinking system to be viable the chemical links should have the oxidative and hydrolytically stable, preferably as stable as the ionomer polymer itself. Devising a crosslink with this type of stability is one of the main challenges in this area. In the mean time, much can be learned about the benefits of crosslinked PFSA membranes even if the links are not stable enough to be used for extended periods of time in a fuel cell.

Figure 12 shows the generalized structure of a PFSA ionomer that contains a latent reaction site.

The "X" represents any number of groups that can be reacted after the membrane is formed. Possibilities include a nitrile group (*6*), a double bond (*8*, *9*), or a halogen (*7*).

Figure 13 shows the generalized reaction one might do with this type of polymer. The reaction conditions will be dependent on the specific chemistry chosen.

We have successfully crosslinked one PFSA ionomer in our labs using a reaction scheme based on that shown in Figure 12. In this case we compounded 100 parts of a PFSA precursor (EW about 900 g/mol) that contained 3 mol percent of a cure site monomer with 1.4 parts of a peroxide initiator and 2.8 parts of a trifunctional crosslinker.

Figure 14 shows the results of a cure experiment where about 15 grams of the compounded polymer was placed in a Monsanto Rheometer at 177°C. The sample is compressed between two plates at the test temperature and one of the plates is oscillated while the torque is measured.

The data is plotted as torque (proportional to melt viscosity) vs. time. Initially the values drop as the polymer temperature increases and the viscosity decreases. At about 30 seconds the torque increases indicating the crosslinking reaction is occurring and a network is being formed. After 1 or 2 minutes the torque values plateau to a slow rise as the reaction nears completion.

Another few grams of the compounded polymer was then pressed at low temperatures (~120°C) into a film about 50 microns thick. The film was then cured at 175°C in a heated press for 15 minutes. The crosslinked film was hydrolyzed to the salt form by soaking in an aqueous solution of 25% potassium hydroxide at 80°C for 30 minutes. This step was repeated 3 times. The membrane was then washed three times in 25% sulfuric acid at 80°C for 30 minutes followed by washing in DI water at room temperature three times to make the proton form of the polymer.

A swelling experiment was conducted to evaluate the effect of crosslinking on the ionomer films ability to absorb water, ethylene glycol, and methanol. Table 1 shows the data tabulated for the crosslinked film and two controls. A one inch diameter disc was cut from each membrane and placed in a plastic bag with the solvent for 18 hours. The swollen diameter was measured and the increase in area calculated. One control is the copolymer (no cure site monomer) of a PFSA membrane that was prepared in the same manner as described above. The other control is the terpolymer that contains the cure site monomer but was not compounded.

This data shows that the crosslinked sample had the desired effect of reducing the amount of swelling in water. The ethylene glycol and methanol, while not seen in most fuel cells, are instructive in evaluating the degree of crosslinking. In the methanol case the polymers are soluble in the absence of a network but display typical swelling behavior when crosslinked.

Downloaded by UNIV OF DELAWARE MORRIS LIB on June 21, 2012 | http://pubs.acs.org
Publication Date (Web): April 30, 2010 | doi: 10.1021/bk-2010-1040.ch002

Downloaded by UNIV OF DELAWARE MORRIS LIB on June 21, 2012 | http://pubs.acs.org
Publication Date (Web): April 30, 2010 | doi: 10.1021/bk-2010-1040.ch002

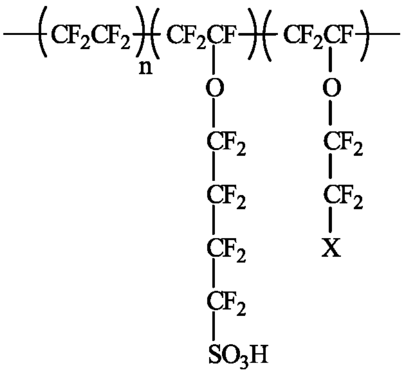

Figure 12. An example of a PFSA polymer with a reactive cure site. X represents any number of groups that can be reacted after the membrane is formed.

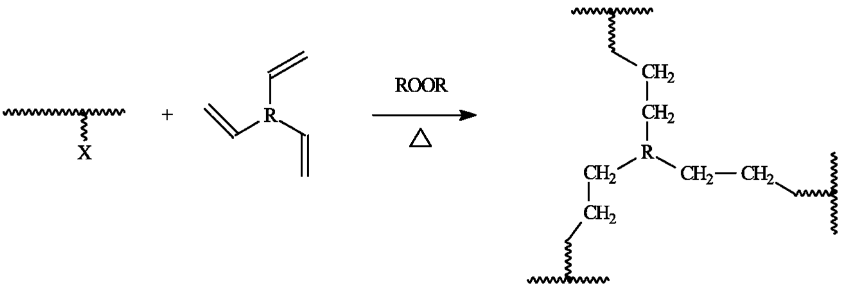

Figure 13. A generalized reaction scheme for crosslinking using a cure site monomer and a multifunctional crosslinker.

Performance Implications of Crosslinked Membranes

The main objective for crosslinking PFSA ionomers used in PEM fuel cells is to minimize the solubility or swelling of ultra low equivalent weight polymers in the presence of liquid water or at high humidity. It is expected that reducing the amount of water an ionomer absorbs will have a negative impact on the proton conductivity under these high humidity conditions. It is also speculated crosslinking the ionomer will not affect the water absorption, and therefore the conductivity, at the very low humidity conditions. In other words, the ultra low EW polymer will provide the required performance both crosslinked and uncrosslinked under dry conditions. Figure 6 shows nicely that a reduction in conductivity is acceptable under high humidity conditions where the performance loss seen for higher EW polymers (less total water and lower conductivity) is negligible compared to the low humidity conditions.

Figure 15 shows this prediction graphically. The conductivity of a 600 EW ionomer was measured at a constant dew point of 80°C at cell temperatures between 80° and 120°C (filled in symbols). Under saturated conditions the conductivity is quite high, about 0.3 S/cm. As the temperature increases the

Downloaded by UNIV OF DELAWARE MORRIS LIB on June 21, 2012 | http://pubs.acs.org
Publication Date (Web): April 30, 2010 | doi: 10.1021/bk-2010-1040.ch002

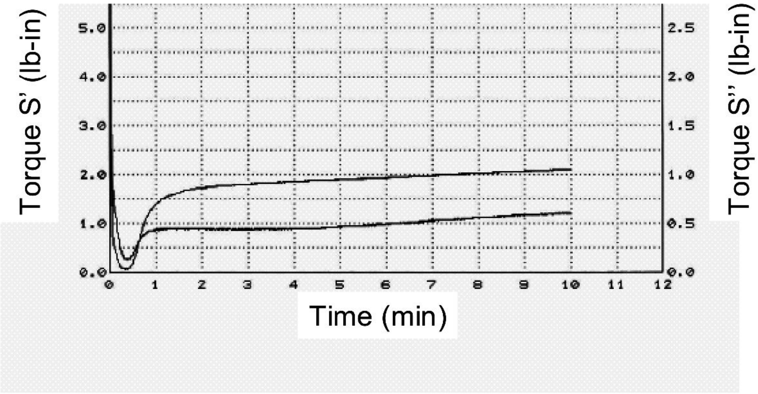

Figure 14. Torque vs. time for a PFSA polymer in the sulfonyl fluoride form compounded with peroxide and a crosslinker.

Table 1. X-Y Swelling data for crosslinked and uncrosslinked ionomers

Sample	*Water*	*Ethylene Glycol*	*Methanol*
Copolymer control	36.0	56.9	soluble
Uncrosslinked control	30.6	63.3	soluble
Crosslinked	24.4	52.4	73.7

humidity and therefore the conductivity decreases to about 0.05S/cm at 120°C. The desired effect from crosslinking the sample is shown in this graph with the open symbols. This data is simply speculated but one would expect a crosslinked membrane to have lower conductivity at the saturated condition (80°C) and decrease as the temperature increases. However, under very dry conditions the ultra low EW would be the dominant factor and, ideally, the conductivity would be the same as the uncrosslinked membrane of the same equivalent weight.

Figure 16 shows the conductivity data measured for the crosslinked film and the two controls described previously. In general, the data for the crosslinked ionomer behaves as expected under the high humidity condition (80°C). The crosslinking did indeed reduce the conductivity from about 0.27 S/cm to about 0.22 S/cm. Unfortunately, this data shows the conductivity at 120°C (low RH) is also lower for the crosslinked sample compared to the controls (0.011 and 0.018 S/cm respectively).

It is difficult to conclude from this one observation if membranes crosslinked in this fashion have lower conductivity at all humidities. Additional experiments are necessary with greater control over crosslink density and the collection of statistically significant number of observations. Nonetheless, crosslinking is likely to be required for ionomers with very low equivalent weights in order to prevent dissolution or mechanical failure due to excessive swelling.

Downloaded by UNIV OF DELAWARE MORRIS LIB on June 21, 2012 | http://pubs.acs.org
Publication Date (Web): April 30, 2010 | doi: 10.1021/bk-2010-1040.ch002

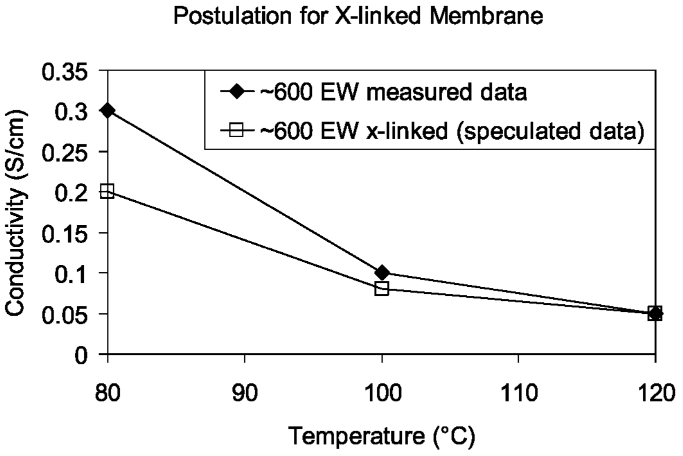

Figure 15. Conductivity vs. Temperature for a 600 EW membrane held at a constant 80°C dew point. The expected effect of crosslinking is shown in the open symbol data.

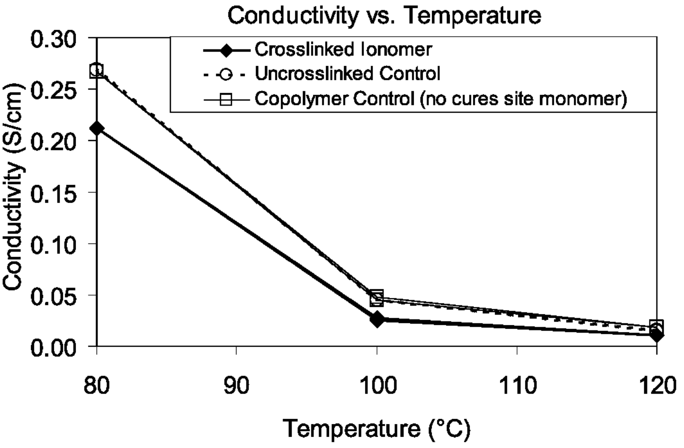

Figure 16. Conductivity vs. temperature for a crosslinked ionomer and two controls. Samples held at a constant dew point of 80°C

Conclusion

In this chapter we attempted to outline the issues associated with proton exchange membranes designed to operate under the dry and hot conditions required by the automobile industry and reflected in the US DOE targets. One strategy to meet these targets is to develop ultra low equivalent weight ionomers. Data from a series of differing EW 3M ionomers suggests that EWs of less than 600 g/mol may be required to meet these targets.

A consequence of equivalent weights in this range would be unacceptable water solubility or swelling. In fact, ionomers with EWs of 700 or lower are often soluble in water. A general scheme for crosslinking PFSA ionomers was discussed as one way to address this problem. The implications for conductivity at both saturated conditions and low humidity conditions were discussed in terms of expected proton conductivity. Preliminary conductivity data for one system was shown. As expected, this system had lower conductivity at the saturated condition compared to a control. Unfortunately the crosslinked polymer exhibited lower conductivity even at the dry and hot condition. Additional work is ongoing in our labs to better characterize this system and provide insight for crosslinked membranes in general.

Downloaded by UNIV OF DELAWARE MORRIS LIB on June 21, 2012 | http://pubs.acs.org
Publication Date (Web): April 30, 2010 | doi: 10.1021/bk-2010-1040.ch002

Acknowledgments

This research was supported in part by the U.S. Department of Energy, Cooperative Agreements No. DE-FC36-02AL67621 and DE-FC36-03GO13098. DOE support does not constitute an endorsement by DOE of the views expressed in this presentation.

References

1. Wipke, K. B.; Sprik, S.; Kurtz, J.; Garbak, J. *ECS Trans.* **2008**, *16* (2), 173.
2. Garland, N. L.; Kopasz, J. P. *J. Power Sources* **2007**, *172*, 94–99.
3. Moore, R. B.; Martin, C. R. *Macromolecules* **1989**, *22* (9), 3594–3599.
4. Gebel, G.; Moore, R. B. *Macromolecules* **2000**, *33* (13), 4850–4855.
5. Savett, S. C.; Atkins, J. R.; Sides, C. R.; Harris, J. L.; Thomas, B. H.; Creager, S. E.; Pennington, W. T.; DesMarteau, D. D. *J. Electrochem. Soc.* **2002**, *149*, A1527.
6. Page, K. A.; Cable, K. M.; Moore, R. B. *Macromolecules* **2005**, *38* (15), 6472–6484.
7. Yandrasits, M. A, ; Hamrock, S. J. ; Grootaert, W. M. ; Guerra, M. A. ; Jing, N. U.S. Patent 7,074,841, 2001.
8. Yandrasits, M. A.; Hamrock, S. J.; Hintzer, K.; Thaler, A.; Fukushi, T. ; Jing, N. ; Lochaas, K. H. U.S. Patent 7,265,162, 2001
9. Wlassics, I.; Tortelli, V. U.S. Patent 6,979,699, 2005.
10. Ishibe, N.; Martin, C. W.; Tran, T. K. U.S. Patent 5,264,508, 1993.

Downloaded by STANFORD UNIV GREEN LIBR on June 21, 2012 | http://pubs.acs.org
Publication Date (Web): April 30, 2010 | doi: 10.1021/bk-2010-1040.ch003

Chapter 3

Synthesis and Characterization of Poly(vinylidene fluoride)-*g*-Sulfonated Polystyrene Graft Copolymers for Proton Exchange Membrane

Zhicheng Zhang,[a] Elena Chalkova,[b] Mark Fedkin,[b] Chunmei Wang,[b] Serguei N. Lvov,[b] Sridhar Komarneni,[c] and T. C. Chung[a,*]

[a]Department of Materials Science and Engineering, The Pennsylvania State University, University Park, PA 16802
[b]Department of Energy and Geo-Environmental Engineering, The Pennsylvania State University, University Park, PA 16802
[c]Department of Crop and Soil Sciences, The Pennsylvania State University, University Park, PA 16802
[*]Corresponding author: chung@ems.psu.edu

A series of poly(vinylidene fluoride)-*g*-sulfonated polystyrene (PVDF-g-SPS) graft copolymers were synthesized and examined with the focus of understanding how the polymer microstructure (backbone molecular weight, graft density, graft length, sulfonic acid concentration, ion exchange capacity, etc.) affects their morphology, water uptake and proton conductivity under various environmental conditions. The PVDF-g-SPS graft copolymer with a combination of a high PVDF backbone, low SPS graft density, and high graft length self-assembles into a microphase-separated morphology with randomly oriented ionic channels imbedded in the hydrophobic PVDF matrix, offers a high ion exchange capacity (IEC=2.75 mmol/g) and resistance to excessive water swelling, which yields notable higher proton conductivity than Nafion under 30-120°C and high humidity conditions.

In Fuel Cell Chemistry and Operation; Herring, A., et al.;
ACS Symposium Series; American Chemical Society: Washington, DC, 2010.

Downloaded by STANFORD UNIV GREEN LIBR on June 21, 2012 | http://pubs.acs.org
Publication Date (Web): April 30, 2010 | doi: 10.1021/bk-2010-1040.ch003

Introduction

The proton exchange membrane (PEM) is a key component in PEMFC (*1–5*), which serves as both an electrolyte and separator. Due to the demanding environment and functions, an ideal PEM material requires a combination of chemical and physical properties; long term chemical and electrochemical stability in the reducing environment at the cathode, and the harsh oxidative environment at the anode; good mechanical strength and dimension stability in tight PEM stacks; and high proton conductivity under various operation conditions (i.e. temperatures and relative humidity). Numerous polymers have been designed and studied in the past decades with some successes and limitations. These polymers are mainly classified as fluoropolymers (*6–8*) and aromatic hydrocarbon polymers (*9–11*). The most commonly known is Nafion (sulfonated fluoropolymer), which shows good stability and good proton conductivity in low temperature and high relative humidity conditions. However, this Nafion based PEM is expensive, and its conductivity dramatically reduces at elevated temperatures (>80°C) and low humidity (<40%) conditions. On the other hand, the membrane based on phosphoric acid doped polybenzimidazole (*12*, *13*) can reach reasonably high proton conductivity at 120-200°C, without any water management. The higher temperature allows for better efficiency, power densities, and reduces the sensitivity to carbon monoxide poisoning. However, these type of membranes exhibit low proton conductivity, especially in low temperature environments.

Sulfonated polystyrene (SPS) (*14*) based PEM was investigated in the 1960s, and showed high water swelling and inadequate chemical stability due to the tertiary C-H bonds. In order to improve its properties, the sulfonated polystyrene was grafted onto fluoropolymers, including poly(tetrafluoroethylene-co-hexafluoropropylene) (*15*) and poly(vinylidene fluoride) (*16–18*) polymer backbones. This chemistry involves an irradiation-mediated free radical polymerization process using monomer-bearing sulfonic acid or styrene followed by a sulfonation reaction of benzyl groups. The lifetime of fuel cells based on this graft copolymer system has been extended to 5000 hours at 85°C (*19*), with the benefits of reduced water uptake and high proton conductivity. Unfortunately, the polymer structure and morphology were poorly controlled and rarely characterized, since the irradiation initiating process results in very complicated molecular structures. More recently, some efforts have been devoted to synthesizing well-defined fluoropolymer/polystyrene block copolymers (*20*, *21*), with a subsequent sulfonation reaction to form the corresponding sulfonated polymer structures (*22*, *23*) that exhibit a microphase separation between hydrophobic and hydrophilic domains. The experimental results show that the conductivity and water swelling of the membrane are strongly related to the chemical structure and morphology, and are proportional to the ion-exchange capacity (IEC). Interestingly, one paper (*24*) compares fluoropolymer/sulfonated polystyrene diblock and graft copolymers containing ~25 mol% SPS content, although these two polymers have a very different molecular weight range (more than one order of magnitude). The graft copolymer, having high graft density and low graft length, bears "cluster-network" ionic domains, similar to that of Nafion, which yields membranes with better mechanical properties and resistance

Downloaded by STANFORD UNIV GREEN LIBR on June 21, 2012 | http://pubs.acs.org
Publication Date (Web): April 30, 2010 | doi: 10.1021/bk-2010-1040.ch003

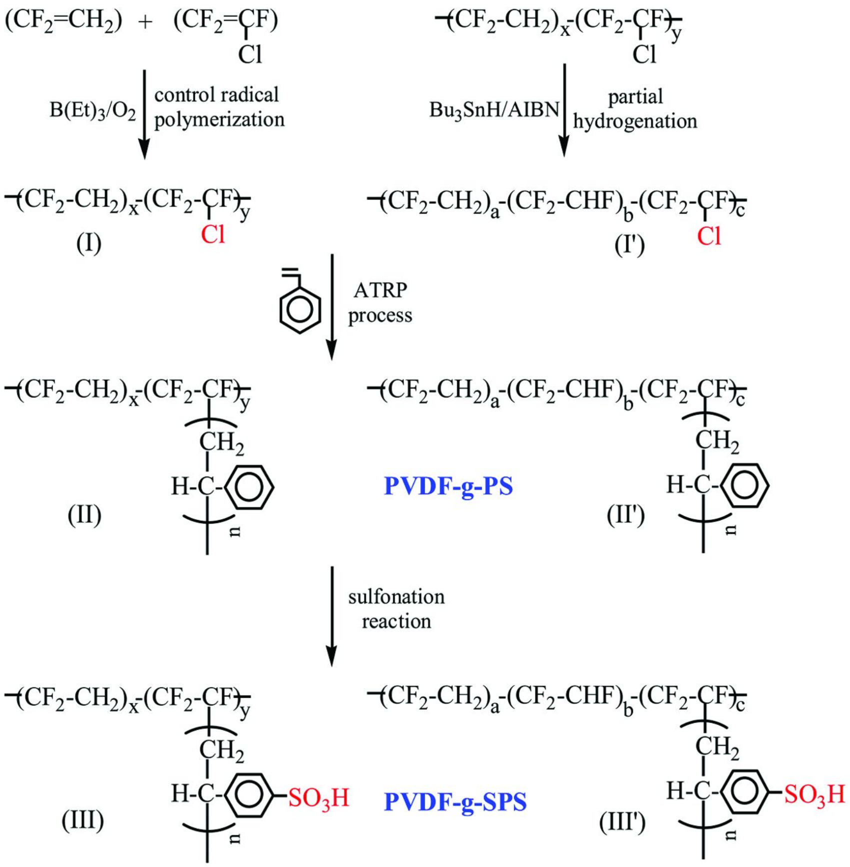
$(CF_2{=}CH_2)$ + $(CF_2{=}CF)$ Cl
B(Et)3/O2
control radical polymerization
$-(CF_2\text{-}CH_2)_x\text{-}(CF_2\text{-}CF)_y-$ Cl
Bu3SnH/AIBN
partial hydrogenation
(I)
(I')
ATRP process
(II)
(II')
PVDF-g-PS
sulfonation reaction
(III)
(III')
PVDF-g-SPS
SO3H

Scheme 1

to water swelling. Some graft copolymers (*24*) with high IEC >2 mmol/g show similar proton conductivity as that of Nafion 117 (IEC =0.9 mmol/g). In contrast, the diblock copolymer membrane—possessing a well segregated and oriented lamellar morphology with long-range ionic order—shows significantly higher proton conductivity (in-plane) than the graft copolymer with the same IEC. However, the combination of in-plane lamella morphology and low molecular weight of the diblock copolymer also leads to excessive swelling and instability in the membrane. More importantly, it lowers the proton conductivity in the through-plane direction that is most relevant to proton conduction in fuel cells.

The ideal PEM should simultaneously provide high through-plane proton conductivity and good dimensional stability to resist excess water swelling or shrinking under various environmental conditions (i.e. temperatures and humidities). Intuitively, a dimensionally stable PEM structure may involve a 3-D hydrophobic (preferred crystalline) matrix with good mechanical properties, in which many hydrophilic micro-size ionic channels (cylinders or lamellas with preferred through-plane orientation) across the membrane matrix are all meant to provide proton conductivity. The combination of strong acidity, high acid concentration, and good proton mobility is essential for high conductivity and suitable water content—offering good proton mobility without diluting the proton concentration. In addition, the hydrophilic polymer chains should anchor to the solid hydrophobic matrix; a high concentration of ions (high IEC) with the associated water molecules can be stationed in the hydrophilic domains without the concern for water-dissolution. It is curious to understand such a hydrophobic-hydrophilic separated morphology responding to elevated temperature and low humidity conditions.

It is worthwhile to systematically investigate poly(vinylidene fluoride)-*g*-sulfonated polystyrene (PVDF-g-SPS) graft copolymer system. A complete range of relatively well-defined graft copolymers with various compositions and microstructures can be prepared, which provides a fair side-by-side comparison of how polymer microstructures (on characteristics of backbone molecular weight, graft density, graft length, IEC, etc.) affect the morphology (sphere, cylinder, bicontineous, lamella, etc.) (*25*, *26*), water uptake, and proton conductivity under various conditions. In addition, the graft copolymer, having a non-linear molecular structure, can form isotropic SPS ionic channels (without specific orientation)—imbedded in the hydrophobic (highly crystalline) PVDF matrix—which provide similar in-plane and through-plane conductivity (*24*).

Downloaded by STANFORD UNIV GREEN LIBR on June 21, 2012 | http://pubs.acs.org
Publication Date (Web): April 30, 2010 | doi: 10.1021/bk-2010-1040.ch003

Experimental Section

Materials

Triethylboron (TEB) was purchased and used as received. Tetrahydrofuran (THF) was dried and distilled from sodium benzophenone ketyl under nitrogen. Vinylidene fluoride (VDF) and CTFE monomers, purchased from SynQuest Laboratory Inc., were quantified in a freeze-thaw process prior to use. Styrene was passed through a column of neutral alumina to remove inhibitors; it was then distilled before use. Low molecular weight P(VDF-co-CTFE)s (Mn=15,000-20,000 g/mol) were synthesized by a procedure described in our previous reports (*27*, *28*). A commercial P(VDF-co-CTFE) (CTFE content=6 mol%) copolymer (PVDF SOLEF$^{®}$ 31008/1001) with a high molecular weight (Mn=312,000 g/mol) was kindly provided by Solvay. To reduce the CTFE content, which determines the branch density in the PVDF-g-PS graft copolymer, a hydrogenation process (*29*) was employed to convert some CTFE units to TrFE (trifluoethylene) units to obtain P(VDF-ter-TrFE-ter-CTFE) terpolymers that have a CTFE content from 1 to 6 mol%. Since VDF and TrFE units are co-crystallizable, a small amount of TrFE units do not have any significant effect to the polymer morphology and melting temperature.

Downloaded by STANFORD UNIV GREEN LIBR on June 21, 2012 | http://pubs.acs.org
Publication Date (Web): April 30, 2010 | doi: 10.1021/bk-2010-1040.ch003

Table 1. A summary of PVDF-g-PS (II) and PVDF-g-SPS (III) graft copolymers prepared from several low molecular weight (VDF-co-CTFE) copolymers (I)

P(VDF-co-CTFE) (I)			PVDF-g-PS (II)[a]			PVDF-g-SPS (III)[d]		
Run	VDF/CTFE (mole ratio)	St (g)	VDF/St (mole ratio)	Graft[b] density	Graft[c] length	VDF/St/SSt[e] (mole ratio)	DS (%)	IEC (mmol/g)
A1-1	99.0/1.0	1	99.0/5.3	0.4	13.2	99.0/2.2/3.1	58.0	0.43
A1-2	99.0/1.0	3	99.0/17.7	0.4	44.3	99.0/4.2/13.5	76.1	1.44
A1-3	99.0/1.0	3	99.0/17.7	0.4	44.3	99.0/2.1/15.6	88.0	1.64
A1-4	99.0/1.0	6	99.0/31.5	0.4	78.8	99.0/11.3/20.2	64.2	1.78
A1-5	99.0/1.0	6	99.0/31.5	0.4	78.8	99.0/10.3/21.2	67.4	1.86
A1-6	99.0/1.0	6	99.0/31.5	0.4	78.8	99.0/0.0/31.5	100	2.57
A2-1	98.0/2.0	1.5	98.0/13.8	0.8	17.3	98.0/5.1/9.9	71.9	1.12
A2-2	98.0/2.0	1.5	98.0/13.8	0.8	17.3	98.0/2.5/12.5	83.0	1.38
A2-3	98.0/2.0	3	98.0/21.5	0.8	26.9	98.0/3.7/18.1	83.0	1.77
A2-4	98.0/2.0	3	98.0/21.5	0.8	26.9	98.0/2.2/19.3	89.6	1.88
A2-5	98.0/2.0	3	98.0/21.5	0.8	26.9	98.0/1.6/19.9	92.7	1.93
A2-6	98.0/2.0	5	98.0/54.2	0.8	67.8	98.0/12.5/41.7	76.9	2.70
A3-1	96.6/3.4	1.8	96.6/14.1	1.4	10.1	96.6/6.5/7.6	46.1	0.88
A3-2	96.6/3.4	1.8	96.6/14.1	1.4	10.1	96.6/2.8/11.3	80.2	1.26
A3-3	96.6/3.4	2.4	96.6/23.6	1.4	16.9	96.6/7.6/16.0	67.7	1.55
A3-4	96.6/3.4	2.4	96.6/23.6	1.4	16.9	96.6/4.9/18.7	79.2	1.78
A3-5	96.6/3.4	3	96.6/36.4	1.4	26.0	96.6/8.9/27.5	75.7	2.19
A3-6	96.6/3.4	3	96.6/36.4	1.4	26.0	96.6/6.8/29.6	81.2	2.32
A4-1	95.4/4.6	1.8	95.4/15.1	1.8	8.4	95.4/7.4/7.7	50.8	0.87
A4-2	95.4/4.6	1.8	95.4/15.1	1.8	8.4	95.4/5.0/10.1	67.1	1.12
A4-3	95.4/4.6	2.3	95.4/22.5	1.8	12.5	95.4/7.4/15.1	67.1	1.48
A4-4	95.4/4.6	2.3	95.4/22.5	1.8	12.5	95.4/1.4/21.1	93.6	1.98
A4-5	95.4/4.6	2.5	95.4/25.5	1.8	14.2	95.4/0.6/24.9	97.5	2.21

a. ATRP graft reaction condition: a mixing solution of 2g P(VDF-co-CTFE), 0.125g CuCl, 0.5g BPy, 40mL NMP and specific amount of styrene was stirred at 120 °C for 24 hours.

b. Number of PS grafts per 100 VDF units in the backbone, estimated from 40% of CTFE units in the copolymer (I) involving ATRP graft-from reaction.

c. Number of styrene units in each graft, calculated from the styrene mole ratio divided by graft density.

d. Sulfonation reaction condition: a mixing solution of 1g PVDF-g-PS (II), 1mL H_2SO_4, 3mL acetic anhydride, and 40 mL 1,2-dichloroethane was performed at 50 °C.

e. St: styrene; SSt: sulfonated styrene.

Synthesis of PVDF-g-PS Copolymers

The synthesis of PVDF-g-PS graft copolymers began with P(VDF-co-CTFE) copolymers and P(VDF-ter-TrFE-ter-CTFE) terpolymers, containing C-Cl moieties (CTFE units) that involve atom transfer radical polymerization (ATRP) with styrene monomers (*21*). In a typical graft reaction, 2.0g of the P(VDF-co-CTFE) copolymer together with 125mg CuCl(1.3mmol) was dissolved in 40mL of NMP in a 100mL three-neck flask with a magnetic stirrer bar under an inert atmosphere. A controlled amount of styrene was then injected into the P(VDF-co-CTFE) solution. Separately, 500mg of 2,2-bipyridine (BPy, 3.2 mmol) was dissolved in 10mL of NMP in a 25mL Schlenk flask under an inert atmosphere, which was transferred into the reaction flask by a N_2-purged syringe. The reaction flask was then immersed in an oil bath at 120°C. After 24h, the

Downloaded by STANFORD UNIV GREEN LIBR on June 21, 2012 | http://pubs.acs.org
Publication Date (Web): April 30, 2010 | doi: 10.1021/bk-2010-1040.ch003

Table 2. A summary of PVDF-g-PS (II') and PVDF-g-SPS (III') graft copolymers prepared from several high molecular weight poly(VDF-ter-TrFE-ter-CTFE) terpolymers (I')

	P(VDF-terTrFE-ter-CTFE) (I')		PVDF-g-PS (II')			PVDF-g-SPS (III')		
Run	VDF/TrFE/CTFE (mole ratio)	St (g)	VDF/St (mole ratio)	Graft[a] density	Graft[b] length	VDF/St/SSt[c] (mole ratio)	DS (%)	IEC (mmol/g)
B1-1	94.0/5.2/0.8	4.6	94.0/36.1	0.3	120	94.0/17.2/18.9	55.1	1.60
B1-2	94.0/5.2/0.8	4.6	94.0/36.1	0.3	120	94.0/0.0/36.1	100	2.75
B2-1	94.0/3.9/2.1	3.0	94.0/29.4	0.8	37	94.0/11.1/8.3	62.1	1.65
B2-2	94.0/3.9/2.1	3.0	94.0/29.4	0.8	37	94.0/4.0/25.4	86.3	2.18
B3-1	94.0/2.6/3.4	3.0	94.0/29.5	1.4	21	94.0/18.0/11.5	39.0	1.08
B3-2	94.0/2.6/3.4	3.0	94.0/29.5	1.4	21	94.0/3.3/26.2	88.9	2.23
B4-1	94.0/1.7/4.3	3.1	94.0/28.1	1.7	17	94.0/14.2/13.9	50.4	1.32
B4-2	94.0/1.7/4.3	3.1	94.0/28.1	1.7	17	94.0/1.5/26.6	94.7	2.28
B5-1	94.0/0.0/6.0	4.0	94.0/32.7	2.4	14	94.0/14.7/18.0	54.9	1.56
B5-2	94.0/0.0/6.0	4.0	94.0/32.7	2.4	14	94.0/6.0/26.7	81.7	2.18

a. Number of PS grafts per 100 VDF units in the backbone, estimated from 40% of CTFE units in the copolymer (I') involving ATRP graft-from reaction.

b. Number of styrene units in each graft, calculated from the styrene mole ratio divided by graft density.

c. St: styrene; SSt: sulfonated styrene.

polymerization was terminated by cooling to room temperature and exposing to air. The reaction mixture was diluted with acetone and then passed through a column filled with silica gel, followed by precipitation in methanol. The resulting PVDF-g-PS graft polymer was dried in a vacuum oven at 60°C overnight.

Sulfonation Reaction of PVDF-g-PS Copolymers

The sulfonation reaction was carried out in 1,2-dichloroethane solvent, following previously reported procedures (*30*). Typically, in a 100mL three-neck flask that was nitrogen-purged, equipped with a dropping funnel, and condenser, 40 mL of 1,2-dichloroethane and 2.0 g of PVDF-g-PS were added, and the mixture was heated to 50°C under stirring until the copolymer completely dissolved. Acetylsulfate was prepared by injecting 3 mL of aceticanhydride and 10mL of dichloroethane into a nitrogen-purged vial. The solution was cooled to 0°C in an ice bath, and 1 mL of 95-97% sulfuric acid was injected. The resulting acetylsulfate solution was immediately transferred to the polymer solution at 40°C using a dropping funnel. Samples were periodically extracted and precipitated in 50/50 ethanol/hexane mixture for determining their sulfonation levels. The precipitate was washed with water until the residual water had a pH=7. The sulfonated polymers were dried under vacuum at ambient temperature overnight. For some graft copolymers, multiple sulfonation reactions were performed to achieve higher sulfonation levels.

Downloaded by STANFORD UNIV GREEN LIBR on June 21, 2012 | http://pubs.acs.org
Publication Date (Web): April 30, 2010 | doi: 10.1021/bk-2010-1040.ch003

Membrane Preparation and Evaluation

Membranes were prepared by dissolving the sulfonated graft copolymers in THF, and followed by casting onto a Teflon substrate. Films were dried at room temperature for several hours before heating at 60°C for 2h under vacuum. The sulfonated membranes were treated with 2M HCl overnight. They were then washed several times with de-ionized water for 30 min periods. Membrane morphology was observed by transmission electron microscopy (TEM). To determine the water uptake and water content λ (molar ratio of water to sulfonic acid) vs. IEC, the membrane was dried under vacuum for 12h at 70°C and cooled to room temperature in a desiccator before measuring the weight in "dry" state (Wd). The membrane was then equilibrated in de-ionized water overnight at room temperature. After removing the water from the surface, the weight in "wet" state (Ww) was measured. The water uptake of the membrane was calculated to determine the percent weight increase from "dry" to "wet" states, [(Ww-Wd)/Wd] x 100%. With the known water uptake and sulfonic acid content (NMR results), the water content λ was then calculated. In addition, the ion exchange capacity (IEC) was calculated in mmol of sulfonic acid in 1 g of the polymer. It has been reported (*23*) that the calculated IEC number coincides very well with the one based on titration.

The membrane conductivity was tested using a BekkTech conductivity cell (BT 115), which was assembled in an ElectroChem fuel cell hardware. The relative humidity (RH) in the cell was achieved by feeding it with humidified nitrogen gas, by passing the gas flow through a humidification column. The RH value in the cell was calculated from the ratio of the saturated water vapor pressures, respectively at the temperatures of the humidification column $P(T_h)$ and the cell $P(T_c)$: RH (%) = $P(T_h) / P(T_c) \times 100$. Testing was performed at 25°C and 120 kPa and at 120°C and 230 kPa (cell pressure). An input flow rate was in a range of 290-390 cm^3/min. A sample was conditioned at 70% RH for two hours before the conductivity measurement. In the subsequent change of RH, a stabilization time about one hour was implemented before each measurement. The membrane resistance measurements were performed by a four-probe method with a Gamry electrochemical impedance spectroscopy system. For some (highly conductive) membranes, data was collected using AC or DC methods. Both methods produced the same result, indicating a pure resistor. Conductivity (in-plane) was calculated using the sample thickness (T), sample width (W), distance between the sensor electrodes in the conductivity cell (L), and the membrane resistance (R) from the equation $\sigma = L/W\times T\times R$.

Results and Discussions

In this paper, we have developed a research strategy to prepare two families of PVDF-g-SPS graft copolymers based on a low and a high molecular weight of PVDF backbones, followed by a variation of branch density, branch length, and sulfonation levels. The graft copolymers were then systematically evaluated

Downloaded by STANFORD UNIV GREEN LIBR on June 21, 2012 | http://pubs.acs.org
Publication Date (Web): April 30, 2010 | doi: 10.1021/bk-2010-1040.ch003

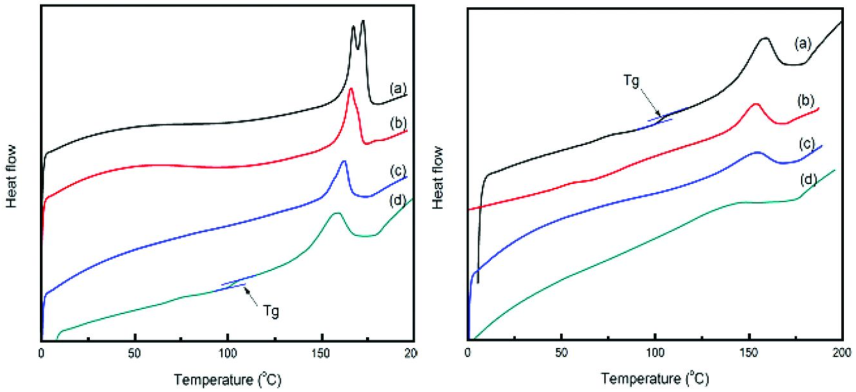

Figure 1. (left) Comparison of DSC curves between (a) a starting P(VDF-co-CTFE) copolymer (I) and three corresponding PVDF-g-PS graft copolymers (II) with 0.4 mole% graft density and various PS graft length (b) 13.2, (c) 44.3, and (d) 78.8 average styrene units per graft, respectively; (right) DSC curve of four PVDF-g-PS graft copolymers having similar PS graft content (VDF/St ~100/30 mole ratio) but different graft density (a) 0.4, (b) 0.8, (c) 1.4, and (d)1.8 mol%, respectively.

by comparing their molecular microstructures, morphologies, water uptakes, and proton conductivities under various environmental conditions.

Synthesis and Structure Characterization

Two families of low molecular weight P(VDF-co-CTFE) copolymers (I) and high molecular weight P(VDF-ter-TrFE-ter-CTFE) terpolymers (I') were employed as the starting polymers in the preparation of PVDF-g-SPS graft copolymers, as illustrated in Scheme 1. The low molecular family of P(VDF-co-CTFE) copolymers, having Mn=15,000-20,000 g/mole and a CTFE content from 1.0 to 4.6 mol% were prepared by a copolymerization reaction, mediated by TEB/O_2 initiator (TEB: triethylborane) (*27*, *28*). On the other hand, the high molecular set of P(VDF-ter-TrFE-ter-CTFE) terpolymers, having few % of TrFE units, and a CTFE content from 1 to 6 mol%, were prepared by a partial hydrogenation (*29*) of a commercial P(VDF-co-CTFE) copolymer, with 6 mol% of CTFE units and Mn=312,000 g/mole. The hydrogenation reaction is very efficient and selective with interconverting some CTFE units to TrFE units, without changing polymer molecular weight.

Both P(VDF-co-CTFE) copolymers (I) and P(VDF-ter-TrFE-ter-CTFE) terpolymers (I') were then applied in the subsequent ATRP graft-from polymerization of styrene, followed by the sulfonation reaction of PS grafts. As shown in Scheme 1, the reactions produce the intermediate P(VDF-co-CTFE)-g-PS (II) and P(VDF-ter-TrFE-ter-CTFE)-g-PS (II'), and the final P(VDF-co-CTFE)-g-SPS (III) and P(VDF-ter-TrFE-ter-CTFE)-g-SPS (III') graft copolymers, respectively. Since both P(VDF-co-CTFE) and

Downloaded by STANFORD UNIV GREEN LIBR on June 21, 2012 | http://pubs.acs.org
Publication Date (Web): April 30, 2010 | doi: 10.1021/bk-2010-1040.ch003

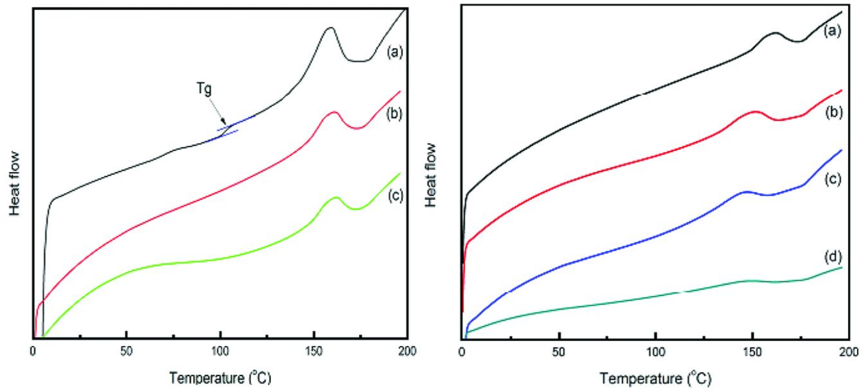

Figure 2. (left) DSC curves of (a) PVDF-g-PS (II) graft copolymer having VDF/St= 99.0/31.5 mole ratio and two corresponding sulfonated PVDF-g-SPS (III) graft copolymers with (b) 64.2 and (c) 100% degree of sulfornation (DS); (right) DSC curve of four PVDF-g-SPS graft copolymers having similar SPS graft content (VDF/SSt ~100/30 mole ratio) but different graft density (a) 0.4, (b) 0.8, (c) 1.4, and (d)1.8 mol%, respectively.

P(VDF-ter-TrFE-ter-CTFE) backbones in all graft copolymers contain ~ 95% VDF units, and both VDF and TrFE units are co-crystalizable, they are basically PVDF polymers with properties that are controlled by backbone molecular weight, and graft density, and graft length. For simplicity's sake, they are identified as PVDF-g-PS (II) and (II') and PVDF-g-SPS (III) and (III') graft copolymers, respectively.

Tables 1 and 2 summarize the experimental results of two graft copolymer systems from low molecular weight P(VDF-co-CTFE) copolymers (I) and high molecular weight P(VDF-ter-TrFE-ter-CTFE) terpolymers (I'), respectively. For studying polymer microstructure effects, the graft copolymers were systematically varied with graft density, graft length, degree of sulfonation (DS), and ion exchange capacity (IEC). In each system, we started with several copolymers (I) or terpolymers (I') containing 1-6 mol% of CTFE units, which provided the graft points in the corresponding graft copolymers. During the ATRP graft reaction, various amount of styrene (St) were added to control the graft length in the PVDF-g-PS graft copolymer. The graft length (average styrene repeating units per PS graft) in the PVDF-g-PS copolymer was calculated from the styrene incorporation (^{1}H NMR) and graft density (40% of the CTFE units in the starting polymer; estimated by ^{19}F NMR). The same graft density and graft length are expected in the corresponding PVDF-g-SPS graft copolymer. On the other hand, the DS value is determined from the ^{1}H NMR spectrum of the PVDF-g-SPS copolymer, by estimating the peak intensity between aromatic protons in styrene (St) units and sulfonated styrene (SSt) units.

It is interesting to note that DS of the PVDF-g-PS copolymer is quite dependent on its PS content and graft density. The copolymer with a lower PS content or higher grafting densities requires a longer sulfonation period or rigorous sulfonation condition. To achieve a high DS in these samples, multiple

Downloaded by STANFORD UNIV GREEN LIBR on June 21, 2012 | http://pubs.acs.org
Publication Date (Web): April 30, 2010 | doi: 10.1021/bk-2010-1040.ch003

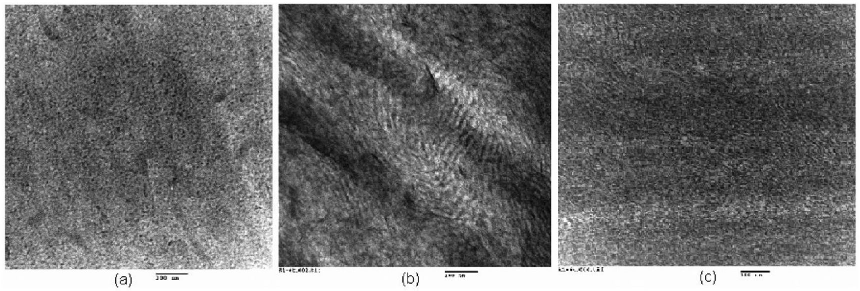

Figure 3. TEM micrographs of three PVDF-g-SPS graft copolymers including (a) run A3-6, (b) run A1-6, and (c) run B1-2.

sulfonation reaction processes have been applied. The ion exchange capacity (IEC) is then calculated from the DS value by estimating the sulfonic acid concentration in the final PVDF-g-SPS graft copolymer. Overall, we have applied three well-controlled reactions: copolymerization (or hydrogenation), ATRP graft reaction, and sulfonation, in order to prepare a wide range of PVDF-SPS graft copolymers with various molecular weight, graft density, graft length, and sulfonic acid concentration. This offers us the opportunity to systematically examine the effects of the polymer microstructure on proton conductivity and water uptake under various conditions (temperature and relative humidity).

Thermal Properties and Morphologies

Since the graft copolymers contain a crystalline backbone and amorphous side chains, it is convenient to apply DSC and TEM techniques to understand their morphologies and thermal properties. Figure 1 (left) compares DSC curves of three PVDF-g-PS graft copolymers (II) (Set A1 in Table 1), which have the same (0.4 mol%) graft density and various PS graft length (13.2, 44.3, and 78.8 average styrene units per graft, respectively). The starting copolymer (I) shows a melting temperature (Tm) at 162.5°C. The increase of PS content leads to only a less than 4°C decrease in Tm, and the decrease of heat of fusion (ΔH) is mainly due to the dilution effect. As the molecular weight of the PS graft increases, the Tg of the PS domain appears at 100°C. The coexistence of the Tm for the P(VDF-co-CTFE) backbone and the Tg for the PS grafts indicates a clear microphase separation morphology in this PVDF-g-PS (99/31.5 mole ratio) graft copolymer that contains semi-crystalline PVDF and amorphous PS domains. Figure 1 (right) compares four PVDF-g-PS graft copolymers having similar PS graft contents (VDF/St~100/30 mole ratio) but different graft densities (0.4, 0.8, 1.4, and 1.8 mol%, respectively). With the increase of graft density, the crystallinity and heat of fusion (ΔH) decreased, and the Tg of the PS graft becomes undetectable due to low molecular weight. The PVDF-g-PS graft copolymer, having 1.8 mol% graft density, shows almost no melting point and no Tg, implying a poor phase separation. Overall, the morphology of the PVDF-g-PS graft copolymer is largely controlled by graft density.

Downloaded by STANFORD UNIV GREEN LIBR on June 21, 2012 | http://pubs.acs.org
Publication Date (Web): April 30, 2010 | doi: 10.1021/bk-2010-1040.ch003

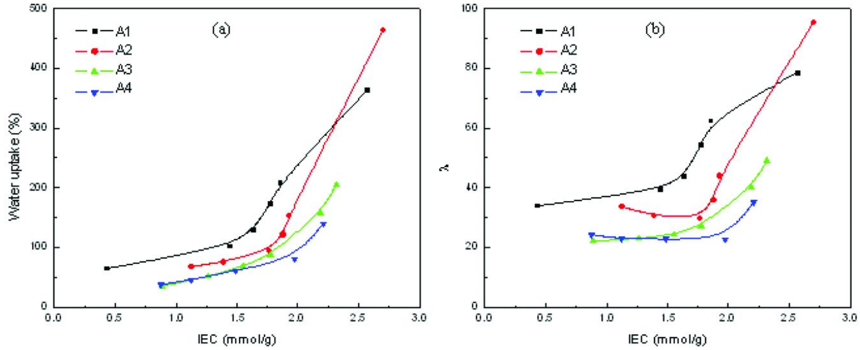

Figure 4. (a) Water uptake and (b) λ vs. IEC for all low Mw PVDF-g-SPS graft copolymers (III) in Table 1. (The lines are used solely for guiding purposes)

It is interesting to examine the effects of sulfonation to the thermal property and morphology of the PVDF-g-PS graft copolymer, which alters the hydrophobic PS grafts to the hydrophilic SPS grafts, along with the ability to absorb a significant amount of water molecules. Figure 2 (left) compares DSC curves of a PVDF-g-PS (II) graft copolymer, having a VDF/St= 99.0/31.5 mole ratio and graft density= 0.4 mol%, and two corresponding sulfonated PVDF-g-SPS (III) graft copolymers, with 64.2% (run A1-4) and 100% (run A1-6) degrees of sulfonation (DS). After sulfonation, the graft copolymers show similar Tm, but lower ΔH. The value of ΔH is gradually decreased as more benzyl sulfonic acids are introduced to the PS grafts, which is largely due to the dilution effect. Figure 2 (right) compares four PVDF-g-SPS graft copolymers, which were prepared by complete sulfonation of the corresponding PVDF-g-PS graft copolymers. In other words, all PVDF-g-SPS graft copolymers (III) have similar SPS contents (VDF/SSt ~100/30 mole ratio) and different graft densities (0.4, 0.8, 1.4, and 1.8 mol%, respectively). The side-by-side comparison, before and after sulfonation, also shows a small effect to the Tm of the PVDF backbone in all compositions. But it also shows a reduction of the overall crystallinity, which may be mostly associated with the bulkiness of benzyl sulfonic acid with the absorbed water molecules.

Figure 3 shows TEM micrographs of the cross-sectional slices of three representative PVDF-g-SPS graft copolymers (runs A1-6, A3-6, and B1-2). In general, they are not as well ordered as the typical morphologies in diblock copolymers. Comparing the first two graft copolymers (III), they have the same low molecular weight PVDF backbone, similar SPS contents (VDF/SSt ~100/30 mole ratio), and different graft densities (0.4 and 1.4 mol%, respectively) and graft lengths (79 and 26 SSt units, respectively). The membrane morphology is clearly affected by graft density and graft length. As predicted by theory (*25*, *26*), the morphology of the graft copolymer is controlled by a combination of volume fraction, graft density, and graft length. The A3-6 sample with higher graft density and lower graft length (Figure 3(a)) shows a cluster-network morphology with a cluster diameter ~5 nm, similar to that of Nafion. On the other hand, Figure 3(b) shows many long range ionic channels (10-15 nm in width) with no specific spatial ordering in the A1-6 sample that possesses low graft density and high graft length. The morphology seems to contain largely lamella structures, and it may also include some cylinder structures. Overall, it is not as well-ordered a morphology as those in the block copolymers. Figure 3(c) shows a TEM micrograph of the B1-2 sample that has more than 10 times the amount of PVDF molecular weight than the A1-6 sample, with higher SPS graft length (120 SSt units; VDF/SSt 94/36.1 mole ratio) and lower graft density (0.3 mol%). Better ordered lamella/cylinder morphology with a smaller channel width of 5-10 nm was observed in the B1-2 membrane. The smaller channel width also showed lower water uptake and resistance to water swelling (discussed later).

Downloaded by STANFORD UNIV GREEN LIBR on June 21, 2012 | http://pubs.acs.org
Publication Date (Web): April 30, 2010 | doi: 10.1021/bk-2010-1040.ch003

Water Uptake

Figures 4 and 5 show water uptake (wt%) and water content λ (molar ratio of water to sulfonic acid) vs. IEC at room temperature for all PVDF-g-SPS graft polymers in Tables 1 and 2, respectively.

They include both low and high molecular weight PVDF backbone systems with various graft densities and IEC values. It is generally known that the water uptake and water content (λ) are directly relative to the sulfonic acid concentration and IEC value, and both sharply increases over a critical IEC value that is associated with the threshold of forming the cohesive ionic (hydrophilic) domains. In these graft copolymers, all factors, including water-uptake, water content, critical IEC value, and water-dissolution point, are dependent on the graft copolymer microstructure, a combination of backbone molecular weight, graft density, and graft length.

For the low molecular weight PVDF-g-SPS (III) graft copolymers with the same IEC value (Figure 4), both water uptake and water content (λ) are inversely proportional to graft density. Lower graft density in sets A1 and A2 results in higher water uptakes and λ values. In detail, the critical IEC value changes from 1.5 mmol/g in the A1 set with a graft density of 0.4 mol%, to 2.0 mmol/g in the A4 set with a graft density of 1.8 mol%. Over the critical IEC values, the A1 and A2 graft copolymers also exhibit a sharper increase in water uptakes and λ values. The λ values reach >80 in sets A1 and A2, which are between the λ values reported in diblock and graft copolymers (*24*). On the other hand, the maximum λ values (~40) in sets A3 and A4 are close to the reported value in the graft copolymer that also has high graft density. It is clear that the PVDF-g-SPS graft copolymer (III) with low graft density is more sensitive to water uptake, especially in the low IEC region. The longer consecutive PVDF and SPS segments form longer range continuous lamella/cylinder ionic channels, as shown in Figure 3(b), increase the water sensitivity and overall water uptake. On the other hand, the graft copolymers with higher graft density and lower graft length, having more dispersed cluster morphology with many small ionic domains imbedded in the hydrophobic PVDF matrix (Figure 3(a)), shows more resistant in absorbing water molecules. With a further increase of the IEC value, the PVDF-g-SPS graft copolymer becomes water-soluble. It is interesting to note that despite the lower water sensitivity in A3 and A4 graft copolymers, they become water-soluble at a lower IEC value

Downloaded by STANFORD UNIV GREEN LIBR on June 21, 2012 | http://pubs.acs.org
Publication Date (Web): April 30, 2010 | doi: 10.1021/bk-2010-1040.ch003

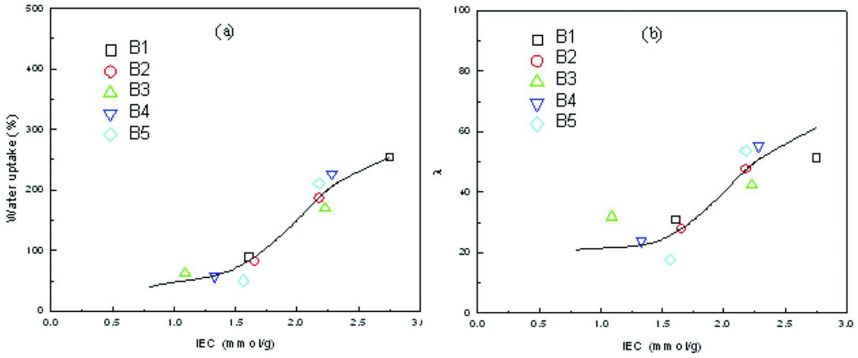

Figure 5. (a) Water uptake and (b) λ vs. IEC for all high Mw PVDF-g-SPS graft copolymers (III') in Table 2. (The lines are used solely for guiding purposes)

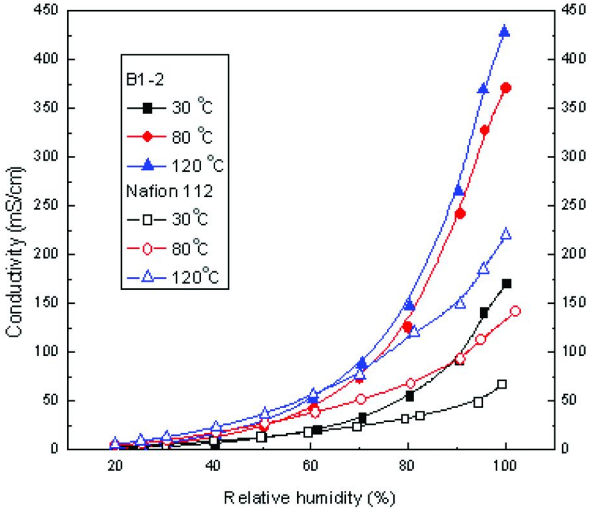

Figure 6. Comparison of proton conductivity vs. relative humility between B1-2 and Nafion 112 PEMs at 30, 80, and 120 °C. (The lines are used solely for guiding purposes)

>2.25. The A1 and A2 graft copolymers show a higher water dissolution point at an IEC value >2.6.

Surprisingly, the PVDF backbone molecular weight has a significant effect to the water swelling behavior in the graft copolymer (III'), as shown in Figure 5. The water uptake, λ value, and critical IEC value become less sensitive to the graft density in the high molecular weight graft copolymers. Four PVDF-g-SPS samples (III'), having similar IEC values ~2.20 mmol/g, but very different graft densities (0.8, 1.4, 1.7, and 2,4 mol%), exhibit similar water uptakes between 170% and 227% and λ values of 48, 42, 55, and 54, respectively. The backbone molecular weight effect is particularly important for the graft copolymers with very low graft density and high IEC value. Comparing A1-6 and B1-2 PEMs, both have similar

Downloaded by STANFORD UNIV GREEN LIBR on June 21, 2012 | http://pubs.acs.org
Publication Date (Web): April 30, 2010 | doi: 10.1021/bk-2010-1040.ch003

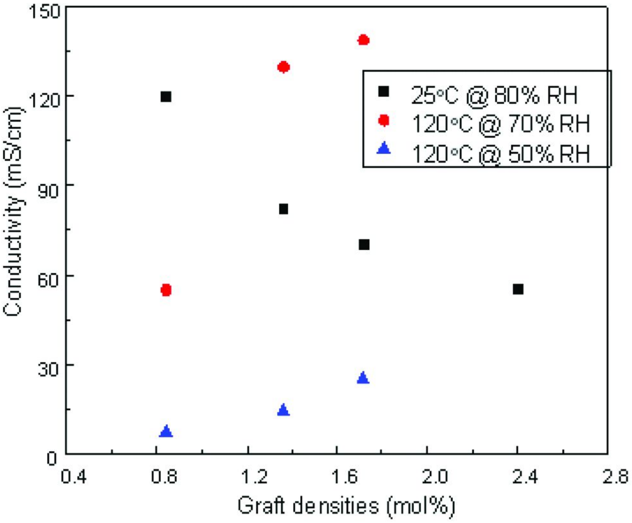

Figure 7. Comparison of proton conductivity vs. graft density of four PVDF-g-SPS (III') graft copolymers having IEC ~2.20 mmol/g and different graft densities 0.8, 1.4, 1.7, and 2.4 mol%, respectively, under 25 °C (80% RH) and 120 °C (70% and 50% RH).

low graft densities (0.4 vs. 0.3 mol%) and IEC values (2.57 vs. 2.75mmol/g), the higher molecular weight B1-2 graft copolymers (III') consistently shows only about half of the water uptake than that of the corresponding lower molecular weight A1-6 graft copolymers (III). The TEM micrographs in Figure 3 (b) and (c) confirm the difference with a significantly larger hydrophilic ion channel width in the A1-6 sample than in the B1-2 sample. Although the B1-2 graft copolymer has a very high IEC value of 2.75 mmol/g, it only shows a relatively mild water uptake of 254 % with a λ value of 53. In contrast, the corresponding A1 sample with IEC >2.57 is completely water-soluble. More importantly, it maintains good film integrity. As will be discussed later, this B1-2 sample exhibits higher proton conductivity than Nafion under high humidity conditions.

Proton Conductivities

In general, the proton conductivity of the low molecular weight PVDF-g-SPS membrane is less reliable and difficult for comparison due to the weakened film integrity subsequent to high water uptake. Like most of the PEMs, the proton conductivity of the PVDF-g-SPS graft copolymer membranes depends on the relative humidity of the environment. Figure 6 shows the plots of proton conductivity (in-plane) vs. relative humidity (RH) under various environmental conditions (i.e. temperature and humidity) for the PEM based on the high molecular weight B1-2 sample. Since the graft copolymer exhibits isotropy continuous SPS ionic channels (Figure 3), it should show similar in-plane

Downloaded by STANFORD UNIV GREEN LIBR on June 21, 2012 | http://pubs.acs.org
Publication Date (Web): April 30, 2010 | doi: 10.1021/bk-2010-1040.ch003

and through-plane conductivity (*24*). For comparison, Nafion 112 (a random copolymer) was also measured under similar conditions.

As expected, the conductivity exponentially increases with RH, and it requires more than 60% RH to show significant proton conductivity. In the RH >60% range, the B1-2 membrane shows notably higher proton conductivity than Nafion 112 in all three measured temperatures (30, 80, and 120 °C), but Nafion 112 performs better under low RH conditions, especially at 120 °C. This conversion may be related to the water content (λ). The short range cluster-network morphology in Nafion may be better in retaining the absorbed water molecules in PEM under high temperature and low humidity conditions. However, under high RH conditions, the water evaporation is no long an issue. The conductivity should directly relate to the IEC value, water content (λ), morphology, and temperature. The B1-2 graft copolymer—with the combination of high molecular weight, low graft density, and isotropic long range hydrophilic-hydrophobic phase separation—allows the incorporation of high sulfonic acid content (IEC=2.75 mmol/g) without showing the excessive water swelling for high proton conductivity under high RH conditions. It is interesting to note that the proton conductivity of the B1-2 PEM increases quickly as testing temperature is elevated from 30 to 80°C, showing only an incremental increase from 80 to 120°C. As reported (*31*, *32*), the increase in conductivity with temperature is attributed to the activation barriers for proton motion. Once the temperature is sufficiently high to overcome the activation barrier, further increasing the temperature has much less effect to the proton conductivity. It seems that 80°C is sufficient for the sample B1-2, but not enough for Nafion 112, which still leads to increased proton conductivity after 80°C.

In order to further understand the influence of the polymer microstructure on proton conductivity of the membrane, a series of high molecular weight PVDF-g-SPS graft copolymers (III') with similar IEC ~2.20 mmol/g and different graft densities (0.8, 1.4, 1.7, and 2.4 mol%) are compared in Figure 7. The major difference between these polymers is their microstructures, and therefore different morphologies, formed in the corresponding membranes. Proton conductivity at a low temperature (25°C) and high humidity (80%) decreases from 120 mS/cm to 55 mS/cm when grafting density is increased from 0.8 mol% to 2.4 mol%. However, at a higher temperature (120°C) and similar humidity (70%), a completely inverse result was observed; in this instance, the polymer with a higher graft density exhibited higher proton conductivity. A similar trend was also observed at the same high temperature (120°C) and lower humidity (50%). Overall, in this PVDF-g-SPS graft copolymer set with the same sulfonic acid content, the lower graft density and longer graft length lead to a larger-scaled hydrophilic domain and lower activation energy. As a result, this polymer shows high conductivity at a low temperature and quickly reaches maximum conductivity at a relatively low temperature, and even starts to exhibit decreased conductivity at a higher temperature (*23*). On the other hand, the corresponding graft copolymer with a higher graft density and a shorter graft length forms cluster-network morphology with higher activation energy. The proton conductivity is relatively low at low temperature, and increases consistently as the temperature is elevated until it reaches a maximum at a relatively high temperature. Generally speaking, the high molecular weight PVDF-g-SPS (III') copolymer with a high IEC value and very low graft density (0.3 and 0.8 mol%) is suitable for PEM under high RH and a wide range of temperatures, while the corresponding higher graft density (1.4 and 1.7 mol%) ones show increased conductivity at higher temperatures. However, the graft copolymer with too high of a graft density (2.4 mol%) lost most of the PVDF crystallinity, and the PEM became too soft to maintain its integrity at 120°C.

As discussed previously, the molecular weight of the PVDF backbone in the PVDF-g-SPS plays an important role in water uptake (Figures 4 and 5) and hydrophilic channel width (Figure 3), which is directly related to proton conductivity. Table 3 compares four pairs of PVDF-g-SPS graft copolymers (III) and (III'), with similar graft density (similar morphology, but different hydrophilic channel width) and almost identical IEC value, but with different backbone molecular weight in each pair of polymers, under various conditions. At a low testing temperature, the molecular weight (Mw) shows little effect on proton conductivity of the PEMs. The proton conductivity of low Mw samples shows even slightly higher proton conductivity than that of high Mw samples. At a high temperature, high Mw PEMs consistently show much higher proton conductivity than low Mw samples, especially with high graft density pairs. It is well known that the water uptake varies with temperature, and a higher temperature usually leads to elevated water uptake (*33*) under high humidity conditions. The low Mw PVDF-g-SPS (III) samples, especially the ones (A3-5 and A4-5) with high graft density and low crystallinity in the PVDF matrix, may be over-swelled at high temperature. As a result, the sulfonic acid concentration is significantly reduced in the enlarged PEM. On the other hand, the high Mw PEMs with stronger hydrophobic domains show better water resistance at high temperature.

Downloaded by STANFORD UNIV GREEN LIBR on June 21, 2012 | http://pubs.acs.org
Publication Date (Web): April 30, 2010 | doi: 10.1021/bk-2010-1040.ch003

Conclusions

A series of PVDF-g-SPS graft copolymers with systematically controlled microstructure (i.e. backbone molecular weight, graft density, and graft length) have been prepared and studied for PEM applications. The microstructure of the graft copolymer directly affects PEM morphology, water uptake, and proton conductivity under various conditions (i.e. temperature and humidity). The PVDF-g-SPS graft copolymer with low graft density (0.3-0.8 mol%) and long SPS graft length forms a well microphase-separated hydrophilic-hydrophobic morphology with long range isotropic ionic channels (lamella/cylinder) imbedded in the high crystalline PVDF matrix. This morphology lowers the critical IEC value and increases water uptake and λ value. The PVDF backbone molecular weight in the hydrophobic matrix controls the width of hydrophilic conduction channels. A high molecular weight PVDF results in a smaller channel width, lower water uptake, and resistance to excessive water swelling at a high IEC value. Although the morphology with long range hydrophilic channels is favorable for proton conductivity with low activation energy, it also leads to high sensitivity to humidity, requiring a high RH to achieve high conductivity. In

Downloaded by STANFORD UNIV GREEN LIBR on June 21, 2012 | http://pubs.acs.org
Publication Date (Web): April 30, 2010 | doi: 10.1021/bk-2010-1040.ch003

Table 3. Comparison of proton conductivity between several pairs of PVDF-g-SPS based PEMs having similar IEC numbers but different (low and high) PVDF backbone molecular weight

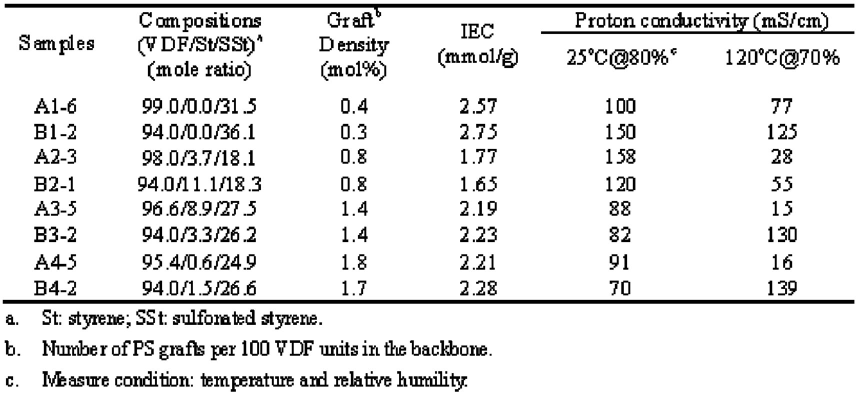

Samples	Compositions (VDF/St/SSt)[a] (mole ratio)	Graft[b] Density (mol%)	IEC (mmol/g)	Proton conductivity (mS/cm)	
				25°C@80%[c]	120°C@70%
A1-6	99.0/0.0/31.5	0.4	2.57	100	77
B1-2	94.0/0.0/36.1	0.3	2.75	150	125
A2-3	98.0/3.7/18.1	0.8	1.77	158	28
B2-1	94.0/11.1/18.3	0.8	1.65	120	55
A3-5	96.6/8.9/27.5	1.4	2.19	88	15
B3-2	94.0/3.3/26.2	1.4	2.23	82	130
A4-5	95.4/0.6/24.9	1.8	2.21	91	16
B4-2	94.0/1.5/26.6	1.7	2.28	70	139

a. St: styrene; SSt: sulfonated styrene.

b. Number of PS grafts per 100 VDF units in the backbone.

c. Measure condition: temperature and relative humility.

contrast, the moderately high graft density (1.4-2.4 mol%) PVDF-g-SPS graft copolymers show dispersed cluster-network morphology with a small cluster diameter—similar to that of Nafion—which is less sensitive to humidity and exhibits smaller water uptake and λ value. The proton conductivity is still proportional to humidity by a smaller slope, and the high activation energy results in a linear increase of proton conductivity with temperature, under the same RH condition. The PVDF-g-SPS graft copolymer with a high graft density (>2.5 mol%)—losing most of its crystallinity—exhibits instability (softness) at a high temperature and also exhibits excessive water swelling with a high IEC value. Generally speaking, the high molecular weight PVDF-g-SPS copolymer with low graft density and a high IEC value is suitable for PEM under a high RH and a wide range of temperatures, while the corresponding higher graft density ones show increased conductivity at higher temperatures.

Acknowledgments

The authors gratefully acknowledge the financial support of this work by the U.S. Department of Energy (Contracts #DE-FG36-06GO16036) and the donation of the high molecular weight VDF/CTFE copolymer from Solvay Solexis, Inc.

References

1. Rikukawa, M.; Sanui, K. *Prog. Polym. Sci.* **2000**, *25*, 1463.
2. Brandon, N. P.; Skinner, S.; Steele, B. C. H. *Annu. Rev. Mater. Res.* **2003**, *33*, 183.
3. Hickner, M. A.; Ghassemi, H.; Kim, Y. S.; Einsla, B. R.; McGrath, G. E. *Chem. Rev.* **2004**, *104*, 4587.

4. Li, Q.; He, R.; Jensen, J. O.; Bjerrum, N. J. *Chem. Mater.* **2003**, *15*, 4896.
5. Zhou, Z.; Dominey, R. N.; Rolland, J. P.; Maynor, B. W.; Pandya, A. A.; DeSimone, J. M. *J. Am. Chem. Soc.* **2006**, *128*, 12963.
6. Grot, W. G. (E. I. DuPont) U.S. Patent 4,433,082, 1984.
7. Savadogo, O. *J. New Mater. Electrochem. Syst.* **1998**, *1*, 47.
8. Gottesfeld, S.; Zawodzinski, T. A. In *Advances in Electrochemical Science and Engineering*; Alkire, R. C., Gerischer, H., Kolb, D. M., Tobias, C. W., Eds.; Wiley: New York, 2002; Vol. 5.
9. Wainright, J. S.; Wang, J.-T.; Weng, D.; Savinell, R. F.; Litt, M. *J. Electrochem. Soc.* **1995**, *142*, L121.
10. Wang, F.; Hickner, M.; Ji, Q.; Harrison, W.; Mecham, J.; Zawodzinski, T. A.; McGrath, J. E. *Macromol. Symp.* **2001**, *175*, 387.
11. Asano, N.; Aoki, M.; Suzuki, S.; Miyatake, K.; Uchida, H.; Watanabe, M. *J. Am. Chem. Soc.* **2006**, *128*, 1762.
12. Wainright, J. S.; Wang, J. T.; Weng, D.; Savinell, R. F.; Litt, M. *J. Electrochem. Soc.* **1995**, *142*, L121.
13. Zhang, J. L.; Tang, Y. G.; Song, C. J.; Zhang, J. J. *J. Power Sources* **2007**, *172*, 163.
14. Wiley, R. H.; Venkatachalam, T. K. *J. Polym. Sci., Part A* **1966**, *4*, 1892.
15. Gupta, B.; Scherer, G. G. *J. Appl. Polym. Sci.* **1993**, *50*, 2129.
16. Flint, S. D.; Slade, R. C. T. *Solid State Ionics* **1997**, *97*, 299.
17. Hietala, S.; Koel, M.; Skou, E.; Elomaa, M.; Sundholm, F. *J. Mater. Chem.* **1998**, *8*, 1127.
18. Torkkeli, M.; Serimaa, R.; Etelaniemi, V.; Toivola, M.; Jokela, K.; Paronen, M.; Sundholm, F. *J. Polym. Sci., Part B* **2000**, *38*, 1734.
19. Kuhn, H.; Gubler, L.; Schmidt, T. J.; Scherer, G. G.; Brack, H. P.; Simbek, K.; Rager, T.; Geiger, F. Proceedings of the 2nd European PEFC Forum, June 30−July 4, 2003, Lucerne, Switzerland; p 69.
20. Shi, Z. Q.; Holdcroft, S. *Macromolecules* **2004**, *37*, 2084.
21. Zhang, M. F.; Russell, T. P. *Macromolecules* **2006**, *39*, 3531.
22. Shi, Z. Q.; Holdcroft, S. *Macromolecules* **2005**, *38*, 4193.
23. Xu, K.; Li, K.; Khanchaitit, P.; Wang, Q. *Chem. Mater.* **2007**, *19*, 5937.
24. Tsang, E. M. W.; Zhang, Z. B.; Shi, Z. Q.; Soboleva, T.; Holdcroft, S. *J. Am. Chem. Soc.* **2007**, *129*, 15106.
25. Milner, S. T. *Macromolecules* **1994**, *27*, 2333.
26. Xenidou, M.; Beyer, F. L.; Hadjichristidis, N.; Gido, S. P.; Tan, N. B. *Macromolecules* **1998**, *31*, 7659.
27. Zhang, Z. C.; Chung, T. C. M. *Macromolecules* **2006**, *39*, 5187.
28. Chung, T. C.; Petchsuk, A. *Macromolecules* **2002**, *35*, 7678.
29. Wang, Z. M.; Zhang, Z. C.; Chung, T. C. M. *Macromolecules* **2006**, *39*, 4268.
30. Veriss, R. A.; Sen, A.; Willis, C. L.; Pottick, L. A. *Polymer* **1991**, *32*, 1867.
31. Damay, F.; Klein, L. C. *Solid State Ionics* **2003**, *162−163*, 261.
32. Alberti, G.; Casciola, M.; Massinelli, L.; Bauer, B *J. Membr. Sci.* **2001**, *185*, 73.
33. Zhou, Z. L.; Dominey, R. N.; Rolland, J. P.; Maynor, B. W.; Pandya, A. A.; DeSimone, J. M. *J. Am. Chem. Soc.* **2006**, *128*, 12963.

Downloaded by STANFORD UNIV GREEN LIBR on June 21, 2012 | http://pubs.acs.org
Publication Date (Web): April 30, 2010 | doi: 10.1021/bk-2010-1040.ch003

Downloaded by OHIO STATE UNIV LIBRARIES on June 21, 2012 | http://pubs.acs.org
Publication Date (Web): April 30, 2010 | doi: 10.1021/bk-2010-1040.ch004

Chapter 4

Rigid Rod Polyelectrolytes with Frozen-In Free Volume: High Conductivity at Low RH

Morton Litt,[1,*] Sergio Granados-Focil,[2] and Junwon Kang[3]

**[1]Macromolecular Science Dept., Case Western Reserve University,
Cleveland, OH 44106
[2]Clark University, Wooster, MA 01610
[3]Samsung Corp., Korea
*mhl2@case.edu**

Aromatic rigid-rod polyelectrolytes have been made that have “frozen-in free volume”. Homopolymers and copolymers form liquid crystalline arrays that cannot pack closely due to steric hindrance. They form nano-channels that absorb and hold water very strongly. This enables them to retain conductivity at very low relative humidities. Conductivity versus λ at various temperatures for two homopolymers, poly(p-phenylene 2, 5-disulfonic acid), PPDSA, and poly(p-biphenylene 3, 3’-disulfonic acid), PBPDSA, is shown. Data are presented and analyzed for PPDSA showing that the “frozen-in free volume” for this material is about 63 cc per -SO_3H group (λ=3.5). Comparison of a graft polymer of PBPDSA with the homopolymer showed that bulky grafted moieties facilitated higher water absorption in the mid relative humidity range, while hydrophobic bonding of the non-polar groups retarded swelling at higher humidities.

Introduction

The basic impetus for work was to develop materials that could hold enough water at low humidity to provide a medium suitable for proton migration. The approach taken was inspired by two well known materials that strongly sequester water, molecular sieves and silica gel. They have highly polar nano-channels that

In Fuel Cell Chemistry and Operation; Herring, A., et al.;
ACS Symposium Series; American Chemical Society: Washington, DC, 2010.

hold water by both hydrogen bonding and capillary attraction. Their absorbed water is in equilibrium with atmospheric water vapor at <0.01% RH (*1*).

The question is: "How can one generate an analogous mechanism that would apply to materials which can be cast as films that would hold water strongly, and also have reasonable proton mobility?" The approach taken was to make aromatic linear rigid-rod polymers that had sulfonic acid groups attached to the backbone. Such molecules tend to form nematic liquid crystals with all backbones parallel. If groups with large cross-sectional areas are attached to the backbone, a small mole fraction, 5 to 20%, can separate the chains over their whole length, and if chosen correctly make the polymers water insoluble. At high humidity, such substituted polysulfonic acids will absorb much water. If water is removed, the will chains move closer to each other. However, bulky substituents would impinge on the neighboring chains before the backbones can touch. Since the chains are rigid rods, the backbones are kept apart and form an array of nano-pores lined with sulfonic acid groups. These should hold water very well by both H-bonding and capillary attraction. Of course, the chains are not completely rigid and may bend, or otherwise distort to approach each other as the last few water molecules are removed. But such distortion requires energy; water molecules are removed with great difficulty and the structure reabsorbs water readily to return to a low energy conformation. We call this "frozen-in free volume".

This was first studied in the naphthalene 1, 4, 5, 8-tetracarbonyl diimide 4, 4'-biphenylene 2, 2'-disulfonic acid system (*2*). However, polyimides hydrolyze slowly at room temperature (*3*) and rapidly in boiling water. Therefore the work was shifted to non-hydrolysable systems, poly(p-phenylenes) with attached sulfonic acid groups. This report discusses the water retention behavior of these materials and its correlation with their morphology.

Results and Discussion

Polymer Synthesis

The first task was to find a good, inexpensive synthetic approach. Poly(p-phenylenes) have been made in many ways; one approach, the Suzuki Reaction, was used successfully to make soluble materials with attached sulfonic acid groups (*4*). However, as described, it could not be used as described to make polymers with high concentrations of acid groups. A synthetic method, using the Ullman Reaction, was developed that produced polymers of reasonable molecular weight that could have one or two sulfonic acid groups on each benzene ring (*5a*). The reaction is shown in Scheme 1. The best counter-ions we found were Li+ and benzyl trimethyl ammonium. As of now, the best molecular weight we obtained for PPDSA is ~40-50K Daltons, and ~10 to 15K Daltons for PBPDSA.

Downloaded by OHIO STATE UNIV LIBRARIES on June 21, 2012 | http://pubs.acs.org
Publication Date (Web): April 30, 2010 | doi: 10.1021/bk-2010-1040.ch004

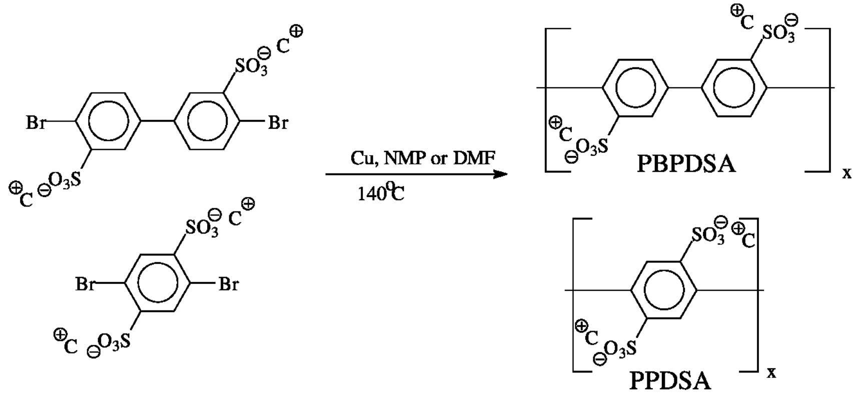

Scheme 1. Ullman polymerization reaction: C^+ is any cation

Grafting

Since the homopolymers are water soluble, much time was spent trying to make water insoluble versions of the basic polymers. Copolymerization has been difficult; a fall-back position was grafting non-polar moieties on the sulfonic acid groups to make sulfones. We used polyphosphoric acid (PPA) at 140°C both as the reaction medium and dehydrating agent. The non-polar moieties that worked well with PBPDSA were biphenyl, t-butyl benzene and 2, 6-di-t-butyl phenol. The biphenyl grafts were water soluble at 25% substitution, but insoluble at 50% substitution. Their films could be post-crosslinked by heating to ~200°C for 10 minutes. The t-butyl substituted moieties gave water insoluble PEMs at lower degrees of substitution. However, the t-butyl group is not very stable under the grafting conditions; it may leave the benzene ring forming isobutene. This can dimerize and reattach. The graft structures cannot be exactly specified. (Recent work uses neopentyl benzene which is stable.)

Reaction conditions were optimized and we obtained grafts that could be cast into highly conductive, dimensionally stable PEMs. The results for dimensional stability are given in Table 1. The % substitution listed for the t-butyl containing grafts is based on calculations from the ^{1}H NMR t-butyl area relative to the aromatic backbone area. However, equivalent weights determined by titration of di-t-butyl phenol and t-butyl benzene grafted samples after drying at 175°C for one hour were quite high, showing higher degrees of substitution and/or water retained after this drying procedure. The measured equivalent weights are listed within the parentheses. The measured mole% grafting for the biphenyl grafts is reasonably accurate. However, we did not measure equivalent weight after cross-linking; the sulfone mole fraction could be up to twice the grafted group mole fraction.

Downloaded by OHIO STATE UNIV LIBRARIES on June 21, 2012 | http://pubs.acs.org
Publication Date (Web): April 30, 2010 | doi: 10.1021/bk-2010-1040.ch004

Downloaded by OHIO STATE UNIV LIBRARIES on June 21, 2012 | http://pubs.acs.org
Publication Date (Web): April 30, 2010 | doi: 10.1021/bk-2010-1040.ch004

Table 1. Grafted PBPDSA films: dimensional changes from 22 to 100% RH

Grafting group	*"Mole %" of grafted group (Equiv. Wt. **)*	*Δx (%)*	*Δy (%)*	*Δz (%)*
Biphenyl*	10	2	2	45
Biphenyl*	20	1	1	35
Biphenyl*	55	~0	1	15
t-Butylbenzene	5 (243)	1	2	85
t-Butylbenzene	25	1	1	50
Di-t-butylphenol	5 (243)	~0	~0	50
Di-t-butylphenol (batch 1)	8 (260)	~0	~0	33
Di-t-butylphenol (batch 2)	10 (265)	~0	~0	17
Di-t-butylphenol (batch 3)	8.4 (235)	~0	~0	26
Di-t-butylphenol (batch 4)	8.4 (235)	~0	~0	28
Di-t-butylphenol	15 (270)	~0	~0	15

* After cross-linking, 10 min at 200°C ** From titration of dried films (Equivalent Wt. homopolymer = 156)

Dimensional Stability

Cast films were equilibrated at 22% relative humidity and their dimensions were measured. The films were then equilibrated at 100% relative humidity and remeasured. The results are given in Table 1. "x" is parallel to the film surface in the casting direction; "y" is parallel to the film surface perpendicular to the casting direction and "z" is the film thickness direction. Swelling was essentially only in the z direction, which implies that the polymer chains oriented parallel to the surface. The di-t-butyl phenol grafted PEMs swelled less than the others when similar equivalent weight materials were compared. Some, with IEC > 4 mEq./gm, swelled less than 30%. The x and y dimensions of all grafts did not change with relative humidity, which is important for fuel cell use. We attribute the lower swelling to a larger aliphatic fraction, generating more hydrophobic bonding at a given degree of substitution.

Water Absorption

Water absorption was measured in many different ways. The usual method; vacuum drying a film, weighing it, exposing it to a given relative humidity atmosphere and reweighing it until the weight stabilized, was used. However, since these materials hold water very strongly, such drying procedures may not dry them completely. A larger than expected equivalent weight was generally found for the homopolymers. If this value were used, it would affect the calculated values of λ. Therefore, several other methods were used to check the results.

Table 2. PBPDSA λ as a function of relative humidity (24°C); measured three ways

	Lambda			
Relative Humidity, %	*By titration*	*By ^1H NMR*	*By TGA**	*Average*
10			2.9	2.9
23	3.7	3.6	3.9	3.7
45	4.3	4.4	4.8	4.5
58	6.0	5.3	5.9	5.6
75	7.0	7.3	7.6	7.3

* Calculated using the measured dried equivalent weight, 170 Daltons/SO_3H, the fractional weight loss from 25 to 230°C and assuming a residual λ of 0.8 at 230°C.

Water retention after drying was checked as follows. PBPDSA homopolymer films were heated for one hour at specified temperatures; they were then weighed and titrated with dilute NaOH. The measured equivalent weight was constant at ~176 Daltons/acid group after heating at 100, 125 and 150°C, but decreased slightly at 175°C and reached 173 Daltons at 200°C. Based on the theoretical equivalent weight of 156 Daltons, the materials still held one water molecule per acid group after this heating. The 200°C TGA plot showed some weight loss during annealing (*6*). However, its low equivalent weight (high IEC) implied that water was lost and there was no acid loss.

PPDSA films were heated under vacuum at 90°C for 24 hrs and weighed. They were then heated at 150°C under vacuum for one hour and reweighed. The weights were constant within the experimental error, ± 1mg, 1 to 2% of the weight, showing that any water retained at 100°C was still held after one hour's heating at 150°C. Equivalent weight determinations were made on five films dried at 90°C for 24 hours. The average was 139.0±0.4 gm/acid group. Since the dry equivalent weight for PPDSA should be118, it held 1.2 waters per acid group after this drying. Sample dimensions were measured after drying, and again after equilibration at a given relative humidity. Low molecular weight polymer was annealed at various temperatures for one hour and then titrated. The equivalent weight was the same for samples annealed at all temperatures up to 240°C; acid loss was noted after annealing one hour at 270°C (*8*).

Water absorption for PPDSA was measured by equilibrating dried films at a given relative humidity, with periodic weighings, until the weight became constant. This was reached in less than one day. Film dimensions before and after equilibration were also measured.

TGA measurements of water absorption of PBPDSA were usually run as follows. A nitrogen stream was equilibrated at a given RH by passing it through a flask containing a LiCl solution of the desired concentration (*5*). PBPDSA films, or their grafts, were equilibrated at room temperature in the apparatus by passing the wet nitrogen over them until their weight stopped increasing. The stream was switched to dry nitrogen; for different sets of runs the homopolymer was kept at room temperature for 60 to 150 min under the dry nitrogen flow and then heated at

Downloaded by OHIO STATE UNIV LIBRARIES on June 21, 2012 | http://pubs.acs.org
Publication Date (Web): April 30, 2010 | doi: 10.1021/bk-2010-1040.ch004

Downloaded by OHIO STATE UNIV LIBRARIES on June 21, 2012 | http://pubs.acs.org
Publication Date (Web): April 30, 2010 | doi: 10.1021/bk-2010-1040.ch004

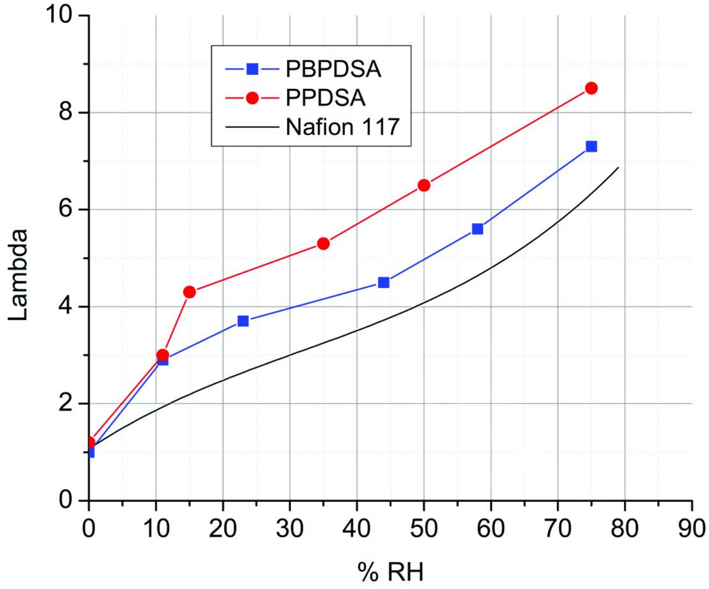

*Figure 1. Comparison of lambda as a function of relative humidity (25°C) for PPDSA, PBPDSA and Nafion117®. Nafion117® λ is from least squares minimization of most literature values (7). (λ=1.358*10^{-5}*(%RH)^{3}-1.297*10^{-3}*(%RH)^{2}+0.09105*(%RH)+1.067) (see color insert)*

20°/min to 600°C. After the room temperature sweep, the polymer lost one more water per acid group, between 175 and 230°C. However, some water may still have been retained even at 240°C, where polymer degradation begins. Water absorption of one graft copolymer was also measured using TGA. In this case, heating began when the dry nitrogen flow was started.

^{1}H NMR measurements of λ for PBPDSA were run as follows. Potassium acetate was dissolved in D_2O to make a calibrated solvent for further measurements. An NMR scan on the solvent was run to determine the ratio of HDO to CH_3. Equilibrated polymer samples were dissolved in the solvent and the ^{1}H NMR spectrum was taken. Solvent H area was subtracted from the HDO peak and the remaining area was compared with the aromatic hydrogen area. There is one acid proton for three aromatic hydrogens. This was subtracted; any remaining HDO area came from absorbed water. PBPDSA retained one water per sulfonic acid after drying under vacuum at 100°C for two hours.

Table 2 lists λ as a function of relative humidity for PBPDSA determined by the methods described above. The 0% relative humidity λ for PBPDSA was taken as that remaining after heating at 100°C under vacuum for several hours. The measured equivalent weight was 174 Daltons, implying that it still retained one water molecule per acid. In the TGA measurements of equilibrated samples, most of the weight loss occurred during the room temperature sweep; the further weight loss at 230°C was equivalent to a λ of 1.0. However, the values calculated for λ from the weight fraction at 230°C, based on the assumption that the material was

In Fuel Cell Chemistry and Operation; Herring, A., et al.;
ACS Symposium Series; American Chemical Society: Washington, DC, 2010.

Downloaded by OHIO STATE UNIV LIBRARIES on June 21, 2012 | http://pubs.acs.org
Publication Date (Web): April 30, 2010 | doi: 10.1021/bk-2010-1040.ch004

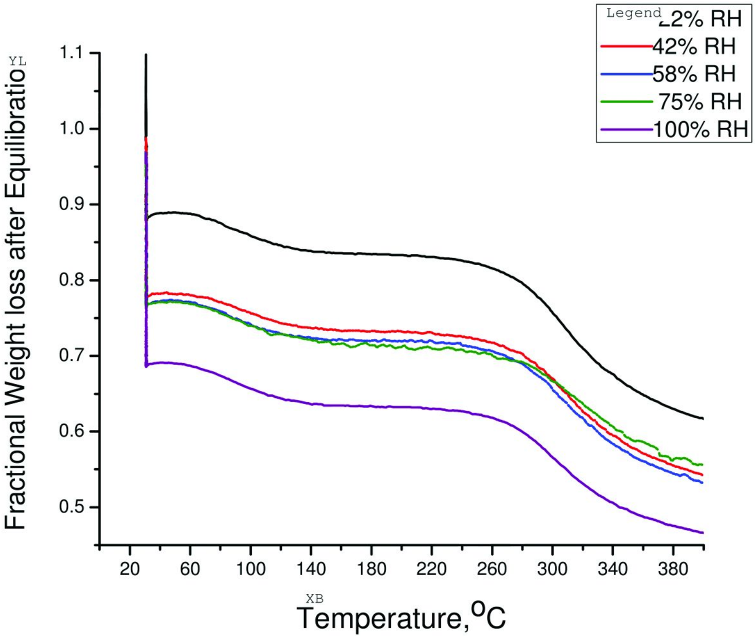

Figure 2. Relative weight loss of PBPDSA di-t-butyl phenol graft ("5%", "dry" Eq. Wt. =243) after equilibration at indicated relative humidity. (TGA scans: 2.5 hrs at 30°C; then ramped at 20°/min.) (see color insert)

anhydrous, were below those found by ^{1}H NMR. PBPDSA dried for one hour at 200°C had an equivalent weight of 170 Daltons. Drying at 200°C could not remove 0.8 waters per acid group. This λ was therefore added to the calculated λs given in Table 2. When these values are compared with the NMR data, they are about 0.4 higher. This could mean that, at this heating rate, PBPDSA retained about 0.4 λ at 230°C. Residual λ for PPDSA was 1.2, measured as described above.

Figure 1 shows λ as a function of relative humidity for PBPDSA, PPDSA and Nafion 117. The PBPDSA values are the averages of the data in Table 2. The Nafion 117 line is a least squares fitting for all literature values we found (*7*). (The Nafion 117 data had one value at 0% (λ = 0) and many at 5% and higher relative humidity. The least squares fitting looked at all the data and minimized to a λ of 1 at 0% relative humidity. This implies that the first water is held much more strongly than the rest, as is well known.) Lambda for both PPDSA and PPDSA rises rapidly at very low relative humidity and then parallels the Nafion curve above 20% relative humidity. PBPDSA λ values are about 1 and PPDSA λ values are 2 to 2.5 higher than those of Nafion117 from 15 to 75% relative humidity. A possible measure for the frozen-in free volume could be the value of λ where the curves become parallel, ~3 for PBPDSA and ~4.3 for PPDSA.

Downloaded by OHIO STATE UNIV LIBRARIES on June 21, 2012 | http://pubs.acs.org
Publication Date (Web): April 30, 2010 | doi: 10.1021/bk-2010-1040.ch004

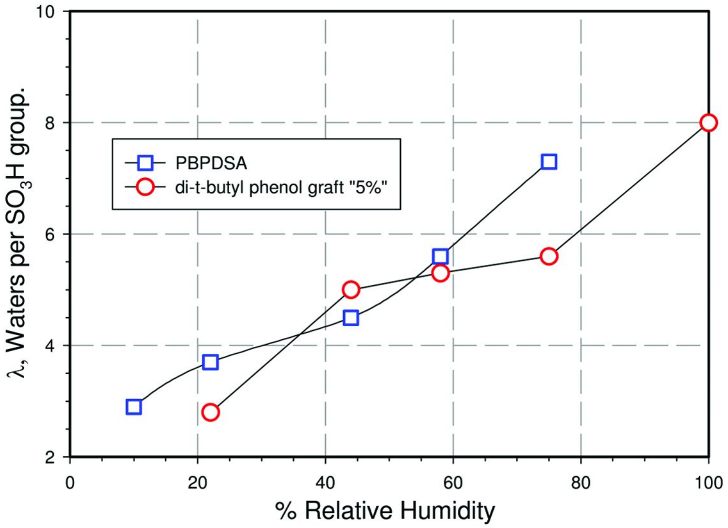

Figure 3. Comparison of λ as a function of relative humidity for PBPDSA (25°C) and its di-t-butyl phenol graft (30°C, "5%", "dry" Eq.Wt. = 243 Daltons) (see color insert)

Graft Polymer Water Absorption

One graft of di-t-butyl phenol on PBPDSA ("5%" in Table 1, Equivalent Wt. = 243.) is reported on here (*6*). It was studied for water uptake by equilibrating at specific relative humidities in a TGA system, switching to dry nitrogen at 30°C for 2.5 hours, and then heating at 20°/min. The weight fraction remaining at 230°C was taken to be the weight of dried polymer; the fractional weight loss is a measure of lambda at that relative humidity. (Since some water is probably still held at 230°C, the λs given could be low by as much 0.5) The TGA weight/temperature curves are shown in Figure 2. The frozen-in free volume effect is obvious here; λ rises rapidly at low humidity but is almost constant from 42 to 75% relative humidity. The weight loss between 60 and 230°C was equivalent to a λ of 1.0, based on the weight at 230°C.

λ measurements for this graft are compared with those for the homopolymer, PBPDSA, in Figure 3. The effect of the bulky aliphatic groups can be seen. At 42% relative humidity, the graft copolymer λ is higher than that of the homopolymer, but rises much more slowly at higher humidity. The hydrophobic groups may be compressed at 22% relative humidity; at higher humidities they separate the backbones and volume equilibrates where the swelling forces are counterbalanced by the hydrophobic interactions of the non-polar tails.

Conductivity

Longitudinal conductivity was measured using the four point method. Strips were cut from the PEM and carbon paper electrodes were clipped to them. The

Downloaded by OHIO STATE UNIV LIBRARIES on June 21, 2012 | http://pubs.acs.org
Publication Date (Web): April 30, 2010 | doi: 10.1021/bk-2010-1040.ch004

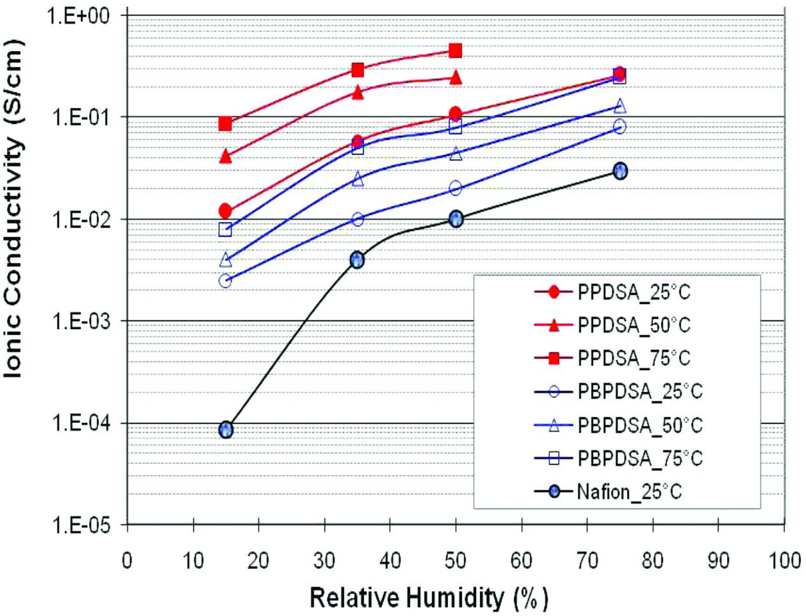

Figure 4. Comparison of PBPDSA, PPDSA and Nafion117 conductivities as a function of temperature and relative humidity. (see color insert)

films were equilibrated over LiCl solutions in capped plastic bottles. Lead wires from the electrodes went through the cap to the electrometer. The complex impedance was measured as a function of frequency and the film resistance was taken at that value where tan(θ) was zero.

Water absorption facilitates conductivity; this is reflected in the data for the homopolymers. Conductivities as a function of relative humidity for the two homopolymers are compared with that of Nafion117 in Figure 4. Both rigid rod polymers have higher room temperature conductivity at all relative humidities than Nafion117 does. The effect of frozen-in free volume is demonstrated in the conductivities; PPDSA conductivity at room temperature matches that of PBPDSA at 75°C. At 15% relative humidity and 25°C, PPDSA conductivity is ~ 0.01 S/cm, 100 times larger than that of Nafion117. At 75°C and 15% relative humidity, PPDSA conductivity reaches 0.10 S/cm, the DOE goal for 2015. Water insoluble copolymers of PPDSA should be able to meet most of the DOE requirements.

Estimation of Frozen-In Free Volume

Can one measure the frozen in free volume? This was attempted for the polyimide disulfonic acid series (*8*). Here the variation of λ as a function of relative humidity was used to determine water activity in the polymer and correlated with the solvation energy due to the proton plus a frozen-in free volume. This was also correlated with TGA scans of copolymers. Both types of measurements gave the

Downloaded by OHIO STATE UNIV LIBRARIES on June 21, 2012 | http://pubs.acs.org
Publication Date (Web): April 30, 2010 | doi: 10.1021/bk-2010-1040.ch004

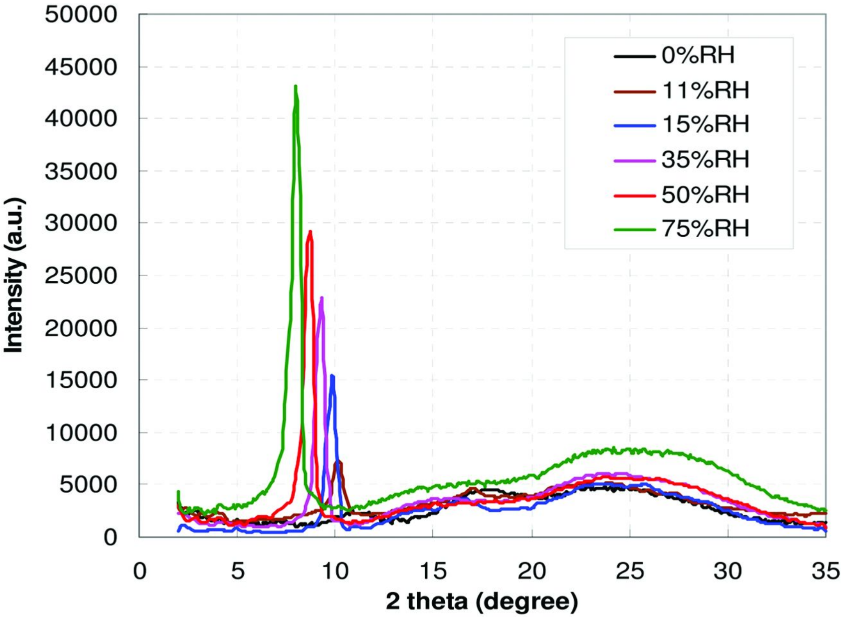

Figure 5. WAXD transmission spectra of PPDSA films as a function of relative humidity (see color insert)

same results; copolymers retained two to four waters per acid group, depending on the comonomer, after room temperature drying. The frozen-in free volume calculated from the TGA curves agreed with that calculated from the variation of λ with relative humidity. We hope to do this for the present materials in a later publication.

Films were cast on silanized glass from 20 to 30% solutions in water by spreading with a Gardiner knife. At these concentrations, we obtained liquid crystalline solutions; they were almost opaque and very viscous. Transmission and reflection WAXD scans were run on PPDSA films conditioned at different relative humidities. Film dimensions were measured both on dried films and after water uptake equilibration. The volume change could therefore be correlated with weight uptake (λ). The humidified films were sandwiched between very thin PVC films to retain the moisture during the scans. Since the shearing might cause chain orientation, scans were taken parallel and perpendicular to the casting shear direction. All transmission WAXD scans showed strong low angle reflections that varied with water content, Figure 5.

The low angle reflections were almost absent from the reflection WAXD scans; this implies that the polymer molecules were oriented mainly perpendicular to the film surface. The measured dimensional changes reflected this; at low relative humidities there was more swelling in the X and Y directions than in the Z direction (*5*). When the molar volumes as a function of relative humidity calculated from the WAXD long spacings (Molar volume = $1.27*d^2$ cc/SO_3H, if the chains are parallel and packed orthogonally, and the d spacing index is 100) were plotted versus the measured molar volumes, a straight line was obtained

Downloaded by OHIO STATE UNIV LIBRARIES on June 21, 2012 | http://pubs.acs.org
Publication Date (Web): April 30, 2010 | doi: 10.1021/bk-2010-1040.ch004

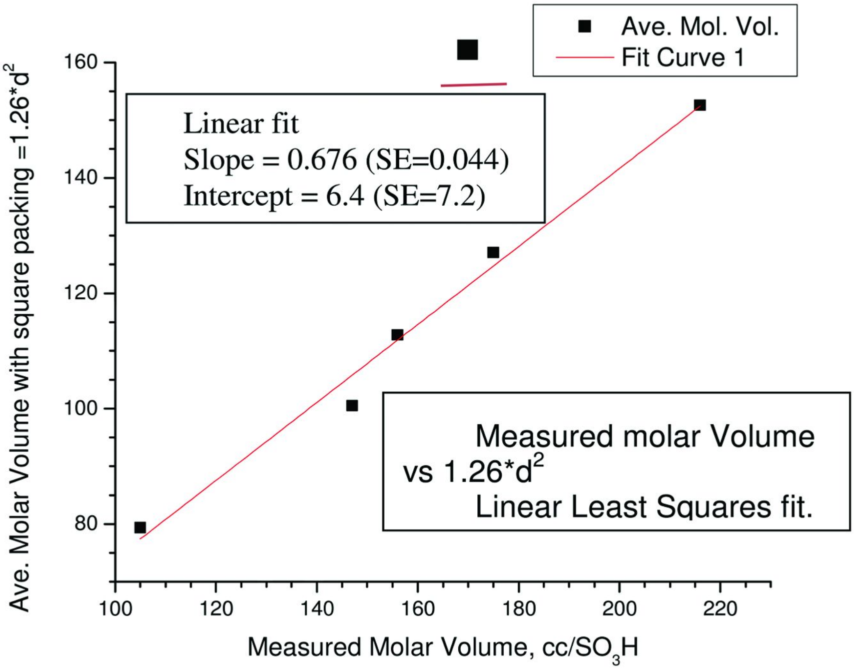

Figure 6. Correlation of molar volume, measured and from averaged d^2, as a function of λ. (Volume at 11% RH was not measured.) (see color insert)

with a slope of 0.676 and an intercept of 0 within one standard error, Figure 6. The correlation of the polymer cross-sectional area with the molar volume shows that the water is sorbed between the parallel molecules, pushing them apart equally along both axes. However, the slope of 0.676 implies that the molecules are not packed orthogonally or hexagonally (For hexagonal organization the slope should be 0.866.). A possibility is that a = b and the angle of the a-b unit cell projection is near 45°; the slope should then be 0.707, about the value found. The packing, while regular, is complicated and not understood at present. We are working on this. The linear fit implies that both the a and b axes of the unit cell expand proportionally with water content, so the data can be analyzed to estimate “frozen-in” free volume.

Estimation of “Frozen-In” Free Volume

The 0% relative humidity WAXD scan in Figure 5 differs from the other scans in that the low angle reflection has low intensity and is very broad. Since the chains must be parallel at all humidities, this implies that the sulfonic acid/benzene bond angles and phenyl/phenyl dihedral angles are distorted if too much water is removed; the chains cannot pack uniformly. These are high energy conformations. In the present analysis, we omitted the 0% relative humidity data, since they reflect this poor packing, and the d-spacings were too broad to be accurately measured.

Downloaded by OHIO STATE UNIV LIBRARIES on June 21, 2012 | http://pubs.acs.org
Publication Date (Web): April 30, 2010 | doi: 10.1021/bk-2010-1040.ch004

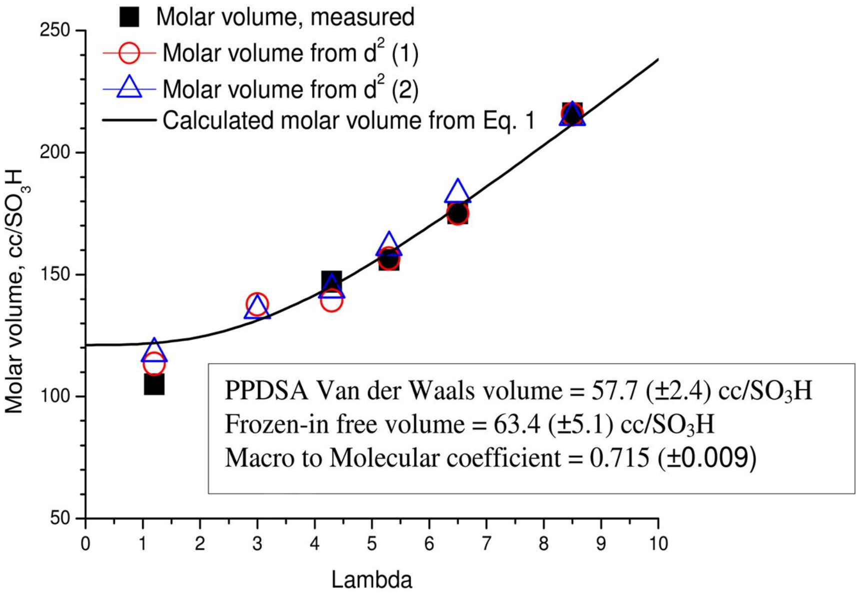

Figure 7. Determination of "frozen-in" free volume using Eq. 1. Data for λ = 1.2 not used. WAXD scans taken through films. d(1) perpendicular to casting direction; d(2) parallel to casting direction. (see color insert)

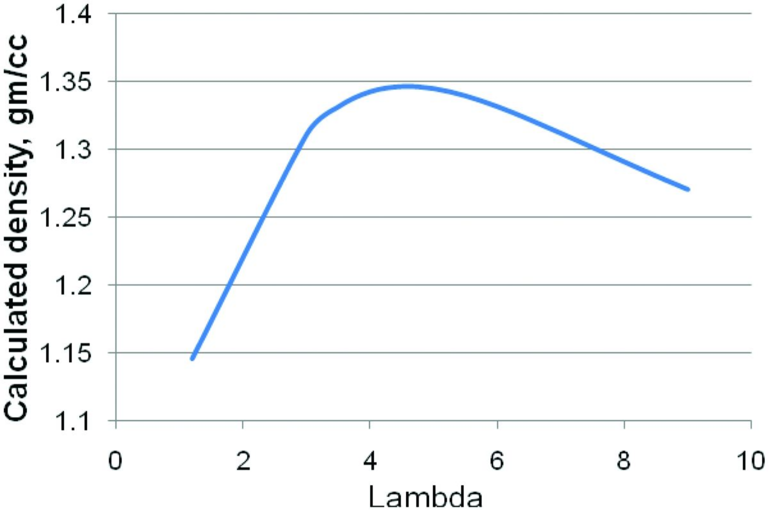

Figure 8. Calculated PPDSA density as a function of Lambda (see color insert)

Many curve fitting equations can be postulated; some might be related to the real system behavior. One, for which all the data was used, has been presented (*8*). In this preprint, the measured molar volumes and d-spacing data were analyzed separately. The frozen-in free volume found was ~35 (±9) cc per SO_3H group

Downloaded by OHIO STATE UNIV LIBRARIES on June 21, 2012 | http://pubs.acs.org
Publication Date (Web): April 30, 2010 | doi: 10.1021/bk-2010-1040.ch004

based on the measured volumes, and ~55 (±13) cc from the d spacing analysis. The relatively large standard errors were due to the inclusion of the 0% relative humidity data.

This approach has been refined. Water is absorbed very strongly into the dry polymer to relieve the compressive strain. For PPDSA, this requires about 3 waters per sulfonic acid (11% relative humidity). It fills most of the frozen-in free volume before the chains start to separate (>15% relative humidity). Eventually the frozen-in free volume is filled completely; further volume increase reflects water absorption with a density of 1gm/cc.

The curve fitting equations are given below, Equations 1 and 2. We use the same equations as before (*8*). The hyperbolic tangent function fits the conceptual approach of the model. The original equation was modified to conform completely to the model. Equation 1 describes water initially absorbing into the dry polymer with no volume increase, but as water fills the free volume the polymer volume/λ slope increases to a final value of 18cc/ λ. This approach eliminated one parameter. Equation 2 includes a macro-to-micro conversion factor that correlates the d-spacings with the measured molar volumes.

$$MV = VdWV + 18 * \lambda + FV * (1 - \tanh(18 * \lambda / FV)) \qquad 1$$

$$1.27 * d^2 = K * MV \qquad 2$$

Definitions:

- *MV* = Molar Volume, per SO_3H group
- *VdWV* = Polymer Van der Waals Molar Volume
- *FV* = Frozen-in free Volume per SO_3H group
- *K* = Macro to molecular volume conversion coefficient (used to match Fig. 6)

Equation 1 was used fit the measured molar volumes; both equations were needed in order to correlate the d-spacings. Non-linear global minimization of the data gave a very good fit. The polymer Van der Waals volume was 57.7 (±2.4) cc/SO_3H, compared to 59-60 cc found earlier (*8*). However, the present frozen-in free volume is 63 (±5) cc (λ = 3.5), a large increase over the earlier values. The conversion coefficient, 0.715 (±0.009), agreed within one SD with that found for the simple plot given in Fig. 6.

The slope of the calculated volume curve in Figure 7 increases with lambda and reaches 18 cc/lambda only at lambda = 8.5. The calculated polymer density as a function of lambda, Figure 8, shows the effect of the frozen-in free volume. Density first increases with lambda to a maximum of ~1.35 gm/cc at λ = 4.5 to 5; at higher λ, the density decreases. At maximum density, about 25% of newly absorbed water is still filling free volume.

Downloaded by OHIO STATE UNIV LIBRARIES on June 21, 2012 | http://pubs.acs.org
Publication Date (Web): April 30, 2010 | doi: 10.1021/bk-2010-1040.ch004

Summary and Conclusions

This paper concentrates on the effect of polymer structure on water absorption at various relative humidities. At low λ, two factors can operate. First, polymer packing can be relatively inefficient; polymers are bulky molecules and even close packing leaves voids that can be filled by small molecules. (Polymers have higher solution densities than their bulk densities.) In addition, linear, rigid rod poly (phenylene sulfonic acids) molecules probably are forced into higher energy conformations when they pack closely as the last few waters are removed. Consequently, an extra term should be added to the heat of water vaporization - the work needed to compress the polymer structure. Therefore, at low λ water is absorbed strongly, filling the voids and expanding the matrix until the polymer structure can relax to a low energy conformation. Above this λ, water should approach its normal heat of vaporization; for polyelectrolytes, this includes the heat of solvation due to H-bonding with the acid proton. We have designated the volume of water per acid group that is needed to relax the polymer structure and fill the packing voids, where the heat of vaporization becomes normal, as the frozen in free volume. This was seen both for PBPDSA and PPDSA. PPDSA λ paralleled that of Nafion117 above 15% relative humidity ($\lambda = 4.3$), while PBPDSA λ paralleled Nafion117 above 11% relative humidity ($\lambda=2.9$).

The use of WAXD combined with measurements of volume and weight increase for PPDSA as a function of relative humidity enabled us to make a direct estimate of frozen-in free volume. While the equation used can be considered curve fitting, it has the correct shape for such an analysis. The square of the low angle WAXD d-spacings correlated exactly with the measured molar volumes; this showed that the volume increase was due to the water absorbed between the chains, and that the chain-to-chain distance increased isotropically. The frozen-in free volume from this analysis was 63 cc/SO_3H, a λ of 3.5. A relatively sharp inter-chain reflection was evident at 11% RH in the WAXD scan ($\lambda=3.0$) showing that most of the packing strain had been removed.

When a small mole fraction of di-t-butyl phenol, a bulky molecule, was grafted on PBPDSA to make it water insoluble, the rigid rod chains were kept apart, even at low humidity. At 45% relative humidity, the graft polymer absorbed more water per acid than the homopolymer, showing that the grafted groups were pushing the backbones apart. However, the lower λ at 22% relative humidity implies that the structure deformed with a lower energy cost, probably by side group rotations. The effect of the alkyl tail hydrophobic bonding was strong; λ increased by less than one unit between 45 and 75% relative humidity. The polymer was dimensionally stable over a large relative humidity range and λ at 45% relative humidity was high enough to give good conductivity at operating temperatures; both factors are important for easy fuel cell operation. We have reported the conductivity of a similar di-t-butyl phenol graft over a large temperature and relative humidity range (*5a*, *8*) (Batch 3 in Table 1); it was higher than PBPDSA homopolymer at 75°C and low humidities and had excellent dimensional stability.

Downloaded by OHIO STATE UNIV LIBRARIES on June 21, 2012 | http://pubs.acs.org
Publication Date (Web): April 30, 2010 | doi: 10.1021/bk-2010-1040.ch004

Acknowledgments

This work was funded by DOE Grant DE-FC36-06GO16039. Early support for work on PBPDSA was from DARPA, with some additional support from T/J Technologies.

References

1. Shugar, G. J.; Dean, J. A. *The Chemist's Ready Reference Handbook*, 25-4; McGraw-Hill Publishing Co.: 1989.
2. Zhang, Y. Ph.D. Thesis, CWRU, 2001. Zhang, Y.; Litt, M.; Savinell, R.; Wainwright, J.; Vendramini, Jerome *Polymer Prepr.* **2000**, *41* (2), 1561.
3. Kim, H.-J.; Litt, M. H.; Shin, E.-M.; Nam, S. Y. *Macromol. Res.* **2004**, *12* (6), 545–552.
4. Vanhee, S.; Rulkins, R.; Lehmann, U.; Rosenauer, C.; Schultze, M.; Koehler, W.; Wegner, G. *Macromolecules* **1996**, *29* (15), 5136–5142. Rulkens, R.; Wegner, G.; Enkelmann, V.; Schultze, M. *Ber. Bunsen Ges.* **1996**, *100* (6), 707–714.
5. (a) Granados-Focil, S. Ph.D. Thesis, CWRU, 2006. (b) Kang, J. W. Ph.D. Thesis, CWRU, 2008. (c) Granados-Focil, S.; Litt M. H. *PMSE Prepr.* **2003**, *89*, 438.
6. Young, T. M.S. Thesis, Case Western Reserve University, 2006.. Original data reanalyzed by M. Litt.
7. Pushpa, K. K.; Nandan, D.; Iyer, R. M. *J. Chem. Soc., Faraday Trans. 1* **1988**, *84* (6), 204, 2056. Morris, D. R.; Sun, X. *J. Appl. Polym. Sci.* **1993**, *50*, 1445–1452. Rivin, D.; Kendrick, C. E.; Gibson, P. W.; Schneider, N. S. *Polymer* **2001**, *42*, 623–635. Reucroft, P. J.; Rivin, D.; Schneider, N. S. *Polymer* **2002**, *43*, 5157–5161. Jalani, N. H.; Choi, P.; Datta, R. *J. Membr. Sci.* **2005**, *254*, 31–38. Choi, P.; Jalani, N. H.; Datta, R. *J. Electrochem. Soc.* **2005**, *152* (3), E84–E89. Zawodzinski, T. A.; Neeman, M.; Shillerud, L. O.; Gottesfeld, S. *J. Phys. Chem.* **1991**, *95*, 6040–6044. Zawodzinski, T. A.; Derouin, C.; Radzinski, S.; Sherman, R. J.; Smith, V. T.; Springer, T. E.; Gottesfeld, S. *J. Electrochem. Soc.* **1993**, *140*, 1041–1047. Zawodzinski, T. A.; Derouin, C.; Radzinski, S.; Sherman, R. J.; Smith, V. T.; Springer, T. E.; Gottesfeld, S. *J. Electrochem. Soc.* **1993**, *140*, 1041–1047. Zawodzinski, T. A; Springer, T. E.; Davey, J.; Jestel, R.; Lopez, C.; Valerio, J.; Gottesfeld, S. *J. Electrochem. Soc.* **1993**, *140*, 1981–1985.
8. Litt, M. H.; Kang, J. W. *ACS Fuel Chemistry Preprints* **2008**, *53* (2), 785–786.

Downloaded by PENNSYLVANIA STATE UNIV on June 21, 2012 | http://pubs.acs.org
Publication Date (Web): April 30, 2010 | doi: 10.1021/bk-2010-1040.ch005

Chapter 5

Molecular Weight Effects on Poly(arylene ether sulfone)-Based Random and Multiblock Copolymers Characteristics for Fuel Cells

Anand S. Badami,[1,2] Hae-Seung Lee,[1] Yanxiang Li,[1,3] Abhishek Roy,[1,4] Hang Wang,[1,5] and James E. McGrath[1,*]

[1]Department of Chemistry, Macromolecular Science and Engineering Program, Macromolecules and Interfaces Institute, Virginia Polytechnic Institute and State University, Blacksburg, VA 24061, USA
[*]Corresponding author. Tel: +1-540-231-5976; Fax: +1-540-231-8517.
E-mail address: jmcgrath@vt.edu.
[2]Present Address: The Dow Chemical Company, 1897 Building, Midland, MI 48667
[3]Present Address: The Dow Chemical Company, 1707 Building, Midland, MI 48674
[4]Present Address: The Dow Chemical Company, 5400 Dewey Hill Rd., Edina, MN 55439
[5]Present Address: Celanese Corporation, 8040 Dixie Highway, Florence, KY 41042

The commercialization of proton exchange membrane (PEM) fuel cells depends largely upon the development of PEMs whose properties are enhanced over current perfluorinated sulfonic acid PEMs. Understanding how a PEM's molecular weight and morphology affect its relevant performance properties is essential to this effort. Changes in molecular weight were found to have little effect on the phase separated morphologies, water uptake, and proton conductivities of random copolymers. Changes in block length, however, have a pronounced effect on multiblock copolymers, affecting surface and bulk morphologies, water uptake, proton conductivity, and hydrolytic stability, suggesting that multiblock copolymer PEM properties may be optimized by changes in morphology.

Downloaded by PENNSYLVANIA STATE UNIV on June 21, 2012 | http://pubs.acs.org
Publication Date (Web): April 30, 2010 | doi: 10.1021/bk-2010-1040.ch005

1. Introduction

The need to reduce our nation's dependence upon foreign oil is well-recognized. A long-term solution to this problem may be H_2 based proton exchange membrane (PEM) fuel cells. These can be quite efficient (60-70% or more) electrochemical energy conversion devices which do not need recharging like batteries because their fuel and oxidant are continuously supplied from an external source (*1*, *2*). Applications for PEM fuel cells range from automobiles, stationary power for homes and other buildings, and portable electronic devices. At the heart of every PEM fuel cell is a proton exchange membrane flanked by two electrodes, whose main function is to conduct protons from the anode to the cathode and provide a barrier between the fuel and oxidant gases. In addition to high protonic conductivity and low fuel and oxidant permeability, there are several other characteristics a PEM must possess to be viable including good mechanical properties, hydrolytic stability, and cost effectiveness (*3*).

The current state-of-the-art PEM material is Nafion®, a poly(perfluorosulfonic acid) manufactured by the E. I. duPont Company (*4*). Despite its good proton conductivity, chemical stability, and mechanical stability, Nafion®'s limitations, which include cost and fuel permeability, have prompted research into alternative PEM materials (*3*, *5*). A promising alternative to Nafion® may be the disulfonated poly(arylene ether sulfone) (or biphenol sulfone in the acid (H) form; BPSH) copolymers, which display good chemical/mechanical stability and proton conductivity, as well as reduced fuel permeability (*6*, *7*). It has been demonstrated that sulfonated poly(arylene ether sulfone) copolymers synthesized with fluorinated comonomer (4,4'-hexafluoroisopropylidene diphenol or 6F-bisphenol; 6FSH) possess the positive membrane characteristics of BPSH copolymers and also bond well to Nafion® electrodes (*8*).

Copolymerizing highly hydrophilic BPSH with hydrophobic oligomers into multiblock copolymers is an additional way to optimize membrane properties. Multiblock copolymers based on BPSH-type copolymers have been shown to display higher proton conductivity at low relative humidity than random BPSH copolymers (*9–21*). It is expected that changes in multiblock copolymer synthesis can be used to control nanophase-separated morphology and membrane properties like water uptake and mechanical strength.

While it is well accepted that molecular weight will directly influence PEM mechanical properties, the influence of molecular weight or block length upon morphology and other membrane properties, such as proton conductivity and water uptake, has not been well-characterized. The present study has investigated the effect of molecular weight upon the morphologies and membrane properties of two random copolymer series (BPSH and 6FSH; Figure 1) and the effect of block length upon the morphologies and membrane properties of two multiblock copolymer series containing BPSH (Figure 2). The first series is comprised of BPSH and naphthalene-based polyimide oligomers at three different block lengths. The second series is comprised of BPSH and poly(2,5-benzophenone) oligomers at two different block lengths.

Downloaded by PENNSYLVANIA STATE UNIV on June 21, 2012 | http://pubs.acs.org
Publication Date (Web): April 30, 2010 | doi: 10.1021/bk-2010-1040.ch005

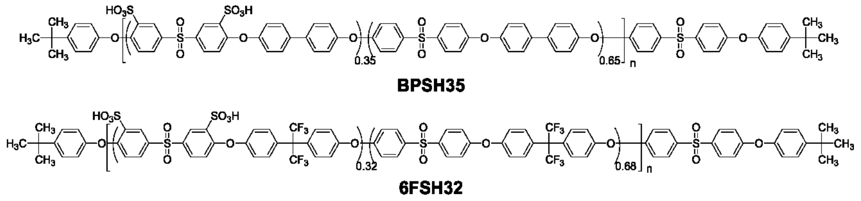

Figure 1. Chemical structure of BPSH35 (top) and 6FSH32 (bottom) copolymers.

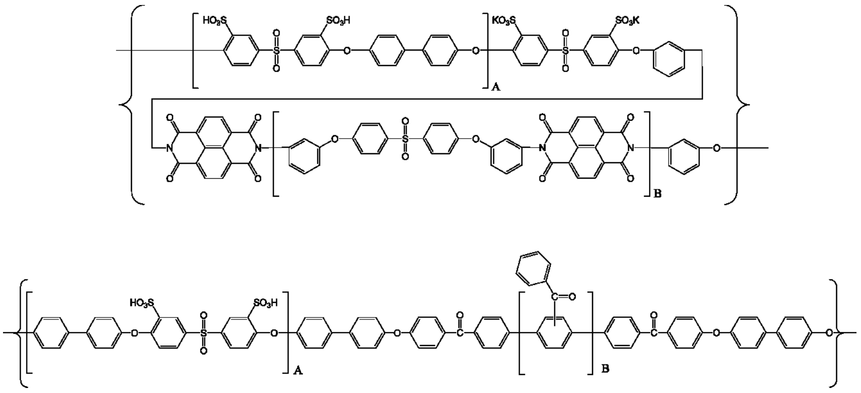

Figure 2. Chemical structure of BPSH100$_x$-PI$_y$ (top) and BPSH100$_x$-PBP$_y$ (bottom) multiblock copolymers.

To achieve the goals of this study, number average molecular weights ($\overline{M_n}$) for random copolymers and block lengths for the oligomers which were coupled into multiblock copolymers were determined by ^{1}H-NMR or ^{13}C-NMR. Unfortunately, the total $\overline{M_n}$ of the multiblock copolymers was not determined. Molecular weight values were compared against intrinsic viscosity values to ensure accuracy. Measurements were made of both the proton conductivity in liquid water and the water uptake of the membranes. The values of these membrane properties were evaluated alongside of surface morphology images obtained by atomic force microscopy. In the case of the multiblock copolymers, they were also characterized by bulk morphology images obtained by transmission electron microscopy (TEM). Dynamic mechanical analysis (DMA) was employed to gain insight about the effect of molecular weight and block length upon the viscoelastic behavior of the membranes.

Downloaded by PENNSYLVANIA STATE UNIV on June 21, 2012 | http://pubs.acs.org
Publication Date (Web): April 30, 2010 | doi: 10.1021/bk-2010-1040.ch005

1.1. Experimental

1.1.1. Materials

Non- and partially-fluorinated disulfonated poly(arylene ether sulfone) random copolymers with 35 and 32 mol% disulfonation (BPS35 and 6FS32, respectively) at varying target molecular weights (20, 30, 40, 50, and 70 or 80 kg/mol) were synthesized as previously reported (*22*, *23*). Multiblock copolymers comprised of oligomers of 100 mol% disulfonated poly(arylene ether sulfone) and naphthalene polyimide at three different target block lengths ($BPSH100_x$-PI_y, where x and y = 5, 10, or 15 kg/mol) were synthesized as described elsewhere (*24*). Multiblock copolymers comprised of oligomers of 100 mol% disulfonated poly(arylene ether sulfone) and poly(2,5-benzophenone) at two different target block lengths ($BPSH100_x$-PBP_y, where x = 6 and 10 kg/mol) were also synthesized as previously reported (*25*). 1-Methyl-2-Pyrrolidinone (NMP; EMD Chemicals) and N,N-Dimethyl-acetamide (DMAc; EMD Chemicals) were used as received.

1.1.2. Film Casting and Membrane Acidification

BPS35 and 6FS32 films were first prepared by dissolving the copolymers in their potassium sulfonate salt form in DMAc (7.5% (w/v) for microscopy, 10% (w/v) for all other characterizations). Solutions were syringe filtered through 0.45 μm Teflon® filters and cast onto clean glass substrates. The transparent solutions were dried under a 120V, 250W infrared lamp for 24 h and the resultant films were dried under vacuum at 100 °C for 24 h. Films were lifted from their substrates by immersion in deionized water. All films were converted to their acid form (BPSH35, 6FSH32) by boiling in 0.5 M sulfuric acid for 2 h, rinsing in deionized (DI) water, and then boiling in DI water for 2 h, termed "Method 2" (*6*). Samples were dried under vacuum at 60 °C for 12 h.

$BPSH100_x$-PI_y films were prepared identically to the random copolymer films with a few exceptions. Copolymers in their potassium sulfonate salt form were dissolved in NMP at 10% (w/v). The cast solutions were dried under the infrared lamp for 48 h and the resultant films were dried under vacuum at 120 °C for 24 h. Acidified films were equilibrated in DI water for 24 h twice.

$BPSH100_x$-PBP_y films were prepared identically to the $BPSH100_x$-PI_y films except the copolymers in their potassium sulfonate salt form were dissolved in DMAc at 5% (w/v) and the equilibrated membranes were dried under vacuum at 60 °C for 3 h.

1.1.3. Molecular Weight Characterization

Number average molecular weights were determined using ^{1}H-NMR (*22–25*), except for poly(2,5-benzophenone) oligomers for which ^{13}C-NMR was used (*25*).

Downloaded by PENNSYLVANIA STATE UNIV on June 21, 2012 | http://pubs.acs.org
Publication Date (Web): April 30, 2010 | doi: 10.1021/bk-2010-1040.ch005

1.1.4. Intrinsic Viscosity

Intrinsic viscosity measurements were determined in NMP at 25 °C with 0.05M LiBr using an Ubbelohde viscometer (*26*).

1.1.5. Proton Conductivity

Conductivity measurements of acidified membranes were performed at 30 °C in water using a Solartron 1252A + 1287 impedance/gain-phase analyzer over a frequency range of 10 Hz-1 MHz. The cell geometry was chosen to ensure that the membrane resistance dominated the response of the system. The resistance of the film was taken at the frequency that produced the minimum imaginary response.

1.1.6. Water Uptake

To obtain water uptake values, membranes were dried for 24 h at 100 °C, weighed, and immersed in deionized water at room temperature for 24 h. The wet membranes were blotted dry and immediately weighed again. Water uptake was calculated as the ratio of the difference between wet and dry membrane weight divided by dry membrane weight and expressed as a weight percent.

1.1.7. Atomic Force Microscopy (AFM)

AFM images of membrane surface morphology were obtained using a Veeco Digital Instruments MultiMode scanning probe microscope with a NanoScope IVa controller in tapping mode (TM-AFM). A silicon probe (Veeco) with an end radius of <10 nm and a force constant of 5 N/m was used to image samples at ambient conditions. Samples were equilibrated at 30% relative humidity (RH) for at least 12 h before being imaged immediately at room temperature and approximately 15-20% RH. Imaging samples in fully hydrated conditions was done with a silicon probe with an end radius of <10 nm and a force constant of 0.9 N/m. Membranes were mounted to mica sheets with Tempfix adhesive and then equilibrated for ≥40 h in DI water prior to imaging in a fluid cell filled with DI water at room temperature.

1.1.8. Dynamic Mechanical Analysis (DMA)

DMA was performed using a TA Instruments 2980 Dynamic Mechanical Analyzer. Measurements were taken at 1 Hz at a constant heating rate of 5 °C/min in air from 100 to 350 °C for the random copolymers and from 100 to 400 °C for the multiblock copolymers. Random copolymers were tested in the acid form. Multiblock copolymer samples were converted to the potassium sulfonate salt form prior to testing by immersion in an excess solution (~91 wt%) of K_2SO_4 in

DI water. Samples to be measured by DMA were dried under vacuum at 100 °C for 12 h and then kept sealed in a vacuum desiccator before analysis.

1.1.9. Transmission Electron Microscopy (TEM)

Electron density contrast within the membrane samples was enhanced by quantitatively titrating the membranes with CsOH solution to exchange the acidic protons with cesium. Membranes were embedded in epoxy and ultramicrotomed into 50-70 nm thin sections with a diamond knife. Transmission electron micrographs were obtained using a Philips EM 420 transmission electron microscope (TEM) operating at an accelerating voltage of 100 kV.

Downloaded by PENNSYLVANIA STATE UNIV on June 21, 2012 | http://pubs.acs.org
Publication Date (Web): April 30, 2010 | doi: 10.1021/bk-2010-1040.ch005

2. Results and Discussion

Two series of acidified films of non- and partially-fluorinated poly(arylene ether sulfone) random copolymers with varying molecular weights (BPSH35 and 6FSH32) were successfully imaged by TM-AFM (Figures 3 and 4). It has been shown previously that adsorbed water on ion-rich regions of Nafion dampen the oscillation of an AFM cantilever, causing an observable phase shift (*27*). Since the ionic domains of the membranes in this study have adsorbed water, the darker regions in the AFM images correspond to the aggregated ionic groups and the lighter regions to the hydrophobic backbones. It can be observed from the images that the differences in the phase separated morphologies of the BPSH35 films with an increase in molecular weight are small to non-existent. Also, the morphologies of the 6FSH32 films appear virtually identical as molecular weight increases. Brighter hydrophobic domain sizes appear roughly the same and the interconnectivity between darker hydrophilic domains remains consistent throughout both series. This is understandable because the ionic and non-ionic units of the random copolymers are distributed randomly throughout the films. While an increase in molecular weight would be expected to increase the number of randomly distributed ionic and non-ionic units of a random copolymer chain, it would not affect the total number of randomly distributed units in the film. Consequently, an increase in molecular weight would not influence the size of the phase separated domains formed by those units, either. Intrinsic viscosity measurements for the films (Tables 1 and 2) confirm that molecular weight is increasing across each series. The consistency in the phase separated morphologies of the copolymers in each series is reflected in the similar values for IEC, water uptake, and proton conductivities of the copolymers (Tables 1 and 2). A look at the three-dimensional height images for these membranes (Figures 5 and 6) reveals that molecular weight does not appear to influence the topography of the membranes. While the topography fluctuates slightly in height from sample to sample, there is no discernable trend with molecular weight for either series indicating that random copolymer topography is independent of molecular weight.

Downloaded by PENNSYLVANIA STATE UNIV on June 21, 2012 | http://pubs.acs.org
Publication Date (Web): April 30, 2010 | doi: 10.1021/bk-2010-1040.ch005

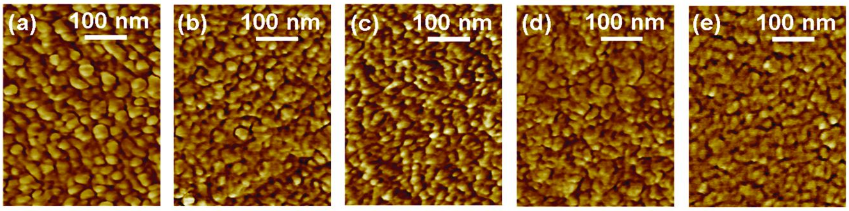

Figure 3. AFM phase images of BPSH35 random copolymer series: (a) 19.9 kg/mol, (b) 28.8 kg/mol, (c) 38.1 kg/mol, (d) 48.0 kg/mol, and (e) 83.1 kg/mol (extrapolated value). Setpoint ratios = 0.98, 0.98, 0.98, 0.98, 0.94.

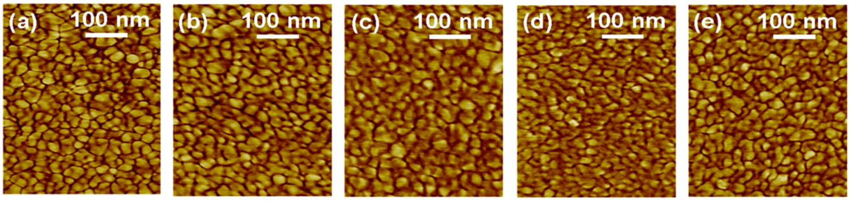

Figure 4. AFM phase images of 6FSH32 molecular weight series: (a) 19 kg/mol, (b) 27.5 kg/mol, (c) 37.8 kg/mol, (d) 49.5 kg/mol, and (e) ~70 kg/mol (estimated). Setpoint ratios = 0.98 (all).

In addition to morphology and topography, the glass transition temperatures of the random copolymers do not change much with molecular weight either. The glass transition temperatures (227, 226, 229, and 233 °C) obtained from the inflection of the storage modulus curves obtained for the 6FSH32 series (Figure 7) indicate that for the molecular weights tested, T_g appears to be fairly independent of molecular weight. Since T_g is a function of chain mobility, which is related to free volume, it is proportional to the number of chain ends of a polymer, which decreases with molecular weight ($\overline{M}_n$). This relationship is expressed in equation 1 where $T_{g\infty}$ is the T_g at infinite molecular weight and K is a constant.

$$T_g \approx T_{g\infty} - \frac{K}{\overline{M}_n} \qquad (1)$$

Each polymer has it own molecular weight above which increases in molecular weight no longer substantially affect its glass transition temperature. It is likely that the molecular weights tested for 6FSH32 are greater than this threshold molecular weight, preventing an increase in molecular weight from noticeably influencing the glass transition. It is important to note that only one glass transition was observed for each copolymer. While it has been shown previously for random ionomers that two glass transitions may be observed—a lower one for the matrix regions with isolated multiplets and a higher one for the aggregated ionic cluster regions (*28–31*), two glass transitions have been difficult to observe

Downloaded by PENNSYLVANIA STATE UNIV on June 21, 2012 | http://pubs.acs.org
Publication Date (Web): April 30, 2010 | doi: 10.1021/bk-2010-1040.ch005

Table 1. Membrane Properties of BPSH35 Random Copolymers[a]

M_n (kg/mol)	I.V.[b] (dL/g)	IEC[c] (meq./g)	Water Uptake (%)	Proton Conductivity (S/cm)[d]
19.9	0.43	1.49	40	0.070
28.8	0.48	1.50	43	0.080
38.1	0.63	1.52	42	0.081
48.0	0.74	1.52	38	0.080
83.1[e]	1.04	1.50	36	0.077

[a] Data taken from reference (*22*) [b] Determined in NMP at 25 °C with 0.05 M LiBr
[c] Ion Exchange Capacity determined by titration [d] Measured at 30 °C in DI water
[e] Extrapolated M_n.

Table 2. Membrane Properties of 6FSH32 Random Copolymers[a]

M_n (kg/mol)	I.V.[b] (dL/g)	IEC[c] (meq./g)	Water Uptake (%)	Proton Conductivity (S/cm)[d]
19.0	0.23	1.02	27.6	NA (brittle)
27.5	0.30	1.06	26.4	0.060
37.8	0.44	1.07	27.3	0.050
49.5	0.53	1.06	27.6	0.055
70[e]	0.60	1.05	23.4	0.050

[a] Data taken from reference (*23*) [b] Determined in NMP at 25 °C with 0.05 M LiBr [c] Ion Exchange Capacity determined by titration [d] Measured at 30 °C in DI water [e] Estimated M_n.

in aromatic poly(arylene ether sulfone) copolymers (*7*, *32*, *33*). Drzewinski and MacKnight (*34*) reported only one glass transition temperature by DMA for sulfonated poly(arylether)sulfones, supporting the results for the 6FSH32 copolymers. The absence of a second glass transition temperature for the 6FSH32 random copolymers is probably a result of its short sequence lengths preventing a high degree of phase separation.

Two multiblock copolymer series were characterized similarly to the random copolymers to evaluate the effect of block length upon the morphologies and properties of the membranes. The structures of these two series of 100 mol% disulfonated poly(arylene ether sulfone)-based multiblock copolymers with varying block lengths, BPSH100$_x$-PI$_y$ and BPSH100$_x$-PBP$_y$, were presented in Figure 2. The morphologies of these multiblock copolymer series are decidedly different from those of the random copolymer series. Phase separation in the BPSH100$_x$-PI$_y$ series (Figure 8) is very distinct compared to the random copolymer series. Brighter hydrophobic domains appear to increase in connectivity as block length increases. Hydrophilic connectivity also increases across the series and is reflected in increased water uptake and proton conductivity (Table 3).

Block length also has a pronounced effect on the morphologies and membrane properties of the BPSH100$_x$-PBP$_y$ multiblock series (Figure 9). Phase separation

Downloaded by PENNSYLVANIA STATE UNIV on June 21, 2012 | http://pubs.acs.org
Publication Date (Web): April 30, 2010 | doi: 10.1021/bk-2010-1040.ch005

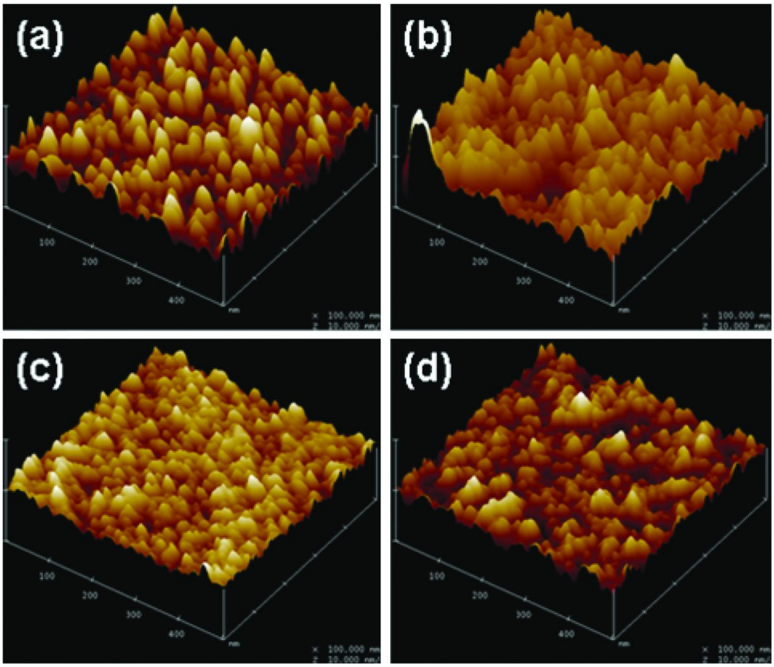

Figure 5. Three-dimensional tapping mode AFM height images for the BPSH35 random copolymers: (a) 19.9 kg/mol, (b) 28.8 kg/mol, (c) 38.1 kg/mol, (d) 48.0 kg/mol; Setpoint Ratios: 0.98; z range = 10 nm.

is very distinct in this multiblock series compared to the random copolymer series. Brighter hydrophobic domains appear to increase in connectivity from spherical to cylindrical as block length increases. Intrinsic viscosity values confirm that oligomer molecular weights are increasing (Table 4). Although the increases in IEC and water uptake with block length may be considered to be negligibly small, there is a 50% increase in proton conductivity with increasing block length. This confirms the results for the BPSH100$_x$-PI$_y$ series that changes in multiblock copolymer block length have a considerable effect on proton conductivity through changes in phase separation.

A look at the three-dimensional height images acquired simultaneously with the AFM phase images for each series of multiblock membranes (Figure 10) reveals that block length appears to influence membrane topography. While the topographies of the BPSH100$_x$-PI$_y$ membranes fluctuate slightly in height, the difference between the highest and lowest features of each membrane appears to increase somewhat with block length (Figure 10a-c). The same trend is observed with the BPSH100$_x$-PBP$_y$ multiblock series (Figure 10d-e). Smaller block lengths result in more uniform topographies while larger block lengths result in a more heterogeneous topography. This result may have implications for membrane electrode assembly (MEA) fabrication. Differences in topography might be expected to result in different contact between a proton exchange membrane and

Downloaded by PENNSYLVANIA STATE UNIV on June 21, 2012 | http://pubs.acs.org
Publication Date (Web): April 30, 2010 | doi: 10.1021/bk-2010-1040.ch005

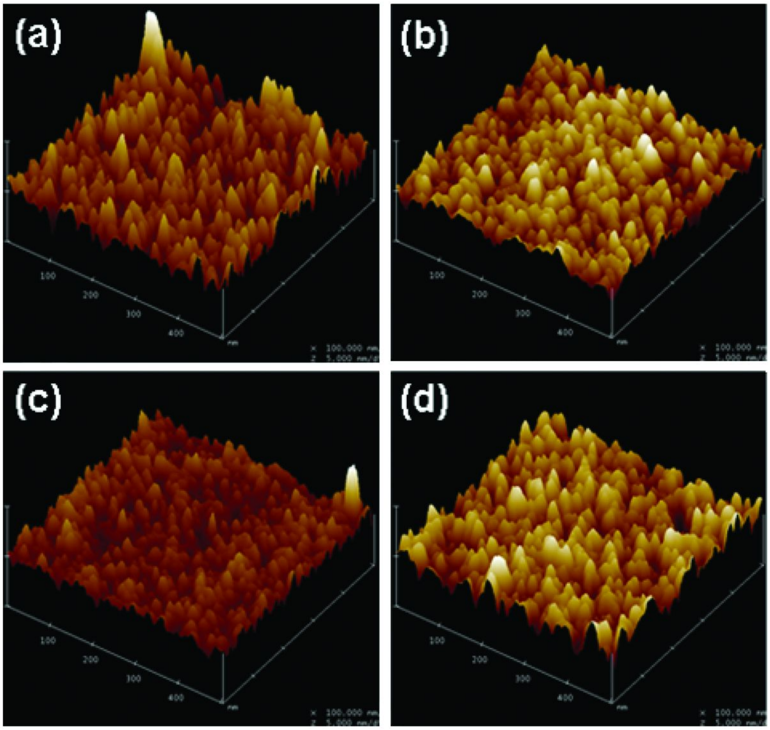

Figure 6. Three-dimensional tapping mode AFM height images for the 6FSH32 random copolymers: (a) 27.5 kg/mol, (b) 37.8 kg/mol, (c) 49.5 kg/mol, (d) ~70 kg/mol; Setpoint Ratios: 0.98; z range = 10 nm.

the electrode dispersion or decal applied to the membrane, ultimately affecting the performance of the fuel cell.

Although the surface morphology of these multiblock copolymer membranes appears to change with block length, the more important question with respect to PEM performance is what effect block length has on the bulk of these membranes and their resulting ability to conduct protons. To determine this, the membranes were imaged by TEM (Figure 11). Generally speaking, the bulk morphologies of these membranes appear to correlate with their surface morphologies. In the BPSH100$_x$-PI$_y$ series (Figure 11a-c), phase separated domains of increasing size appear in the TEM images, however they appear to be smaller than the domains observed on the surface (Figure 8). The domains in the BPSH100-PBP micrograph (Figure 11d) also look smaller than those in the corresponding AFM micrograph (Figure 9a). This difference is attributed in part to the differences in moisture content during AFM and TEM imaging. The high vacuum in the TEM column is likely responsible for drawing moisture from the thin sample sections, thereby shrinking the domain sizes within the membrane. Another reason for the difference in domain sizes between the surface and the bulk of the membranes is that the TEM sections are cut perpendicular to the plane of the membrane surface. Anisotropic domains would consequy look different in each direction.

Downloaded by PENNSYLVANIA STATE UNIV on June 21, 2012 | http://pubs.acs.org
Publication Date (Web): April 30, 2010 | doi: 10.1021/bk-2010-1040.ch005

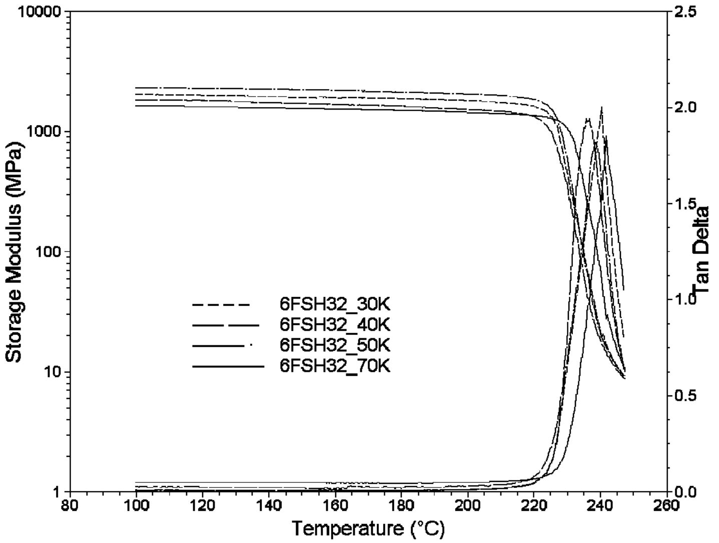

Figure 7. Storage modulus and tan delta curves for 6FSH32 random copolymer series.

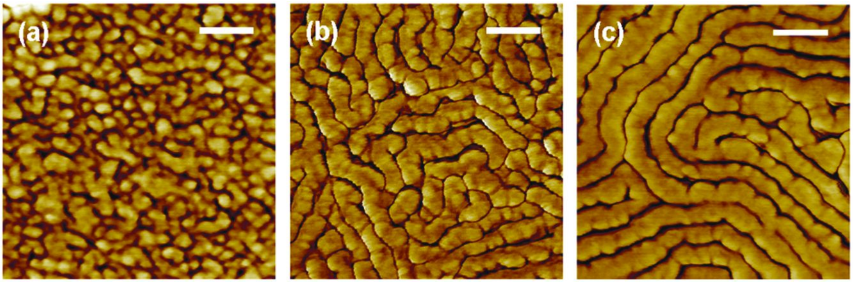

Figure 8. AFM phase images of BPSH100x-PIy multiblock copolymer series. (a) x = 5.5 kg/mol, y = 5.9 kg/mol, (b) x = 9.8 kg/mol, y = 10.5 kg/mol, (c) x = 14.5 kg/mol, y = 19.2 kg/mol. Setpoint ratios = 0.98, 0.90, 0.98. Scale bars = 100 nm. Images adapted from (24). Reprinted by permission from John Wiley & Sons, Inc.

The BPSH100$_x$-PI$_y$ series was subjected to a DMA single frequency temperature sweep in an attempt to ascertain the effect of block length upon glass transition temperature. The BPSH100$_x$-PBP$_y$ membranes were not tested because they were too brittle. The BPSH100$_x$-PI$_y$ membranes were first converted from the acid form (BPSH) into their potassium salt form (BPS) prior to testing. This was done because the sulfonic acid groups of highly sulfonated BPSH have been shown to degrade at temperatures as low as 230 °C (*35*), which is well below the expected glass transition temperature of the polyimide blocks of around 320 °C (based on unpublished DSC data). The samples were then tested without recasting so that their original acid form morphology would be retained as much as possible. An unfortunate side effect of the neutralization by K$_2$SO$_4$

Downloaded by PENNSYLVANIA STATE UNIV on June 21, 2012 | http://pubs.acs.org
Publication Date (Web): April 30, 2010 | doi: 10.1021/bk-2010-1040.ch005

Table 3. Water Uptake and Proton Conductivities of BPSH100$_x$-PI$_y$ Multiblock Copolymers

Sample	*Block Length (kg/mol)*		*Overall I.V. (dL/g)*[a]	*IEC (meq./g)*[b]	*Water Uptake (%)*	*Proton Conductivity (S/cm)*[c]
	x	*y*				
5k-5k	5.5	5.9	0.50	1.65	59	0.080
10k-10k	9.8	10.5	0.63	1.57	67	0.085
15k-15k	14.5	19.2	0.68	1.55	85	0.100

[a] Determined in NMP at 25 °C with 0.05 M LiBr [b] Ion Exchange Capacity determined by titration [c] Measured at 30 °C in DI water.

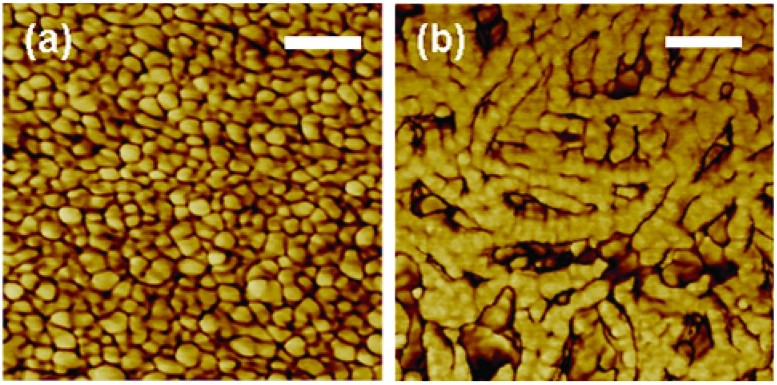

Figure 9. AFM phase images of BPSH100x-PBPy multiblock copolymer series; (a) x = 5.9 kg/mol, y = 5.5 kg/mol, (b) x = 9.5 kg/mol, y = 9.4 kg/mol; Setpoint ratios = 0.89 (both); Scale bars = 100 nm. Images adapted from (25). Reprinted by permission from John Wiley & Sons, Inc.

was embrittlement of the membranes, which may reflect partial base-catalyzed cleavage of the imide ring. As a result, the membrane with the lowest block length, the “5k-5k” sample, was too brittle to withstand the oscillations of the instrument. The membrane with the next longest block length, the “10k-10k” sample, fractured before the full temperature sweep was completed. Only the sample with the largest block length, the “15k-15k” sample, was robust enough to withstand the full temperature sweep to 400 °C (Figure 12). While no quantitative measurements of strength were made, these differences in brittleness between the BPS100$_x$-PI$_y$ samples implicitly suggest that mechanical strength increases with block length.

Downloaded by PENNSYLVANIA STATE UNIV on June 21, 2012 | http://pubs.acs.org
Publication Date (Web): April 30, 2010 | doi: 10.1021/bk-2010-1040.ch005

Table 4. Water Uptake and Proton Conductivities of BPSH100$_x$-PBP$_y$ Multiblock Copolymers[d]

Sample	*Block Length (kg/mol)*		*Block I.V. (dL/g)*[a]		*IEC (meq./g)*[b]	*Water Uptake (%)*	*Proton Conductivity (S/cm)*[c]
	x	*y*	*x*	*y*			
6k-6k	5.9	5.5	0.24	0.32	1.65	59	0.080
10k-10k	9.5	9.4	0.35	0.48	1.57	67	0.085

[a] Determined in NMP at 25 °C with 0.05 M LiBr [b] Ion Exchange Capacity determined by titration [c] Measured at 30 °C in DI water [d] Data taken from reference (*25*).

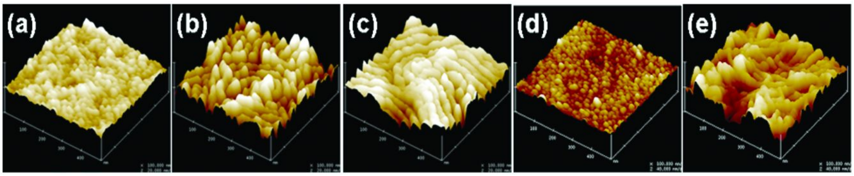

Figure 10. Three-dimensional tapping mode AFM height images for the BPSH100x-PIy multiblock copolymers: (a) x = 5.5 kg/mol, y = 5.9 kg/mol, (b) x = 9.8 kg/mol, y = 10.5 kg/mol, (c) x = 14.5 kg/mol, y = 19.2 kg/mol. Setpoint ratios = 0.98, 0.90, 0.98; z range = 20 nm; and the BPSH100$_x$-PBP$_y$ multiblock copolymers: (d) x = 5.9 kg/mol, y = 5.5 kg/mol, (e) x = 9.9 kg/mol, y = 9.4 kg/mol. Setpoint ratios = 0.89 (both); z range = 40 nm.

Glass transition temperatures of 352 and 346 °C were obtained from the inflections of the storage modulus curves in Figure 12 for the 10k-10k and 15k-15k samples, respectively. Although it is difficult to deduce a conclusive trend from two points, these data suggest that the T_g of these multiblock copolymers does not increase with block length in this range. This behavior is similar to that of the 6FSH32 random copolymer series. It is likely that the overall molecular weights of the multiblock copolymer chains, like the molecular weights of the 6FSH32 series, exceed the molecular weight above which increases in molecular weight no longer substantially affect T_g. This conclusion is tenable considering that the intrinsic viscosities of the two multiblock copolymers in Figure 12 exceed those of the copolymers in the 6FSH32 series.

Although non-ionic block copolymers often exhibit a separate glass transition for each of their component blocks (*36*), only one glass transition appears in the tan delta curve of the 15k-15k sample. No glass transition corresponding to the BPS100 block can be observed in the storage modulus or tan delta curves. If it were present, the T_g of BPS100 would be expected to be higher than 283 °C, the T_g reported for BPS60 (*7*), because T_g rises with ionic content (*28*). Two glass transitions have been observed via DSC for the BPSH100-PBP 6k-6k multiblock copolymer (*25*). Given that the block lengths of the BPSH100-PI 15k-15k multiblock copolymer are over twice as large as those of the BPSH100-PBP 6k-6k multiblock copolymer, and that DMA is more sensitive to transitions than DSC, it is not clear why only one transition is observed for the BPSH100-PI.

Downloaded by PENNSYLVANIA STATE UNIV on June 21, 2012 | http://pubs.acs.org
Publication Date (Web): April 30, 2010 | doi: 10.1021/bk-2010-1040.ch005

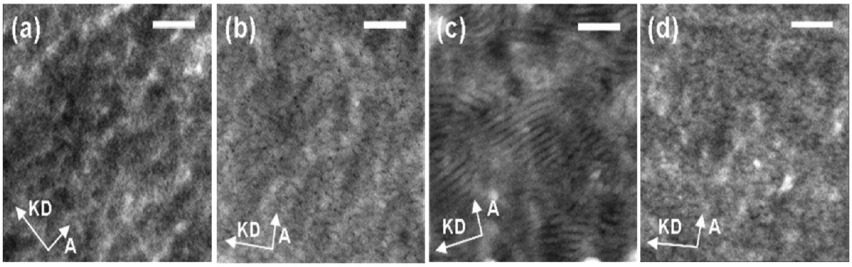

Figure 11. TEM micrographs of multiblock copolymers: (a) BPSH100-PI 5k-5k, (b)BPSH100-PI 10k-10k, (c) BPSH100-PI 15k-15k, and (d) BPSH100-PBP 6k-6k. "A" denotes direction of air side. "KD" denotes the knife direction during microtoming. Scale bars = 100 nm.

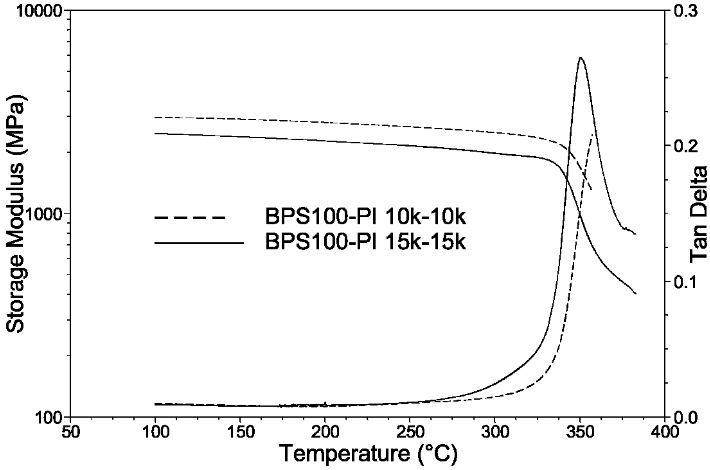

Figure 12. Storage modulus and tan delta curves for BPSH100x-PIy multiblock copolymer series

Further research is required to understand the seeming absence of the second glass transition.

Given that hydrolytic stability is an important characteristic of a successful proton exchange membrane (*3*), TM-AFM was performed in liquid water to gauge the influence of block length on the morphological stability of fully hydrated membranes. The 6FSH32 membrane with a molecular weight of approximately 70 kg/mol was chosen as the first sample because its random structure. The BPSH100$_x$-PI$_y$ multiblock copolymers were also tested. The resulting micrographs (Figure 13) suggest that block length may increase hydrolytic stability. When fully hydrated, the randomly distributed hydrophilic domains of the 6FSH32 membrane swell and phase separation is lost and the surface morphology of the membrane becomes very homogenous (Figure 13a). This result matches an earlier observation made by Kim et al. (*37*) for BPSH40 membranes, in which high ion content induced swelling produced featureless morphology. Whether this effect occurs only on the surface or in the bulk as well is not clear from these data. The multiblock copolymers, in contrast, appear to retain their phase separated morphology to a greater degree as block length increases (Figure 13b-d). This occurs despite an increase of 60 mol% disulfonation in the hydrophilic blocks of BPSH100 compared to the random BPSH40 imaged by Kim et al. (*37*). These data show that the phase separated morphology of the multiblock copolymers, which increases with block length, enhances the membranes' ability to resist swelling when hydrated due to the hydrophobic blocks.

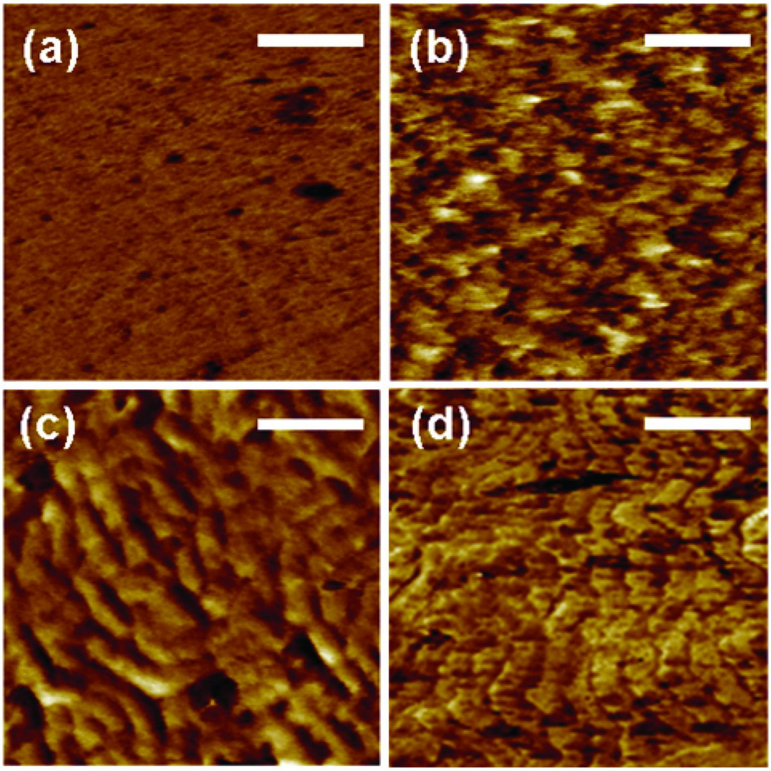

Figure 13. AFM phase images of fully hydrated membranes: (a) 6FSH32 ~70 kg/mol, and BPSH100-PI series (b) 5k-5k, (c) 10k-10k, and (d) 15k-15k. Setpoint ratios = 0.38, 0.52, 0.54, 0.46. Scale bar = 100 nm.

3. Conclusions

It can be concluded that changes in molecular weight above a minimum value have little effect on the morphologies, water uptake, proton conductivities, and glass transition temperatures of these random copolymers. However changes in block length do have a pronounced effect on multiblock copolymers, affecting

Downloaded by PENNSYLVANIA STATE UNIV on June 21, 2012 | http://pubs.acs.org
Publication Date (Web): April 30, 2010 | doi: 10.1021/bk-2010-1040.ch005

surface and bulk morphologies as well as water uptake, proton conductivity, and even for the polyimide hydrolytic stability. Data suggest that multiblock copolymer glass transition temperature is independent of block length, but more study is required before a definitive conclusion can be made, especially regarding the absence of a second glass transition. Interestingly, the multiblock membrane properties affected by block length appear to improve as the degree of nanophase separation increases, suggesting that PEM properties such as the water self diffusion coefficient may be optimized by changes in morphology. The authors thus recommend that future research into multiblock copolymers as PEMs should also include alternative methods of casting the multiblock films to manipulate their morphologies to an optimum state.

Downloaded by PENNSYLVANIA STATE UNIV on June 21, 2012 | http://pubs.acs.org
Publication Date (Web): April 30, 2010 | doi: 10.1021/bk-2010-1040.ch005

Acknowledgments

The authors wish to thank the National Science Foundation "Partnership for Innovation" Program (HER-0090556) and IGERT Program (DGE-0114346), the Department of Energy (DE- FG36-06G016038), and the Nissan Motor Company for supporting this research.

References

1. Winter, M.; Brodd, R. J. *Chem. Rev.* **2004**, *104* (10), 4245–4269.
2. Perry, M. L.; Fuller, T. F. *J. Electrochem. Soc.* **2002**, *149* (7), S59–S67.
3. Hickner, M. A.; Ghassemi, H.; Kim, Y. S.; Einsla, B. R.; McGrath, J. E. *Chem. Rev.* **2004**, *104* (10), 4587–4611.
4. Mauritz, K. A.; Moore, R. B. *Chem. Rev.* **2004**, *104* (10), 4535–4585.
5. Savadogo, O. *J. New Mater. Electrochem. Syst.* **1998**, *1* (1), 47–66.
6. Kim, Y. S.; Wang, F.; Hickner, M.; McCartney, S.; Hong, Y. T.; Harrison, W.; Zawodzinski, T. A.; McGrath, J. E. *J. Polym. Sci., Part B: Polym. Phys.* **2003**, *41* (22), 2816–2828.
7. Wang, F.; Hickner, M.; Kim, Y. S.; Zawodzinski, T. A.; McGrath, J. E. *J. Membr. Sci.* **2002**, *197* (1−2), 231–242.
8. Kim, Y. S.; Sumner, M. J.; Harrison, W. L.; Riffle, J. S.; McGrath, J. E.; Pivovar, B. S. *J. Electrochem. Soc.* **2004**, *151* (12), A2150–A2156.
9. Wang, H.; Badami, A. S.; Roy, A.; McGrath, J. E. *PMSE Prepr.* **2006**, *95*, 202–203.
10. Li, Y.; Roy, A.; Badami, A. S.; Hill, M.; Yang, J.; Dunn, S.; McGrath, J. E. *J. Power Sources* **2007**, *172* (1), 30–38.
11. Roy, A.; Hickner, M. A.; Lee, H.-S.; Badami, A.; Yu, X.; Li, Y.; Glass, T.; McGrath, J. E. *ECS Trans.* **2007**, *2* (24), 45–54 (Direct Methanol Fuel Cells).
12. McGrath J. E. Abstracts of Papers, 234th ACS National Meeting, Boston, MA, United States, August 19−23, 2007; 2007:POLY-068.
13. Einsla, M. L.; Kim, Y. S.; Hawley, M.; Lee, H. S.; McGrath, J. E.; Liu, B.; Guiver, M. D.; Pivovar, B. S. *Chem. Mater.* **2008**, *20*, 5636–5642.

Downloaded by PENNSYLVANIA STATE UNIV on June 21, 2012 | http://pubs.acs.org
Publication Date (Web): April 30, 2010 | doi: 10.1021/bk-2010-1040.ch005

14. Roy, A.; Hickner, M. A.; Einsla, B. R.; Harrison, W. L.; McGrath, J. E. *J. Polym. Sci., Part A: Polym. Chem.* **2008**, *47* (2), 384–391.
15. Roy, A.; Lee, H.-S.; McGrath, J. E. *Polymer* **2008**, *49* (23), 5037–5044.
16. Roy, A.; Yu, X.; Dunn, S.; McGrath, J. E. *J. Membr. Sci.* 2008, doi:10.1016/j.memsci.2008.1011.1016.
17. Roy, A.; Hickner, M. A.; Lane, O.; McGrath, J. E. *J. Power Sources* **2009**, *191*, 550–554.
18. Yu, X.; Roy, A.; Dunn, S.; Badami, A. S.; Yang, J.; Good, A. S.; McGrath, J. E. *J. Polym. Sci., Part A: Polym. Chem.* **2009**, *47* (4), 1038–1051.
19. Badami, A.; Roy, A.; Lee, H.-S.; Li, Y.; McGrath, J. E. *J. Membr. Sci.* 2008, doi:10.1016/j.memsci.2008.1012.1007.
20. Badami, A. S.; Lane, O.; Lee, H.-S.; Roy, A.; McGrath, J. E. *J. Membr. Sci.* **2009**, *333*, 1–11.
21. Lee, H.-S.; Roy, A.; Lane, O.; McGrath, J. E. *Polymer* **2008**, *49* (25), 5387–5396.
22. Li, Y.; Wang, F.; Yang, J.; Liu, D.; Roy, A.; Case, S.; Lesko, J.; McGrath, J. E. *Polymer* **2006**, *47* (11), 4210–4217.
23. Li, Y.; Yang, J.; Roy, A.; Einsla, B.; Wang, F. *Prepr. Pap. - Am. Chem. Soc., Div. Fuel Chem.* **2005**, *50* (2), 573.
24. Lee, H.-S.; Roy, A.; Badami, A. S.; McGrath, J. E. *J. Polym. Sci., Part A: Polym. Chem.* **2007**, *45* (21), 4879–4890.
25. Wang, H.; Badami, A. S.; Roy, A.; McGrath, J. E. *J. Polym. Sci., Part A: Polym. Chem.* **2007**, *45* (2), 284–294.
26. Yang, J.; Li, Y.; Roy, A.; McGrath, J. E. *Polymer* **2008**, *49* (24), 5300–5306.
27. James, P. J.; Antognozzi, M.; Tamayo, J.; McMaster, T. J.; Newton, J. M.; Miles, M. J. *Langmuir* **2001**, *17* (2), 349–360.
28. Eisenberg, A.; King, M.; Navratil, M. *Macromolecules* **1973**, *6* (5), 734–737.
29. Hara, M.; Jar, P.; Sauer, J. A. *Polymer* **1991**, *32* (9), 1622–1626.
30. Weiss, R. A.; Fitzgerald, J. J.; Kim, D. *Macromolecules* **1991**, *24* (5), 1071–1076.
31. Hird, B.; Eisenberg, A. *Macromolecules* **1992**, *25* (24), 6466–6474.
32. Johnson, R. N.; Farnham, A. G.; Clendinning, R. A.; Hale, W. F.; Merriam, C. N. *J. Polym. Sci., Polym. Chem. Ed.* **1967**, *5*, 2375.
33. Johnson, B. C.; Yilgor, I.; Tran, C.; Iqbal, M.; Wightman, J. P.; Lloyd, D. R.; McGrath, J. E. *J. Polym. Sci., Part A: Polym. Chem.* **1984**, *22* (3), 721–737.
34. Drzewinski, M.; MacKnight, W. J. *J. Appl. Polym. Sci.* **1985**, *30* (12), 4753–4770.
35. Harrison, W. L.; Wang, F.; Mecham, J. B.; Bhanu, V. A.; Hill, M.; Kim, Y. S.; McGrath, J. E. *J. Polym. Sci., Part A: Polym. Chem.* **2003**, *41* (14), 2264–2276.
36. Noshay, A.; McGrath, J. E. *Block Copolymers: Overview and critical survey*; New York: Academic Press, 1977.
37. Kim, Y. S.; Dong, L.; Hickner, M. A.; Pivovar, B. S.; McGrath, J. E. *Polymer* **2003**, *44* (19), 5729–5736.

Downloaded by DUKE UNIV on June 21, 2012 | http://pubs.acs.org
Publication Date (Web): April 30, 2010 | doi: 10.1021/bk-2010-1040.ch006

Chapter 6

Mesoscopic Simulations of the Hydrated Morphology of the Short-Side-Chain Perfluorosulfonic Acid Ionomer

Dongsheng Wu and Stephen J. Paddison*

Department of Chemical and Biomolecular Engineering, University of Tennessee, Knoxville, Tennessee 37996
***spaddiso@utk.edu**

Dissipative particle dynamics simulations have been utilized to study the morphology of the short-side-chain (SSC) perfluorosulfonic acid (PFSA) ionomer as a function of equivalent weight (EW) and degree of hydration. Equilibrated morphologies were determined for SSC PFSA membranes with EWs of 678 and 1278 g/mol at hydration levels corresponding to 5, 7, 9, 11 and 16 H_2O/SO_3H. Water contour plots reveal that isolated water clusters at lower water contents increase in size with increasing hydration, and form continuous water domains at the highest hydration level. The ionomer with an EW=1278 induces stronger aggregation of the water and results in larger water domains that are less connected when compared to the lower EW ionomer at 16 H_2O/SO_3H. The size of the water clusters are estimated from radial distribution functions and indicate that the spacing between the water domains increases with increasing EW of the ionomer.

Introduction

Fuel cells have received increasing interest over the last two decades due to utilization in automobiles and portable devices. Polymer electrolyte membrane (PEM) fuel cells are particularly attractive due to their high power energy density. Current efforts in the improvement of these devices include the development and characterization of novel high performance membranes that serve as the

In Fuel Cell Chemistry and Operation; Herring, A., et al.;
ACS Symposium Series; American Chemical Society: Washington, DC, 2010.

electrolyte, and the desire to understand how the structure and chemistry of these membranes along with the hydrated morphology determine proton conductivity in existing PEMs (*1*).

Perfluorinated ionomers are the most widely utilized electrolyte in PEM fuel cells functioning not only as a proton conductor but also as a separator of the electrodes and fuel gases. The archetypal electrolyte Nafion®, a perfluorosulfonic acid (PFSA) membrane, has been extensively studied included determination of structural and transport properties (*2*). The short-side-chain (SSC) PFSA membrane (*2–15*), originally synthesized by Dow Chemical (*16*) possesses a shorter side chain, $–OCF_2CF_2SO_3H$, as compared to that of Nafion. Although the original SSC PFSA membranes showed improved properties (*17–19*) and enhanced performance in a fuel cell (*6*), they did not see widespread application mainly due to a complex synthesis process. This ionomer, however, has recently returned to the forefront of interest due to a much simpler synthesis route developed by Solvay Solexis and is commercialized as Hyflon® (*8*, *10*).

Early investigations by Tant *et al.* (*2*, *3*) and Moore and Martin (*5*) on SSC PFSA membranes with different equivalent weights (EWs) have highlighted property differences when compared to Nafion. Their studies revealed that the SSC PFSA membranes have higher crystallinity at similar EWs and a higher glass transition temperature (T_g) thereby allowing a wider range of operating temperatures for use as the electrolyte in fuel cells. The increase in water uptake with decreasing EW has also been evaluated and attributed to the lower crystallinity at lower EWs (*5*). Recently, the conductivity and hydrogen permeability of SSC PFSA membranes have been reported in sub-freezing conditions, and remarkable durability of fuel cells employing these membranes has also been demonstrated (*12*). An investigation into the chemical degradation of SSC PFSA membranes revealed that temperature has a negligible effect on degradation while reactant humidification has a large influence (*11*). Recently, Kreuer *et al.* (*13*) have attempted to establish the relationship between performance and various properties including: water sorption, proton and water transport, microstructure, and visco-elasticity. This study demonstrated, in comparison to Nafion, that the combination of high ion exchange capacity (IEC) and high mechanical stability of the SSC ionomer may offer better performance in PEM fuel cells.

X-ray and neutron scattering technologies have been widely utilized to probe the hydrated morphology of PFSA membranes. Moore and Martin used small-angle X-ray scattering (SAXS) to estimate the size of ionic clusters based on a hard-sphere interference model (*4*, *20*). Later, Gebel and Moore carried out a further structural studies on dry and water-swollen SSC PFSA membranes with SAXS and SANS rxperiments (*7*). The detailed crystalline contribution was studied from the scattering data based on a local order model (*21*). Kreuer has also undertaken SAXS studies on SSC PFSA membranes and Nafion at various hydration levels and showed that the SSC ionomer exhibits greater rigidity (*13*).

Downloaded by DUKE UNIV on June 21, 2012 | http://pubs.acs.org
Publication Date (Web): April 30, 2010 | doi: 10.1021/bk-2010-1040.ch006

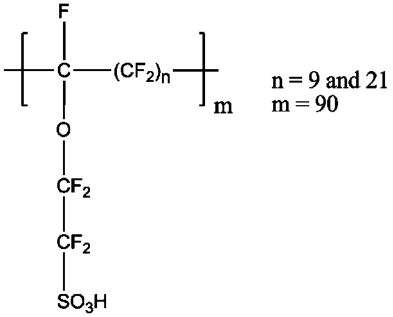

Figure 1. General molecular structures of SSC PFSA ionomers used in the simulations.

Downloaded by DUKE UNIV on June 21, 2012 | http://pubs.acs.org
Publication Date (Web): April 30, 2010 | doi: 10.1021/bk-2010-1040.ch006

Several authors have reviewed computational investigations undertaken to elucidate both molecular-level and meso-scale chemical and structural functionalities of PFSA membranes using a variety of different simulation techniques (*22–24*). The effects of structure and local chemistry on proton dissociation and separation of hydrated side chains, have been undertaken on oligomeric fragments of SSC PFSA membranes with a few explicit water molecules for hydration levels up to 3 H_2O/SO_3H with *ab initio* electronic structure calculations (*25–28*). *Ab initio* molecular dynamics (AIMD) calculations have also been performed to investigate proton transfer and dynamics for model systems exhibiting a high density of perfluorinated sulfonic acid groups (*29–32*). On a larger scale are the classical molecular dynamics (MD) simulations on structural correlations and transport properties of PEMs (*33–43*). These include empirical valence bond (EVB) models of the solvation and transport of hydrated protons (*44*, *45*). To examine length and time scales that are several orders of magnitude greater and longer than atomistic simulations, it is necessary to employ coarse-grained simulations (*46–49*). Mesoscale modeling involving dissipative particle dynamics (DPD) simulations has been employed to study the modeling morphology evolution of a wide range of copolymer systems, including ionomers, during phase separation (*49–56*). Yamamoto and Hyodo (*49*) used DPD simulations to investigate the mesoscopic structure of Nafion membranes at varying degrees of hydration. Self-consistent mean field (SCMF) simulations have been used to study phase separation, and morphological changes in PEMs as a function of temperature and water content (*46*). For example, a recent mesoscale simulation on the morphology of hydrated PFSA membranes analogous to Nafion 117 has been carried out by Wescott *et al.* (*48*), using MESODYN code, which is based on a mean-field free energy functional approach. Finally, the present authors performed a comparative study of the hydrated morphologies of three PFSA ionomers with side chains of different length using DPD simulations (*54*).

Table I. Computed χ-parameters and Repulsion Parameters Describing Pair Wise Interactions of the Selected Beads for the SSC PFSA ionomer

Pair[a]	χ	a_{ij} (k_BT)
A–B	0.15	25.5
A–C	6.86	47.4
A–W	3.28	35.7
B–C	6.24	45.4
B–W	3.15	35.3
C–W	1.24	29.0

[a] DPD beads in pairs are: *A*, $–CF_2CF_2CF_2CF_2CF_2CF_2–$; *B*, $–CF_2CF_2CF_2CF(OCF_3)–$; *C*, $CF_3SO_3H·3H_2O$; and *W*, $6H_2O$.

In the present work we have carried out DPD simulations to investigate the morphology of the SSC PFSA ionomer with EWs of 678 and 1278 g/mol. Intermediate hydration levels were selected corresponding to water contents of 5, 7, 9, 11 and 16 H_2O/SO_3H. In the DPD simulations, the SSC PFSA polymer molecules were modeled by connecting soft spherical particles, or "beads", which represent groups of several atoms. Water was also modeled as a collection of several water molecules. Flory-Huggins χ-parameters were calculated for each coarse-grained particle based on optimized structures and further used to derive the corresponding interaction parameters for the DPD simulations. The radial distribution functions (RDFs) of water particles were generated from DPD calculated densities and used to characterize the water clusters and their average sizes. Finally, the scattering intensities have also been calculated according to the Fourier transform of RDFs, and later used to evaluate the average spacing between water clusters.

Model and Theoretical Methodology

I. DPD Simulations and Modeling of SSC PFSA Membranes

Hoogerbrugge and Koelman introduced the DPD method for simulating complex hydrodynamic behavior of isothermal fluids (*57*, *58*). It was further developed by Español who included stochastic differential equations and conservation of energy (*59*, *60*). The interaction between two DPD particles can be expressed as the sum of: a conservative force $\mathbf{F}_{ij}^{\mathrm{C}}$, a dissipative force $\mathbf{F}_{ij}^{\mathrm{D}}$, a random force $\mathbf{F}_{ij}^{\mathrm{R}}$, and a harmonic spring force $\mathbf{F}_{ij}^{\mathrm{S}}$ for the system:

$$\mathbf{f}_i = \sum_{j \neq i} (\mathbf{F}_{ij}^{\mathrm{C}} + \mathbf{F}_{ij}^{\mathrm{D}} + \mathbf{F}_{ij}^{\mathrm{R}} + \mathbf{F}_{ij}^{\mathrm{S}}). \tag{1}$$

Downloaded by DUKE UNIV on June 21, 2012 | http://pubs.acs.org
Publication Date (Web): April 30, 2010 | doi: 10.1021/bk-2010-1040.ch006

The conservative force is derived from a potential exerted on particle *i* by the *j*-th particle (*50*), and treated as a soft repulsion acting along the line of centers with the form (*51*, *52*):

$$\mathbf{F}_{ij}^{C} = \begin{cases} -a_{ij}(r_c - r_{ij})\mathbf{n}_{ij} & r_{ij} < r_c \\ 0 & r_{ij} \geq r_c \end{cases} \tag{2}$$

where a_{ij} is a maximum repulsion force between particle *i* and *j*, r_c is a selected cutoff radius of the interaction, $\mathbf{r}_{ij} = \mathbf{r}_i - \mathbf{r}_j$, $r_{ij} = |\mathbf{r}_{ij}|$, and $\mathbf{n}_{ij} = \mathbf{r}_{ij}/|\mathbf{r}_{ij}|$.

Once the interactions between all the DPD particles are calculated, the positions and velocities of the DPD particles are solved according to Newton's equation of motion and a modified version of the velocity-Verlet algorithm (*50*), as implemented in the Materials Studio software package (*61*).

Figure 1 shows the molecular structure of a monomer of the SSC PFSA ionomer as used in our simulations. The ionomer is modeled by connecting spherical soft particles (beads), which contain groups of atoms and/or molecules. The ionomer consists of three distinct DPD beads in all simulations, denoted *A*, *B* and *C*, which correspond to $–CF_2CF_2CF_2CF_2CF_2CF_2–$, $–CF_2CF_2CF_2CF(OCF_3)–$ and $–CF_2SO_3H·3H_2O$, respectively. We chose to include the water molecules of the first hydration sphere of the terminal sulfonic acid group in the *C* bead as our interest is in the morphologies at intermediate levels of hydration where the protons are dissociated. Another independent water particle, denoted *W*, was constructed from six water molecules. The structures of particles *A*, *B* and *W* were optimized using molecular mechanics with COMPASS parameters using the Forcite module in Materials Studio. The structure of particle *C* was optimized using electronic structure calculations at the B3LYP/ 6-31G** level with Gaussian 03 (*62*).

EWs of 678 and 1278 g/mol were chosen for the simulations and as indicated in Figure 1 require n = 9 and 21, respectively. We set m = 90 which gives molecular weights (MWs) of 61020 and 115020 g/mol for EWs of 678 and 1278, respectively. A simulation box size of 64 × 64 × 64 nm^3 was generated for the DPD simulations, which resulted in 1536000 DPD particles at a selected density $\rho = 3$. The spring constant was set to the default value of $4.0k_BT$ in the DPD module in Materials Studio. The repulsive interaction parameters a_{ij} required for the calculation of conservative forces are related to the Flory-Huggins χ-parameters according to (*50*, *51*):

$$a_{ij} = a_{ii} + 3.27\chi \tag{3}$$

where a_{ii} is the repulsion parameter between particles of the same type and has the value of $25k_BT$, which gives a pure DPD fluid with compressibility similar to that of liquid water. The Flory-Huggins χ-parameters were calculated using the Blends module in Materials Studio and our computed repulsion parameters are listed in Table I. The interaction radius r_c was determined to be about 8.14 Å, and

Downloaded by DUKE UNIV on June 21, 2012 | http://pubs.acs.org
Publication Date (Web): April 30, 2010 | doi: 10.1021/bk-2010-1040.ch006

Downloaded by DUKE UNIV on June 21, 2012 | http://pubs.acs.org
Publication Date (Web): April 30, 2010 | doi: 10.1021/bk-2010-1040.ch006

the simulated time step was 5.35 ps (*55*). Further details concerning the other interaction parameters are to found in our previous investigations (*54*, *56*).

II. Radial Distribution Functions and Bragg Spacing Calculations

While the DPD simulation generates the densities of beads on lattice sites, the distributions of beads about a lattice point P is assumed to have a Gaussian form (*63*):

$$D_p(r) = \frac{N}{(2\pi\sigma^2)^{3/2}} \exp(-\frac{r^2}{2\sigma^2}) \tag{4}$$

in which r is the distance from a reference lattice point, N is the number density on the reference lattice point, and σ is a standard distance. When considering the distribution of beads on a certain lattice point other than the reference lattice point, a more practical asymmetric distribution function has been used and is given by:

$$D(r) = \frac{N}{(2\pi)^{1/2}\sigma} \frac{r}{r_p} \left[\exp(-\frac{(r-r_p)^2}{2\sigma^2}) - \exp(-\frac{(r+r_p)^2}{2\sigma^2}) \right] \tag{5}$$

where r_p is the distance from a lattice point P to the reference lattice point N. By summing distributions from all the lattice points around the reference lattice point, we obtain (*63*):

$$4\pi r^2 n g(r) = \frac{r}{(2\pi)^{1/2}} \sum_i \frac{N_i}{r_i \sigma_i} \left[\exp(-\frac{(r-r_i)^2}{2\sigma^2}) - \exp(-\frac{(r+r_i)^2}{2\sigma^2}) \right] \tag{6}$$

where n is the average number density, and $g(r)$ is the RDF.

The scattering intensities I(Q) were related to the radial distribution function $g(r)$ by Fourier transformation for our finite-sized system (*64*, *65*), according to:

$$I(Q,R) \equiv 4\pi\rho \int_0^R dr\, r^2 \left[\frac{\sin(Qr)}{Qr} \right] [g(r) - 1] \tag{7}$$

where Q is the magnitude of the scattering vector and ρ is the average density over all space. The physical dimension or Bragg spacing (d) associated with the first peak at the maximum small angle scattering vector Q_m was then evaluated from the Bragg relationship, $d = 2\pi/Q_m$.

Downloaded by DUKE UNIV on June 21, 2012 | http://pubs.acs.org
Publication Date (Web): April 30, 2010 | doi: 10.1021/bk-2010-1040.ch006

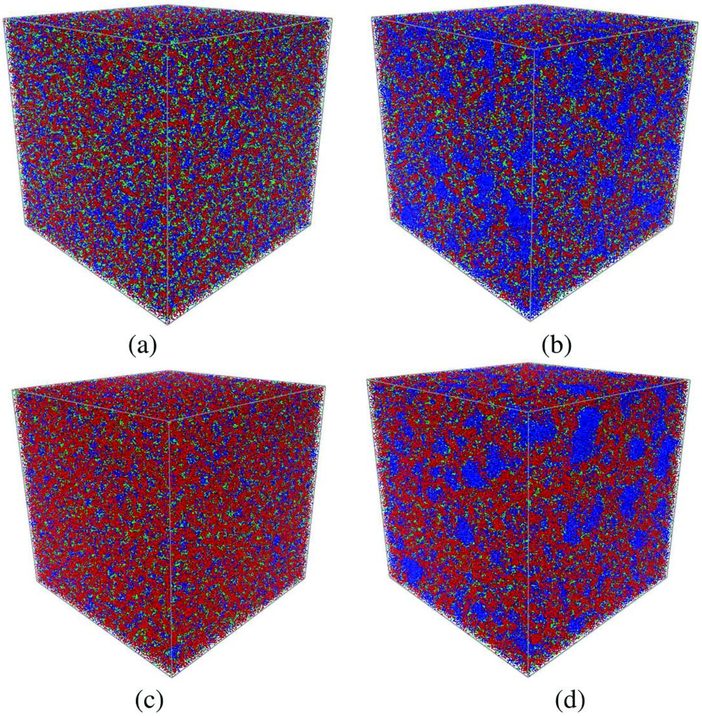

Figure 2. The morphologies of the hydrated SSC PFSA membranes with: (a) EW = 678 and λ = 9; (b) EW = 678 and λ = 16; (c) EW = 1278 and λ = 9; and (d) EW = 1278 and λ = 16. The backbone beads A and B are shown in red, the terminal portion of side chain C bead in green, and the water, W bead, in blue. (see color insert)

Results and Discussion

I. Hydrated Morphology of the SSC PFSA Systems

Figure 2 shows the hydrated morphologies of SSC PFSA membranes, with EW = 678 and 1278 g/mol, at hydration levels λ = 9 and 16 H_2O/SO_3H, respectively. It can be seen from Figure 2(a) that the hydrophobic and hydrophilic phases in SSC PFSA membrane with EW = 678 g/mol have established some degree of segregation at the hydration level λ = 9 H_2O/SO. The water clusters (in blue) with irregular shape distribute among the porous structure. As the hydration level is increased, the segregation of hydrophobic and hydrophilic domains increases. Discrete water domains are evident in both systems and the size of the water clusters increase remarkably at a hydration level where λ = 16 H_2O/SO_3H (see Figure 2(b) and 2(d)). There is a much smaller fraction of water clusters in the SSC ionomer with an EW = 1278 g/mol due to the much large amount of PTFE backbone in the fixed volume simulation cell and this is evident at both

Downloaded by DUKE UNIV on June 21, 2012 | http://pubs.acs.org
Publication Date (Web): April 30, 2010 | doi: 10.1021/bk-2010-1040.ch006

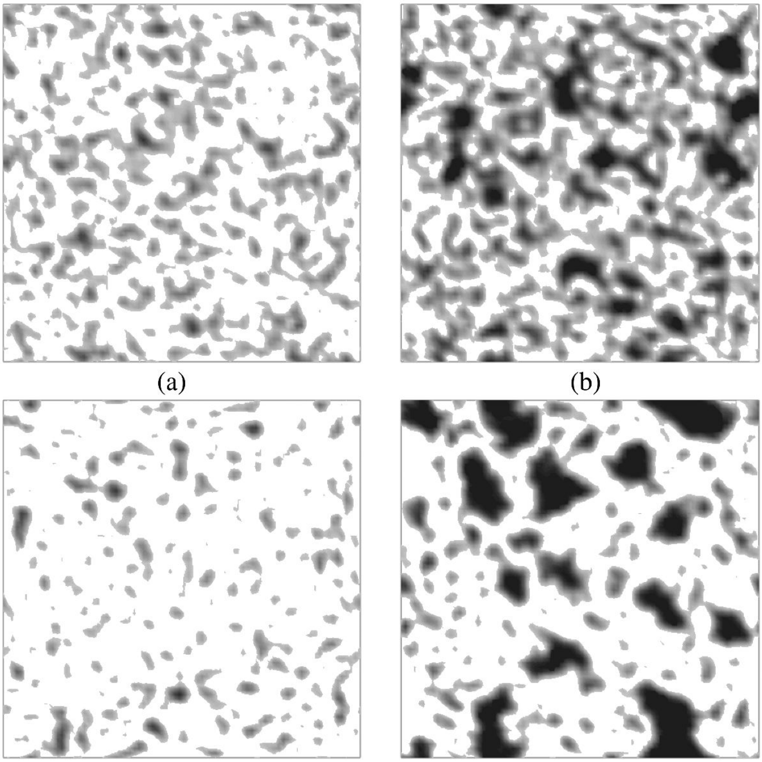

(a) (b)

(c) (d)

Figure 3. Contour plots of the density of water, W beads, shown as a two dimensional cross section for the SSC PFSA membranes with: (a) EW = 678 and λ = 9; (b) EW = 678 and λ = 16; (c) EW = 1278 and λ = 9; and (d) EW = 1278 and λ = 16.

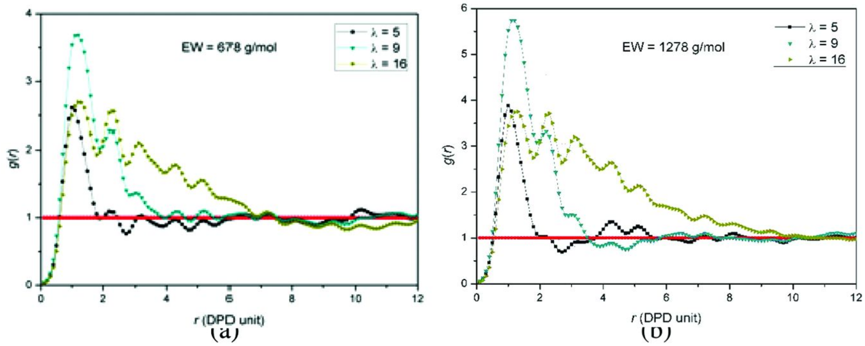

Figure 4. Radial distribution functions g(r) of water particles for the SSC PFSA membrane with EWs of (a) 678 and (b) 1278 g/mol at three distinct water contents. (see color insert)

Downloaded by DUKE UNIV on June 21, 2012 | http://pubs.acs.org
Publication Date (Web): April 30, 2010 | doi: 10.1021/bk-2010-1040.ch006

water contents. The greater EW also results in larger spacing among the water clusters, also seen in Figure 2, at the higher water content and is quantitatively discussed in the context of the computed Bragg spacing below.

Figure 3 shows contour plots of the density of the water (*W*) beads in two dimensional (2D) cross sections for the corresponding 3D models shown in Figure 2. The 2D slices were generated by averaging the projection of water density onto the planes parallel to the first and second axes, and the darkness of the grey level is linearly proportional to the water density over the range from 0.00 to 3.50. Comparing the systems at the two distinct EWs (i.e., Figures 3(a) and (b) with (c) and (d)) clearly indicates the much greater connectivity of the water of the SSC ionomer with an EW = 678 g/mol at both water contents. It is also worth noting that the shapes of the water clusters are neither spherical nor cylindrical in any of the systems although the water domains are certainly more elongated in appearance at the lower EW. At the higher hydration levels (see Figures 3(b) and 3(d)) significant aggregation of the water occurs resulting in much larger domains, particularly with the 1278 EW ionomer where the water forms quite discreet regions. This is in contrast to our earlier simulations of Nafion (*54*) with an EW = 1244 where the water appeared to aggregate in more elongated regions resembling channels or pores.

The different grey levels of water density imply the coexistence of sulfonic acid groups and the dark areas have much higher density of water with the sulfonic acid groups at their interfaces. This reduced connectivity (when compared to the EW = 678 ionomer) will undoubtedly manifest itself in much lower proton conductivity in the system (at a water content where $\lambda = 16$ H_2O/SO_3H).

II. Structural Analysis of Phase Segregated Morphologies

The *W*-*W* RDFs, $g(r)$'s, were computed to quantify the average size of the domains containing the water and their average separation. A comparison of the RDFs for water beads at three distinct hydration levels ($\lambda = 5$, 9 and 16 H_2O/SO_3H) are depicted in Figure 4. At the lowest water content the vast majority of the water is contained in single clusters with slight dispersion (shoulder in the $g(r)$ around 2 DPD units). As the degree of hydration is increased to $\lambda = 9$ H_2O/SO_3H, the first, second and third peak emerge indicating an increase in the size and swelling of the water domains. At the highest hydration level $\lambda = 16$ H_2O/SO_3H, the tails of $g(r)$ extend even further before crossing the mean density of the water (i.e., $g(r) = 1$), particularly for the higher EW ionomer. By comparing $g(r)$ values in Figure 4(a) and 4(b), we can see that the density of the water clusters in the SSC PFSA membrane with EW = 1278 g/mol are larger than that in the membrane with EW = 678 g/mol at the same hydration level. Since the total amount of water in the systems with the higher EW is even lower at a specific hydration level, the higher density of water in local domain implies that the aggregation of water in the membrane with higher EW is much stronger. To be noticed here is that in our previous work (*55*), this phenomenon was not obvious. This is in part due to the smaller difference in EWs (678 *vs.* 978 g/mol) in our previous work, but more importantly is due to the much larger MWs of the ionomer, which is nearly

Downloaded by DUKE UNIV on June 21, 2012 | http://pubs.acs.org
Publication Date (Web): April 30, 2010 | doi: 10.1021/bk-2010-1040.ch006

an order of magnitude larger than those in our previous work. At this point we can also see that the larger MWs stimulate the segregation of hydrophobic and hydrophilic phases in hydrated condition when the EWs are kept the same.

The RDFs for the *C* beads provide information concerning the separation of the sulfonic acid groups and are shown in Figure 5 for the SSC ionomer at both EWs (678 and 1278 g/mol), each at 3 distinct levels of hydration (λ = 5, 9, 16 H_2O/SO_3H). The profile and position of the peaks of the RDFs are quite similar at different hydration levels and even for the membranes with two different EWs. This latter result is somewhat surprising in view of the fact that sulfonic acid groups pendant to the same PTFE backbone are spaced more than twice as frequently on the lower EW ionomer (see Figure 1: $(CF_2CF_2)_4$ vs $(CF_2CF_2)_{10}$). These simulations would suggest that the SO_3H groups organize in a similar manner, particularly at the lower water contents, independent of the EW. As the hydration is increased, the curves only extend to a little greater *r* distance. The minor changes in the RDFs for the *C* beads at different hydration levels suggest that it is impossible for a single (or as few as possible) macromolecule to support the water clusters with only its side chains. Otherwise, the RDFs for *C* beads will show significant difference at different water contents. As a result, it can be inferred that the sulfonic acid groups from different polymers co-capture the water clusters.

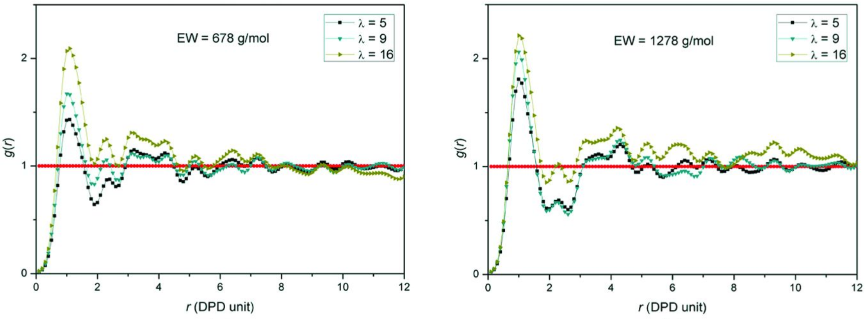

(a) (b)

Figure 5. Radial distribution functions g(r) of the C beads for the SSC PFSA membrane with EWs of (a) 678 and (b) 1278 g/mol at three distinct water contents. (see color insert)

Figure 6 shows computed average radii of water clusters for the SSC ionomer with EW = 678 and 1278 g/mol at hydration levels from 5 to 16 H_2O/SO_3H. The average size of the water domains in each of the PFSA membranes has been evaluated by considering the width of the first two breaking points where $g(r) = 1$ in the corresponding RDFs. The plot clearly shows that the radius of the water clusters increases nearly linearly at the lower hydration levels (5 – 9 H_2O/SO_3H) for both EWs. However, while this relationship remains linear as the water content is increased for the lower EW ionomer, there is an abrupt change in slope for the ionomer at the higher EW from. Evidently, in this hydration region (9 to 11 H_2O/SO_3H) there is substantial swelling of the water domains.

Downloaded by DUKE UNIV on June 21, 2012 | http://pubs.acs.org
Publication Date (Web): April 30, 2010 | doi: 10.1021/bk-2010-1040.ch006

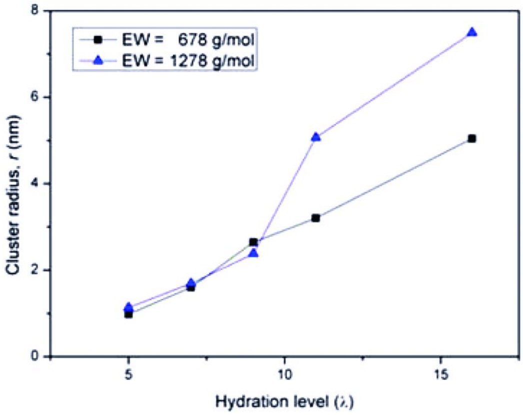

Figure 6. Average radius of the water domains in the two PFSA membranes as a function of hydration level.

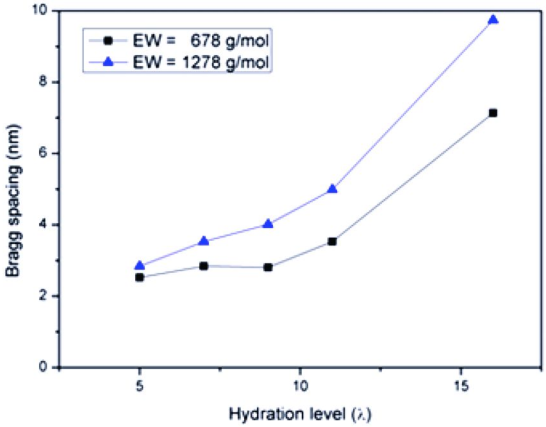

Figure 7. Bragg spacing, d, of water domains in the two SSC PFSA membranes as a function of hydration level.

Finally, a comparison of the Bragg spacing, *d*, of the water peak computed from the first peak of the structure factor as a function of hydration for the two ionomers is shown in Figure 7.

It can be seen that the spacing of the water domains ranges from about 2 to 10 nm in these ionomers as the water content is increased from 5 to 16 H_2O/SO_3H. The effect of increasing EW results in increasing the average spacing of the water-rich domains for a given hydration level. Unlike the similarity in average size of water clusters at low water contents between the two ionomer EWs, the spacing of water clusters show significant difference even at low hydration levels.

Downloaded by DUKE UNIV on June 21, 2012 | http://pubs.acs.org
Publication Date (Web): April 30, 2010 | doi: 10.1021/bk-2010-1040.ch006

Conclusions

We have undertaken DPD simulations to determine the effects of EW and hydration on the morphology of the SSC PFSA membrane at MWs of 61020 and 115020 g/mol. The equilibrated morphologies were determined for the SSC PFSA ionomer with EWs of 678 and 1278 g/mol at hydration levels corresponding to 5, 7, 9, 11 and 16 H_2O/SO_3H. As the water content of the system is increased, the isolated water clusters present at the lower water contents increase in size eventually forming continuous regions which resemble channels or pores in the system with the lower EW ionomer. The simulations suggest that the high EW ionomer exhibits greater dispersion of the water within the polymer and therefore less connectivity. The high EW ionomer also seems to exhibit greater segregation of hydrophobic and hydrophilic regions. The present work also reveals that MW is another critical factor that affects and may even dominate (over EW) the hydrated morphology. Since PEM materials contribute to the performance of fuel cells, selection of EW and MW along with specific ionomer chemistry will be important in optimizing performance of the device over a range of humidity. This will, of course, require validation from experimental studies due to the complexity of hydrated morphologies in PFSA membranes.

References

1. Hamrock, S. J.; Yandrasits, M. A. *Polym. Rev.* **2006**, *46*, 219–244.
2. Tant, M. R.; Lee, K. D.; Darst, K. P.; Martin, C. W. *Polym. Mater. Sci. Eng.* **1988**, *58*, 1074.
3. Tant, M. R.; Darst, K. P.; Lee, K. D.; Martin, C. W. *ACS Symp. Ser.* **1989**, *395*, 370–400.
4. Moore, R. B.; Martin, C. R. *Macromolecules* **1989**, *22*, 3594–3599.
5. Prater, K. *J. Power Sources* **1990**, *29*, 239–250.
6. Eisman, G. A. *J. Power Sources* **1990**, *29*, 389–398.
7. Gebel, G.; Moore, R. B. *Macromolecules* **2000**, *33*, 4850–4855.
8. Arcella, V.; Ghielmi, A.; Tommasi, G. *Ann. N. Y. Acad. Sci.* **2003**, *984*, 226–244.
9. Ghielmi, A.; Vaccarono, P.; Troglia, C.; Arcella, V. *J. Power Sources* **2005**, *145*, 108–115.
10. Arcella, V.; Troglia, C.; Ghielmi, A. *Ind. Eng. Chem. Res.* **2005**, *44*, 7646–7651.
11. Merlo, L.; Ghielmi, A.; Cirillo, L.; Gebert, M.; Arcella, V. *J. Power Sources* **2007**, *171*, 140–147.
12. Merlo, L.; Ghielmi, A.; Cirillo, L.; Gebert, M.; Arcella, V. *Sep. Sci. Technol.* **2007**, *42*, 2891–2908.
13. Kreuer, K. D.; Schuster, M.; Obliers, B.; Diat, O.; Traub, U.; Fuchs, A.; Klock, U.; Paddison, S. J.; Maier, J. *J. Power Sources* **2008**, *178*, 499–509.
14. Gorri, D.; De Angelis, M. G.; Giacinti Baschetti, M.; Sarti, G. C. *J. Membr. Sci.* **2008**, *322*, 383–391.

15. Navarrini, W.; Scrosati, B.; Panero, S.; Ghielmi, A.; Sanguineti, A.; Geniram, G. *J. Power Sources* **2008**, *178*, 783–788.
16. Ezzell, B. R.; Carl, W. P.; Mod, W. A. U.S. Patent 4,358,412, 1982.
17. Zawodzinski, T. A.; Derouin, C.; Radzinski, S.; Sherman, R. J.; Smith, V. T.; Springer, T. E.; Gottesfeld, S. *J. Electrochem. Soc.* **1993**, *140*, 1041–1047.
18. Edmondson, C. A.; Stallworth, P. E.; Chapman, M. E.; Fontanella, J. J.; Wintersgill, M. C.; Chung, S. H.; Greenbaum, S. G. *Solid State Ionics* **2000**, *135*, 419–423.
19. Edmondson, C. A.; Fontanella, J. J. *Solid State Ionics* **2002**, *152*, 355–361.
20. Kumar, S.; Pineri, M. *J. Polym. Sci., Polym. Phys. Ed.* **1986**, *24*, 1767–1782.
21. Gebel, G.; Lambard, J. *Macromolecules* **1997**, *30*, 7914–7920.
22. Paddison, S. J. *Annu. Rev. Mater. Res.* **2003**, *33*, 289–319.
23. Kreuer, K. D.; Paddison, S. J.; Spohr, E.; Schuster, M. *Chem. Rev.* **2004**, *104*, 4637–4678.
24. Elliott, J. A.; Paddison, S. J. *Phys. Chem. Chem. Phys.* **2007**, *9*, 2602–2618.
25. Paddison, S. J.; Elliott, J. A. *J. Phys. Chem. A* **2005**, *109*, 7583–7593.
26. Paddison, S. J.; Elliott, J. A. *Phys. Chem. Chem. Phys.* **2006**, *8*, 2193–2203.
27. Paddison, S. J.; Elliott, J. A. *Solid State Ionics* **2006**, *177*, 2385–2390.
28. Paddison, S. J.; Elliott, J. A. *Solid State Ionics* **2007**, *178*, 561–567.
29. Eikerling, M.; Paddison, S. J.; Pratt, L. R.; Zawodzinski, T. A. *Chem. Phys. Lett.* **2003**, *368*, 108–114.
30. Roudgar, A.; Narasimachary, S. P.; Eikerling, M. *J. Phys. Chem. B* **2006**, *110*, 20469–20477.
31. Roudgar, A.; Narasimachary, S. P.; Eikerling, M. *Chem. Phys. Lett.* **2008**, *457*, 337–341.
32. Narasimachary, S. R.; Roudgar, A.; Eikerling, M. *Electrochim. Acta* **2008**, *53*, 6920–6927.
33. Vishnyakov, A.; Neimark, A. V. *J. Phys. Chem. B* **2000**, *104*, 4471–4478.
34. Jang, S. S.; Molinero, V.; Cagin, T.; Goddard, W. A. *J. Phys. Chem. B* **2004**, *108*, 3149–3157.
35. Urata, S.; Irisawa, J.; Takada, A.; Shinoda, W.; Tsuzuki, S.; Mikami, M. *J. Phys. Chem. B* **2005**, *109*, 4269–4278.
36. Urata, S.; Irisawa, J.; Takada, A.; Shinoda, W.; Tsuzuki, S.; Mikami, M. *J. Phys. Chem. B* **2005**, *109*, 17274–17280.
37. Blake, N. P.; Petersen, M. K.; Voth, G. A.; Metiu, H. *J. Phys. Chem. B* **2005**, *109*, 24244–24253.
38. Blake, N. P.; Mills, G.; Metiu, H. *J. Phys. Chem. B* **2007**, *111*, 2490–2494.
39. Venkatnathan, A.; Devanathan, R.; Dupuis, M. *J. Phys. Chem. B* **2007**, *111*, 7234–7244.
40. Devanathan, R.; Venkatnathan, A.; Dupuis, M. *J. Phys. Chem. B* **2007**, *111*, 8069–8079.
41. Devanathan, R.; Venkatnathan, A.; Dupuis, M. *J. Phys. Chem. B* **2007**, *111*, 13006–13013.
42. Hristov, I. H.; Paddison, S. J.; Paul, R. *J. Phys. Chem. B* **2008**, *112*, 2937–2949.
43. Cui, S. T.; Liu, J. W.; Selvan, M. E.; Paddison, S. J.; Keffer, D. J.; Edwards, B. J. *J. Phys. Chem. B* **2008**, *112*, 13273–13284.

Downloaded by DUKE UNIV on June 21, 2012 | http://pubs.acs.org
Publication Date (Web): April 30, 2010 | doi: 10.1021/bk-2010-1040.ch006

44. Dokmaisrijan, S.; Spohr, E. *J. Mol. Liq.* **2006**, *129*, 92–100.
45. Petersen, M. K.; Wang, F.; Blake, N. P.; Metiu, H.; Voth, G. A. *J. Phys. Chem. B* **2005**, *109*, 3727–3730.
46. Khalatur, P. G.; Talitskikh, S. K.; Khokhlov, A. R. *Macromol. Theory Simul.* **2002**, *11*, 566–586.
47. Galperin, D. Y.; Khokhlov, A. R. *Macromol. Theory Simul.* **2006**, *15*, 137–146.
48. Wescott, J. T.; Qi, Y.; Subramanian, L.; Capehart, T. W. *J. Chem. Phys.* **2006**, *124*, 134702.
49. Yamamoto, S.; Hyodo, S. A. *Polym. J.* **2003**, *35*, 519–527.
50. Groot, R. D.; Warren, P. B. *J. Chem. Phys.* **1997**, *107*, 4423–4435.
51. Groot, R. D.; Madden, T. J. *J. Chem. Phys.* **1998**, *108*, 8713–8724.
52. Groot, R. D.; Rabone, K. L. *Biophys. J.* **2001**, *81*, 725–736.
53. Grafmuller, A.; Shillcock, J.; Lipowsky, R. *Phys. Rev. Lett.* **2007**, *98*, 4.
54. Wu, D.-S.; Paddison, S. J.; Elliott, J. A. *Energy Environ. Sci.* **2008**, *1*, 284–293.
55. Khokhlov, A. R.; Khalatur, P. G. *Chem. Phys. Lett.* **2008**, *461*, 58–63.
56. Wu, D.-S.; Paddison, S. J.; Elliott, J. A. *Macromolecules* **2009**, *42*, 3358.
57. Hoogerbrugge, P. J.; Koelman, J. M. V. A. *Europhys. Lett.* **1992**, *19*, 155–160.
58. Koelman, J. M. V. A.; Hoogerbrugge, P. J. *Europhys. Lett.* **1993**, *21*, 363–368.
59. Español, P.; Warren, P. B. *Europhys. Lett.* **1995**, *30*, 191–196.
60. Español, P. *Europhys. Lett.* **1997**, *40*, 631–636.
61. *Materials Studio*, 4.1; Accelrys Software Inc.: San Diego, 2006.
62. Frisch, M. J.; Trucks, G. W.; Schlegel, H. B.; Scuseria, G. E.; Robb, M. A.; Cheeseman, J. R.; Montgomery, J. A.; Vreven, T.; Kudin, K. N.; Burant, J. C.; Millam, J. M.; Iyengar, S. S.; Tomasi, J.; Barone, V.; Mennucci, B.; Cossi, M.; Scalmani, G.; Rega, N.; Petersson, G. A.; Nakatsuji, H.; Hada, M.; Ehara, M.; Toyota, K.; Fukuda, R.; Hasegawa, J.; Ishida, M.; Nakajima, T.; Honda, Y.; Kitao, O.; Nakai, H.; Klene, M.; Li, X.; Knox, J. E.; Hratchian, H. P.; Cross, J. B.; Adamo, C.; Jaramillo, J.; Gomperts, R.; Stratmann, R. E.; Yazyev, O.; Austin, A. J.; Cammi, R.; Pomelli, C.; Ochterski, J. W.; Ayala, P. Y.; Morokuma, K.; Voth, G. A.; Salvador, P.; Dannenberg, J. J.; Zakrzewski, V. G.; Dapprich, S.; Daniels, A. D.; Strain, M. C.; Farkas, O.; Malick, D. K.; Rabuck, A. D.; Raghavachari, K.; Foresman, J. B.; Ortiz, J. V.; Cui, Q.; Baboul, A. G.; Clifford, S.; Cioslowski, J.; Stefanov, B. B.; Liu, G.; Liashenko, A.; Piskorz, P.; Komaromi, I.; Martin, R. L.; Fox, D. J.; Keith, T.; Al-Laham, M. A.; Peng, C. Y.; Nanayakkara, A.; Challacombe, M.; Gill, P. M. W.; Johnson, B.; Chen, W.; Wong, M. W.; Gonzalez, C.; Pople, J. A. *Gaussian 03*, Revision C.02; Gaussian Inc.: Wallingford, CT, 2004.
63. Yoon, B. J.; Jhon, M. S.; Eyring, H. *Proc. Natl. Acad. Sci. U.S.A.* **1981**, *78*, 6588–6591.
64. Salacuse, J. J.; Denton, A. R.; Egelstaff, P. A. *Phys. Rev. E* **1996**, *53*, 2382–2389.
65. Salacuse, J. J.; Denton, A. R.; Egelstaff, P. A.; Tau, M.; Reatto, L. *Phys. Rev. E* **1996**, *53*, 2390–2401.

Downloaded by DUKE UNIV on June 21, 2012 | http://pubs.acs.org
Publication Date (Web): April 30, 2010 | doi: 10.1021/bk-2010-1040.ch006

Downloaded by UNIV OF GUELPH LIBRARY on June 21, 2012 | http://pubs.acs.org
Publication Date (Web): April 30, 2010 | doi: 10.1021/bk-2010-1040.ch007

Chapter 7

Broadband Dielectric Spectroscopy and Conductivity Mechanism of Nafion 117 and Nafion/[ZrO_2] Hybrid Inorganic-Organic Membranes

V. Di Noto,[1,2,*] E. Negro,[1] and S. Lavina[1]

[1]Dipartimento di Scienze Chimiche, Università di Padova, 35131 Padova (PD), Italy
[2]Istituto di Scienze e Tecnologie Molecolari, ISTM-CNR c/o Dipartimento di Scienze Chimiche, 35131 Padova (PD), Italy
[*]Corresponding author. E-mail: vito.dinoto@unipd.it. Active ACS member.

In this report is described the dielectric characteriation by Broadband Dielectric Spectroscopy (BDS) of a Nafion 117 reference membrane and of a hybrid inorganic-organic membrane based on Nafion and ZrO_2 nanopowders with formula Nafion/[ZrO_2]. The measurements on the two systems were collected both in completely dry and in fully-humidified (wet) conditions. Results allowed the identification of two polarization phenomena and of several dielectric relaxation modes, which were assigned taking into account: a) the primary and secondary structure of the Nafion polymer; and b) the interactions Nafion-water and Nafion-ZrO_2 nanofiller. The dependence on temperature of conductivity ($\sigma_{dc,i}$), relaxation frequencies (f_k), dielectric strength ($\Delta\varepsilon_k$) and shape parameters (m_k and n_k) for the investigated systems in both dry and wet conditions is studied in detail. It is shown that the ZrO_2 nanofiller: a) stabilizes both the hydrophobic and the hydrophilic domains of the Nafion/[ZrO_2] membrane; and b) promotes the coupling between the various relaxation modes of Nafion. In fully-humidified conditions, the stability range of conductivity and the conductivity of the Nafion/[ZrO_2] membrane at 125°C are respectively $5°C < T < 135°C$ and $9.51 \cdot 10^{-2}$ S/cm. For the pristine Nafion 117 membrane, the

In Fuel Cell Chemistry and Operation; Herring, A., et al.;
ACS Symposium Series; American Chemical Society: Washington, DC, 2010.

corresponding values are 5°C < T < 95°C and $1.22 \cdot 10^{-2}$ S/cm. Results allowed to propose a coherent model describing the conductivity mechanism in Nafion-based systems.

Introduction

Polymer electrolyte membrane fuel cells (PEMFCs) are a class of energy conversion devices intended to exploit the chemical energy of a fuel, such as hydrogen or a water-alcohol mixture, and of an oxidant such as oxygen to produce direct electrical current, heat and reaction products (*1*). PEMFCs are particularly attractive owing to their high efficiency, high energy density, simple structure, silent operation, and environmental compatibility (*2*). However, their application is not very widespread yet owing to important drawbacks involving both the high costs and the relatively poor performance of PEMFCs fundamental components (*3*, *4*). The heart of a PEMFC is the membrane-electrode assembly (MEA), where the proton exchange membrane separates the two electrode layers (*5*). Nowadays, the most widely used material for proton exchange membranes is Nafion. While this material is characterized by a good proton conductivity and a high chemical stability, it reaches its optimal performance at the relatively low temperature of ~80-90°C in fully humidified conditions (*6–8*). This leads to fuel cell power plants requiring bulky and expensive heat and water management modules. In order to address these issues, it was proposed to devise hybrid systems were Nafion is doped with nanometric inorganic nanofillers such as metal oxides, heteropolyacids, zeolites and zirconium phosphate (*9–18*). With respect to pristine Nafion, nanocomposite inorganic-organic hybrid membranes present enhanced performance in terms of: a) mechanical properties, as thinner membranes can be prepared resulting in an overall reduction of ohmic losses; b) thermal stability, since the membranes can operate at high temperatures (T up to 120°C), exhibiting an improved efficiency and solving several engineering problems; and c) proton conduction at a low relative humidity, improving the water management in the overall fuel cell system. The chemical structure of Nafion is complex, being characterized by a polytetrafluoroethylene backbone endowed with perfluorinated polyether side chains terminated with a sulfonic acid group (*19*). There are several models which have been proposed to rationalize the supramolecular structure of Nafion and its interaction with water molecules; the situation becomes even more complex when inorganic nanofillers are added to a Nafion-based system. In order to devise better materials, it is necessary to understand the origins of the electrical relaxations in Nafion and Nafion-based hybrid materials. Preliminary studies on the dielectric response of Nafion-based materials carried out by Broadband Dielectric Spectroscopy (BDS) are reported in the literature (*20–26*). The goals of this work are: a) to reconcile the assignment of BDS relaxation phenomena of Nafion and Nafion-based materials; b) to study the evolution of the relaxation phenomena in both the hydrophilic and the hydrophobic domains of the materials caused by the interactions Nafion-H_2O and

Downloaded by UNIV OF GUELPH LIBRARY on June 21, 2012 | http://pubs.acs.org
Publication Date (Web): April 30, 2010 | doi: 10.1021/bk-2010-1040.ch007

Nafion-nanofiller in bulk materials; and c) to elucidate the transport dynamics and the proton conductivity mechanism of the materials.

Experimental

Reagents

Nafion™ ionomer 5 wt% solution (perfluorosulfonic acid PTFE copolymer solution) with a proton exchange capacity of 0.80 meq·g^{-1} (Alfa Aesar, ACS grade) was used as purchased. ZrO_2 nanometric oxoclusters (Aldrich, ACS grade) were purified by standard methods (*27*). The ZrO_2 oxide was characterized by a density of 5.19 g·mL^{-1}. All solvents used were supplied by Aldrich and further purified by standard methods. Bidistilled/milli-Q water was used in all procedures.

Nanofiller Preparation

ZrO_2 nanopowders were extensively ground by a planetary ball mill in a tungsten carbide jar. The size of the ZrO_2 nanofiller grains was determined by HR-TEM image analysis and resulted equal to 20-30 nm (data not shown). 2.65 g of ZrO_2 were quantitatively transferred into a 100 mL volumetric flask and brought to volume with DMF. The homogeneous precursor solution A was prepared: first, by adding 2 mL of 30 wt% NH_3 solution to 893 μL of the ZrO_2-based suspension; and second, by treating the obtained mixture with an ultrasonic bath for 1 hour.

Membrane Preparation

Three Nafion-based nanocomposite membranes have been prepared by a general solvent casting procedure as follows. A suitable amount of Nafion emulsion (0.45 g) suspended in DMF and prepared as described elsewhere (*9–11*) was added to a suitable amount of A solution. The mixture was homogenized by a treatment in ultrasonic bath for 2 h. The resulting solution was recast in a Petri dish with a diameter of 2.5 cm, at 100 °C, for 10 h, under a hot air stream. The resulting membrane was: (a) first, dislodged from the Petri dish by a treatment with hot milli-Q water; (b) second, partially dried under air at room temperature for 1 h; and (c) third, hot pressed at $T = 100$ °C and $p = 70$ bar for 5 min to improve its mechanical properties. The thickness of the prepared film was about 200 μm. The overall mass of ZrO_2 in the membrane was 0.024 g, which corresponds to $\Psi ZrO_2 = 0.534$; and $\Phi = 0.770$, where $\Psi ZrO_2 = molZrO_2 / mol\text{-}SO_3H$ and $\Phi = (meq_{Nafion} + meqZrO_2)/g_{composite}$. A Nafion 117 membrane (Ion Power) was used as the reference.

Downloaded by UNIV OF GUELPH LIBRARY on June 21, 2012 | http://pubs.acs.org
Publication Date (Web): April 30, 2010 | doi: 10.1021/bk-2010-1040.ch007

Downloaded by UNIV OF GUELPH LIBRARY on June 21, 2012 | http://pubs.acs.org
Publication Date (Web): April 30, 2010 | doi: 10.1021/bk-2010-1040.ch007

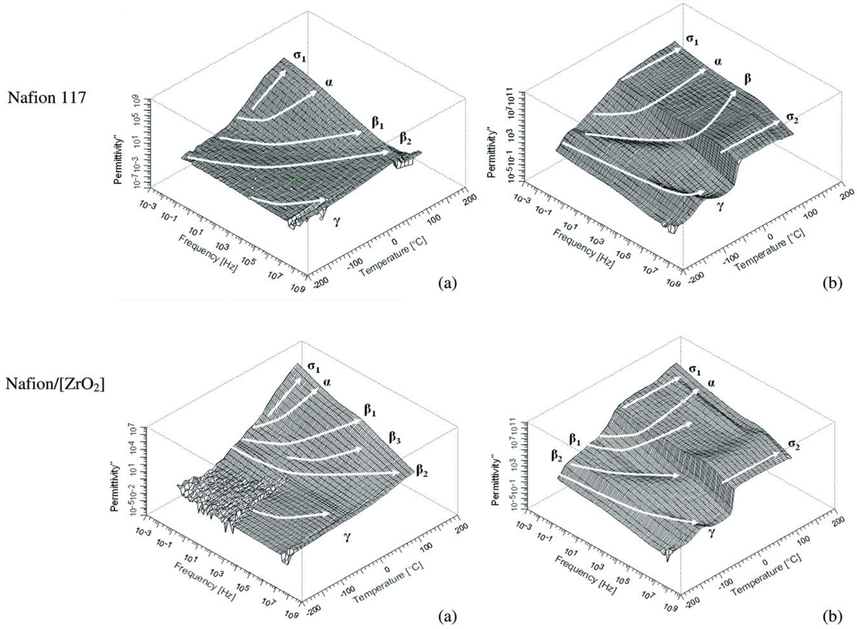

Figure 1. Plots of ε"(ω) as a function of temperature for Nafion 117 and Nafion/[ZrO$_2$] membranes in both the dry (a) and the wet state (b).

Membrane Conditioning and Humidity Reference Conditions

The purification and conditioning of the membranes were carried out as follows. First, the membranes were heated at 80 °C in bidistilled water for 1 h. Second, the membranes were treated twice with a 3 wt% solution of H_2O_2 at 80 °C. Third, the films were soaked twice for 1 h in a solution of 1M H_2SO_4 at 80 °C. Then, the membranes were purified by washing them three times for 1 h at 80 °C with bidistilled water. Finally, each proton-conducting membrane was hydrated in an autoclave at RH 100%, T = 135 °C and P = 3.3 bar, giving so rise to the "wet" samples. The obtained membranes were stored in milli-Q water at room temperature inside PET bags. The "dry" samples were obtained inside a dry box by dehydrating "quasi dry" membranes at 110°C under a vacuum of 10^{-3} mbar for 8 hours. The water concentration in the N_2 dry box was < 1 ppm.

Instruments and Methods

Electrical spectra were measured in the 10^{-2} Hz – 10 MHz frequency range using an Alpha Analyzer (Novocontrol). The temperature range from -155 to 155 °C was explored by using a home-made cryostat operating with an N_2 gas jet heating and cooling system. As described in detail elsewhere (*28*), the measurements were performed by sandwiching the fully hydrated samples

Downloaded by UNIV OF GUELPH LIBRARY on June 21, 2012 | http://pubs.acs.org
Publication Date (Web): April 30, 2010 | doi: 10.1021/bk-2010-1040.ch007

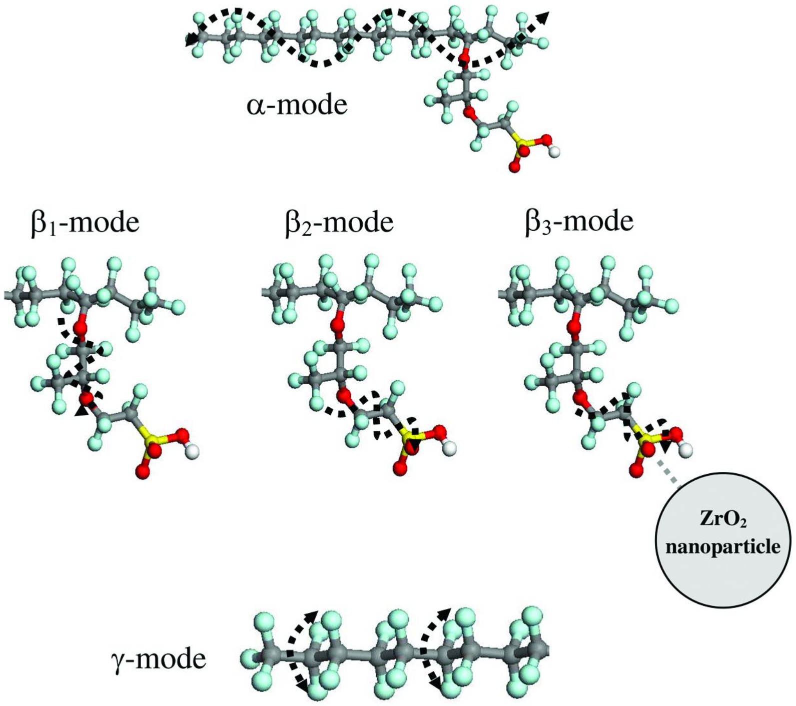

Scheme 1. Dielectric relaxations modes observed in Nafion 117 and Nafion/[ZrO_2] membranes (see color insert)

between two circular platinum electrodes sealed within a CR2032 button battery case with a free volume of ca. 0.3 cm^3. The geometrical constant of the cell was obtained by measuring the electrode–electrolyte contact surface and the distance between electrodes with a micrometer. No corrections for thermal expansion of the cell were carried out. The temperature was measured with an accuracy greater than ±0.1 °C. The complex impedance ($Z^*(\omega)$) was converted into complex conductivity ($\sigma^* = \sigma' + i\sigma''$) and permittivity ($\varepsilon^* = \varepsilon' - i\varepsilon''$) as described elsewhere (*9*, *28*). σ^* spectra were employed to measure accurately the conductivity of samples, σ_{dc}, as described previously (*9*, *28*).

Results and Discussion

Nafion 117 and Nafion/[ZrO_2] membranes were extensively characterized by broadband dielectric spectroscopy (BDS) in order to: a) study their conductivity mechanisms and the correlations between their structural features and proton charge transfer mechanisms; and b) determine the effect of the ZrO_2 nanofiller on the overall conductivity both in the wet and in the dry state. The plots of $\varepsilon''(\omega)$ as a function of temperature for Nafion 117 and Nafion/[ZrO_2] membranes in both the dry and the wet state are reported in Figure 1. It is observed that

Downloaded by UNIV OF GUELPH LIBRARY on June 21, 2012 | http://pubs.acs.org
Publication Date (Web): April 30, 2010 | doi: 10.1021/bk-2010-1040.ch007

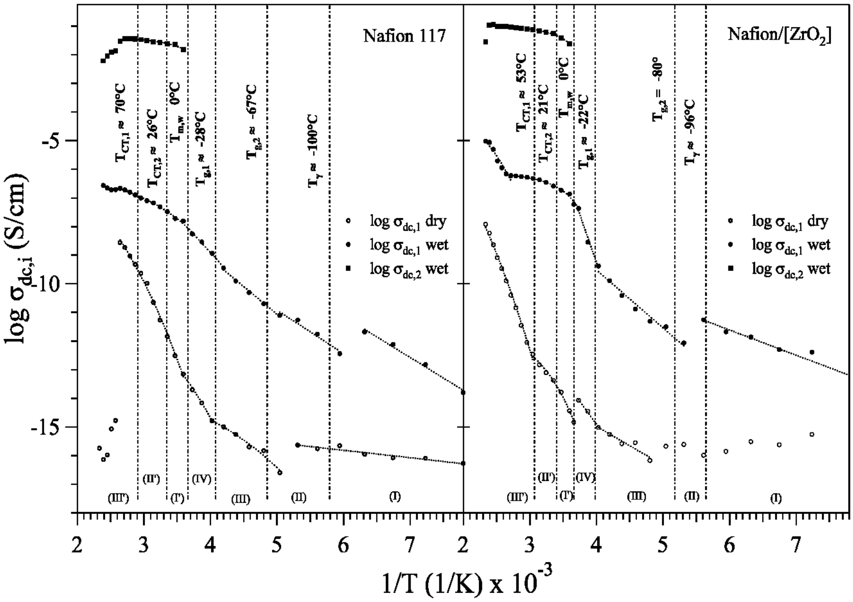

Figure 2. Plots of $\sigma_{dc,i}$ profiles vs. 1/T for Nafion 117 (left) and Nafion/[ZrO$_2$] membranes (right) in both the dry and the wet state. Dotted lines correspond to fitted curves as described in Table II and Table III.

Table I. $\sigma_{dc,i}$ and SRC values for Nafion 117 and Nafion/[ZrO$_2$] membranes[a]

Material	*Humidity condition*					
	Dry	*Wet*		*Dry*	*Wet*	
	$\sigma_{dc,1}$ at 105°C (S/cm)	*$\sigma_{dc,1}$ at 125°C (S/cm)*	*$\sigma_{dc,2}$ at 125°C (S/cm)*	*SRC $\sigma_{dc,1}$ (°C)*	*SRC $\sigma_{dc,1}$ (°C)*	*SRC $\sigma_{dc,2}$ (°C)*
Nafion 117	$2.7 \cdot 10^{-9}$	$2.0 \cdot 10^{-7}$	$1.22 \cdot 10^{-2}$	5<T<105	5<T<145	5<T<95
Nafion/[ZrO$_2$]	$1.0 \cdot 10^{-10}$	$1.9 \cdot 10^{-6}$	$9.51 \cdot 10^{-2}$	5<T<155	5<T<155	5<T<135

[a] The Stability Range of Conductivity (SRC) is the range of temperatures at T > 5°C where: $\partial \log(s)/\partial(1/T) < 0$ (*9*, *12*).

at frequencies below 300 Hz and in the range 1 kHz – 1 MHz two distinct polarization phenomena are revealed at T > 0 in the wet samples, while only one phenomenon is observed at T < 0 for both dry and wet samples. The presence of two distinct polarization phenomena is commonly observed in ion-conducting polymer electrolytes, where spherical nanocomposite particles characterized by a high dielectric constant ε are included in a bulk matrix with a low ε (*29*). The static dielectric constant of the Teflon-like hydrophobic domains of Nafion is ca. 2.2, while that of the hydrated hydrophilic domains is characterized by much higher values, up to that of water (~80). On these basis, the new polarization event peaking at low frequencies characterizing Nafion-based materials ($\sigma_{dc,1}$) has been attributed to the interfacial polarization, also known as the Maxwell-Wagner

Downloaded by UNIV OF GUELPH LIBRARY on June 21, 2012 | http://pubs.acs.org
Publication Date (Web): April 30, 2010 | doi: 10.1021/bk-2010-1040.ch007

phenomenon (*30*), while the polarization event peaking at high frequencies was ascribed to the electrode polarization phenomenon (*31*). The other dielectric relaxations observed in Figure 1 and outlined in Scheme 1 have been attributed as follows:

- *α-mode*. This dielectric relaxation is corresponding to the conformational transitions of the fluorocarbon chains (i.e., the segmental motions).
- *β-modes*. These dielectric relaxations are corresponding to the motions of the polyether side chains. Three β modes have been identified: β_1-mode, a fluctuation of the dipole moment of the portion of the ether side chain bound to the perfluorinated backbone; β_2-mode, a relaxation event of the dipole moment of the ether side chain bound to the sulfonic acid groups; and β_3-mode, a relaxation mode of the dipole moment of the ether side chain bound to the sulfonic acid groups strongly interacting with the environment.
- *γ-mode*. This dielectric relaxation corresponds to the short-range motion of CF_2 units of PTFE backbone chains.

Furthermore, the complex BDS spectra of the membranes were analyzed using the following empirical equation (*32*, *33*) (1):

$$\varepsilon^*(\omega) = \varepsilon_\infty + \sum_{i=1}^{2} \frac{\sigma_{dc,i} \cdot (i\omega\tau_{el,i})^{\gamma_i}}{i\omega\left[1 + (i\omega\tau_{el,i})^{\gamma_i}\right]} + \sum_{k=1}^{n} \frac{\Delta\varepsilon_k}{\left[1 + (i\omega\tau_k)^{\alpha_k}\right]^{\beta_k}} \tag{1}$$

$\sigma_{dc,i}$ corresponds to the interfacial (i = 1) and sample (i = 2) DC conductivity; γ_i are shape parameters describing the relaxation times; α_k and β_k are parameters describing the broadening and asymmetry of the k-th relaxation peaks; $\tau_k = 1/(2\pi f_k)$ is the dielectric relaxation time, where f_k is the frequency of the peak position in Hz; $\Delta\varepsilon_k$ is the dielectric strength and τ_{el} is the relaxation time associated with the electrode polarization phenomena. The second term of (1) describes the electrode polarization phenomena and the σ_{dc} conductivity; the third term of (1) models the dielectric relaxations of the materials. Figure 2 reports $\sigma_{dc,i}$ as a function of 1/T for Nafion 117 and Nafion/[ZrO_2] membranes in both the dry and the wet state. The overall σ_{dc} of each material is equal to the sum of the $\sigma_{dc,1}$ and $\sigma_{dc,2}$ contributions. However, since $\sigma_{dc,2}$ is at least five orders of magnitudes higher with respect to $\sigma_{dc,1}$, it can be safely be assumed that $\sigma_{dc} = \sigma_{dc,2}$ when $T > 0$ and the materials are in the wet state. In all the other conditions, $\sigma_{dc} = \sigma_{dc,1}$. With respect to the materials in the dry state, $\sigma_{dc,1}$ of the wet systems is always larger by at least one order of magnitude, even at $T < 0$°C. The dependence of σ_{dc} vs. 1/T for both dry and wet samples shows several discontinuities, marked by the following labels: $T_{CT,1}$, $T_{CT,2}$, $T_{M,W}$, $T_{g,1}$, $T_{g,2}$, $T_{g,\gamma}$ (Figure 2). The latter are attributed to structural rearrangements of the materials evidenced by DSC and DMA measurements (data not shown). These results are the object of a paper currently under preparation. Thus, for $T < 0$°C four distinct regions are revealed (I, II, III and IV), while at $T > 0$°C three distinct regions can be observed (I', II' and III'). The values of $\sigma_{dc,i}$ of the materials at 105°C and 125°C are reported in Table I, together with the SRC values (*9*, *12*).

Downloaded by UNIV OF GUELPH LIBRARY on June 21, 2012 | http://pubs.acs.org
Publication Date (Web): April 30, 2010 | doi: 10.1021/bk-2010-1040.ch007

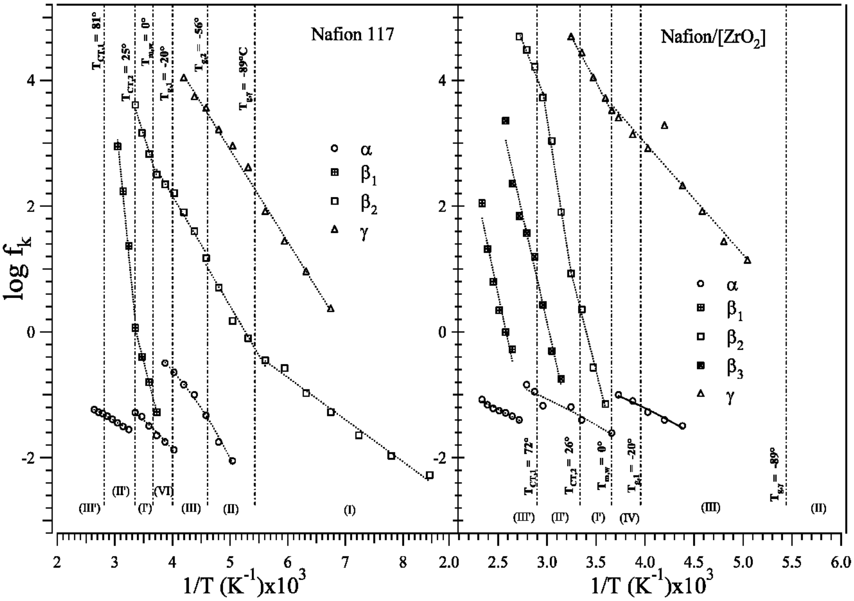

Figure 3. Dependence of the frequencies of the dielectric relaxations on 1/T for Nafion 117 (left) and Nafion/[ZrO₂] membranes (right) in the dry state. Dotted lines correspond to fitted curves as described in Table II.

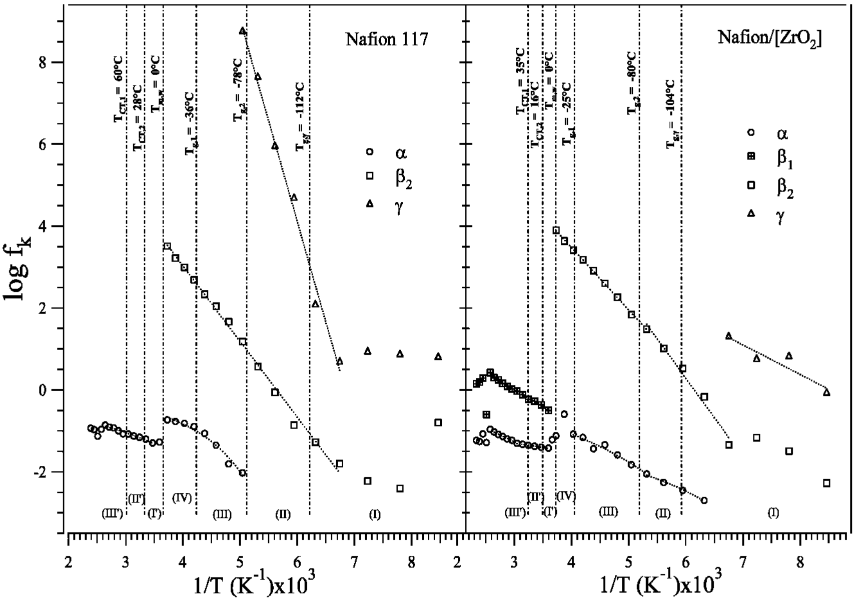

Figure 4. Dependence of the frequencies of the dielectric relaxations on 1/T for Nafion 117 (left) and Nafion/[ZrO₂] membranes (right) in the wet state. Dotted lines correspond to fitted curves as described in Table III.

Downloaded by UNIV OF GUELPH LIBRARY on June 21, 2012 | http://pubs.acs.org
Publication Date (Web): April 30, 2010 | doi: 10.1021/bk-2010-1040.ch007

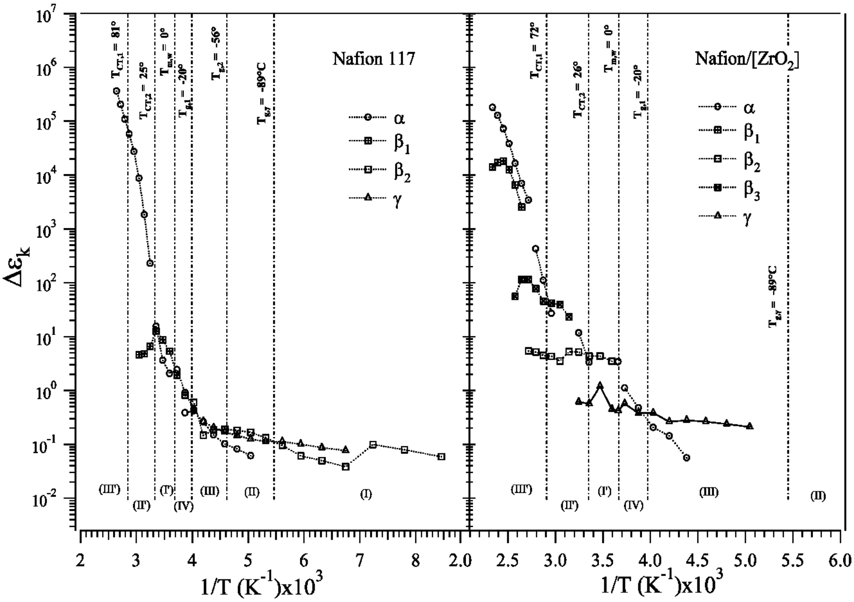

Figure 5. Dependence of $\Delta\varepsilon_k$ on 1/T for Nafion 117 (left) and Nafion/[ZrO$_2$] membranes (right) in the dry state.

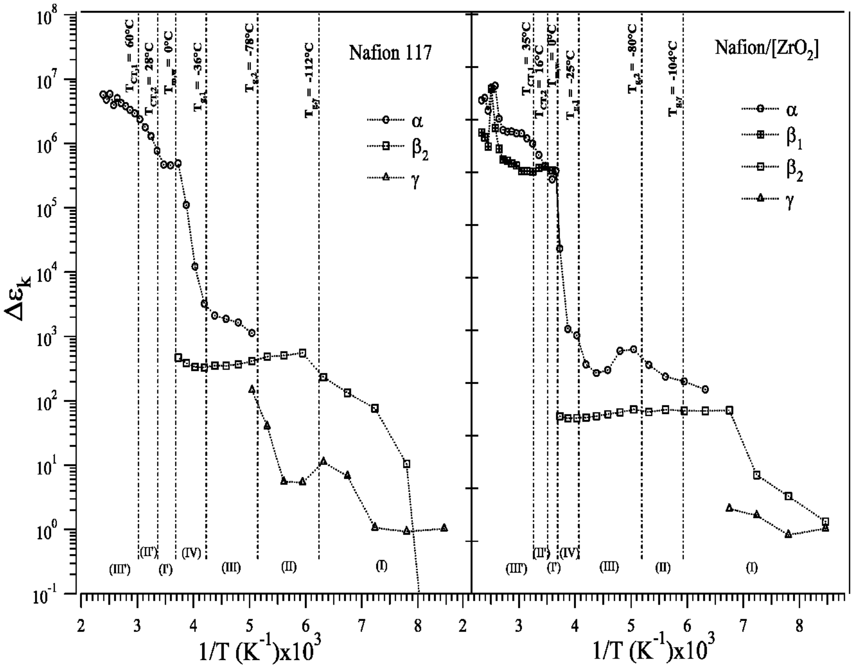

Figure 6. Dependence of $\Delta\varepsilon_k$ on 1/T for Nafion 117 (left) and Nafion/[ZrO$_2$] membranes (right) in the wet state.

With respect to the pristine Nafion 117, it is observed that the presence of the nanofiller enhances the $\sigma_{dc,i}$ values of the hybrid Nafion/[ZrO_2] membrane in the wet state by ca. one order of magnitude. The SRC of the latter system is also enhanced significantly, as observed in similar hybrid inorganic-organic systems described in the literature (*9*, *12*). It is to be highlighted that the hybrid Nafion/[ZrO_2] membrane in the wet state has a SRC of $\sigma_{dc,2}$ extending up to 135°C. This SRC range is ca. 40°C higher with respect to pristine Nafion 117. The dependence on 1/T of the dielectric relaxations frequencies is shown in Figure 3 and Figure 4 for the membranes in the dry and wet state, respectively. Results indicate that the α-modes of both the pristine Nafion 117 and the Nafion/[ZrO_2] membrane are not significantly affected by the hydration level. However, discontinuities are revealed at temperatures corresponding to those evidenced in the plot of σ_{dc} vs. 1/T (Figure 2). This suggests that host reorganization takes place after a thermal transition, probably generated by a change in the nanostructure of the hydrophobic PTFE domains. In pristine Nafion 117 membrane, only one β-mode is detected (β_2) in the wet sample (Figure 4), while in the dry membrane this mode splits into two modes (β_1 and β_2), which are shifted to lower frequencies (Figure 3). In the wet Nafion/[ZrO_2] membrane two β-modes are detected (β_1 and β_2), which split into three modes in the dry sample (β_1, β_2 and β_3). These evidences indicate that β-relaxation modes are very sensitive to the interactions between the side groups and the environment, and that in the Nafion/[ZrO_2] membranes strong Nafion-nanofiller interactions occur. The dependence of $\Delta\varepsilon_k$ on 1/T is shown in Figure 5 and Figure 6 for the membranes in the dry and wet state, respectively. It is observed that the dielectric strength $\Delta\varepsilon_k$ of dry systems decreases as T decreases for all the relaxation modes (Figure 5). This result indicates that: a) the relaxations of the fluorocarbon backbone chains are strongly coupled with the fluctuation dynamics of side group dipoles; and b) the strength of the interactions between side groups and the nanofiller in the Nafion/[ZrO_2] membrane increases as T is decreased. In addition, in wet systems (Figure 6), it is observed that Δε values are at least one order of magnitude higher than that of dry samples. This indicates that the interactions [side chain]-[side chain] and [side-chain]-[nanofiller] are weaker when water is present in bulk materials. With respect to the other β relaxations $\Delta\varepsilon\beta_2$ values are lower, thus indicating that this relaxation mode is associated with ether side chains of $-SO_3H$ groups strongly interacting with water molecules. The dependence of shape parameters m_k and n_k on temperature for the dry and wet membranes is shown in Figure 7 and 8, respectively. The shape parameters m_k and n_k are defined as follows (2):

$$\begin{aligned} m_k &= \alpha_k \\ n_k &= \alpha_k \cdot \beta_k \end{aligned} \tag{2}$$

Downloaded by UNIV OF GUELPH LIBRARY on June 21, 2012 | http://pubs.acs.org
Publication Date (Web): April 30, 2010 | doi: 10.1021/bk-2010-1040.ch007

Downloaded by UNIV OF GUELPH LIBRARY on June 21, 2012 | http://pubs.acs.org
Publication Date (Web): April 30, 2010 | doi: 10.1021/bk-2010-1040.ch007

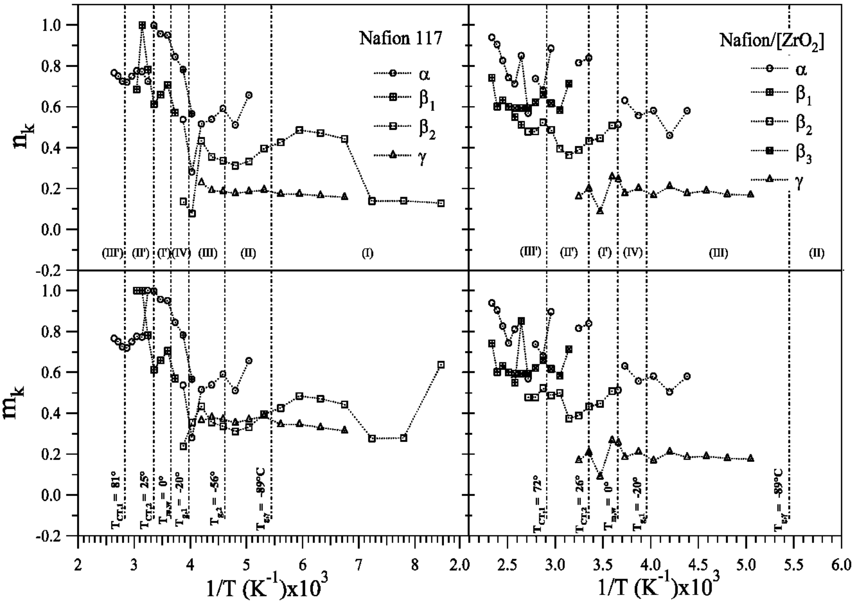

Figure 7. Dependence of shape parameters m_k and n_k on 1/T for Nafion 117 (left) and Nafion/[ZrO$_2$] membranes (right) in the dry state.

α_k and β_k are fitting parameters of the k-th relaxation peak as reported in expression (1). It is observed that in dry systems (Figure 7): a) at $T < 0$, $0 \leq m_k \leq 0.6$ and $0 \leq n_k \leq 0.5$, thus indicating that the relaxation modes owing to intermolecular interactions are associated with relaxations of hindered local motions; and b) at T > 0°C, the values of m_k and n_k increase as T is raised; this evidence confirms that the crosslinking interactions involving sulfonic groups are weakened as T rises. The formation of $-SO_3H\cdots[ZrO_2]\cdots HSO_3-$ bridges in the Nafion/[ZrO$_2$] membrane influences significantly the local motion of acid side groups and the segmental relaxation phenomena of hydrophilic PTFE domains in the dry state. Results of the wet systems (Figure 8) indicate that in the whole temperature range the n_k and m_k parameters range from 0.4 to 0.9. This suggests that, with respect to dry samples, the local chain dynamics of fluorocarbon backbone segments and side groups are less hindered by the environment. Therefore, it is hypothesized that water solvating the nanoparticles composing the bulk materials acts as an interfacial plasticizing agent. Table II and Table III report the pseudo-activation energies of $\sigma_{dc,i}$ and f_k of the membranes in the dry and the wet state, respectively.

It is determined that for both Nafion 117 and Nafion/[ZrO$_2$] systems the conduction mechanism responsible of the conductivity values $\sigma_{dc,i}$ is regulated by the relaxation modes, f_k. Indeed, it is observed that that the relaxation modes responsible of the charge transfer processes in bulk materials in each temperature region are those which are characterized by pseudo-activation energy values very similar to that determined for $\sigma_{dc,i}$. These observations allowed to conclude that when $T > 0$: a) in dry materials, the charge transfer is correlated to the segmental motions of fluorocarbon backbone chains; b) in wet systems, the proton migration

Downloaded by UNIV OF GUELPH LIBRARY on June 21, 2012 | http://pubs.acs.org
Publication Date (Web): April 30, 2010 | doi: 10.1021/bk-2010-1040.ch007

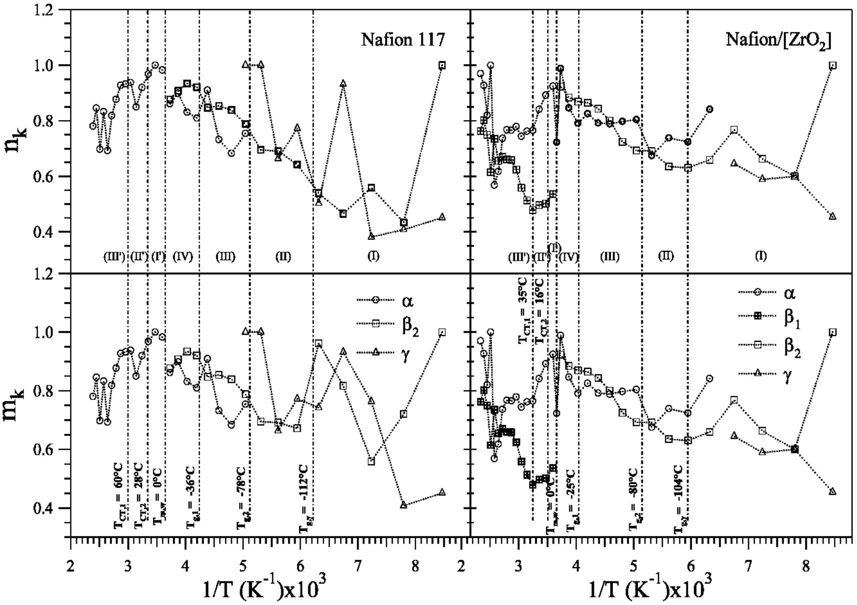

Figure 8. Dependence of shape parameters m_k and n_k on 1/T for Nafion 117 (left) and Nafion/[ZrO$_2$] membranes (right) in the wet state.

Table II. Pseudo-activation energies of σ_{dc} and f_k for Nafion 117 and Nafion/[ZrO$_2$] membranes in the dry state. The various temperature regions are shown

Material		*X*	*E_a/kJ·mol^{-1}*							*T > 0*	*T < 0*
			III'[a]	*II'*[a]	*I'*[a]	*IV*[a]	*III*[a]	*II*[a]	*I*[a]		
Nafion 117[b]		σ_{dc}	25.0±0.5^V			11.5±0.6^V	6.3±0.5^V		5±1^A	σ_{dc} ↔ α	σ_{dc} ↔ α, β_2
	f_k	α	2.97±0.02^H		3.0±0.2^H		5.1±0.2^H				
		β_1		179±14^A	68±2^A						
		β_2			56±4^A	30±2^A		30±3^A	12.8±0.6^A		
		γ					28.1±0.7^A				
Nafion/[ZrO$_2$][b]		σ_{dc}	42±1^V	4.9±1.7^V		61±5^A	26±5^A			σ_{dc} ↔ α	σ_{dc} ↔ α
	f_k	α	4.6±0.2^H	3.7±0.4^H		3.7±0.4^H					
		β_1	141±15^A								
		β_2	131±8^A								
		β_3	76±10^A	190±10^A	117±8^A						
		γ			55±2^A	34±4^A					

[a] Temperature regions → I: T < -100°C; II: -100 < T < -67°C; III: -67 < T < -28°C; IV: -28 < T < 0°C; I': 0 < T < 26°C; II': 26 < T < 70°C; III': T > 70°C.

[b] The pseudo-activation energies were determined by fitting the data of Figure 2 and Figure 3 in the different temperature regions by VTF (V), VTFH (H) or Arrhenius-like (A) equations *(12, 33)*.

of Nafion 117 is strongly dependent on the dynamics of water, while the proton transfer mechanism of the Nafion/[ZrO$_2$] membrane is strongly correlated to segmental motion of fluorocarbon PTFE chains. In addition, when T < 0: a) in dry materials, the conductivity mechanism of Nafion 117 is correlated to the α and β_2 relaxations, while that of Nafion/[ZrO$_2$] is correlated to the segmental motion

Table III. Pseudo-activation energies of σ_{dc} and f_k for Nafion 117 and Nafion/[ZrO$_2$] membranes in the wet state. The various temperature regions are shown

Material	X		E_a/kJ·mol^{-1}							T > 0	T < 0
			III'^{a}	II'^{a}	I'^{a}	IV^{a}	III^{a}	II^{a}	I^{a}		
Nafion 117^{b}	$\sigma_{dc,1}$	1	3.9 ± 0.1^{V}			49 ± 3^{A}	37 ± 2^{A}	29 ± 4^{A}	27.5 ± 2^{A}	$\sigma_{dc,2}$ $E\sigma_{dc2} \ll E_\alpha$	$\sigma_{dc,1} \leftrightarrow \beta$
		2	0.5 ± 0.2^{V}								
	f_k	α	2.6 ± 0.2^{H}			1.8 ± 1^{H}					
		β				35.3 ± 0.8^{A}					
		γ						94 ± 4^{A}			
Nafion/[ZrO$_2$]^{b}	$\sigma_{dc,1}$	1	12 ± 1^{V}	0.7 ± 0.1^{V}		34 ± 5^{V}	39 ± 3^{A}	17 ± 1^{A}		$\sigma_{dc,2} \leftrightarrow \alpha$	$\sigma_{dc,1} \leftrightarrow \beta_2$
		2	0.46 ± 0.04^{V}								
	f_k	α	3.4 ± 0.2^{H}	0.73 ± 0.06^{H}			3.4 ± 0.3^{H}	1.6 ± 0.1^{H}			
		β_1	15.7 ± 0.3^{A}								
		β_2				29.2 ± 0.3^{A}		37 ± 3^{A}			
		γ							14 ± 4^{A}		

[a] Temperature regions → I: T < -100°C; II: -100 < T < -67°C; III: -67 < T < -28°C; IV: -28 < T < 0°C; I': 0 < T < 26°C; II': 26 < T < 70°C; III': T > 70°C.

[b] The pseudo-activation energies were determined by fitting the data shown in Figure 2 and Figure 4 by VTF (V), VTFH (H) or Arrhenius-like (A) equations *(12, 33)*.

(α relaxation) of PTFE chains; b) in wet systems, the proton migration of both materials is strongly correlated with the relaxation modes of side chains.

Conclusions

In this work, a careful study on the molecular origins of the dielectric relaxation events of Nafion 117 and Nafion/[ZrO$_2$] was carried out. It was found that the materials are characterized by two distinct polarization events: interfacial and electrode polarization. Interfacial polarization corresponds to the build-up of space charge near the interfaces between the various phases characterizing the material, while electrode polarization gives rise to conductive relaxations associated with ion accumulation processes near the electrodes. The conductivity of Nafion/[ZrO$_2$] is mainly regulated by the segmental motions of the host matrix; a significant coupling between the relaxation modes of the ether side chains and the dynamics of hydrophobic PTFE domains was observed. It was demonstrated that the ZrO$_2$ nanofiller stabilizes both the hydrophobic and the hydrophilic domains owing to the formation of $-SO_3H\cdots[ZrO_2]\cdots HSO_3-$ bridges. These interactions create a three-dimensional hybrid polymer network, consisting of bundles of fluorocarbon chains of Nafion bonded together through nanofiller bridges. BDS is a very powerful technique to characterize hybrid Nafion-based materials. For example, the present study shows that the ZrO$_2$ nanofiller: a) stabilizes the hydrophobic and the hydrophilic domains of materials; and b) promotes coupling between the relaxation phenomena ascribed to the motions of either the hydrophilic polar domains (β relaxations) and the hydrophobic PTFE doimains (α and γ relaxations) of Nafion. Finally, owing to the strong correlation taking place between α and β relaxations, a peristaltic-like conduction mechanism is proposed for the hybrid Nafion/[ZrO$_2$] nanocomposite material: long-range charge transfer migration occurs in the wet material by a hopping process when

Downloaded by UNIV OF GUELPH LIBRARY on June 21, 2012 | http://pubs.acs.org
Publication Date (Web): April 30, 2010 | doi: 10.1021/bk-2010-1040.ch007

different solvated hydrophilic domains come into contact following the molecular relaxation events of the material.

Acknowledgments

This research was funded by the Italian MURST, project NUME, of FISR2003, “Sviluppo di membrane protoniche composite e di configurazioni elettrodiche innovative per celle a combustibile con elettrolita polimerico”.

It is a pleasure to acknowledge the benefit of several very stimulating discussions with Prof. J. J. Fontanella and Prof. M. C. Wintersgill of Physics Department, US. Naval Academy, Annapolis, MD.

Downloaded by UNIV OF GUELPH LIBRARY on June 21, 2012 | http://pubs.acs.org
Publication Date (Web): April 30, 2010 | doi: 10.1021/bk-2010-1040.ch007

References

1. Larminie, J.; Dicks, A. *Fuel Cell Systems Explained*, 2nd ed.; John Wiley & Sons: Chichester, 2003.
2. O’Hayre, R.; Cha, S. W.; Colella, W.; Prinz, F. B. *Fuel Cell Fundamentals*; John Wiley & Sons: New York, 2006.
3. Gasteiger, H. A.; Kocha, S. S.; Sompalli, B.; Wagner, F. T. *Appl. Catal., B* **2005**, *56*, 9.
4. Borup, R.; Meyers, J.; Pivovar, B.; et al. *Chem. Rev.* **2007**, *107*, 3904.
5. Srinivasan, S. *Fuel Cells - From Fundamentals to Applications*; Springer: New York, 2006.
6. Grot, W. *Fluorinated Ionomers*; William Andrew Inc.: 2008.
7. Sone, Y.; Ekdunge, P.; Simonsson, D. *J. Electrochem. Soc.* **1996**, *143*, 1254.
8. Alberti, G.; Casciola, M.; Massinelli, L.; Bauer, B. *J. Membr. Sci.* **2001**, *185*, 73.
9. Di Noto, V.; Gliubizzi, R.; Negro, E.; Pace, G. *J. Phys. Chem. B* **2006**, *110*, 24972.
10. Di Noto, V.; Gliubizzi, R.; Negro, E.; Vittadello, M.; Pace, G. *Electrochim. Acta* **2007**, *53*, 1618.
11. Di Noto, V.; Piga, M.; Piga, L.; Polizzi, S.; Negro, E. *J. Power Sources* **2008**, *178*, 561.
12. Di Noto, V.; Lavina, S.; Negro, E.; Vittadello, M.; Conti, F.; Piga, M.; Pace, G. *J. Power Sources* **2009**, *187*, 57.
13. Vittadello, M.; Negro, E.; Lavina, S.; Pace, G.; Safari, A.; Di Noto, V. *J. Phys. Chem. B* **2008**, *112*, 16590.
14. Alberti, G.; Casciola, M. *Annu. Rev. Mater. Res.* **2003**, *33*, 129.
15. Yang, C.; Srinivasan, S.; Bocarsly, A. B.; Tulyani, S.; Benziger, J. B. *J. Membr. Sci.* **2004**, *237*, 145.
16. Bauer, F.; Willert-Porada, M. *J. Membr. Sci.* **2004**, *233*, 141.
17. Song, M. K.; Kim, Y. T.; Hwang, J. S.; Ha, H. Y.; Rhee, H.W . *Electrochem. Solid State Lett.* **2004**, *7*, A127.
18. Tricoli, V.; Nannetti, F. *Electrochim. Acta* **2003**, *48*, 2625.

19. Mauritz, K. A.; Moore, R. B. *Chem. Rev.* **2004**, *104*, 4535.
20. Paddison, S. J.; Bender, G.; Kreuer, K. D.; Nicoloso, N.; Zawodzinski, T. A. *J. New Mater. Electrochem. Syst.* **2000**, *3*, 291.
21. Paddison, S. J.; Reagor, D. W.; Zawodzinski, T. A. *J. Electroanal. Chem.* **1998**, *459*, 91.
22. Lu, Z. J.; Polizos, G.; Macdonald, D. D.; Manias, E. *J. Electrochem. Soc.* **2008**, *155*, B163.
23. Rhoades, D. W.; Hassan, M. K.; Osborn, S. J.; Moore, R. B.; Mauritz, K. A. *J. Power Sources* **2007**, *172*, 72.
24. Di Noto, V.; Piga, M.; Pace, G.; Negro, E.; Lavina, S. *ECS Trans.* **2008**, *16*, 1183.
25. Thayumanasundaram, S.; Piga, M.; Lavina, S.; Negro, E.; Jeyapandian, M.; Ghassemzadeh, L.; Müller, K.; Di Noto, V. *Electrochim. Acta* **2009**, in press.
26. Di Noto, V.; Piga, M.; Lavina, S.; Negro, E.; Yoshida, K.; Ito, R.; Furukawa, T. *Electrochim. Acta* **2009**, in press.
27. Armarego, W. L. F.; Perrin, D. D. *Purification of laboratory chemicals*, 4th ed.; Butterworth-Heinemann: Oxford, 1996; p 19.
28. Di Noto, V.; Vittadello, M.; Zago, V.; Pace, G.; Vidali, M. *Electrochim. Acta* **2006**, *51*, 1602.
29. Furukawa, T.; Yasuda, K.; Takahashi, Y. *IEEE Trans. Dielectr. Electr. Insul.* **2004**, *11*, 65.
30. Beek, L. H. H. Dielectric behaviour of heterogeneous systems. In *Progress in dielectrics*; Birks, J. B., Ed.; Heywood: London, 1969; Vol. 7, pp 69−114.
31. Schönhals, A.; Kremer, F. Analysis of dielectric spectra. In *Broadband Dielectric Spectroscopy*; Kremer, F., Schönhals, A., Eds.; Springer-Verlag: Berlin, 2003.
32. Furukawa, T.; Imura, M.; Yuruzume, H. *Jpn. J. Appl. Phys.* **1997**, *36*, 1119.
33. Di Noto, V.; Vittadello, M.; Greenbaum, S.G.; Suarez, S.; Kano, K.; Furukawa, T. *J. Phys. Chem. B* **2004**, *108*, 18832.

Downloaded by UNIV OF GUELPH LIBRARY on June 21, 2012 | http://pubs.acs.org
Publication Date (Web): April 30, 2010 | doi: 10.1021/bk-2010-1040.ch007

Downloaded by CORNELL UNIV on June 21, 2012 | http://pubs.acs.org
Publication Date (Web): April 30, 2010 | doi: 10.1021/bk-2010-1040.ch008

Chapter 8

Broadband Dielectric Spectroscopic Studies of Nafion®/Silicate Membranes

Mohammad K. Hassan[1,2] and Kenneth A. Mauritz[1,*]

[1]The University of Southern Mississippi School of Polymers and High Performance Materials 118 College Drive, Hattiesburg, Mississippi 39406
[2]Bani Suef University, Faculty of Science, Chemistry Department, Bani Suef, Egypt
[*]Correspondence: The University of Southern Mississippi, School of Polymers and High Performance Materials, 118 College Drive, Hattiesburg, Mississippi 39406. E-mail: kenneth.mauritz@usm.edu.

Nafion®/silicate nanocomposite membranes were prepared using *in situ* sol-gel reactions for tetraethylorthosilicate in pre-hydrated and methanol-swollen acid films. Chemical bonding in incorporated silicate nanostructures was characterized using ATR-FTIR and broadband dielectric (BDS) spectroscopies. BDS examined chain dynamics and approximate nature of charge hopping pathways. The behavior of the β relaxation on loss permittivity vs. frequency spectra was investigated. The peak maximum shifted only to somewhat higher frequencies with different silica percent indicating that the silicate component is confined to acid aggregates, not significantly perturbing the main chain. A parameter N obtained from fitting dielectric spectra to the Havriliak-Negami equation adjusted for d.c. conductivity, was used to characterize charge hopping pathways and charge mobility constraints. N showed a broad range suggesting morphological variation with silicate content and increased with temperature.

In Fuel Cell Chemistry and Operation; Herring, A., et al.;
ACS Symposium Series; American Chemical Society: Washington, DC, 2010.

Downloaded by CORNELL UNIV on June 21, 2012 | http://pubs.acs.org
Publication Date (Web): April 30, 2010 | doi: 10.1021/bk-2010-1040.ch008

Introduction

The general morphology of unmodified Nafion® in acid and cation-exchanged forms consists of aggregates of the long SO_3H-terminated perfluoralkylether sidechains in a perfluorocarbon matrix with relatively low degree of crystallinity (*1*). Quasi-order exists over the ensemble of clusters where inter-cluster spacings are ~ 3-5 nm according to small angle x-ray scattering (SAXS) and small angle neutron scattering investigations as well as high resolution TEM and AFM studies (*2*).

Mauritz et al. exploited the polar/nonpolar nanophase-separated morphologies of Nafion® perfluorosulfonic acid membranes as interactive templates that direct the location of *in situ* sol-gel hydrolysis → condensation polymerizations of inorganic alkoxides and organoalkoxysilanes that result in metal oxide or organically modified silicate nanophases (*3*, *4*). The dispersion of high surface/volume, intimately-incorporated inorganic phases can cause material synergism relative to the properties of each component in their pure bulk states.

Spectroscopic, microscopic, x-ray scattering, thermal, mechanical tensile, dynamic mechanical, dielectric relaxation and gas permeation tools were employed to interrogate the structures and properties of these heterogeneous materials.

Here, modern broadband dielectric spectroscopy (BDS) was used to interrogate molecular dynamics in these hybrids. This is a powerful tool because motional processes that occur over broad time and distance scales can be investigated vs. temperature (*5*). In addition to polymer relaxations, significant differences in dielectric permittivity and electrical conductivity across phase boundaries can cause a relaxation of interfacial polarization (*6*).

Dielectric spectroscopy deals with the interaction of an applied alternating electric field with the orientable dipoles on a polymer that account for overall polarizability. Conformational fluctuations on different distance scales affect dipole reorientation and the long range chain segmental mobility that is affected at the glass transition is a cooperative process.

The dielectric spectrum of an amorphous polymer generally shows multiple relaxations at different temperatures, where each relaxation is indicated by a peak in loss permittivity ε'' and an associated step decrease in storage permittivity (ε') versus frequency at a fixed temperature.

This work reported here involves the influence of sol-gel imparted silicate structures, grown within the hydrophilic sulfonic acid domains of Nafion®, on the dynamics of chain motions and possible polarization at the interface between hydrophobic and hydrophilic domains.

Downloaded by CORNELL UNIV on June 21, 2012 | http://pubs.acs.org
Publication Date (Web): April 30, 2010 | doi: 10.1021/bk-2010-1040.ch008

Experimental

Materials and Nafion®/Silicate Hybrid Preparation

Nafion® 112 films (1100 equivalent weight, 2 mil thick) were obtained from E.I. DuPont Co. To remove impurities, membranes were cleaned in refluxing 8M HNO_3 for 2h, rinsed three times with deionized water, and then boiled in deionized water for 1h. Films were then dried at 70° C under vacuum for 24h.

Nafion®/silicate nanocomposites were prepared by swelling films in methanol/water (3:1 vol/vol) for one day. Tetraethylorthosilicate (TEOS)/ methanol solution (3:1 vol/vol) was then added in the mole ratio H_2O/TEOS = 4:1. Different silicate uptake percents were achieved by varying the time between adding TEOS/methanol and the removal of the sample from this mixture, which is referred to as 'permeation time'. Upon removal from the solutions, the films were surface-blotted dry and finally placed under vacuum for 24h at 100° C to remove trapped volatiles as well as to promote further silicon oxide network condensation. The percent weight uptakes, relative to the initial dry acid form, for the final dried-annealed samples vs. permeation time used were comparable to those reported for earlier similar nanocomposite preparations (*6–8*).

After *in situ* sol-gel processes, samples were stored in a humidity chamber at 18% RH for at least 4d prior to dielectric testing.

Fourier Transform Infrared Spectroscopy (FTIR)

FTIR was used to identify silicate structures formed within Nafion® polar clusters. Absorption spectra for modified and unmodified films were obtained using a Bruker Equinox 55 FTIR optical bench. The attenuated total reflectance (ATR) technique was used on the same films which were used for the AFM and BDS measurements. ATR-FTIR spectra were produced using a SensIR 3-Reflection horizontal ATR module. The crystals were composed of ZnSe/Diamond composite materials. All spectra were collected after 32 scans with 4 cm^{-1} resolution. A background spectrum of the crystal was substracted from each spectrum obtained for the samples. At least 8 spectra were obtained at different locations of the same sample and averaged.

Dielectric Spectroscopy Experiments

Dielectric spectra were collected isothermally using a Novocontrol GmbH Concept 40 Broadband Dielectric Spectrometer over the frequency range 0.1 Hz - 3 MHz and temperature range of -130 to +200° C. Temperature stability was controlled to within ±0.2° C. Membrane sample discs of 2 cm diameter covered with two aluminum sheets on both sides were sandwiched between two gold-coated copper electrodes of 2 cm diameter and then transferred to the instrument for data collection.

Downloaded by CORNELL UNIV on June 21, 2012 | http://pubs.acs.org
Publication Date (Web): April 30, 2010 | doi: 10.1021/bk-2010-1040.ch008

The data is represented in terms of the real and imaginary permittivities, ε' and ε'', respectively.

Each dielectric experiment consisted of frequency sweep iterations at 70° C for 5.3h followed by iterations for temperatures from -130 to 200° C in 10° C increments. This procedure allows for more data reproducibility for different pieces of the same film for each sample.

Results and Discussion

FTIR spectroscopy can probe the degree of intramolecular connectivity in silicate, metal oxide and organically-modified silicate nanophases. In order to isolate silicate fingerprint bands by excluding interfering Nafion® bands, the spectrum of an unfilled membrane was subtracted from that of the composite and the result is shown in Figure 1. Owing to the large absorbance of Nafion® films of usual thickness, the ATR mode must be used. It must be realized that FTIR-ATR only probes around 1 μm beneath the surface so that spectra may differ somewhat from that in the middle of the specimen.

It was seen in earlier work that for pure sol-gel-generated silicate nanophases in Nafion®, difference spectra depicted a network that grows to be increasingly less branched, i.e., less intra-connected in terms of Si-O-Si links, with progressively fewer cyclic molecular substructures and more linearity (*3*, *8*, *9*). This is also the case for the sample with 34% silica in Figure 1. These being acid-catalyzed reactions, there is a large fraction of ≡SiOH groups distributed throughout these nanoparticles which is increasingly the case in proceeding outward toward their surfaces. The concept of "surface" becomes blurred with regard to particles whose granularity exists on the level at which individual atoms are seen. These structures are more accurately described as hyperbranched.

The peak for asymmetric stretching vibration in Si-O-Si groups (~1000-1100 cm^{-1}) verifies and quantifies the extent of *in situ* condensation reactions. Moreover, the Si-O-Si band splits into two components corresponding to Si-O-Si groups in cyclic and linear molecular substructures so that the linear/cyclic absorbance ratio, A_{linear}/A_{cyclic}, is a measure of molecular connectivity. The Si-OH stretching vibration peak (~960 cm^{-1}) is a fingerprint of uncondensed SiOH groups and these are hydration sites (*4*).

Dielectric Relaxation Spectral Behavior of Film Samples

Acid form Nafion® exhibits signatures of its characteristic polymer motions as crests on $\varepsilon'' - f$ - T 'response surfaces' as seen in Figure 2. Two major motions are observed: the β relaxation with onset at 0° C and the α relaxation with onset at ~80° C. The β relaxation is attributed to the onset of segmental motions along the backbone within an electrostatic network and is thought to be the glass transition of Nafion® (*6*). The α relaxation is attributed to the onset of long range mobility of chains/sidechains as a result of destabilization of the electrostatic network (chain

Downloaded by CORNELL UNIV on June 21, 2012 | http://pubs.acs.org
Publication Date (Web): April 30, 2010 | doi: 10.1021/bk-2010-1040.ch008

motions within a dynamic electrostatic network). The chain motions of the α relaxation involve a significant contribution from ion-hopping processes that may influence high temperature conductivity. At temperatures above the α relaxation, significant morphological reorganization may occur. The nature of the β relaxation and how it is affected by incorporated silica will be discussed.

Figure 3 shows ε'' vs. f at 60 °C for films with different silica loading. The β relaxation peak maxima for 6 and 10% silica increased by a small amount to higher frequencies to higher frequencies (shorter relaxation time) with silica insertion. The peak for 34% shifts downward, i.e., the relaxation is suppressed, and a shoulder on the higher f side.

In the low f region, changes in ε'' can be directly correlated with d.c. conductivity, σ_{dc}, according to the following equation:

$$\varepsilon'' \approx \sigma_{dc} / 2\pi f \varepsilon_0 \qquad (1)$$

ε_0 = vacuum permittivity. In this frequency region for $T > T_g$, log ε'' vs. log f plots are linear such that the slopes are slightly less than 1.0 (*10*). This feature is the signature of d.c. conductivity.

d.c. conductivity in this context involves the instrumental sampling of charge hopping pathways that become progressively longer at increasingly lower frequencies. As the experimental time scale, or half period of oscillation = $(2f)^{-1}$, increases, charge carriers, likely protons in this case, can execute more elementary hops before the applied field reverses.

The ε'' curve at low f initially elevates slightly with increased silica content then drops considerably for the sample with highest silica loading. This large drop could be explained in terms of decreasing d.c. conductivity, according to equation 1, due to trapping protons in $-SO_3H$ groups within silica cages at this high silica content.

All hybrids as well as the unfilled control, display very high values of the storage permittivity, ε', in the low frequency regime as shown in Figure 4. These values are too large to be accounted for by simple dipole reorientation. Two possibilities accounting for this phenomenon are as follows. First, there could be membrane|blocking electrode interfacial polarization relaxation that causes a capacitive layer in these regions. This mechanism can be represented by an ε'' vs. f peak with a characteristic relaxation time (*11*). Such peaks, or curve downturns at the lowest frequencies are not seen in Figure 3, although they may be off-scale.

Another mechanism involves internal (bulk) interfacial polarization relaxation in the form of accumulation ↔ dissipation of charges at interfaces between the clusters and perfluorocarbon phase owing to differences in dielectric contrast and charge mobility gradients across the phase boundaries. This phenomenon is referred to as the Maxwell-Wagner-Sillars effect (*12–14*).

Permittivity data were fitted to the Havriliak-Negami (HN) equation with an added d.c. contribution term (*15–17*).

In Fuel Cell Chemistry and Operation; Herring, A., et al.;
ACS Symposium Series; American Chemical Society: Washington, DC, 2010.

Downloaded by CORNELL UNIV on June 21, 2012 | http://pubs.acs.org
Publication Date (Web): April 30, 2010 | doi: 10.1021/bk-2010-1040.ch008

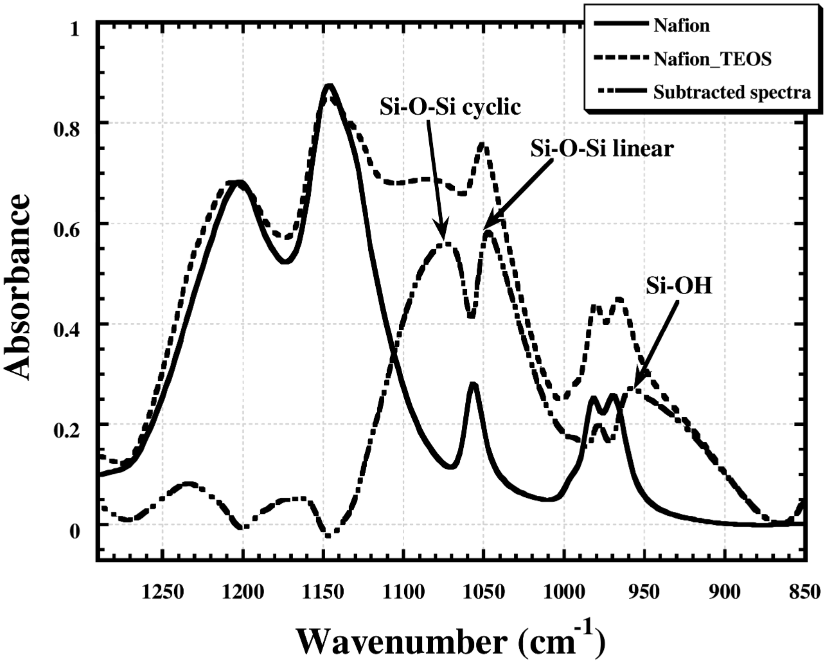

Figure 1. ATR-FTIR difference spectra (Nafion®/silicate - dry unfilled Nafion®) for sample with 34% silica loading.

$$\varepsilon^*(\omega)=\varepsilon'(\omega)-i\varepsilon''(\omega)=-i\left(\frac{\sigma_0}{\varepsilon_0\omega}\right)^N+\sum\left[\frac{\Delta\varepsilon}{\left(1+(i\omega\tau_{HN})^\alpha\right)^\beta}+\varepsilon_\infty\right] \qquad (2)$$

$\Delta\varepsilon_k$ = $(\varepsilon_R$ - $\varepsilon_\infty)_k$ = difference between the real permittivities (ε') at very low and very high frequencies, respectively for the *k*th relaxation; ε_0 = vacuum permittivity; τ_{HN}= Havriliak-Negami relaxation time; α and β ($0 < \alpha < 1$, $\alpha\beta \leq 1$) quantify the breadth and asymmetry for the *k*th distribution of relaxation times. σ_0 = d.c. conductivity. The exponent *N* characterizes the conduction process as explained later. σ_0, *N*, τ_{HN}, $\Delta\varepsilon$, α, and β are treated as free variables extracted by fitting the HN equation to permittivity spectra. Curve fitting was performed using the WinFit program (Novocontrol). τ_{HN} is related to $\tau_{\max}$ by the equation (*ref. (5), p 64*):

$$\tau_{\max} = \tau_{HN}\left[\frac{\sin\left(\frac{\pi\alpha\beta}{2(\beta+1)}\right)}{\sin\left(\frac{\pi\alpha}{2(\beta+1)}\right)}\right]^{\frac{1}{\alpha}} \qquad (3)$$

Note that $\tau_{HN} = \tau_{\max}$ when β=1.

Downloaded by CORNELL UNIV on June 21, 2012 | http://pubs.acs.org
Publication Date (Web): April 30, 2010 | doi: 10.1021/bk-2010-1040.ch008

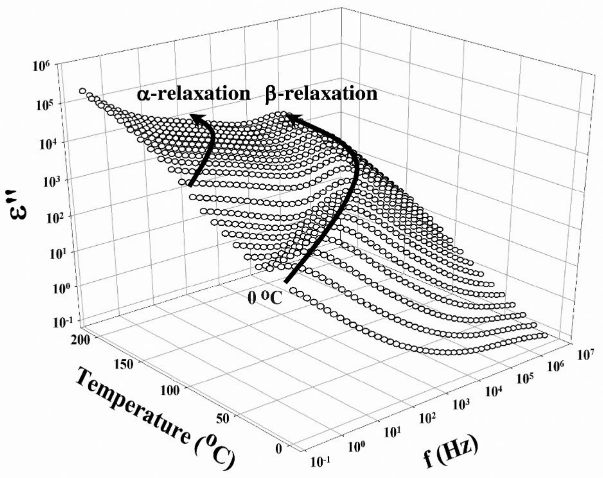

Figure 2. ε" – f - T surface for a Nafion® acid film. Curves are spaced at 10° C increments from the onset of the β relaxation up to 200°. Arrows show crests of peaks on the surface

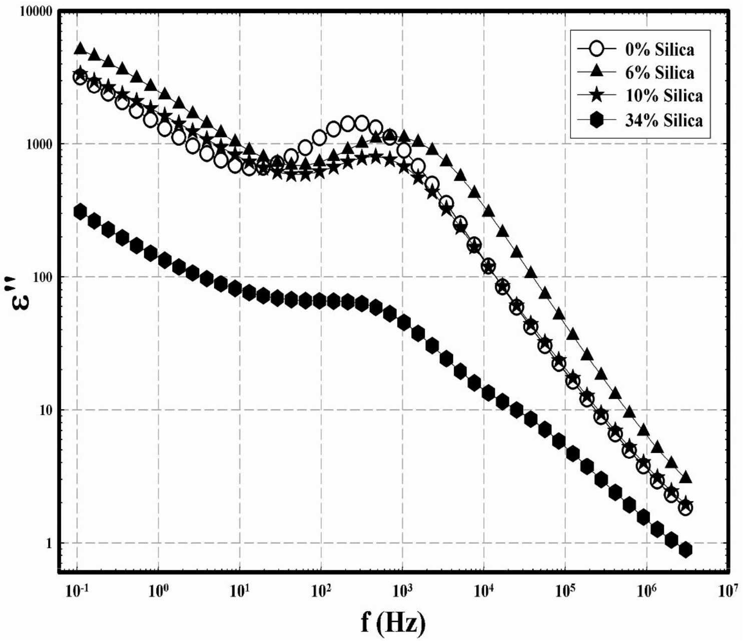

Figure 3. ε" vs. f at 60 ° C for films with different silica loading compared to an unmodified Nafion® control sample.

The first term in equation 2 accounts for d.c. conductivity loss that is often subtracted from the spectrum for the purpose of uncovering loss peaks corresponding to macromolecular motions. This subtraction is especially

Downloaded by CORNELL UNIV on June 21, 2012 | http://pubs.acs.org
Publication Date (Web): April 30, 2010 | doi: 10.1021/bk-2010-1040.ch008

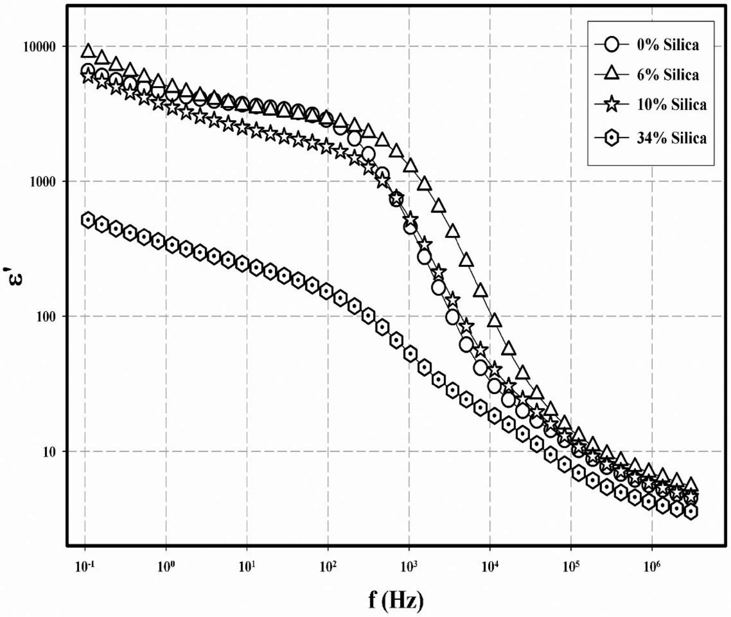

Figure 4. Dielectric storage permittivity vs. f at 60 ° C for films with different silica loading compared to an unmodified Nafion® control sample.

necessary to resolve relaxation times at temperatures approaching T_g at which d.c. conduction becomes stronger (*18*).

d.c. – subtracted loss spectra for samples with different silica loadings, as well as for untreated Nafion®, are shown in Figure 5. Subtraction of the d.c. contribution causes the peaks to be more distinct and their shift to higher frequencies (shorter relaxation times) with change in silica content is seen with more clarity and precision. The curves show an excellent fit of the HN equation to the data points.

Given that the β relaxation involves chain segmental motions and the relaxation times do not greatly change, as seen in Table I at 70° C, it might be concluded that this is indirect evidence that the silicate structures are largely confined to the acid-terminated sidechain aggregate domains.

There is a high frequency shoulder for the sample with 34% silica whose origin is unknown. It is offered in the realm of speculation that this could be due to a cluster/matrix relaxation of interfacial polarization mechanism owing to the large volume fraction of the inorganic phase (*6*). Clusters in the Nafion®/silicate hybrid contain numerous ≡SiOH groups. It is conceivable that protons from $-SO_3H$ groups can hop along hydrogen bonding pathways within hydration structures bound to ≡SiOH groups. Moreover, the clusters are close enough, specially in the case of the sample with 34% silica, so that energetic barriers for intercluster proton hopping would be low. Certainly, this suggestion needs to be verified.

In the first term in equation 3, the exponent $0 < N \leq 1$ characterizes the conduction process in terms of the nature of charge hopping pathways and charge

Downloaded by CORNELL UNIV on June 21, 2012 | http://pubs.acs.org
Publication Date (Web): April 30, 2010 | doi: 10.1021/bk-2010-1040.ch008

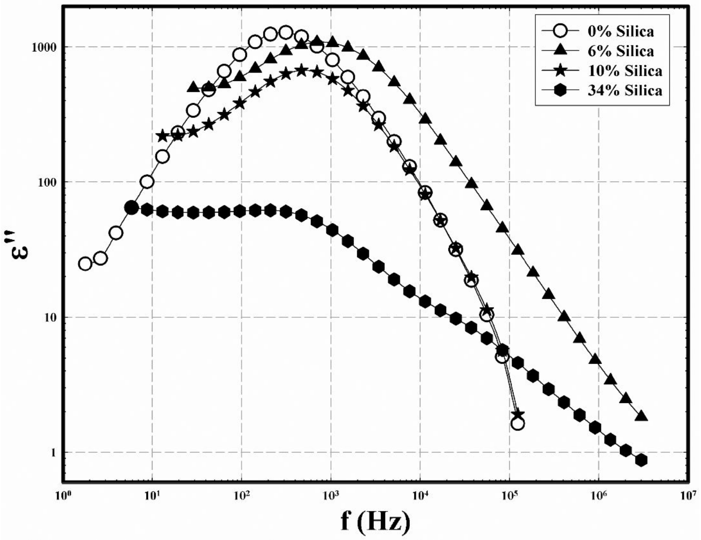

Figure 5. log ε'' vs. log f at 60 ° C for samples with various silica contents as well as unmodified Nafion® with d.c. conductivity contribution subtracted.

Table I. Relaxation times at 70° C for samples with various silica contents as well as unmodified Nafion® calculated from the Havriliak-Negami equation fitted spectra with subtraction of the d.c. conductivity contribution

Sample	*Relaxation time (s)*
0% Silica	5.43×10^{-4}
6% Silica	1.97×10^{-4}
10% Silica	3.18×10^{-4}
34% Silica	6.11×10^{-4}

mobility constraints. *N* might be considered as a rough index of morphological "texture", or charge network topology, over an array of polar clusters and the degree to which they are connected as earlier discussed (*19–24*).

Fitted values of *N* were plotted against temperature for different samples as shown in Figure 6. In principle, $N = 1$ corresponds to an 'ideal' textbook conductor wherein contiguous charge pathways span the entire sample dimensions and charge drift is dominant over random hopping. $N < 1$ indicates charge traps or dead ends on the conductivity grid and $N = ½$ is suggestive of random hopping. It is seen that, overall, the degree of charge pathway connectedness increases because *N* decreases and this, in turn, is related to the degree of morphological order and polymer dynamics in the membrane.

For any of the membrane silicate compositions as well as unmodified Nafion® the range of *N* is broad, being between 0.2 and 1.0. This is indicative of considerable charge network topology variance with temperature and might be thought of as being generated by more rapid macromolecular motions as well as morphological shifting due to transitions. The unfilled acid membrane has an overall downward trend in *N* until around 114° C – which is around the region of the α transition for this form - followed by a large upward step, after which *N* increases monotonically. A downturn in *N*, in any case, with increasing temperature, might reflect gradual disruption of proton-conductive pathways by thermal agitation of polymer chains.

Even the highest *N* values for the composite membranes, at ~ 0.45 below 100° C, are more reflective of approximate diffusion control and tortuous pathways than of unimpeded long range charge drift.

It might be imagined that, while increased charge mobility is affected on a local level (H^+ hopping within SO_3^- aggregates) with increased temperature, more long-range structural disorder might also be imparted such that morphology becomes less ordered causing *N* to decrease.

For temperatures beyond the β relaxation (> 100° C), *N* for unmodified Nafion® undergoes a sharp rise to being somewhat greater than values for all hybrid membranes. The jump in *N* correlates with the onset of the α transition which is ascribed to an ion-hopping mechanism. Thereafter, *N* continues to increase with increase in temperature. The hybrids undergo a rise in *N* over this range, as well.

For the silicate filled samples, in the 80-100° C range, *N* rises at an earlier temperature and the values are higher than that of pure Nafion®. Perhaps this is due to the inserted hyperbranched silicate particles that structure continuous hydrogen-bonded water molecule pathways along which protons can migrate. *N* continues to increase with temperature as the pathways possibly become more extensive and interknitted. Different values for different silicate contents reflect the formation of different degrees of connectivity of proton-conductive pathways owing to different abilities to structure hydrogen bonded water molecules. The above interpretations are offered in the realm of speculation.

Conclusions

Nafion®/silicate nanocomposite membranes were produced via *in situ* sol-gel reactions for TEOS in pre-hydrated and methanol-swollen perfluorosulfonic acid films. ATR-FTIR spectra of nanocomposites indicated uncondensed ≡SiOH and Si-O-Si groups, the latter being a sign of successful chemical bond formation, the former being hydration sites. The Si-O-Si band splits into two components corresponding to groups in cyclic and linear molecular substructures.

Polymer chain dynamics and the nature of charge hopping pathways in these membranes were examined using broadband dielectric spectroscopy. The β relaxation signature on dielectric loss permittivity vs. frequency spectra of samples was investigated. The β loss peak maximum shifted to somewhat higher frequencies with different silica percents which might indicate that the silicate phase is confined to the acid aggregates and not perturbing the main chain to a large degree.

Downloaded by CORNELL UNIV on June 21, 2012 | http://pubs.acs.org
Publication Date (Web): April 30, 2010 | doi: 10.1021/bk-2010-1040.ch008

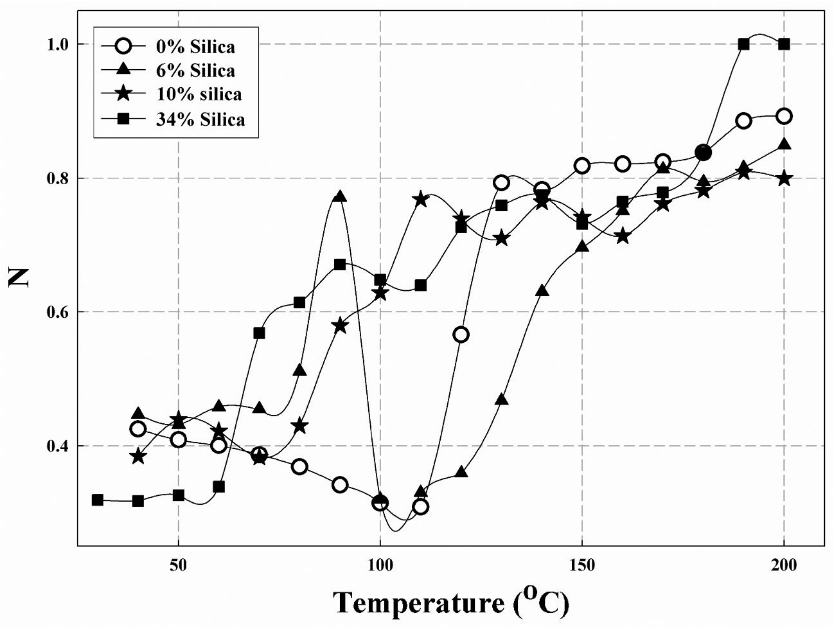

Figure 6. N vs. temperature for Nafion® and Nafion®/silicate membranes.

There is the signature of inter-cluster hopping of protons on dielectric loss spectra in all cases and a parameter *N*, regarded as a coarse degree of connectivity of proton pathway networks, was derived. The observed range of *N* over the range of temperature is broad suggesting considerable morphological differentiation with silicate content and increasing trends in *N* with temperature – reflective of better-developed charge pathways, are seen.

It concluded that broadband dielectric spectroscopy is a potentially powerful tool in the interrogation of polymer and charge motions in Nafion®/inorganic oxide structures.

Acknowledgments

The authors gratefully acknowledge The DOE Office of Energy Efficiency and Renewable Energy; contract # DE-FG36-08GO88106 for financial support.

References

1. Shchipunov, Y. A.; Karpenko, T. Y.; Krekoten, A. V. *Compos. Interfaces* **2005**, *11*, 587.
2. Mauritz, K. A.; Moore, R. B. *Chem. Rev.* **2004**, *104*, 4535.
3. Mauritz, K. A. *Mater. Sci. Eng.* **1998**, *C6*, 121.
4. Mauritz, K. A.; Hassan, M. K. *Polym. Rev.* **2007**, *47*, 1.

Downloaded by CORNELL UNIV on June 21, 2012 | http://pubs.acs.org
Publication Date (Web): April 30, 2010 | doi: 10.1021/bk-2010-1040.ch008

5. Kremer, F.; Schönhals, A. *Broadband Dielectric Spectroscopy*; Springer: Berlin, 2003; p 225.
6. Mauritz, K. A.; Stefanithis, I. D. *Macromolecules* **1990**, *23*, 1380.
7. Mauritz, K. A.; Storey, R. F.; Jones, C. K. *Multiphase Polymer Materials: Blends, Ionomers and Interpenetrating Networks*; Utracki, L. A., Weiss, R. A., Eds.; ACS Symposium Series 395; American Chemical Society: Washington, DC, 1989; Chapter 16.
8. Mauritz, K. A.; Warren, R. M. *Macromolecules* **1989**, *22*, 1730.
9. Deng, Q.; Moore, R. B.; Mauritz, K. A. *Chem. Mater.* **1995**, *7*, 2259.
10. McCrum, N. G.; Read, B. E.; Williams, G. *Anelastic and Dielectric Effects in Polymeric Solids*; Dover: New York, 1991.
11. Klein, R. J.; Zhang, S.; Dou, S.; Jones, B. H.; Colby, R. H.; Runt, J. *J. Chem. Phys.* **2006**, *124*, 144903.
12. Maxwell, J. C. *Electricity and Magnetism I*, 3rd ed.; Oxford University: London, 1892.
13. Wagner, K. W. *Arch. Elektrotech. Berlin* **1914**, *2*, 371.
14. Sillars, R. W. *Proc. R. Soc. London, Ser. A* **1939**, *169*, 66.
15. Havriliak, S.; Negami, S. *J. Polym. Sci.: Polym. Symp.* **1966**, *14*, 99.
16. Havriliak, S.; Negami, S. *Polymer* **1967**, *8*, 161.
17. Negami, S.; Ruch, R. J.; Myers, R. R. *J. Colloid Interface Sci.* **1982**, *90*, 117.
18. Zhang, S.; Painter, P. C.; Runt, J. P. *Macromolecules* **2004**, *37*, 2636.
19. Mauritz, K. A. *Macromolecules* **1989**, *22*, 4483.
20. Mauritz, K. A.; Fu, R-M. *Macromolecules* **1988**, *21*, 1324.
21. Deng, Z. D.; Mauritz, K. A. *Macromolecules* **1992**, *25*, 2369.
22. Mauritz, K. A.; Yun, H. *Macromolecules* **1989**, *22*, 220.
23. Mauritz, K. A.; Yun, H. *Macromolecules* **1988**, *21*, 2738.
24. Deng, Z. D.; Mauritz, K. A. *Macromolecules* **1992**, *25*, 2739.

Downloaded by CORNELL UNIV on June 21, 2012 | http://pubs.acs.org
Publication Date (Web): April 30, 2010 | doi: 10.1021/bk-2010-1040.ch008

Downloaded by UNIV OF DELAWARE MORRIS LIB on June 21, 2012 | http://pubs.acs.org
Publication Date (Web): April 30, 2010 | doi: 10.1021/bk-2010-1040.ch009

Chapter 9

Chemical Durability Studies of PFSA and Nonfluorinated PEM Materials

David A. Schiraldi,*,[1,2] Chun Zhou,[1] Deepa Savant,[1] and Thomas A. Zawodzinski Jr.[1,2]

[1]Department of Macromolecular Science and Engineering, Case Western Reserve University, Cleveland, OH 44106
[2]Department of Chemical Engineering, Case Western Reserve University, Cleveland OH, 44106
***das43@case.edu**

Small molecule model compounds can be used to understand oxidative degradation of fuel cell membranes under simulated operating conditions. Using models of perfluorinated membrane polymers, the degradation of carboxylic acid end groups on the polymer chains is supported, as in radical cleavage of perfluorinated ether side chains. Trapping experiments further support the location of ether side chain cleavage. Initial work with non-perfluorinated model compounds is encouraging, and will hopefully allow for discrimination of different aromatic membrane polymers without lengthy synthetic and testing programs.

Introduction

The broad, commercial implementation of fuel cells will of course be largely decided on economic issues. Whether hydrogen, methanol or other fuel-based fuel cells are in fact deemed to be economically competitive will decided by energy costs in the marketplace, and by the costs of technology. To this latter point it will be important to understand how best to deploy expensive catalyst metals, and how to optimize and prolong the lifetime of fuel cell components. In the specific case of polymer electrolyte membrane (PEM) fuel cells, maximizing the lifetime of expensive, polymeric membrane will be a key to technological and economic success. These PEM membranes are typically produced by solution casting of perfluorinated ionomers, such as DuPont's Nafion® material, and the shorter side-chain alternative material of 3M (Figure 1).

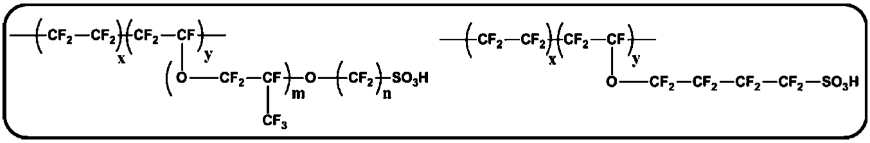

Figure 1. Nafion® (left) and 3M ionomer (right).

The membranes in question serve the dual purposes of separating oxidizing gas (air or oxygen) and fuel, and transporting both the protons and water necessary for charge and mass balance during operation of the cell. Any breach in these membranes will serve as a short circuit leading rapidly to cell death. The structural features of Nafion® have been the subject of numerous papers, which are well summarized in a recent review (*1*). The subject of PEM durability has also been reviewed, and is both an interesting and controversial topic (*2*). In addition to disagreements as to the mechanism of chemical degradation of the perflorinated ionomers, important operational considerations, such as cyclic and catastrophic changes in membrane hydration (with accompanying changes in physical size due to swelling), migration of corrosion metals throughout the systems, and electrical load cycling (*3*–*6*).

The use of non-perfluorinated membrane polymers in fuel cells is a more recent development, driven by the synthetic work of McGrath and others (*7*, *8*). The durability of this broad family of sulfonated poly(aryl sulfones), poly(aryl ethers) and other aromatic-rich materials has been speculated upon, but neither well evaluated in operating fuel cells nor scrutinized by mechanistic studies.

The present work is our attempt to bring order and mechanistic understanding to chemical degradation of both the perfluorinated sulfonic acid (PFSA) and non-fluorinated PEM materials under conditions which can reasonably be considered as mimicking fuel cell operating conditions (*9*, *10*). The approach that we have taken is to incubate small molecule model compounds in the presence of hydroxyl radicals, analyzing the rates of by-product production, and the composition of these degraded substances. The use of such model compounds allows for the tools of the organic chemist to be applied to this problem, whereas similar changes to large molecules, especially to the largely intractable, (and in the case of PFSAs) poorly characterized starting polymers is extraordinarily difficult and fraught with inaccuracy. Two key assumptions in the model compound approach are that the small molecules do in fact faithfully model reactivity patterns of those polymers they intend to mimic, and that the production of hydroxyl radicals, whether generated using Fenton's reagent (*11*) or via UV photolysis of hydrogen peroxide, are in fact a meaningful representation of operating fuel cell chemical degradation. To the best of our knowledge, and without significant disagreement from the literature, we believe that this approach should provide useful guidance to the field.

Downloaded by UNIV OF DELAWARE MORRIS LIB on June 21, 2012 | http://pubs.acs.org
Publication Date (Web): April 30, 2010 | doi: 10.1021/bk-2010-1040.ch009

Downloaded by UNIV OF DELAWARE MORRIS LIB on June 21, 2012 | http://pubs.acs.org
Publication Date (Web): April 30, 2010 | doi: 10.1021/bk-2010-1040.ch009

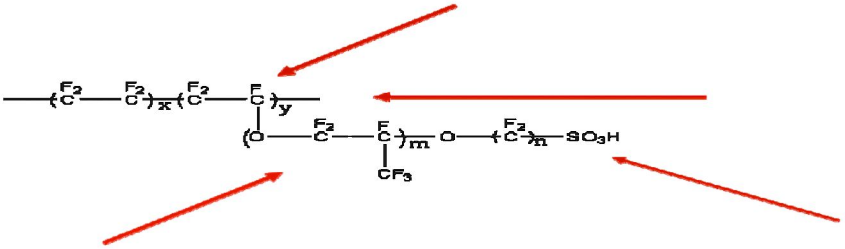

Figure 2. Potential sites of radical attack on Nafion®.

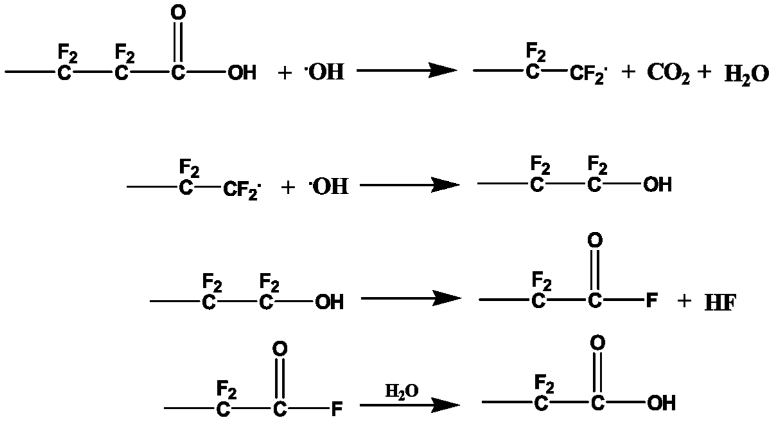

Figure 3. Chain end attack mechanism for PFSA membranes.

PFSA Model Studies

The perfluorinated sulfonic acid polymers typically employed in PEM fuel cells at the present time provide for a rich set of potential reaction sites for radical species (Figure 2). Peroxy radicals can be generated from the homolysis of hydrogen peroxide, which is a product of incomplete oxidation of hydrogen (and other fuels) with oxygen on platinum and other catalyst metal surfaces (*12*, *13*). Peroxy radicals have been directly observed within operating fuel cells by Roduner and coworkers (*14*). The literature suggests that hydrogen peroxide is present in operating fuel cells in the range of 1-10 ppm (*15*), but this number should be treated cautiously, given that specific operating conditions of the cell will impact its production, that the catalyst metals used to produce them can also reverse that reaction, and that the presence of other ionic species can also significantly alter equilibrium concentrations of peroxide (*16*).

The most commonly-cited mechanism for PFSA membrane degradation relies upon radical attack at carboxylic acid end groups present as unwanted impurities in the polytetrafluoroethylene backbone of the polymers (*17*). Such carboxylic

Downloaded by UNIV OF DELAWARE MORRIS LIB on June 21, 2012 | http://pubs.acs.org
Publication Date (Web): April 30, 2010 | doi: 10.1021/bk-2010-1040.ch009

acid end groups are an artifact of the manufacturing processes used to produce these polymers; the concentration of carboxylic acid groups can be reduced to very low levels using proprietary fluorination processes. Nonetheless, the chain end process (Figure 3) appears to remain an important process even in well-fluorinated polymers. In the chain end attack mechanism, a peroxy radical abstracts a hydrogen atom from the carboxylic acid group. The resultant carboxylate radical can then decarboxylate to produce a terminal alkyl difluoro radical, which then captures a second hydroxide radical. This radical capture produces an unstable perfluorinated alcohol, which is known to eliminate HF, generating a acyl fluoride intermediate which then hydrolyzes in the wet environment of a fuel cell, with the regeneration of a new, one carbon-shorter, carboxylic acid end group. Such a process can proceed down the carbon backbone of the polymer, sequentially eliminating carbon dioxide and HF which is constantly observed during fuel cell operation. A very important observation, however, is that while a linear relationship exists between the polymeric carboxylic acid concentration and the rate of fluoride generation (consistent with the chain end attack), there is a considerable, non-zero intercept in that relationship, demanding that at least one additional mechanism for degradation/fluoride generation be present in these operating systems (*18*).

In order to examine the roles of the chain end attack and other postulated mechanisms in the overall radical degradation of PFSA membranes, a series of model compounds (Figure 4) were subjected to treatment with Fenton's reagent, and to treatment with hydrogen peroxide with UV photolysis (*9*, *10*). The generation of fluoride ions was followed using an ion selective electrode which was shown experimentally to be accurate to 0.05 ppm [F^-] over the range of concentrations of interest here. We also demonstrated that while Fe(II) and pH did not effect the fluoride measurements, Fe(III) did cause the electrode to under-report the actual fluoride concentration. By diluting the samples twenty-fold with deionized water prior to fluoride ion measurement, the interference by Fe(III) was eliminated, while maintaining fluoride in a concentration range which could still be accurately measured (*9*, *10*). The nitrogen sweep through the flask used for Fenton's degradation of model compounds was bubbled through a phenolphthalein solution, which would be acidified by any carbon dioxide generated during degradation. For those model compounds containing carboxylic acid groups, carbon dioxide generation was indeed observed during Fenton's degradations; model compounds lacking carboxylic acid groups did not generate observable changes in the phenolphthalein solution. Typical results of these fluoride measurements are given in Figure 5; from this work, two important lessons were learned:

Lesson 1: MCs containing -COOH react at least one order of magnitude faster than MCs without -COOH.

Lesson 2: MCs without -COOH do react and generate fluoride.

Solutions of model compounds, before and after Fenton's and hydrogen peroxide/UV degradation experiments, were analyzed using liquid chromatography/mass spectroscopy (LCMS) analysis, using a Zorbax Reverse-Phase C18, crosslinked & end-capped column, electrospray ionization/negative ion detector, and (1) water/6 mM ammonium acetate, (2)

Downloaded by UNIV OF DELAWARE MORRIS LIB on June 21, 2012 | http://pubs.acs.org
Publication Date (Web): April 30, 2010 | doi: 10.1021/bk-2010-1040.ch009

95/5 acetonitrile/water/6 mM ammonium acetate elution solvent system. Typical results of LCMS measurements (in this case for MC4) are given in Figure 6. This specific model compound is important in that it closely resembles the carboxylic acid-terminated poly(tetrafluoroethylene) backbone of Nafion® and its 3M competitor, discussed above. True to the chain end degradation mechanism, the LCMS results clearly indicate a sequential loss of CF_2, just as predicted by that proposed pathway, and leading to the third lesson learned in this study:

Lesson 3: Chain end degradation mechanism appears to be valid for -COOH containing MCs.

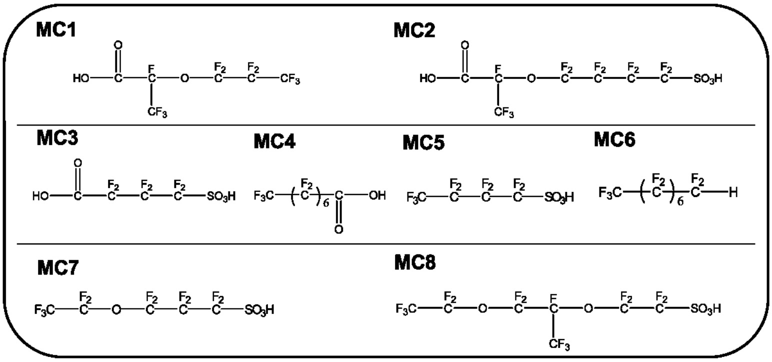

Figure 4. PFSA model compounds.

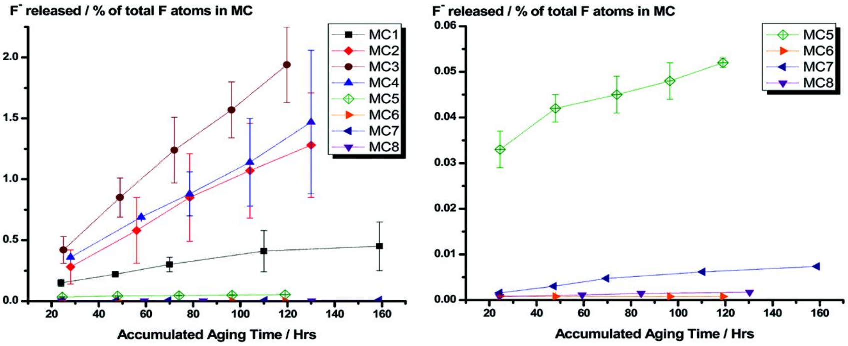

Figure 5. Chain end attack mechanism for PFSA membranes. (Reproduced from reference (9). Copyright 2007 American Chemical Society)

From among the perfluorinated model compounds, radical degradation results of MC8 and MC7 are especially important to this study, in that they directly model the side chain and backbone links of Nafion® and the 3M ionomer, respectively (Figures 7 and 8) (*19*). From these experiments we observed that side chain ether groups were readily cleaved by hydroxyl radicals, a result of direct importance to fuel cell durability concerns. The specific locations of ether cleavage are given in

Downloaded by UNIV OF DELAWARE MORRIS LIB on June 21, 2012 | http://pubs.acs.org
Publication Date (Web): April 30, 2010 | doi: 10.1021/bk-2010-1040.ch009

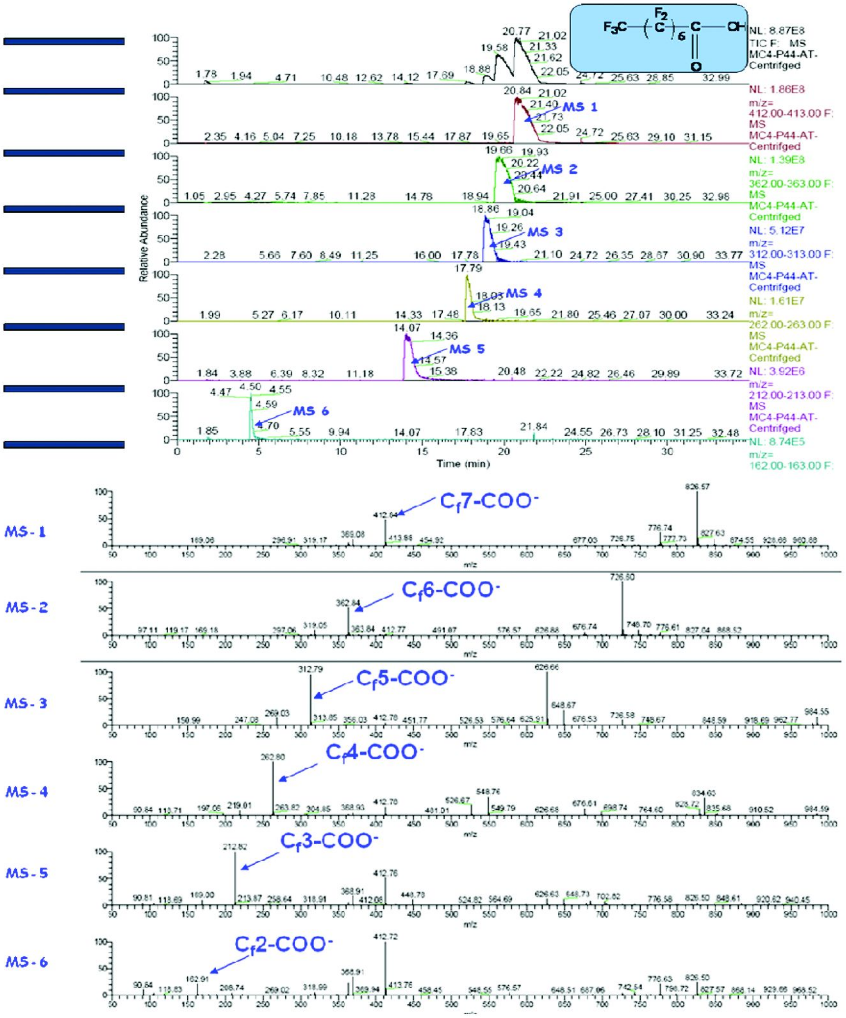

Figure 6. Typical LCMS results (for MC4 in this case). (Reproduced from reference (9). Copyright 2007 American Chemical Society)

the figures, and show that each of the ethers are subject to attack under simulated fuel cell operating conditions, providing another important teaching:

Lesson 4: Small molecule MCs of PFSAs appear to degrade via ether cleavage.

To further confirm the site specificity of radical attack upon PFSA model compounds, Fenton's degradation of those materials was repeted in the presence of the radical trap, 2,2,6,6-Tetramethylpiperidine-1-oxyl (TEMPO). Aliquots of TEMPO were added to the nitrogen-purged flask containing model compounds and Fenton's reagent. Samples were withdrawn by syringe, and injected into the LCMS under the same conditions described above. If the ether cleavage pathways postulated as a result of the initial LCMS work are correct, then it would be

Downloaded by UNIV OF DELAWARE MORRIS LIB on June 21, 2012 | http://pubs.acs.org
Publication Date (Web): April 30, 2010 | doi: 10.1021/bk-2010-1040.ch009

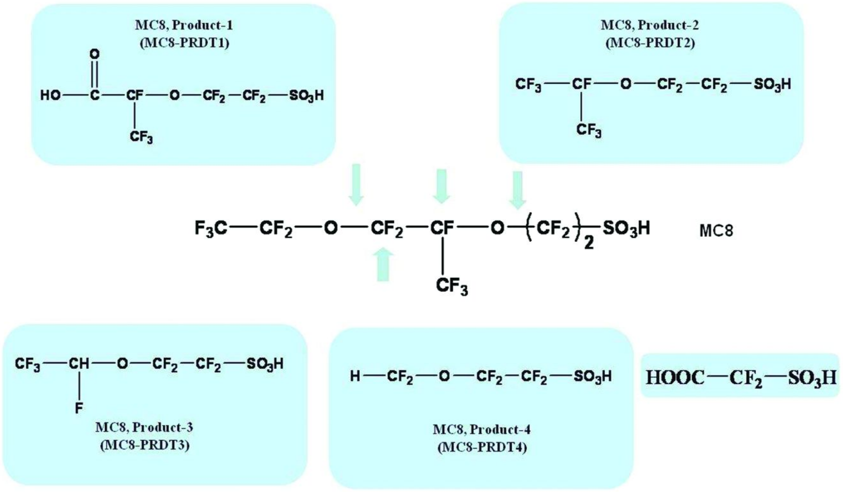
MC8, Product-1
(MC8-PRDT1)
MC8, Product-2
(MC8-PRDT2)
MC8
MC8, Product-3
(MC8-PRDT3)
MC8, Product-4
(MC8-PRDT4)
HOOC—CF2—SO3H

Figure 7. LCMS Results for MC8. (Reproduced from reference (19). Copyright 2009 American Chemical Society).

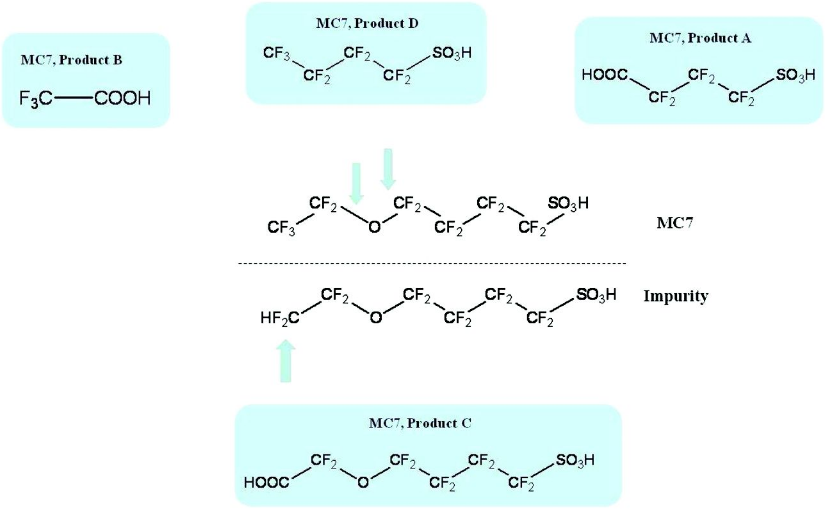
MC7, Product B
MC7, Product D
MC7, Product A
MC7
Impurity
MC7, Product C

Figure 8. LCMS Results for MC7. (Reproduced from reference (19). Copyright 2009 American Chemical Society).

reasonable to expect that molecular fragments resulting from the breaking of carbon-oxygen bonds could be trapped; such potential trapping products with TEMPO and MC8 are given in Figure 9 (*10*, *19*). Results of these trapping experiments, carried out with MC7 and MC8 are summarized in Figure 10, which both confirms the ether cleavages previously proposed, and provides some guidance as to which bonds are preferentially broken. An interesting difference noted between the models of Nafion® and the 3M ionomer is that for the branched

Downloaded by UNIV OF DELAWARE MORRIS LIB on June 21, 2012 | http://pubs.acs.org
Publication Date (Web): April 30, 2010 | doi: 10.1021/bk-2010-1040.ch009

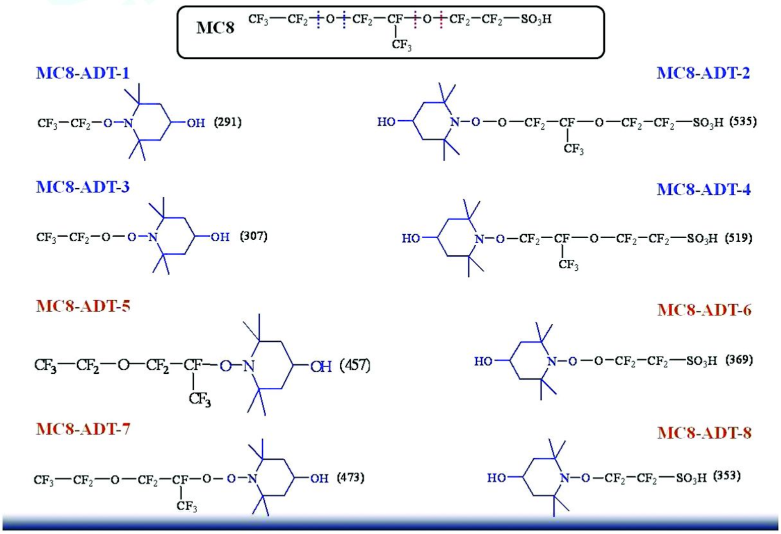

Figure 9. Potential trapping products from MC8. (Reproduced from reference (19). Copyright 2009 American Chemical Society).

side-chain Nafion®, the most prevalent degradation appears to involve breaking the ether link directly next to the branch point, generate a more stable, secondary radical. For the 3M ionomer, which lacks such branch points, the most abundantly trapped product was that which resulted from cleaving the entire side chain from the polymeric backbone. From these trapping experiments, an additional learning was obtained:

Lesson 5: Trapping of MCs during radical degradation supports ether cleavage mechanism.

Armed with these results, polymeric Nafion® and 3M ionomer were treated with Fenton's reagent under condidtions analogous to those used to degrade the model compounds. Two side-chain degradation products were identified as a result of Nafion degradation. Interestingly, contrary to the trapping experiments, degradation products derived from attack at the most highly substituted side-chain carbon were not observed among the ether cleavage products. It is possible that such products were themselves highly reactive and were further degraded and not detected, or that the trapping agent, TEMPO, influenced the mechanistic pathway when present. It is also possible that the weak points in the molecule were protected to some extent by polymer conformations. For the 3M ionomer, the by-product expected from complete side-chain cleavage was obtained, as would have been expected from the TEMPO trapping experiments. Combining these results, additional insights into the mechanism of PFSE membranes can be presented:

Lesson 6: Major decomposition of Nafion / 3M ionomers appears to result from ether/side chain cleavage.

Downloaded by UNIV OF DELAWARE MORRIS LIB on June 21, 2012 | http://pubs.acs.org
Publication Date (Web): April 30, 2010 | doi: 10.1021/bk-2010-1040.ch009

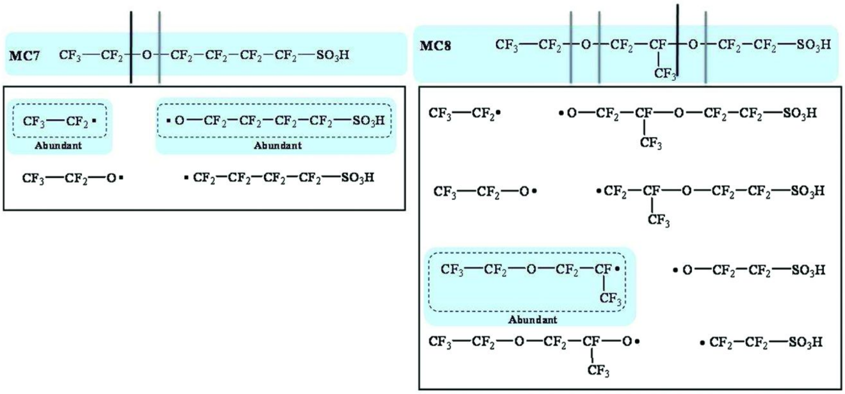
MC7
$CF_3—CF_2—O—CF_2—CF_2—CF_2—CF_2—SO_3H$
$CF_3—CF_2•$
Abundant
$•O—CF_2—CF_2—CF_2—CF_2—SO_3H$
Abundant
$CF_3—CF_2—O•$
$•CF_2—CF_2—CF_2—CF_2—SO_3H$
MC8
$CF_3—CF_2—O—CF_2—CF(CF_3)—O—CF_2—CF_2—SO_3H$
$CF_3—CF_2•$
$•O—CF_2—CF(CF_3)—O—CF_2—CF_2—SO_3H$
$CF_3—CF_2—O•$
$•CF_2—CF(CF_3)—O—CF_2—CF_2—SO_3H$
$CF_3—CF_2—O—CF_2—CF(CF_3)•$
Abundant
$•O—CF_2—CF_2—SO_3H$
$CF_3—CF_2—O—CF_2—CF(CF_3)—O•$
$•CF_2—CF_2—SO_3H$

Figure 10. Trapping experiment results for MC7 and MC8. (Reproduced from reference (19). Copyright 2009 American Chemical Society)

Conclusions from the PFSA Model Compound/Membrane Studies

From the above work with perfluorinated model compounds and membranes, a self-consistent set of conclusions can be reached. It should again be mentioned that while these results are self-consistent, they still are an approximation of what actually occurs within operating fuel cells. With that reminder in place, we note that these conclusions appear to be consistent with all of the published literature in the field that we are aware of, and can be summarized as follows:

1. Carboxylic acid end groups are indeed reactive; results support the unzipping mechanism
2. Non-carboxylic acid MCs appear to degrade *via* a possible -O-CF2- or -O-CF(CF3)- cleavage. These positions in the molecules are not as reactive as -COOH ends (but are available in much higher concentrations).
3. The degradation of Nafion® also appears to include a contribution from side chains cleavage (ether cleavage) under test conditions. The 3M ionomer degrades in a similar manner.
4. We see no evidence for attack on the sulfonic acid groups.

Preliminary Model Studies of Non-Fluorinated PEM Materials

Given the success in using model compound studies with Fenton's reagent, UV photolysis of hydrogen peroxide, and with radical trapping agents, one would expect to be able to conduct similar programs with models of non-perfluorinated PEM polymer candidates. Given the potential for hydrocarbon groups to be oxidized under radical conditions, such examination of broad families of structures could be especially important, and could potentially prevent long synthetic optimization programs which would simply produce oxidatively unstable membranes. Figure 12 illustrates a prototypical non-perfluorinated

Downloaded by UNIV OF DELAWARE MORRIS LIB on June 21, 2012 | http://pubs.acs.org
Publication Date (Web): April 30, 2010 | doi: 10.1021/bk-2010-1040.ch009

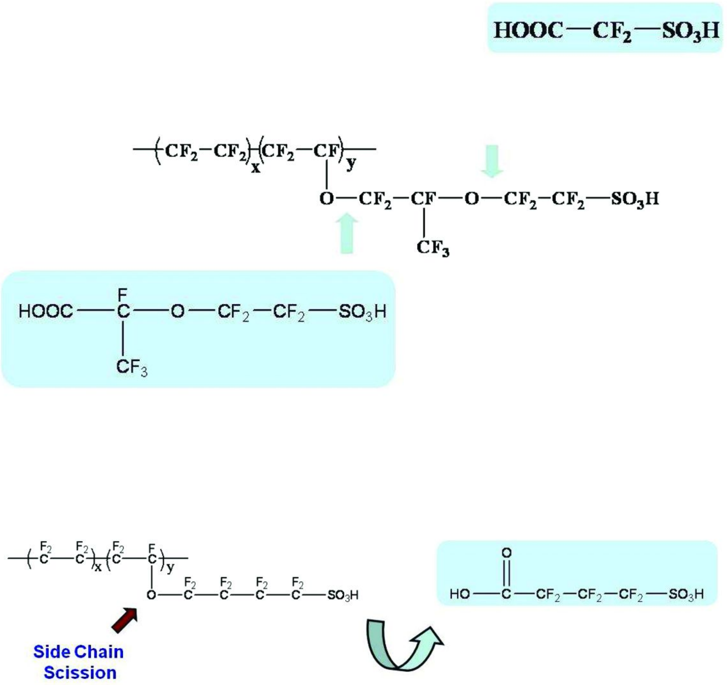

Figure 11. Fenton's degradation results for Nafion® (top) and 3M ionomer (bottom). (Reproduced from reference (19). Copyright 2009 American Chemical Society)

membrane polymer candidate, as well as several aromatic model compounds (AMCs) which could provide insights into different portions of the polymer's structure (*7*, *8*). We then propose to carry out model compound mechanistic studies with such materials, analogous to those presented with PFSA compounds above. It needs to be pointed out that in the absence of sulfonation, many such AMCs will not possess sufficient solubility in aqueous Fenton's reagent to provide useful insights into degradation mechanisms under homogeneous conditions. These samples would need to either be subjected to two-phase degradation, be sulfonated then homogeneously degraded, or be treated with hydroxyl radicals in non-aqueous or mixed solvent conditions. All of these approaches are currently being examined in our group. Preliminary results for the simplest of the AMCs, one that is water soluble, are illustrated in Figure 13. For this initial model compound, benzene sulfonic acid, we observe sequential hydroxylation of the aromatic ring, no evidence for ring cleavage, and no carbon dioxide generation when treated with Fenton's reagent under conditions analogous to those used with the perfluorinated model compounds. These preliminary results are consistent with a literature report (*20*) and are encouraging, as aromatic hydroxylation, if this proves to be a pattern with aromatic membrane polymers, could well be less damaging than cleavage of perfluorinated side chains in the current generation of PEM membrane polymers.

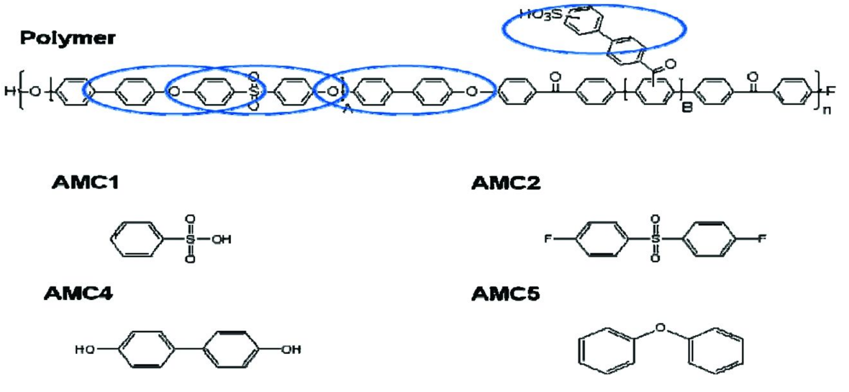

Figure 12. Prototypical non-perfluorinated PEM membrane polymer and associated aromatic model compounds (AMCs)

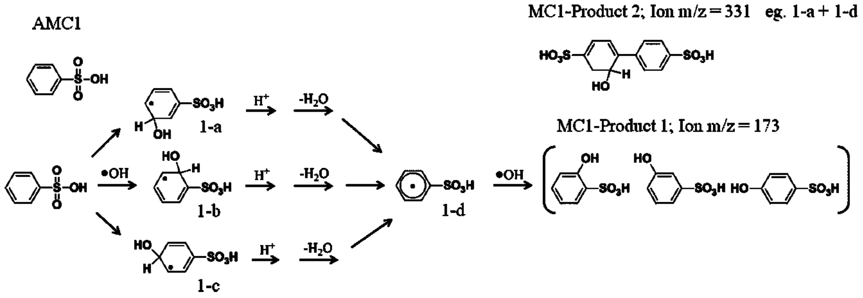
AMC1
MC1-Product 2; Ion m/z = 331 eg. 1-a + 1-d
MC1-Product 1; Ion m/z = 173
•OH
1-a
1-b
1-c
1-d
H+
-H2O

Figure 13. Preliminary Fenton's degradation results with AMC1

Conclusions

Model compound studies mimicking perfluorinated polymers used in PEM fuel cells appear to provide a clear mechanistic model for degradation in the presence of hydroxyl radicals. This model confirms the rapid degradation of carboxylic acid end groups, when present in the polymer backbone, but also confirms that perfluorinated ether sidechains are also labile. Given the large excess of ether sidechains, compared to carboxylic acid end groups, it is reasonable to assume that with the current generation of well-produced, high stability PEM membranes, ether side chain degradation is probably the major mechanism for degradation. Initial work with non-perfluorinated membrane model compounds suggest that with the development of proper conditions, reactivity patterns should be observable in these systems as well. It is hoped that such mechanistic work will be of great use to synthetic workers in the field who are working on a second generation of PEM membrane materials.

Downloaded by UNIV OF DELAWARE MORRIS LIB on June 21, 2012 | http://pubs.acs.org
Publication Date (Web): April 30, 2010 | doi: 10.1021/bk-2010-1040.ch009

Acknowledgments

This research was supported in part by the Department of Energy, Cooperative Agreements Nos. DE-FC36-03GO13098 and DE-FG36-07G017006. DOE support does not constitute an endorsement by DOE of the views expressed in this presentation.

References

1. Mauritz, K. A.; Moore, R. B. *Chem. Rev.* **2004**, *104* (10), 4535.
2. Schiraldi, D. A. *Polym. Rev.* **2006**, *46* (3), 315.
3. Xie, J.; Wood, D. L., III; Wayne, D. M.; Zawodzinski, T. A.; Atanassov, P.; Borup, R. L. *J. Electrochem. Soc.* **2005**, *152* (1), A104.
4. de Bruijn, F. A.; Dam, V. A. T.; Janssen, G. J. M. *Fuel Cells* **2008**, *1*, 3.
5. McDonald, R. C.; Mittelsteadt, C. K.; Thompson, E. L. *Fuel Cells* **2004**, *4*, 208.
6. Darling, R. M.; Meyers, J. P. *J. Electrochem. Soc.* **2003**, *151*, A1523.
7. Ghassemi, H.; McGrath, J. E. *Polymer* **2004**, *45* (17), 5847.
8. Ghassemi, H.; Ndip, G.; McGrath, J. E. *Polymer* **2004**, *45* (17), 5855.
9. Zhou, C.; Zawodzinski, T. A., Jr.; Schiraldi, D. A. *Macromolecules* **2007**, *40*, 8695–8707.
10. Schiraldi, D. A.; Zhou, C.; Reinardy, A. E.; Zawodzinski, T. A., Jr. Presented at the 236th ACS National Meeting, Philadelphia, PA, August 2008, Paper 128 Fuel.
11. Walling, C. *Acc. Chem. Res.* **1975**, *8*, 125.
12. Morcos, I.; Yeager, E. *Electrochim. Acta* **1970**, *15*, 953.
13. Antoine, O.; Durand, R. *J. Appl. Electrochem.* **2000**, *30*, 839.
14. Vogel, B.; Eleksandrova, E.; Mitov, S.; Krafft, M.; Dreizler, A.; Kerres, A. J.; Hein, M.; Roduner, E. *J. Electrochem. Soc.* **2008**, *155* (6), B570.
15. Liu, H.; Zhang, J.; Coms, F. D.; Gu, W.; Litteer, B.; Gasteiger, H. A. *ECS Trans.* **2006**, *3* (1), 493.
16. Schmidt, T. J.; Paulus, U. A.; Gasteiger, H. A.; Behm, R. J. *J. Electroanal. Chem.* **2001**, *508*, 41.
17. Curtin, D. E.; Lousenberg, R. D.; Henry, T. J.; Tangeman, P. C.; Tisack, M. E. *J. Power Sources* **2004**, *131*, 41.
18. Schwiebert, K.; Raiford, K.; Nagarajan, G.; Principe, F.; Escobedo, G. *KFTCA International Symp.*; December 2005, Washington, D.C.
19. Zhou, C.; Zawodzinski, T. A., Jr.; Schiraldi, D. A. *Macromolecules*, submitted for publication.
20. Hubner, G; Roduner, E. *J. Mater. Chem.* **1999**, *9*, 409.

Downloaded by UNIV OF DELAWARE MORRIS LIB on June 21, 2012 | http://pubs.acs.org
Publication Date (Web): April 30, 2010 | doi: 10.1021/bk-2010-1040.ch009

Downloaded by PENNSYLVANIA STATE UNIV on June 21, 2012 | http://pubs.acs.org
Publication Date (Web): April 30, 2010 | doi: 10.1021/bk-2010-1040.ch010

Chapter 10

Open Circuit Voltage Fuel Cell Durability Testing Using Multiple PEM MEAs

Greg Haugen, Sara Barta, Mike Emery, Steven Hamrock,* and Mike Yandrasits

3M Company
***sjhamrock@mmm.com**

This chapter reports the novel use of multiple membrane layers used to fabricate PEM MEAs in order to gain an understanding of the degradation mechanisms ongoing in an operating fuel cell. Open circuit voltage conditions were used for this accelerated durability experiment. The role of catalyst surface area on the degradation rate is examined using a variety catalyst support systems. The prescense of platinum in the membrane, its location, and the relation of that location to where the predominance of degradation is occurring is discussed. In addition we will examine the effects of using a peroxide mitigating agents on reduction of fluoride release rate and improved lifetimes.

Introduction

Fuel cells are at the heart of the coming hydrogen economy, offering a clean renewable energy alternative for transportation, stationary, and portable power needs. At the center of today's fuel cell is the proton exchange membrane (PEM). Great strides have been made in increasing the proton exchange membrane's oxidative stability in fuel cells. The use of peroxide mitigating additives such as manganese (*1*) and cerium (*2*), have provided orders of magnitude improvement in MEA lifetimes. The use of additives and improved MEA constructions has led to lifetimes in excess of ten thousand hours in an automotive humidity/load cycle testing (*3*). One of the tests that have been crucial for this development is the OCV (open circuit voltage) accelerated durability test. There are two commonly

In Fuel Cell Chemistry and Operation; Herring, A., et al.;
ACS Symposium Series; American Chemical Society: Washington, DC, 2010.

practiced protocols, one from the U.S. Fuel Cell Council (USFCC) and the other from the Department of Energy (*4*), both protocols accelerate membrane degradation by using high cell temperature and low relative humidity. There are slight operational differences between the two methods with the main difference being oxidant concentration, the DOE protocol uses air and the USFCC protocol uses oxygen.

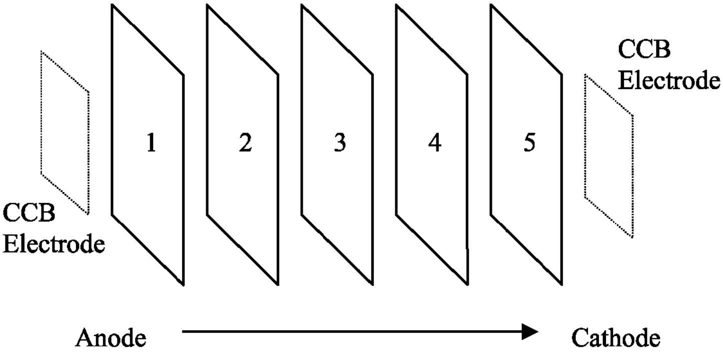

Figure 1. MEA construct for multi-PEM MEAs

Experimental

The MEA (Membrane Electrode Assembly) construct used here is shown in Figure 1. The individual PEMs are 825 equivalent weight 3M ionomer or 1000 equivalent weight cast Nafion™ (*5*), 20-30um in thickness, and were all continuously coated on pilot scale equipment. The predominace of studies were carried out with the 1000 equivalent weight Nafion™ while the 825 equivalent weight was used only in those studies involving the use of peroxide mitigation additives. The PEMs along with gaskets and gas diffusion electrodes are assembled between two bonding plates. The MEA is bonded at 135°C for 10 minutes at a pressure of 1.5tons/50cm^2 active area. Testing of similar MEAs made using this multi PEM construct have shown no interfacial resistance between the PEM layers as measured by impedance (30um 1000 ew has the same resistance whether made by one or six PEMs). Further, no MEA tested has shown any premature failure from its layered structure. It is important to note that all the polymers used in these studies have fluorinated end groups. The electrode used was in the form of a catalyst coated gas diffusion layer refered to as a catalyst coated backing (CCB). Unless otherwise noted, the CCB came from one lot of gas diffusion media coated with the electrode (0.4 mg/cm^2 Pt loading, Pt/C with Nafion™ 1100 ionomer). The initial geometric surface area of the electrodes was 200 cm^2/cm^2 (cm$^2_{\mathrm{Pt}}$/cm$^2_{\mathrm{planar}}$). In the experiments carried out to look at the effect of catalyst type we used a variety of supports – different carbons from graphitized to high surface area, unsupported catalysts (platinum black and vacuum coated PEM) and 3M's nano structured thin film (NSTF) catalyst support (*6*). In this

Downloaded by PENNSYLVANIA STATE UNIV on June 21, 2012 | http://pubs.acs.org
Publication Date (Web): April 30, 2010 | doi: 10.1021/bk-2010-1040.ch010

Downloaded by PENNSYLVANIA STATE UNIV on June 21, 2012 | http://pubs.acs.org
Publication Date (Web): April 30, 2010 | doi: 10.1021/bk-2010-1040.ch010

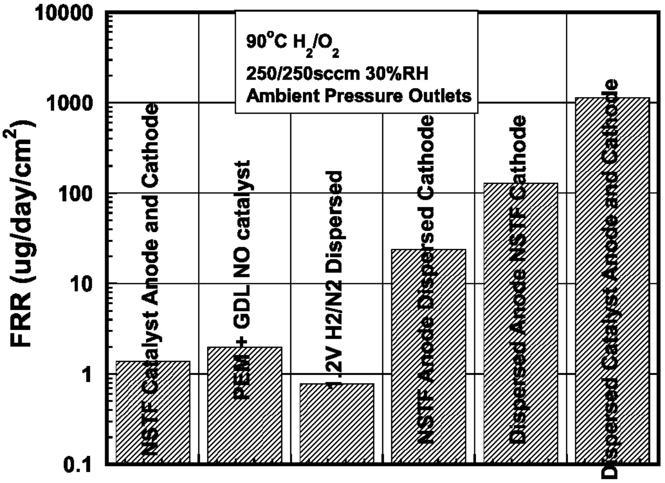

Figure 2. Fluoride release rate as a function of MEA constructions.

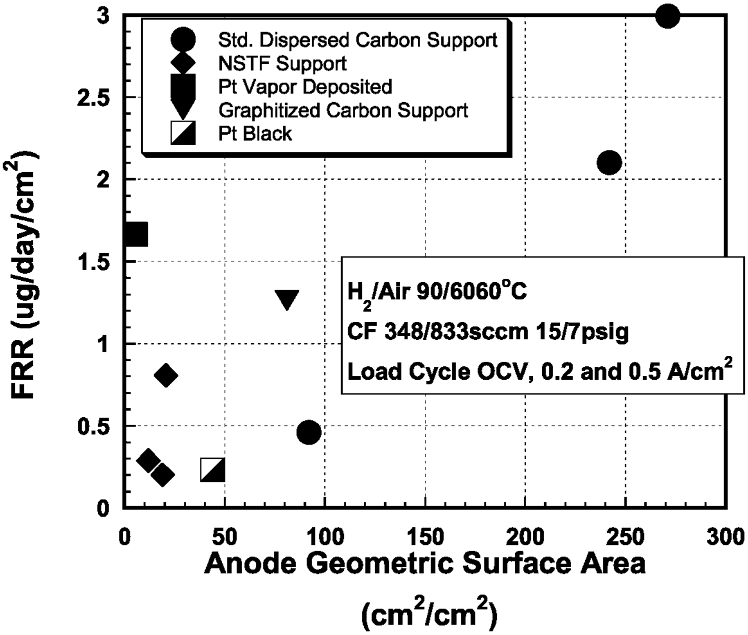

Figure 3. FRR as a function of anode catalyst geometric surface area for a range of catalyst both carbon supported and unsupported.

study we looked only at platinum NSTF catalysts and none of the NSTF platinum alloys that are more typically used. NSTF MEAs were made by a lamination transfer of the catalyst into the membrane to form a catalyst coated membrane (CCM).

Downloaded by PENNSYLVANIA STATE UNIV on June 21, 2012 | http://pubs.acs.org
Publication Date (Web): April 30, 2010 | doi: 10.1021/bk-2010-1040.ch010

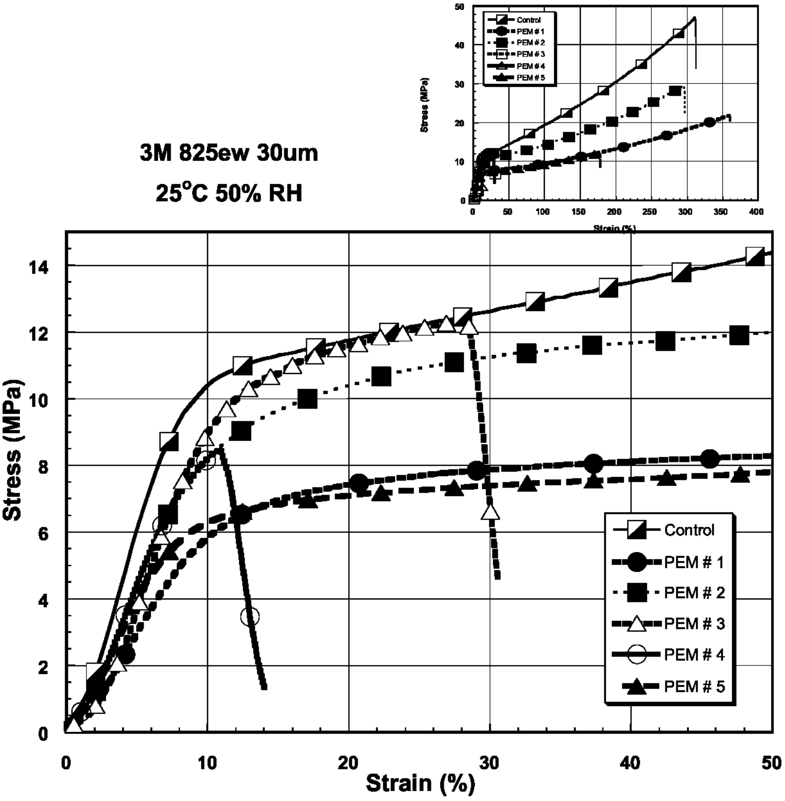

Figure 4. Representative tensile measurements made for a five PEM MEA (1 anode - 5 cathode). The control is the un-run PEM. The differences in PEMs 1 and 5 are attributable to the residual catalyst layer left on the PEM. The insert is the full stress strain curve.

Fuel cell testing was carried out on a modified Fuel Cell Technologies test station. Unless otherwise noted the MEAs were run at 90°C cell temperature, hydrogen/oxygen, 250/250 sccm flows, 30%RH and ambient pressure outlets. Two different cells were used, both based on the Fuel Cell Technologies 50cm^2 active area quad serpentine flow field. In one cell, the cathode side flow field was modified to be an IR/visible transmissive window using metal screen for voltage measurement. In these experiments an IR camera was used to monitor any hole or non-homogeneous thinning which will manifest as a hot spot. All effluent water was collected from the anode and cathode gas streams by the use a separatory funnel connected to the gas outlets. Time and mass of water was recorded for each collection. Effluent water is analyzed using a Chromex ion chromatography system using three decades of calibration concentration standards with each sample series.

Downloaded by PENNSYLVANIA STATE UNIV on June 21, 2012 | http://pubs.acs.org
Publication Date (Web): April 30, 2010 | doi: 10.1021/bk-2010-1040.ch010

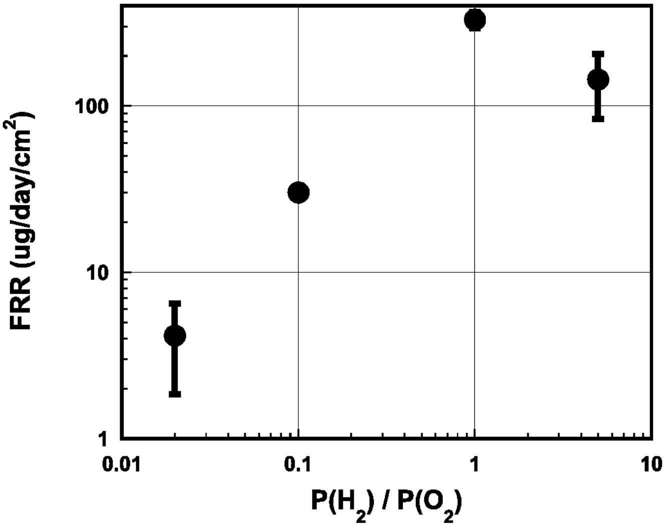

Figure 5. Flouride release rate as a function of fuel and oxidant concentration ratio.

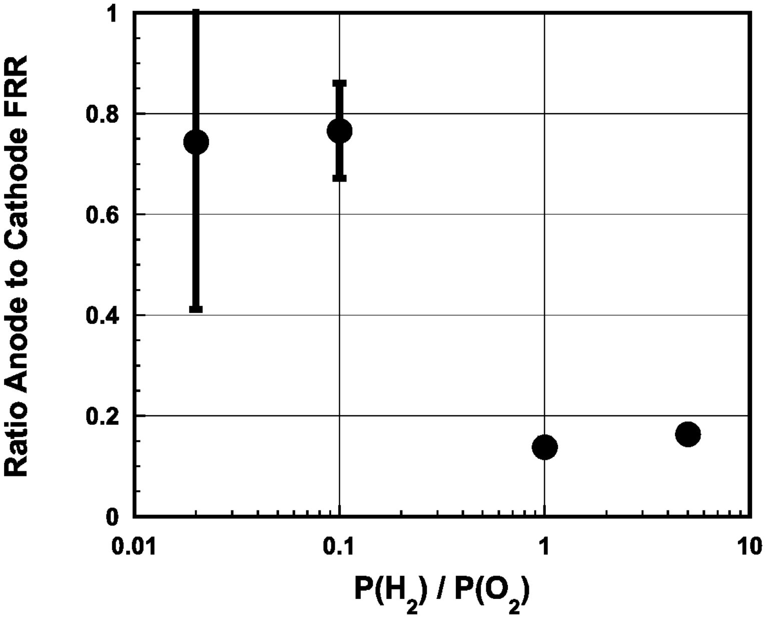

Figure 6. The ratio of anode to cathode effluent flouride release rate as a function of the ratio of fuel to oxidant partial pressures.

All mechanical tensile testing was carried out in humidity chamber at 25°C 50%RH. The test stand is custom built and uses a 1kg load cell. Samples tested are 1x3 cm. Data shown is the average of at least three samples. The samples are dried for at least 24 hours before testing. Control samples were first wet in DI water then air dried as there can be a large variation in tensile properties of PEMs just off the liner. Most of the observed differences in the resutlts of the tensile tests are manifest in changes in the maximum strain and the shape of the stresss strain curve beyond the yield point. A convenient value for comparison between samples is the toughness, which is the integral area of the stress strain curve.

Catalyst surface area measurements were made under H_2/N_2, 250/400 sccm, 40°C cell temperature, 70°C inlet dew points and ambient pressure outlets. Four sets of cyclic voltammagrams are taken, initial, cleaning, baseline and cleaned. Initial and cleaned series are one hundred cycles at 100mV/s 0.1-06 volts vs. SHE. The cleaning is twenty cycles of 100mV/s 0.1-1.2 volts vs. SHE. The baseline is three cycles of 2mV/sec 0.1-0.6 volt vs. SHE. The baseline scan is used to correct for electronic shorts, crossover, and double layer capacitance. The geometric surface area is determined for the three other series and is defined as the platinum surface area from CV divided by the active area of the MEA under test.

A Perkin Elmer Optima 3300DV ICP optical emission spectrophotometer was used for elemental analysis of the degraded membranes. The samples were analyzed against external calibration curves generated using acid-matched solution standards containing 0, 0.2, 0.5, and 1 ppm of each analyte. A 0.5 ppm quality-control standard was used to monitor the accuracy of the calibration curves during the analysis. A 1 ppm solution of scandium was run in-line with the samples and standards to serve as an internal standard. Platinum and manganese were the only elements screened during this analysis. The samples (approximately 30 mg) were weighed to the nearest 0.01 mg into 15-mL polypropylene centrifuge tubes. 5 mL of concentrated hydrochloric acid, 1.25 mL of deionized water, and 2 mL of 30% hydrogen peroxide were added (in that order). The same reagents were added to two empty centrifuge tubes for use as blanks. The tubes were quickly sealed, inverted several times to mix the contents, and the caps were then loosened to permit the release of reaction gases from any peroxide decomposition. The tubes were stored overnight in a fume hood at room temperature.

Downloaded by PENNSYLVANIA STATE UNIV on June 21, 2012 | http://pubs.acs.org
Publication Date (Web): April 30, 2010 | doi: 10.1021/bk-2010-1040.ch010

Results and Discussion

Before using the OCV test protocol as a screening test, a series of experiments were done to understand important test variables. The first and most important factor affecting Fluoride Release Rates (FRR) using the established fuel cell OCV test protocols is the catalyst geometric surface area. An indication of this can be found in the study summarized in Figure 2. This study shows the FRR for a number of MEA constructs. The PEM used here was two pieces of cast 30 um thick Nafion™ 1000. The FRR number represents the average of several water collections between twelve and thirty six hours of testing. The first set of three samples grouped at about 1 ug/day/cm^2 consist of a very low surface area NSTF catalyst, an MEA with no catalyst and lastly an MEA with standard dispersed catalyst but under H_2/N_2 gas streams held at 1.2 volts vs. SHE. This group probably

Downloaded by PENNSYLVANIA STATE UNIV on June 21, 2012 | http://pubs.acs.org
Publication Date (Web): April 30, 2010 | doi: 10.1021/bk-2010-1040.ch010

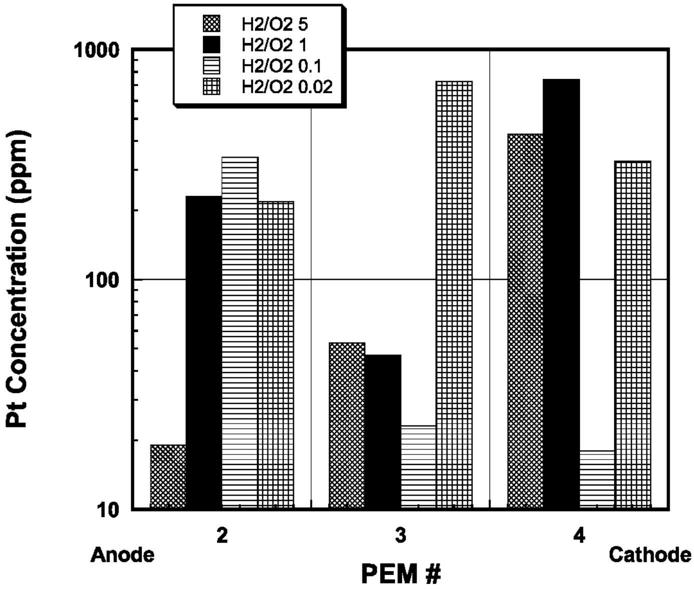

Figure 7. Pt concentration as measured by ICP for the center three PEMs of a five PEM MEA under four different fuel to oxidant partial pressure ratios (Refer to Figure 1 MEA construct and PEM layer location).

better represents a baseline for FRR for this test. The more important result is comparing the high surface area dispersed catalyst (200 cm^2/cm^2) vs. the low surface area NSTF catalyst (12 cm^2/cm^2) and the permutations between them.

It could be argued that the results of Figure 1 were due to the differences in catalyst support and the six fold increased activity of the NSTF catalyst (*7*). In order to explore this hypothesis a series of single PEM MEAs were made where only the anode catalyst was varied. Various loadings were tested of five different catalyst systems – e-beam deposited Pt catalyst on the PEM, NSTF supported catalyst, Pt black coated CCB, Pt on graphitized carbon and Pt on a high surface area carbon. The fuel cell test protocol use here was a load cycle test where the cell is held at 90°Ccell temperature and 60°C inlet dew points with a constant flow of hydrogen and air while the load changes rapidly from OCV to 0.2amps/cm^2 to 0.5 amps/cm^2. The results of this study can be seen in Figure 3. All samples showed greater than 550mV performance at the highest current density hence any differences in FRR can not be attributed to high cathode overpotentials. Unfortunately, it is difficult for such different catalyst types to overlap this wide range of geometric surface areas. With the exception of the Pt deposited on the PEM, the FRR appears proportional to the anode geometric surface area. These results are consistent with studies carried out at 3M studying anode and cathode loading under fully saturated operation (*8*). In those studies, cathode geometric surface area was proportional to FRR under galvanostatic operation. Further, FRR was also proportional to platinum and platinum-ruthenium loading under the accelerated condition of high air bleed The PtRu alloy used on the anode had two

Downloaded by PENNSYLVANIA STATE UNIV on June 21, 2012 | http://pubs.acs.org
Publication Date (Web): April 30, 2010 | doi: 10.1021/bk-2010-1040.ch010

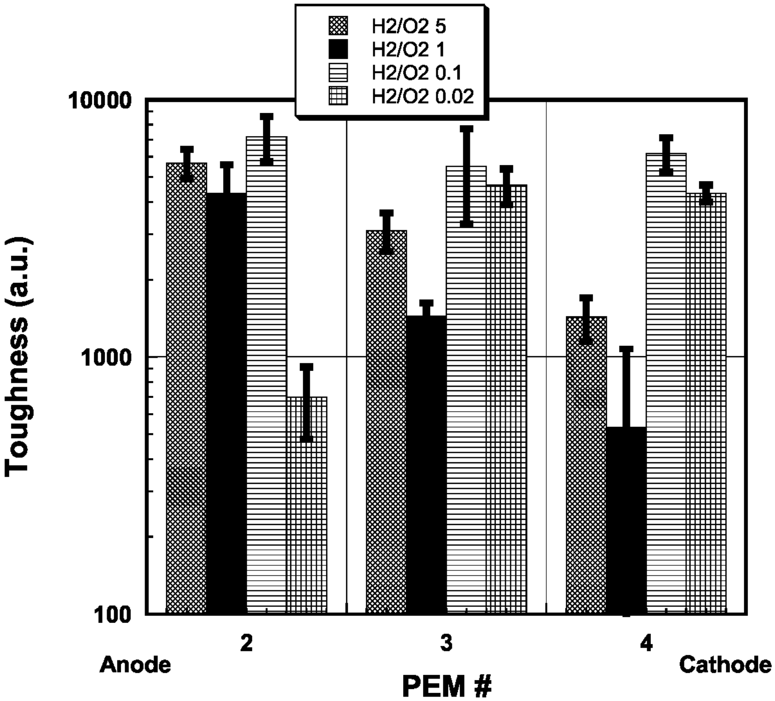

Figure 8. Tensile measurement toughness measured at 25°C 50%RH for the center three PEMs of a five PEM MEA under four different fuel to oxidant partial pressure ratios.

orders of magnitude reduction in FRR over the Pt electrodes under the same test conditons.

By the same reasoning one can have a false low for FRR if there is a contaminant in the PEM and/or in the catalyst layer, that upon humidification poisons a fraction of the catalyst surface and reduces the geometric surface area of the catalyst.

The uniqueness of this MEA construction shown in Figure 1 is in its ease of post mortem analysis. After the MEA has been run the electrodes are removed and the individual PEMs are separated in water. Some of the catalyst and micro layer from the gas diffusion layer remains on the outermost PEMs when the backing is removed, so most of the characterization is confined to the inner PEMs which are uncontaminated by catalyst transfer from the electrodes. In some cases, a PEM layer has been so degraded that it can be only removed as fragments or in the worst case only the edge under the gasket remains. Thickness measurements using a digital micrometer showed no real change in thickness of the individual PEMs, although with the disappearance of entire PEM layers the overall MEA was thinning with time. The concept is that the degrading PEM layers are full of very small voids that are unifomily distributed. This is consistent with the observed mechanical changes in the PEM and the lack of any observed changes in chemical features of the PEM – no change in NMR, FTIR and the conductivity.

This hypothesis would be consistent with a thinning of the PEM layer under compression that may not be observed using a digital micrometer in post mortem. Many of the PEMs used in these studies have a slight brown discoloration due to minor impurities that do not effect performance. This by-product does not impede sample performance or durability and can be easily removed with a dilute peroxide treatment rendering the PEM colorless. During accelerated testing this color is completely removed, presumably from peroxide generated in the fuel cell. The PEM layers that first lose their color are those that later show the most degradation. The loss of color is very uniform throughout the active area with the exception of the perimeter, where the loss of discoloration is somewhat slower. With time of operation the next visual observation of membrane degradation is the formation of a slight discoloration, before the PEM loses its mechanical integrity and breaks into fragments. This new discoloration is likely due to dissolved platinum in the membranes. The total fluoride relase measured is consistent with complete loss of a membrane in the cells tested.

A number of chemical and physical properties of the post mortem PEMs were tested to ascertain what was changing during degradation. Sometimes it is as important to note what is not changing, as well as what is changing. Conductivity measurements of degraded and non degraded PEMs showed no difference when measured at 80°C at humidities ranging from 100-25% RH. Fluorine NMR and FTIR showed no significant changes in the polymer. WAX studies show no changes in the crystallinty of the polymer. All these observations are consistent with the end group unzipping mechanism postulated by Curtin et al (*9*).

The most dramatic change observed in degraded PEMs was in terms of their mechanical properties. Representative tensile measurements of the five Nafion™ PEMs tested under the OCV protocol for 87 hours in a single MEA can be seen in Figure 4. A large change in the maximum strain as a function of PEM location is observed. PEMs 1 and 5 have a lower yield point and different Young's modulus as these PEMs have a residual catalyst layer transferred to them from being bonded with the anode and cathode PEMs respectively. In general, the Young's modulus does not vary within experimental error but the maximum strain changes appreciably with level of degradation. Further, the instanteous modulus above the yield point and even the yield point can change with increased degradation. The aggregate toughness value which is defined as the integral of the area under the stress strain curve provides a convenient method of comparison.

It has been theorized that much of the peroxide generated comes from a "platinum band" that is formed in the PEM of the MEA (*10*). The platinum comes from the dissolution of Pt in the electrode and travels through the PEM until it comes out of solution at a position determined by a ratio of the partial pressures of hydrogen and oxygen at the anode and cathode respectively. We performed series of experiments to examine this conclusion and to see if this is where the maximum damage occurs in the membrane. In this experiment we used various permutations of 100% hydrogen, 1% hydrogen in nitrogen, 100% oxygen, and air at four different ratios of partial pressures of hydrogen and oxyen – 5, 1, 0.1 and 0.02. All other test conditons were the same as those described at the beginning of this chapter. The PEM layers consisted of 30μm thick cast Nafion™ 1000ew membranes.

Downloaded by PENNSYLVANIA STATE UNIV on June 21, 2012 | http://pubs.acs.org
Publication Date (Web): April 30, 2010 | doi: 10.1021/bk-2010-1040.ch010

Downloaded by PENNSYLVANIA STATE UNIV on June 21, 2012 | http://pubs.acs.org
Publication Date (Web): April 30, 2010 | doi: 10.1021/bk-2010-1040.ch010

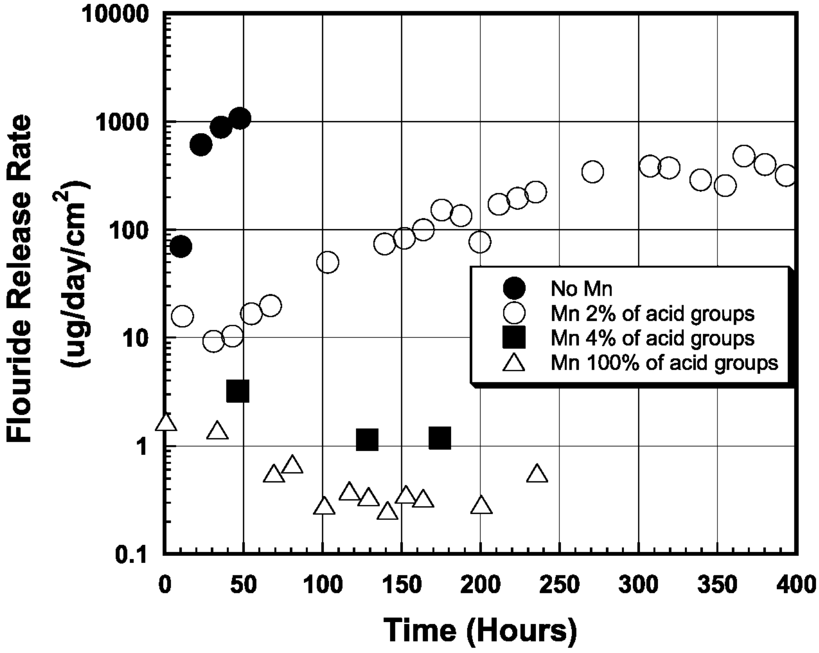

Figure 9. Flouride release rate as a function of time for different Mn loadings in a 3M 825ew polymer.

The results for the four different partial pressure ratios for the FRR seen in Figure 5 are consistent with more of both reactants leading to higher FRR. It is important to note that this series of samples were run for approximately the same length of time. As such with two orders of magnitude difference in FRR there is a large difference in total fluoride loss. This is in part reflected by the large error bars associated with the ratio of anode to cathode FRR plotted in Figure 6 at low values of $P(H_2)/P(O_2)$. This is also consistent with the results for post-mortem platinum concentrations and toughness values plotted in Figure 7 and Figure 8 respectively. Like the fluoride release rate, the platinum concentration distribution results are dependant on the ratio of fuel to oxidant concentrations with higher platinum levels observed in the cases where the reactant concentration was highest. Membrane damage, as determined by lower tensile toughness values are also consistent with the platinum concentrations with lower values measured for the membranes with higher platinum.. The presence of platinum alone, however, does not damage the membrane, but rather the combination of the platinum and run time leading to peroxide formation/decomposition, resulting in membrane degradation leds to the damage. For comparison, control membranes that have been humidified but not run in a fuel cell have a toughness value of about 800 +/- 100(MPa).

In subsequent studies we moved to seven membrane layers in the MEAs to better spatially resolve the Pt concentrations and damaged regions. In the next study we looked at a series of different concentrations of manganese cations

Downloaded by PENNSYLVANIA STATE UNIV on June 21, 2012 | http://pubs.acs.org
Publication Date (Web): April 30, 2010 | doi: 10.1021/bk-2010-1040.ch010

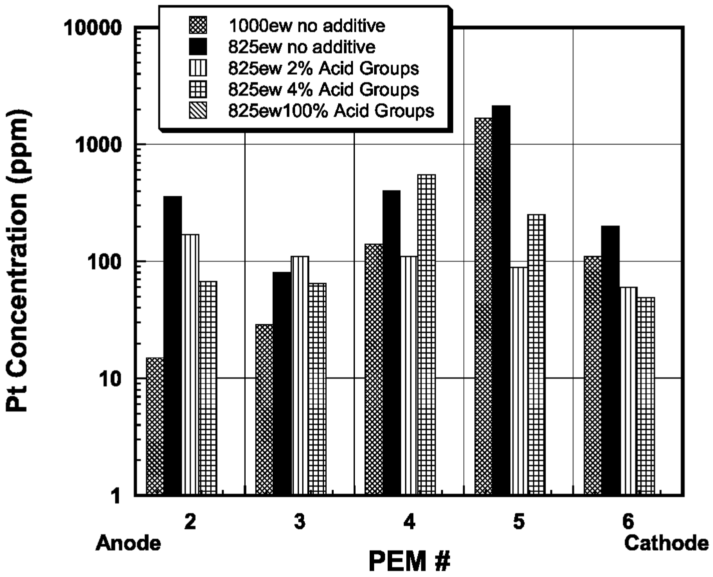

Figure 10. Pt concentration as measured by ICP for a variety of different multiple PEM MEAs with different run times. Note that no Pt was seen in any of the PEMs in the case of 100% of acid groups Mn above the detection limit of 1ppm.

exchanged for the proton on the sulfonic acid group. The addition of manganese to the PEM has a large effect on the FRR and subsequently orders of magnitude increased lifetimes under typical automotive testing protocols (*1*). The effect of manganese addition can be seen in Figure 9. In this case, two and four percent of acid groups are neutralized with Mn^{+2} by adding a soluable manganese salt to the ionomer solution prior to casting. The membrane with 100% of the acid groups neutralized with manganese was achieved by imbibing a membrane in a solution of excess manganese salt followed by rinsing three times in deionized water. Resistance measurements made by hydrogen pump measurements, confirmed that effectively all the acid groups were exchanged with Mn.

Following MEAs testing, a post-mortem examination was carried out. Platinum concentrations were measured by ICP and the tensile properties of each individual membrane layer in each MEA was measured. In addition we looked at managanese concentration in the membranes before and after operation and saw no significant change in concentration. The results for Pt concentration and tensile properties of these MEAs can be seen in Figure 10 and Figure 11 respectively. Of first note is that for the case where all the acid groups have been exchange with Mn there is no observed Pt. This is consistent with the fact that there are no available charge carriers to allow the Pt ions to move through the PEM. Further, in this MEA the largest degree of degradation is near the anode where most of the peroxide might be formed in an OCV test if there was no platinum in the PEM.

In order to garner further understanding of the degradation process we made a series of five PEM MEAs where one PEM had 100% of its acid groups exchanged with Mn while all the others were in the original acid form. Five MEAs were

Downloaded by PENNSYLVANIA STATE UNIV on June 21, 2012 | http://pubs.acs.org
Publication Date (Web): April 30, 2010 | doi: 10.1021/bk-2010-1040.ch010

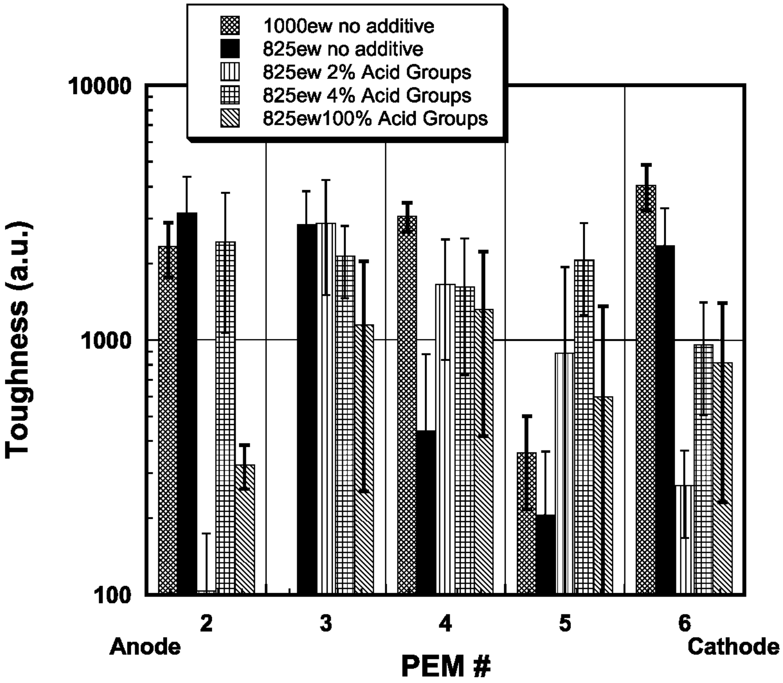

Figure 11. Tensile measurement toughess measured at 25°C 50%RH for a variety of different multiple PEM MEAs with different run times.

made with each having a different location for the manganese containing layer. All samples were tested under the OCV protocol. As can be seen in Figure 12 by the end of the test all of these MEAs have approximately the same FRR which is almost an order of magnitude lower than the control MEA which has no Mn. Post mortem analysis of the PEM layers in the MEAs by ICP showed that all five PEMs had an equivalent Mn concentration, about one fifth of the initial value of the highly doped layer. What is of interest in this experiment is the change in FRR during the OCV test as a function of where the highly doped layer is placed in the PEM stack as seen in Figure 12. Of particular interest is the case of putting the highly doped layer near the anode. This seems to have the largest effect implying that for at least the early stages of the OCV oxidative stablility test the most important place to have the Mn near the anode.

In another study we attempted to study the time dependence of the platinum concentration gradient. A series of three identical MEAs made with seven cast Nafion™ 1000ew layers were tested. The results are plotted in Figure 13. The conclusion drawn from this data is that Pt migration happens very quickly at first but it may reach a solubility limit. Additional samples need to be tested to confirm this concept and to probe earlier times.

Downloaded by PENNSYLVANIA STATE UNIV on June 21, 2012 | http://pubs.acs.org
Publication Date (Web): April 30, 2010 | doi: 10.1021/bk-2010-1040.ch010

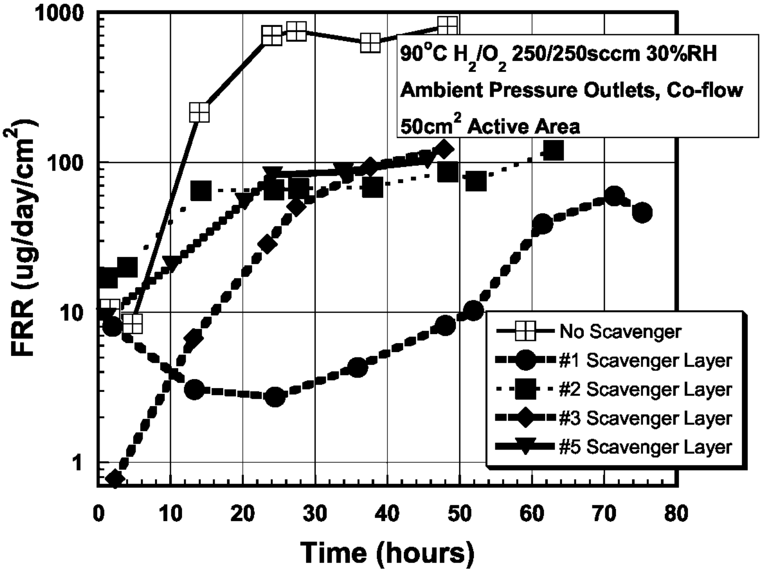

Figure 12. Flouride release rate as a function of time for five PEM MEAs where the location of the highly Mn doped PEM is at different locations. Layer one is the PEM closest to the anode and layer five is the PEM closest to the cathode.

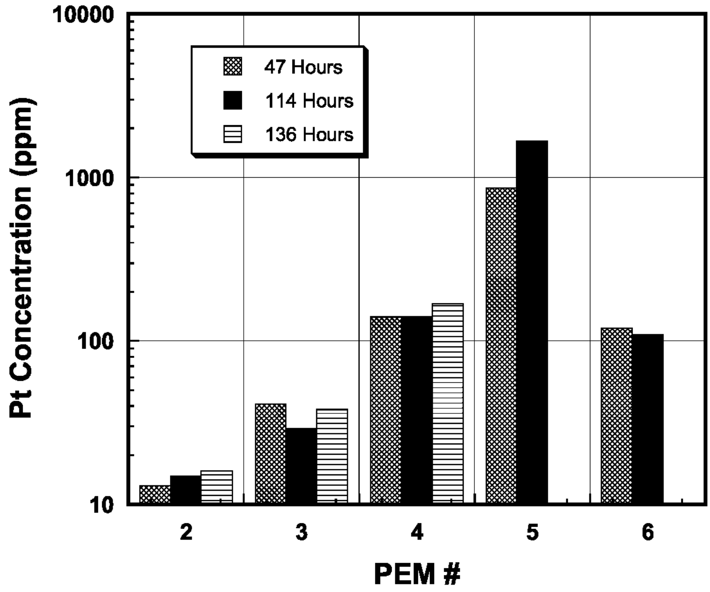

Figure 13. Platinum concentration as a function of time of operation. Note PEMs 5 and 6 of 136 hour MEA were too degraded to measure.

Downloaded by PENNSYLVANIA STATE UNIV on June 21, 2012 | http://pubs.acs.org
Publication Date (Web): April 30, 2010 | doi: 10.1021/bk-2010-1040.ch010

Conclusions

We have shown that the platinum geometric surface area, of both the anode and cathode, is proportional to the fluoride release rate for the same polymer independent of catalyst support type. This has implications for test results comparing data between labs that use the DOE and US Fuel Cell Council's test protocols. The results imply high activity, low surface area, catalyst's like 3M's NSTF catalysts are beneficial for lower FRR.

With our multiple PEM MEA approach we were able to confirm the relationship between platinum distribution in the PEM and the ratio of the partial pressures of hydrogen and oxygen. Further we observed that in general the damage to the PEM, as observed by postmortem tensile measurements, was consistent with the location of the platinum band. We observed no change in the PEM conductivity, crystallinity, FTIR and NMR properties despite large changes in the membrane mechanical properties. Whole PEMs were seen to essentially disappear in the longest tests consistent with membrane thinning. All these observations are consistent with the polymer unzipping model of degradation.

We presented data showing FRR as a function of managese loading and location. The dramatic reduction in FRR for this highly accelerated test with Mn addition has lead to orders of magnitude lifetime increase under automotive tests. We also observed that manganese reaches an equilibrium concentration and does not leave the MEA during operation and that when introduced in one layer at high concentrations will equilibrate equally in all the membrane layers.

Acknowledgments

This research was supported in part by the U.S. Department of Energy, Cooperative Agreements No. DE-FC36-02AL67621 and DE-FC36-03GO13098. DOE support does not constitute an endorsement by DOE of the views expressed in this presentation. In addition the authors would like to thank Dr. David Aeschliman for his timely ICP test results and discussion.

References

1. Frey, M. H.; Hamrock, S. J.; Haugen, G. M.; Pham P. T. U.S. Patent Applications US2006063054 and US2006063055.
2. Panaglotis, T.; Parrondo, J.; Ramani, V. *Electrochem. Solid-State Lett.* **2008**, *11* (7), B113–B116.
3. Hamrock et al. 2009 DOE Annual Merit Review.
4. Borup, R. Scientific aspects of polymer electrolyte fuel cell durability and degradation. *Chem. Rev.* **2007**, *107* (10), 3904.
5. Hamrock, S. J.; Yandrasits, M. A. Proton Exchange Membranes for Fuel Cell Applications. *J. Macromol. Sci., Part C: Polym. Rev.* **2007**, *46*, 219–244.

6. Debe, M. K. In *Handbook of Fuel Cells – Fundamentals, Technology and Applications*; Vielstich, W., Lamm, A., Gasteiger, H. A., Eds.; John Wiley & Sons: 2003; Ch. 45.
7. Debe et al. 2007 Fuel Cell Seminar, Miami Beach, Florida, Nov. 3−7, 2003.
8. U.S. Department of Energy, Cooperative Agreements No. DE-FC36-02AL67621 final report.
9. Curtin, D. E.; Lousenberg, R. D.; Henry, T. J.; Tangeman, P. C.; Tisack, M. E. *J. Power Sources* **2004**, *131* (1−2), 41–48.
10. Bi, W.; Gray, G. E.; Fuller, T. F. *Electrochem. Solid-State Lett.* **2007**, *10* (5), B101–B104.

Downloaded by PENNSYLVANIA STATE UNIV on June 21, 2012 | http://pubs.acs.org
Publication Date (Web): April 30, 2010 | doi: 10.1021/bk-2010-1040.ch010

Chapter 11

Metal Oxides and Heteropoly Acids as Anodic Electrocatalysts in Direct Proton Exchange Membrane Fuel Cells

Jack R. Ferrell III and Andrew M. Herring[*]

Department of Chemical Engineering, Colorado School of Mines, Golden, CO 80401
[*]aherring@mines.edu

Downloaded by STANFORD UNIV GREEN LIBR on June 21, 2012 | http://pubs.acs.org
Publication Date (Web): April 30, 2010 | doi: 10.1021/bk-2010-1040.ch011

In this chapter, the development of metal oxides in the anodic electrocatalyst layer for proton exchange membrane (PEM) fuel cells is reviewed. There have been many efforts to incorporate various metal oxides in the anode catalyst layer of proton exchange membrane fuel cells whcih has been motivated mainly by the high cost of platinum, which is the current catalyst of choice in PEM fuel cell electrodes. Many electro-oxidation reactions of small hydrocarbon molecules on platinum are also rather slow. In this chapter, first the development of hydrogen-tungsten-bronze materials is explained. Next, the use of Pt / WO_3 materials, for use in methanol electrooxidation, is reviewed, Followed by the development of PtRu / WO_3. Then the use of various other metal oxides in working PEM fuel cell anodes is reviewed. Finally, the use of heteropoly acids in direct methanol and direct dimethyl ether proton exchange membrane fuel cells will be presented.

Introduction

The hydrogen oxidation reaction proceeds rapidly on platinum in the proton exchange membrane (PEM) fuel cell anode. So much so that when pure hydrogen is used as the fuel the cost of the necessary Pt loading is acceptable for commercialization of the device. In fact for the fuel cell anode the cots of manufacturing the electrode exceeds the cost of buying the Pt for this electrode.

In Fuel Cell Chemistry and Operation; Herring, A., et al.;
ACS Symposium Series; American Chemical Society: Washington, DC, 2010.

Downloaded by STANFORD UNIV GREEN LIBR on June 21, 2012 | http://pubs.acs.org
Publication Date (Web): April 30, 2010 | doi: 10.1021/bk-2010-1040.ch011

Of course this is not true on the fuel cell cathode where large amounts of expensive Pt are required to catalyze the oxygen reduction reaction at a reasonable rate. The problem with the fuel cell anode is that the Pt catalyst is easily poisoned by small molecules such as CO which is a by product of producing H_2 from the reformation of hydrocarbons. The need to use ultra pure H_2 for low temperature fuel cells adds significantly to the cost of the fuel. In addition it would be desirable to use liquid or easily compressible hydrocarbon fuels for portable applications, but again the oxidation of these molecules on Pt is sluggish. It is, therefore, desirable that new more versatile or less expensive catalysts be developed for the PEM fuel cell anode. In this chapter we describe the effort that is under way to improve Pt based PEM fuel cell anode catalyst with metal oxides.

Hydrogen-Tungsten-Bronze Materials and Hydrogen Spillover

The use of various metal oxides to mitigate CO poisoning dates back to the 1960s. Niedrach and Weinstock (*1*) have shown that mixtures of platinum with certain oxides are less susceptible to CO poisoning than platinum controls. They tested oxides of tungsten, notably WO_3, W_2O_5, and WO_2. The authors suggested that this CO tolerance effect happened because carbon monoxide and water molecules could exist on adjacent surface sites at the platinum-oxide interface. CO would be present on the platinum site, and activated water would be present on the tungsten oxide, since CO adsorbs only weakly on the oxide surface. Compared to a pure platinum control, proportions of platinum could be as low as 10 % (thus 90 % WO_x) with no reduction in performance. However, no definite conclusions were drawn concerning the function of the oxide during the anodic oxidation of pure hydrogen (*1*).

Another possibility to explain the enhanced CO tolerance seen above is the rapid formation of hydrogen-tungsten-bronzes, (*2*). These compounds were first reported by Glemser and Naumann (*3*). Hydrogen-tungsten-bronzes have a general formula of H_xWO_3 ($0.3 < x < 0.5$), are acid resistant, and metallic conductors, and often blue in color. Benson, *et al.* (*2*) studied the formation of these compounds, and found that the reduction of WO_3 by H_2 proceeds at temperatures above 400 °C. When the WO_3 powder was mixed with platinum black, this reduction started at temperatures below 100 °C. When the platinum black and tungsten oxide powder mixture was made to adsorb water, the reduction by hydrogen rapidly took place at room temperature. Gaseous hydrogen dissociatively chemisorbs on the Pt site then migrates across the metal/oxide interface to form the hydrogen-tungsten-bronze, H_xWO_3. The presence of water was found to increase the rate of hydrogen surface diffusion from the metal surface to the oxide surface (*2*). This was one of the first striking examples of how surface diffusion can be an important aspect in catalysis. With the aid of water, the amount of hydrogen present to reduce the oxide surface was a 35-fold increase over the amount when only platinum was present (*2*).

Hydrogen-tungsten-bronzes are indeed interesting materials, and could function as intermediates in the anodic oxidation of hydrogen on platinum /

tungsten trioxide electrodes (*4*). This would take advantage of the so-called hydrogen spill-over effect, whereby the hydrogen oxidation reaction can be spilled over onto a WO_3 support, thus increasing the activity of the catalyst system. Since there is a limit to the size of platinum crystallites, the use of active supports for the platinum would enable some of the catalytic steps for hydrogen oxidation to be spilled over to the support, and improve the overall efficiency for the hydrogen oxidation reaction. The hydrogen spill-over effect on Pt / WO_3 is shown below in Equation 1:

$$\mathbf{WO_3 + x\ Pt\text{-}H \rightarrow H_xWO_3 + Pt \rightarrow WO_3 + x\ e^- + x\ H^+} \qquad (1)$$

As shown above, the hydrogen spill-over takes advantage of the formation of hydrogen-tungsten-bronzes. Thus protons formed on a platinum site can be passed on to the tungsten trioxide support, forming a hydrogen-tungsten-bronze. In an electrochemical environment, the hydrogen-tungsten-bronze can liberate the protons and electrons to an external circuit. This mechanism would depend on the electron transfer step on the platinum being slow relative to the chemisorption of hydrogen and its migration to the oxide (*4*). Hobbs and Tsueng investigated the participation of tungsten trioxide in the hydrogen oxidation reaction, with tantalum carbide as the control substrate. They found significantly higher performance using tungsten trioxide than tantalum carbide. However, differences in electrode structural parameters, such as platinum dispersion and morphology and wetting characteristics, made final conclusions difficult based on this result alone. Therefore, this did not prove that the hydrogen spill-over effect was actually occurring in their original paper on the subject (*4*).

A few years later, Hobbs and Tseung developed a better method to confirm the occurrence of the hydrogen spill-over effect (*5*, *6*). In this new method, stock samples of platinum supported by either WO_3 or B_4C were prepared by a freeze drying technique (*5*). These samples were then mixed with various amounts of either WO_3 or B_4C. Next, these samples were made into electrodes and tested in 5 N sulfuric acid. Hydrogen was fed to the working electrode via a diffuser. The hydrogen oxidation activity was plotted in terms of mA/mg Pt at a fixed overpotential. In this manner, if the support did not partake in the hydrogen oxidation, the activity per mg of Pt would be independent of the platinum loading in the electrode. It was found that hydrogen bronzes, formed in platinized hydrogen electrodes, contributed to the net anodic current (*5*). Specifically, at 100 mV of overpotential, 14 mA/cm^2 was achieved with 0.06 mg/cm^2 of Pt on B_4C, while 680 mA/cm^2 resulted from using 0.06 mg/cm^2 of Pt on a WO_3 support. These hydrogen-tungsten-bronzes were formed by H-atom migration from the Pt site to the oxide. Consequently, the hydrogen-tungsten-bronze was oxidized electrochemically. This is shown above in Equation 1.31. Thus the reaction zone is extended onto the support and the overall electrode activity was increased by the presence of WO_3 (*5*, *6*).

Once the hydrogen spillover effect was proven for the hydrogen oxidation reaction, it became evident that the number of Pt / WO_3 interfaces should be maximized. At that time, the WO_3 powders used had been prepared by

Downloaded by STANFORD UNIV GREEN LIBR on June 21, 2012 | http://pubs.acs.org
Publication Date (Web): April 30, 2010 | doi: 10.1021/bk-2010-1040.ch011

Downloaded by STANFORD UNIV GREEN LIBR on June 21, 2012 | http://pubs.acs.org
Publication Date (Web): April 30, 2010 | doi: 10.1021/bk-2010-1040.ch011

impregnation via a decomposition of tungstic salts (*4*). This technique produced tungsten oxide powders with a low surface area of approximately 3-5 m^2/g (*7*). This low surface area, combined with the need to maximize the number of Pt / WO_3 interfaces, led to the development of new preparation techniques. One alternate preparation technique involved dissolving W powder with H_2O_2 in a solution containing alcohol (*8*). Next, the excess hydrogen peroxide was decomposed using a platinized Pt gauze. Using this co-deposition method, it was possible to plate thin films of Pt / WO_3. In this study, the authors used TEM and powder x-ray diffraction to verify that small Pt crystallites (~ 4 nm) were dispersed uniformly on amorphous WO_3 (*8*). This method produces more Pt / WO_3 interfaces than the powder methods discussed above; however, thin film electrodes are only suitable for use in fuel cells using a liquid fuel. A gas diffusion layer is required for effective oxidation of gaseous fuels, such as hydrogen.

The Use of Pt / WO_3 Catalysts for Electrochemical Methanol Oxidation

The prototypical direct PEM fuel cell uses methanol. There have been several studies using Pt / WO_3 electrodes for methanol electrooxidation. These studies are often compared to Pt and PtRu electrodes, as PtRu is widely recognized as the state-of-the-art anode electrocatalyst for the DMFC (*9*). The mechanism of methanol decomposition on Pt / WO_3 electrodes was first proposed in 1994 (*10*). In this study, a 1 cm^2 gold foil was used as the substrate, and Pt and WO_3 were co-deposited onto the gold foil. These thin film electrodes were made using the same process as above (*8*), resulting in 4 nm Pt particles supported on an amorphous tungsten oxide layer. Loadings of 1 mg/cm^2 were used for both Pt and tungsten trioxide. For methanol electrooxidation, the Pt / WO_3 electrode showed significantly higher performance than the Pt control electrode. The co-deposited electrode produced 100 mA/cm^2 at 200 mV. The Pt control, with a similar Pt loading, only produced 10 mA/cm^2 at 450 mV, and became severely poisoned after twenty minutes (*10*). Thus, it was clear that the inclusion of WO_3 aided methanol oxidation for Pt electrodes. The proposed mechanism (*10*) is shown below in Equations 2−8.

$$H_2O \rightarrow OH_{ads} + H^+ + e^- \tag{2}$$

$$CH_3OH + 2Pt \rightarrow Pt\text{-}CH_2OH + Pt\text{-}H \tag{3}$$

$$Pt\text{-}H + WO_3 \rightarrow Pt + H_xWO_3 \rightarrow WO_3 + H^+ + e^- \tag{4}$$

$$Pt\text{-}CH_2OH + 2Pt \rightarrow Pt_2\text{-}CHOH + Pt\text{-}H \tag{5}$$

$$Pt_2\text{-}CHOH + 2Pt \rightarrow Pt_3\text{-}COH + Pt\text{-}H \tag{6}$$

$$Pt_3\text{-}COH \rightarrow Pt\text{-}CO + Pt + Pt\text{-}H \tag{7}$$

$$Pt\text{-}CO + 2OH_{ads} \rightarrow CO_2 + H_2O + 2Pt \qquad (8)$$

Starting with Equation 2, water is adsorbed on the surface. This can happen on both Pt sites and the WO_3 surface, but this water activation step requires a large overpotential to occur on Pt sites (*11*). Next, in Equation 3, the first hydrogen atom is stripped off of the methanol molecule, resulting in a hydrogen atom adsorbing onto a vacant Pt site. In Equation 4, it is shown that this hydrogen atom occupying the Pt site can be spilled over onto the tungsten oxide surface, and forming a hydrogen-tungsten-bronze, and freeing up a Pt site in the process. This hydrogen-tungsten-bronze is then oxidized electrochemically, regenerating the original WO_3 surface. The rest of the mechanism is standard for electrochemical methanol oxidation on platinum (*12*). Methanol adsorbs on the surface, producing a strongly bound CO intermediate, as seen in Equations 3, 5, 6, and 7. Tungsten trioxide aids this process in two ways. First, every time a proton is produced on a Pt site, it is spilled over to the WO_3 support. In the above mechanism, this spillover occurs for Equations 3, 5, 6, and 7. This means that there are more free Pt sites available to adsorb more methanol molecules. Second, WO_3 can adsorb water more easily than Pt (*1*), and this OH_{ads} on the WO_3 surface reacts with an adjacent Pt-CO species, freeing the Pt site of the CO poison. This is shown in Equation 8, where the OH_{ads} species is on the WO_3 surface. In this manner, Pt / WO_3 electrodes have shown increased activity for the electrochemical oxidation of methanol, compared to Pt control electrodes. Again, the above studies have only been performed in conventional three-electrode cells. Also, due to the morphology of the produced Pt / WO_3 films, these materials would only be applicable to thin film fuel cells (*10*).

In 1995, Shukla *et al.* studied methanol oxidation on carbon supported Pt-WO_{3-x} in solution (*13*). In this study, chemically co-deposited Pt-WO_{3-x} of varying composition were supported on Ketjen black, a high surface area carbon. Varying ratios of chloroplatinic acid and a heteropoly acid ammonium metatungstate, $(NH_4)_6H_2W_{12}O_{40}$, were prepared in homogeneous solution. Next, 2.5 g of Ketjen black was suspended in 100 ml of water at 80 °C, and 50 ml of the catalyst solution was slowly added and allowed to impregnate for 1 hour. This slurry was dried and powdered, then mixed in 100 ml of water and reduced by dropwise addition 0.2 M $NaBH_4$ at a pH value of 1. This catalyst was then applied to Toray carbon paper (Toray TGP90). These electrodes were used as the working electrode in a three-electrode cell, with a Pt flag counter electrode. Total loadings of up to 5 mg/cm^2 were achieved. The electrolyte was 2.5 M sulfuric acid, and when methanol was used, it was present in a 1 M concentration. For methanol electrooxidation, the highest performace was seen with a 3:1 Pt/WO_{3-x}/C electrode. Ratios of 3:2 and 6:1 were also tested, but showed poorer performance than the Pt control. Tafel slopes were extracted from the data, and were in agreement with the trends from the polarization results. For the 3:1 Pt/WO_{3-x}/C electrode, the Tafel slope was 88 mV/decade, compared to 102 mV/decade for the Pt control. The 6:1 Pt/WO_{3-x}/C electrode had a Tafel slope of 117 mV/decade, and the 3:2 Pt/WO_{3-x}/C electrode had a Tafel slope of 135

Downloaded by STANFORD UNIV GREEN LIBR on June 21, 2012 | http://pubs.acs.org
Publication Date (Web): April 30, 2010 | doi: 10.1021/bk-2010-1040.ch011

Downloaded by STANFORD UNIV GREEN LIBR on June 21, 2012 | http://pubs.acs.org
Publication Date (Web): April 30, 2010 | doi: 10.1021/bk-2010-1040.ch011

mV/decade. This technique, while still not tested in a fuel cell environment, came closer to mimicking actual fuel cell electrodes. The electrodes created are not thin film electrodes, but typical electrode architectures where Pt was supported on a high surface area carbon, and this catalyst was applied to the surface of a gas diffusion layer. With this more realistic electrode architecture, Pt / WO_{3-x} electrodes were still found to possess increased catalytic activity compared to Pt alone.

A similar study by Park *et al.* (*14*) studied methanol oxidation using Pt / WO_3. Thin films of Pt / WO_3 were made using a co-sputtering system (*15*) using indium tin oxide as the substrate. Nanoparticle catalysts were also fabricated, using a typical impregnation route. In this impregnation, chloroplatinic acid was mixed with WO_3 powder and DI water; the salt reduction was done using $NaBH_4$, creating Pt nanoparticles on the WO_3 surface. This was a solution electrochemical study, using a three-electrode cell with a Pt wire counter electrode, and a Ag/AgCl reference electrode. For both nanoparticles and thin film electrodes, Pt / WO_3 was found to have higher catalytic activity for methanol electrooxidation, with respect to control electrodes. This was evidenced by both a lower onset potential for methanol oxidation, and also by a higher specific current reached, in terms of amps per gram of Pt. What is unique about this study is that the hydrogen spillover effect was observed *in situ*, taking advantage of the electrochromic properties of the tungsten oxide (*14*). Hydrogen-tungsten-bronzes are colored, while WO_3 is bleached. A He-Ne laser (633 nm) was used as a light source, and the optical signal was monitored during a CV with methanol in solution. Indium tin oxide was chosen as the substrate because it is optically transparent and electrically conductive. As hydrogen atoms were stripped off the methanol molecule, they migrated onto the tungsten oxide surface; this was seen *in situ* by a reduced optical signal, proving the hydrogen-tungsten-bronze was formed during methanol oxidation.

Pt / WO_3 thin films have also been used for formic acid electrochemical oxidation (*16*). Formic acid, HCOOH, is a two electron oxidation, compared to six electrons for methanol. Also, formic acid has been identified as an intermediate in methanol electrooxidation (*11*). In a three-electrode cell, Pt / WO_3 electrodes, synthesized by the co-deposition method (*8*), were tested for activity for formic acid oxidation, and compared to the experimental Pt control (*16*). The Pt / WO_3 electrode was found to oxidize formic acid at room temperature, with 50 mA/cm^2 of current produced at ~350 mV. These results were steady over a test period of 180 h, with no drop in performance. The Pt control electrode was poisoned, only yielding 43 mA/cm^2 at 480 mV, and even this result was not steady over time. This is another result showing that the inclusion of WO_3 into Pt electrode structures can increase the catalytic activity for the oxidation of small organic molecules (*16*).

Up to this point, Pt / WO_3 catalysts had been tested both in thin film and carbon-supported electrodes. In what follows, several other architectures for Pt / WO_3 catalyst will be briefly described. One such study used the sol-gel approach to make Pt / WO_x catalysts (*17*).

WO_x sols were created using a $W(OC_2H_5)_6$ precursor, while Pt sols were made using $NaOC_2H_5$ and H_2PtCl_6. These two sols were then mixed together to achieve the desired WO_x : Pt molar ratio. Working electrodes were prepared by coating a 1.25 cm^2 glass slide with the combined sol, and allowing it to dry. Thus these electrodes were still in the form of films, with thicknesses between 0.2 and 5 µm. Electrocatalytic methanol oxidation currents were similar between the Pt / WO_x and Pt control electrodes. However, the currents from the Pt control decayed quickly in a steady state measurement, while the Pt / WO_x electrode exhibited much more stable behavior (*17*).

Another electrode architecture was formulated based on making tungsten trioxide microspheres and using them as a support for Pt nanoparticles (*18*). The tungsten trioxide microspheres were made by first heating composites composed of resorcinol-formaldehyde polymer, as a carbon precursor, and ammonium metatungstate salt, as a tungsten precursor. This created a gel which was dried at room temperature, then heated at 1173 K for 1 hour in argon flow, followed by 2 h in a hydrogen flow. This created tungsten carbide microspheres. The carbon in the microspheres was selectively removed by calcining at 773 K in an oxygen atmosphere for 3 h; this created the tungsten trioxide microspheres. Platinum particles were supported on the microspheres by the conventional borohydride reduction method. To make working electrodes, the Pt / WO_3 catalysts were made into a catalyst ink with water and 5 wt% Nafion® solution. This catalyst ink was then coated on the surface of a glassy carbon electrode. The BET surface area of the WO_3 microspheres was found to be 18 m^2/g. An SEM image is shown in Figure 1.

Downloaded by STANFORD UNIV GREEN LIBR on June 21, 2012 | http://pubs.acs.org
Publication Date (Web): April 30, 2010 | doi: 10.1021/bk-2010-1040.ch011

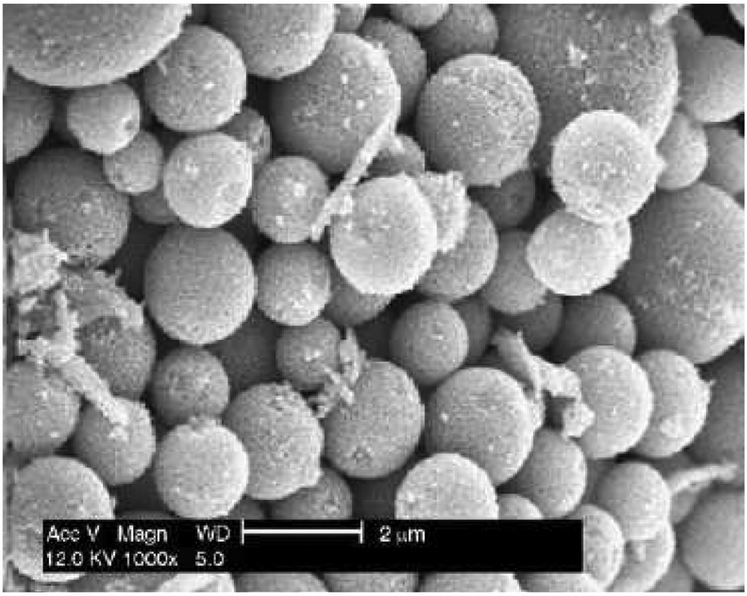

Figure 1. SEM image of the WO_3 microspheres, reproduced from (18).

As seen in Figure 1, the WO_3 microspheres appear to be between 1 and 3 microns in size. Upon looking closer at the tungsten trioxide microspheres, it was seen that they are actually composed of smaller particles. An HRTEM image of the microspheres is shown in Figure 2.

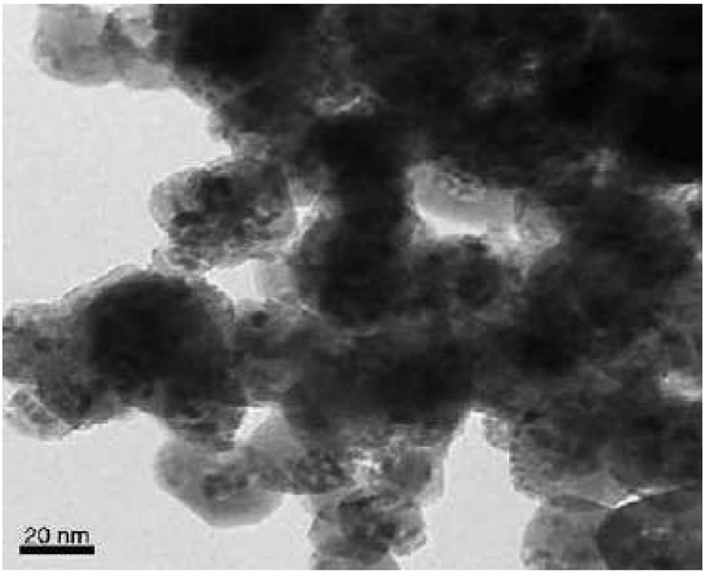

Figure 2. HRTEM image of WO_3 microsphere, reproduced from (18).

As seen in Figure 2, a close-up view of the microspheres shows that they are actually composed of WO_3 nanoparticles that are roughly 15 nm in size. This material is called mesoporous because a large number of pores were found to be on the order of 45 nm. The large pore size was believed to be due to the inter-particle spacing between the WO_3 nanoparticles.

Electrochemical testing of the bare WO_3 microspheres showed no activity for methanol electrooxidation. This is a typical result, as platinum is needed to oxidize the methanol molecule (*11*). Upon testing Pt / WO_3 microspheres for methanol oxidation, it was seen that this catalyst had a higher activity than a commercial 20 % PtRu/C catalyst purchased from E-TEK. Mass activities, in terms of mA/mg Pt, taken at 0.75 V showed that the Pt / WO_3 microspheres were higher than the PtRu/C commercial catalyst by a factor of 1.9 (*18*). This study showed that powdered catalysts, with an atypical catalyst support, can be synthesized and outperform commercial catalysts that have been optimized for the DMFC anode.

In another study (*19*), mesoporous tungsten oxide was created by a template replicating method. Parent mesoporous silica with cubic *Ia3d* symmetry (designated as KIT-6) was used as a hard template. Phosphotungstic acid was used as the tungsten source. Phosphotungstic acid was dissolved in ethanol and incorporated into the structure of KIT-6 by an incipient wetness impregnation technique. Ethanol was evaporated, and the sample was calcined at 773 K for 3 h to yield the tungsten trioxide inside the silica template. The silica template was removed using 2 M HF solution, and the template-free WO_3 was collected via centrifugation. Platinum nanoparticles were made on the tungsten trioxide

Downloaded by STANFORD UNIV GREEN LIBR on June 21, 2012 | http://pubs.acs.org
Publication Date (Web): April 30, 2010 | doi: 10.1021/bk-2010-1040.ch011

surface by reduction, using sodium borohydride, of a chloroplatinic acid solution. Working electrodes were fashioned by making a catalyst ink comprised of ethanol, water, and 5 wt% Nafion® solution; this ink was coated onto the surface of a glassy carbon electrode at a catalyst loading of 0.35 mg/cm^2. Electrochemical properties were determined in solution using a three-electrode cell. From XRD measurements, average crystallite sizes of 6.5 nm and 6.2 nm were found for Pt and WO_3, respectively. These findings were confirmed by TEM. For WO_3, this is in accordance with the template, which had a pore size of 6.51 nm. From BET, the surface area of the prepared mesoporous WO_3 was found to be 86 m^2/g. A bimodal pore size distribution was found for the WO_3. Pores sized 2 – 4 nm were produced from the removal of the silica walls, and pores sized 9 – 12 nm were caused by the textural porosity among the tungsten trioxide particles. Electrochemically, the catalytic activity was higher for the 20 wt% Pt on WO_3 than for a commercial 20 wt% Pt/C catalyst. At 0.7 V, 27.1 mA/cm^2 was produced for the commercial catalyst, while 41.9 mA/cm^2 of oxidation current as achieved for the Pt / WO_3. Again, this increased activity was attributed to the hydrogen-spillover effect aiding in the dehydrogenation of methanol.

Maiyalagan *et al.* (*20*) studied Tungsten oxide nanorods made using an alumina template membrane with 200 nm diameter pores (Anodisc 47 – Whatman Corp.). A suspension of phosphotungstic acid in methanol was infiltrated into the alumina disc under vacuum. Formation of the nanorods inside the alumina was achieved first by temperature programmed thermal decomposition from 95 to 500 °C. Following this, the sample was calcined in air at 873 K for 3 h. The template was then removed by dissolution using HF. Platinum nanoparticles were formed on the surface of the tungsten oxide nanorods by conventional impregnation methods. A suspension of the Pt / WO_x nanorods was dropped onto the surface of a glassy carbon surface. This was covered with 5 wt% Nafion® solution, and then dried, forming the working electrode. Electrochemical properties were gauged using a standard three-electrode cell. The powdered catalyst was characterized using TEM. As expected, the diameter of the tungsten oxide nanorods was found to be 200 nm, matching that of the template. Pt crystallites were in the range of 3 – 4 nm. For methanol oxidation, Pt / WO_x was found to have a higher activity than a commericial 20 wt% Pt supported on Vulcan XC-72 carbon. For the same Pt loading, the Pt / WO_x produced 62.0 mA/cm^2 of current, while the commercial Pt / C electrode yielded 29.5 mA/cm^2.

PtRu / WO_3 Materials for Methanol Electrooxidation

With respect to electrochemical methanol oxidation, there have been several studies using PtRu catalysts supported on WO_3. One such study by Park *et al.* (*15*) prepared a nanostructured alloy electrode on tungsten oxide using a multigun sputtering system. Sputtering methods are often used for the fabrication of thin film electrodes. Electrodes made via conventional sputtering methods often have a fixed composition and nanostructure. In this paper (*15*), an rf magnetron sputtering system was used, but different sputtering guns were used at different

Downloaded by STANFORD UNIV GREEN LIBR on June 21, 2012 | http://pubs.acs.org
Publication Date (Web): April 30, 2010 | doi: 10.1021/bk-2010-1040.ch011

Downloaded by STANFORD UNIV GREEN LIBR on June 21, 2012 | http://pubs.acs.org
Publication Date (Web): April 30, 2010 | doi: 10.1021/bk-2010-1040.ch011

powers, to deposit either the Pt, Ru, or WO_3. X-ray diffraction confirmed the presence of PtRu alloy, and TEM confirmed the presence of the porous amorphous tungsten oxide phase. Also, PtRu alloy nanoparticles of size 5 – 6 nm were detected via TEM. Electrocatalytic activity was determined using a conventional three-electrode cell. The controls were thin film electrodes of Pt and of PtRu. For anodic methanol oxidation, the order of catalytic activity was PtRu-WO_3 > PtRu > Pt. This trend was seen both in a cyclic voltammogram, and also in a steady state potentiostatic experiment at 0.6 V, where current decay was monitored. The maximum current densities seen were 0.15, 0.4, and 1.4 mA/cm^2 for Pt, PtRu, and PtRu-WO_3 electrodes, respectively. This study introduced a novel sputtering technique for production of multi-component thin film electrodes. In addition, hydrogen spillover was observed *in situ*, taking advantage of the electrochromic properties of tungsten oxide. Upon scanning the potential in the positive direction, a decreased optical signal was seen in the PtRu-WO_3 electrode, corresponding to electrosorption and subsequent dehydrogenation of methanol on the PtRu nanoparticles. This shows that hydrogen spillover, from the PtRu catalyst to the WO_3 support, is occurring on the electrode surface (*21*).

Up to this point, all of the Pt / WO_3 and PtRu / WO_3 data related to methanol electrooxidation was in agreement. The results showed that the inclusion of tungsten oxide increased the catalytic activity. In 2004, a paper was published by Yang *et al.* that created some controversy (*22*) with respect to the findings of previous work. Platinum based catalysts were supported on high surface area carbon: Pt/C, PtWO_x/C, PtRu/C, and PtRuWO_x/C were used. The catalysts were prepared by a chemical reduction method, as described in reference (*13*). Working electrodes were made from these catalysts by first making a catalyst ink, comprised of the catalyst powder, water, and 5 wt% Nafion® solution. The ink was then applied to the surface of a gold foil. From TEM analysis, catalyst particles were found to be in the nanoscale range, and the addition of Ru was found to decrease the particle size. The size distribution of the catalyst particles was as follows: PtWO_x/C (6 – 15 nm) > Pt/C (6-25 nm) > PtRu/C (2.5 – 5 nm). The addition of WO_x to make the PtRuWO_x/C catalyst resulted in a high degree of catalyst agglomeration, making a particle size estimation difficult. The agglomerated particles of the PtRuWO_x/C catalyst appeared to form a network of loosely attached catalyst particles. A few, small particles (2.5 – 5 nm) were observed for the PtRuWO_x/C catalyst. CO stripping voltammetry was used to characterize the active electrochemical surface area. From the polarization data for electrochemical methanol oxidation, the PtRuWO_x/C catalyst was found the have the highest activity, followed by PtRu/C, and PtWO_x/C, with the Pt/C control showing the lowest activity. While the polarization results showed that the PtRuWO_x/C catalyst had the highest performance, the authors argued that it is important to choose the proper metric with which to normalize these results. Similar studies in the past have compared these results based on the total mass of noble metal in the electrode. Here, the results are compared based on electrochemical surface area. While the PtRuWO_x/C catalyst produced the highest methanol electrooxidation currents, even when normalized by the total amount of precious metal, it also had the highest electrochemical surface area. Thus, when normalized by the active area, all the catalysts had a similar performance. The authors concluded that differences in CH_3OH oxidation activities per mass of noble metal were due to physical changes in the catalyst layer, such as electroactive surface area (*13*).

Jayaraman *et al.* (*23*) studied a wide range of compositions of Pt / WO_3 catalysts were electrochemically synthesized, using fluorine-doped tin oxide as the substrate, and tested in a three-electrode cell. In contrast with previous work, CO stripping was not used to determine the Pt surface area, as CO as two adsorption modes exist on Pt (linear vs. bridged). This ambiguity in adsorption mode could lead to an uncertainty in the surface area value obtained. Instead, a copper underpotential deposition method (*24*), which is sensitive to Pt sites but not to WO_3 sites, was used in determining the Pt surface area. All electrochemical results in this paper were normalized to the Pt surface area. One useful contribution comes from a CV for a pure WO_3 electrode. No difference in electrochemical performance was seen between solely sulfuric acid and sulfuric acid with methanol. This indicated that the WO_3 surface neither adsorbs nor oxidizes methanol. Similarly for a pure WO_3 electrode, during CO stripping a small peak was seen at ~0.25 V. The authors noted that this could be due to oxidation of CO on the WO_3 surface; however, the exact mechanism required further study. In general, the authors found that Pt / WO_3 electrodes with more than 50% Pt showed higher activity compared to pure Pt, with several compositions around 80 % Pt showing performance 5.8 times higher than the Pt control. Since all the results were normalized to an accurate representation of active Pt sites, this paper showed that the existence of WO_3, in combination with Pt, resulted in an improvement in methanol oxidation which was due to a catalytic effect. This is in contrast to results presented above (*22*) which attributed higher currents to a physical effect.

Other Pt / Metal Oxide Materials for Methanol Electrooxidation

The majority of the work related to transition metal oxides, in combination with noble metals, has been performed on tungsten oxides. There have been several studies of other transition metal oxides. One such study involves the use PtM_yO_x materials for methanol electrooxidation, where M is Sn, Mo, Os, or W (*25*). Here, these catalyst materials were prepared by the decomposition of polymeric precursors, using Ti plates as the substrate, and tested via solution electrochemistry. Precursor solutions for Sn and Mo were prepared by dissolution of tin citrate or $MoCl_5$ in a citric acid and ethylene glycol solution. H_2PtCl_6 and $OsCl_3$ were dissolved in HCl, then added to a citric acid and ethylene glycol solution to obtain the respective precursor solution. A similar precursor solution was made for tungsten, by dissolving WCl_6 in isopropanol. These precursor solutions were then mixed to obtain the desired chemical composition, maintaining a metal : citric acid : ethylene glycol molar ratio of 1 : 3 : 10. Electrodes were made by applying the desired solution to a Ti plate by brushing. The electrodes were calcined in air at 400 °C for 1 hr. In all electrodes, the y and x values in PtM_yO_x were between 0 and 0.5.

Downloaded by STANFORD UNIV GREEN LIBR on June 21, 2012 | http://pubs.acs.org
Publication Date (Web): April 30, 2010 | doi: 10.1021/bk-2010-1040.ch011

Downloaded by STANFORD UNIV GREEN LIBR on June 21, 2012 | http://pubs.acs.org
Publication Date (Web): April 30, 2010 | doi: 10.1021/bk-2010-1040.ch011

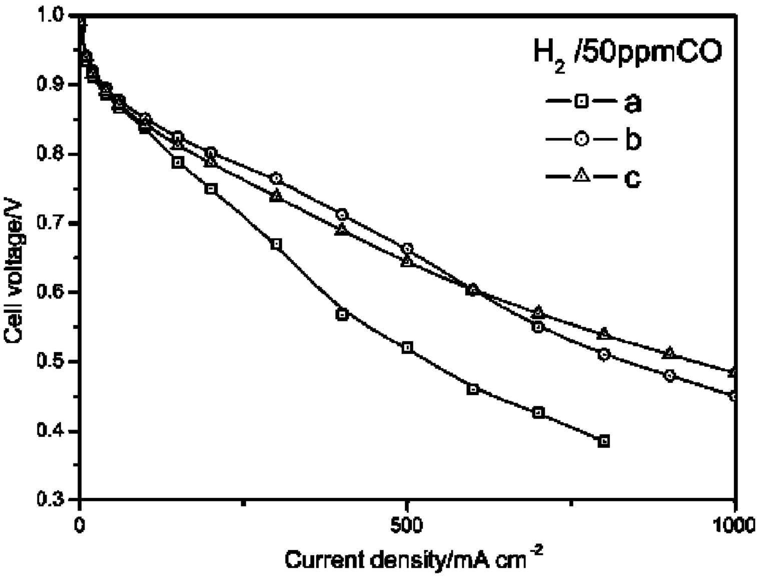

Figure 3. PEMFC single cell performance at 80 °C of (a) PtRu/C, (b) PtRu-HxWO3/C, and (c) PtRu-HxMoO3/C. Reproduced from (35).

Analysis of the film morphologies showed that electrodes containing Mo had the roughest surface (*25*). These electrodes had a highly cracked surface. Electrodes containing Sn and W had a similar morphology, with some smooth regions and some regions containing cracks. For electrodes containing Os, a high loss of Os was observed, most likely due to the volatility of the OsO_4 phase that could be formed during calcination. Electrochemical surface areas were calculated from CO stripping experiments, with the following order in electroactive area: Pt-Os < Pt < Pt-Mo < Pt-W < Pt-Sn. Electroactivities of these electrodes towards methanol oxidation were investigated by cyclic voltammetry, with 0.1 M CH_3OH and 0.5 M H_2SO_4. Electrodes containing Os and Mo showed roughly the same voltammograms as did a pure Pt electrode, while Mo had a higher peak current than the Pt control. Tungsten containing electrodes had a similar peak current as Pt, but W electrodes exhibited an onset potential 100 mV lower than the control. $PtSn_yO_x$ electrodes had the highest peak current, and an onset potential 200 mV below that of the Pt control electrode. In this study, the authors did not provide an explanation as to the reason for these electrocatalytic improvements. However, they did suggest that the addition of these metal oxides could increase activity by one of three mechanisms. The first option was the bifunctional mechanism, where the transition metal oxide surface adsorbs water, producing an OH species on the surface, which could combine with a nearby Pt-CO species, and produce CO_2 at lower potentials than Pt alone. Second, the addition of these transition metal oxides could shift the electronic structure the Pt present, and weaken the binding energy of CO on Pt. A third possibility is that the activity enhancement is due to a structural effect. For example, the presence

Downloaded by STANFORD UNIV GREEN LIBR on June 21, 2012 | http://pubs.acs.org
Publication Date (Web): April 30, 2010 | doi: 10.1021/bk-2010-1040.ch011

of these transition metal oxides could have resulted in the formation of smaller crystallites of platinum (*25*). While this study did not provide definitive evidence of how these materials are functioning, it did provide valuable electrochemical data for the methanol electrooxidation activity of various transition metal oxides.

In 2001, Wang *et al.* did made a contribution taking advantage of an electrochemical codeposition of platinum and molybdenum oxide on a glassy carbon surface (*26*). To do this electrochemical codeposition, potassium hexachloroplatinate (K_2PtCl_6) and sodium molybdate (Na_2MoO_4) were combined in 2.2 M sulfuric acid. Next, the potential was scanned between 0.55 and -0.7 V vs. Hg/Hg_2SO_4 at 20 mV/s for 30 cycles; this codeposited the Pt/MoO_x catalyst on the glassy carbon electrode, forming the working electrode. Catalytic performance for methanol electrooxidation was characterized in a standard three electrode cell. A range of concentrations of potassium hexachloroplatinate and sodium molybdate solutions were used to create electrodes with different compositions. From SEM analysis, it was seen that Pt/MoO_x microparticles were uniformly dispersed on the glassy carbon electrode, proving the utility of this method of electrode preparation. The average diameters of these Pt/MoO_x microparticles were 120 to 250 nm. From electrochemical characterization with methanol present, these electrodes were seen to possess good activity for methanol electrooxidation. However, a control electrode was not presented in this study. The methanol electrooxidation current, as a function of $Pt:MoO_x$ ratio, was presented; a maximum was seen in this plot. The ideal $Pt:MoO_x$ ratio was found to be between 1.5 and 2.0 (*26*). While this study did not have a control electrode for comparison, it did present useful information with respect to the desired ratio between Pt and MoO_x.

A two-step process was used to produce $PtRu\text{-}MoO_x$ nanoparticles (*27*). First, carbon-supported molybdenum oxides were prepared by impregnation of Vulcan XC-72 with a $MoCl_5$ precursor. In the second step Pt and Ru were loaded on the MoO_x using a colloidal method. The particle size of the metal active phase was found to be 3-4 nm, using XRD and TEM analysis. Several of these $PtRu\text{-}MoO_x$ samples showed a significant increase in CO tolerance, when compared to a commercial 30 wt% PtRu/C catalyst purchased from Johnson Matthey. Using differential electrochemical mass spectrometry (DEMS), the first appearance of CO_2 was monitored as a function of electrode potential. For these molybdenum oxide catalysts, CO was oxidized to CO_2 at potentials 200 mV less than the commercial catalyst. Results from *in situ* FTIR suggested that the PtRu surface was less poisoned by CO when molybdenum oxide was present. Electrochemical methanol oxidation was also performed in solution, and once again the $PtRu\text{-}MoO_x/C$ catalysts outperformed the commercial PtRu/C catalyst (*27*). This study serves as an example of the many unique ways to make transition metal oxide catalysts. In all of these examples, good CO tolerance and methanol electrooxidation activity has been seen, regardless of the many different morphologies.

Mukerjee *et al.* has studied Pt/Mo catalysts for CO tolerance (*28–30*). Also, some first principles modeling studies have been published by Neurock's group at the University of Virginia (*31–33*). While these studies are not directly relevant in the context of this review article, they do present detailed mechanisms related to water dissociation, and CO and methanol oxidation.

Pt / Metal Oxide Materials in Direct PEM Fuel Cell Anodes

The above studies have built a precedent for the use of transition metal oxide catalysts, in combination with platinum, in the anode catalyst layer of direct PEM fuel cells. While much great work has been done regarding methanol electrooxidation, there have not been many studies that actually test these materials in a DMFC. The electrooxidation of methanol is well understood on platinum surfaces (*11*). Methanol decomposes on platinum and results in a carbon monoxide intermediate, which strongly binds to the Pt sites, poisoning the catalyst. In this manner, the testing of PEM fuel cells with CO in H_2 is similar to the DMFC, at least as far as anode catalysis is concerned. In what follows, the development of CO-tolerant anode catalysts using transition metal oxides will be reviewed, focusing on studies that performed fuel cell tests using these materials.

Many different methods have been developed to deal with CO tolerance in PEM fuel cells (*34*) including using an air bleed, advanced reforming systems, alloying platinum with one or more metals, and using a membrane to purify the hydrogen stream. Of interest here is the use of oxides of molybdenum or tungsten, in combination with platinum and PtRu. In 2003, Hou et al developed a composite catalyst system composed of PtRu-H_xMeO_3/C, where Me = Mo or W (*35*). To prepare the composite support, first sodium tungstate or ammonium molybdate solution was mixed with Vulcan XC-72 carbon, and the mixture was stirred. Chloride acid was then added to the solution to form the H_xMeO_3 colloid, and this solution was stirred to ensure the colloid was adsorbed on the carbon surface. This mixture was washed and dried to form the composite support. Next, appropriate amounts of chloroplatinic acid, H_2PtCl_6, and $RuCl_3$ solution were coprecipitated on the composite support. The noble metals were reduced by formaldehyde under alkalescent medium at 80 °C with nitrogen blowing over the reaction. The catalyst was then washed and dried. The noble metal content in the catalysts was 20 wt% Pt and 10 wt% Ru, with H_xMeO_3 having a loading of 20 wt%. The remaining wt% in the catalyst was comprised of Vulcan XC-72 carbon.

Both solution electrochemistry, in a three-electrode cell, and fuel cell experiments using a 5 cm^2 cell were performed. Catalyst inks were prepared by dispersing the catalyst powder in ethanol, and adding 5 wt% Nafion® solution. To test carbon monoxide electrochemical oxidation, CO was bubbled through the 0.5 M H_2SO_4 electrolyte solution while holding the working electrode at -0.2 V to ensure CO achieved saturation coverage on the working electrode. For fuel cell tests, catalyst inks were applied to traditional gas diffusion electrodes. Membrane electrode assemblies (MEAs) were fabricated by hot pressing the gas diffusion electrodes on a Nafion® 112 membrane. The platinum loading on the anode was 0.3 mg/cm^2, and a Pt/C cathode was used, loaded at 0.5 mg/cm^2 of Pt. From XRD and TEM analysis of the catalysts, it was found that a good dispersion of noble metals of ~2nm was present, with no evident difference between the

Downloaded by STANFORD UNIV GREEN LIBR on June 21, 2012 | http://pubs.acs.org
Publication Date (Web): April 30, 2010 | doi: 10.1021/bk-2010-1040.ch011

Downloaded by STANFORD UNIV GREEN LIBR on June 21, 2012 | http://pubs.acs.org
Publication Date (Web): April 30, 2010 | doi: 10.1021/bk-2010-1040.ch011

carbon and composite supports. The surface area was found to be 133 m^2/g for PtRu/C and PtRu-H_xWO_3/C, and 117 m^2/g for PtRu-H_xMoO_3/C. From CO oxidation experiments in solution, it was found that the onset potential of CO oxidation occurred 350 mV earlier on the PtRu-H_xMeO_3/C catalysts than on PtRu/C. The lower onset potential was attributed to hydrogen spillover, and also to the presence of MeO_3 aiding in the bifunctional removal of CO, since these metal oxides adsorb water.

Fuel cell tests in this study were undertaken with pure H_2, H_2/50 ppm CO, and H_2/100 ppm CO. All catalysts were found to have similar performance when pure H_2 was the fuel. For single cell tests using 50 ppm CO in hydrogen, the results are reproduced (*35*) in Figure 3. As seen in Figure 3, both PtRu-H_xWO_3/C and PtRu-H_xMoO_3/C catalysts produce higher currents than the PtRu/C control. Similar results for the 5 cm^2 PEMFC were obtained using 100 ppm CO in hydrogen. These polarization curves can be seen in Figure 4.

In Figure 4, again the catalysts incorporating with W or Mo oxide show higher currents than the PtRu control. This is significant because the control in this experiment is considered to be the state-of-the-art CO oxidation catalyst. Also, this is an important finding as these catalysts were tested in a fuel cell environment. The noble metal loadings for all electrodes were the same, and the noble metal surface areas were also very similar. Therefore, the higher currents seen in Figure 3 and Figure 4 were attributed to a catalytic effect, due to the hydrogen spillover effect, and also due to the fact that both H_xWO_3 and H_xMoO_3 adsorb water at low potentials. This active water, in the form of an OH species on the amorphous transition metal oxide, enhanced catalysis through a bifunctional effect. This occured via an OH species on the oxide existing adjacent to a CO species on the noble metal, allowing CO to be oxidized at lower potentials than in the PtRu/C electrode. For this to happen, sufficient interfaces must exist between the noble metal particles and amorphous transition metal oxides (*35*). This has shown that these electrode architectures, incorporating amorphous transition metal oxides, are effective in an actual fuel cell environment.

In 2006, another relevant paper was published by Pereira *et al.* (*36*). This paper presented CO tolerance on PEMFC anodes prepared with $PtWO_x$/C and Pt/C impregnated with phosphotungstic acid ($H_3PW_{12}O_{40}$ – abbreviated HPW). The $PtWO_x$/C catalysts were prepared by the formic acid reduction method, which consists of dissolution of H_2PtCl_6 and WCl_6 in water. This solution was then drop-wise added to a suspension of Vulcan XC-72 carbon in water containing formic acid. Two compositions, of varying Pt : W atomic ratios, were prepared: $Pt_{85}W_{15}O_x$/C and $Pt_{70}W_{30}O_x$/C, where the subscripted numbers represent atomic ratios. To test these catalysts in a fuel cell, catalyst inks were made and applied to gas diffusion electrodes. The inks were comprised of Nafion® solution, the desired catalyst, and isopropyl alcohol. To prepare the phosphotungstic acid impregnated Pt/C catalyst layers, phosphotungstic acid was simply mixed with Pt/C, Nafion® solution, and isopropyl alcohol and made into an ink. These inks were ultrasonicated and applied to the gas diffusion electrodes by an air brushing method. In all MEAs, the metal loading was 0.4 mg/cm^2. The phosphotungstic acid loading was varied between 0 and 3 mg/cm^2. MEAs were fabricated by hot pressing anode and cathode electrodes to a Nafion® 115 membrane.

Downloaded by STANFORD UNIV GREEN LIBR on June 21, 2012 | http://pubs.acs.org
Publication Date (Web): April 30, 2010 | doi: 10.1021/bk-2010-1040.ch011

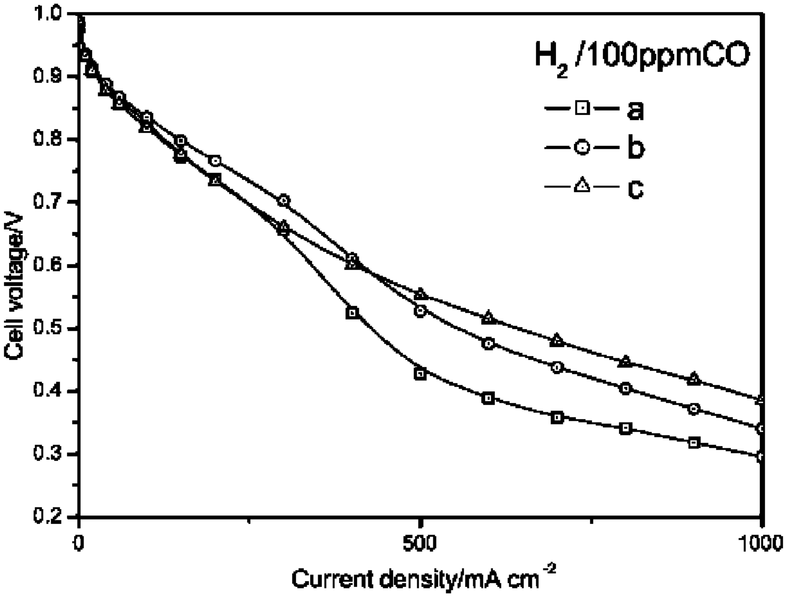

Figure 4. PEMFC single cell performance at 80 °C of (a) PtRu/C, (b) PtRu-HxWO₃/C, and (c) PtRu-HxMoO₃/C. Reproduced from (35).

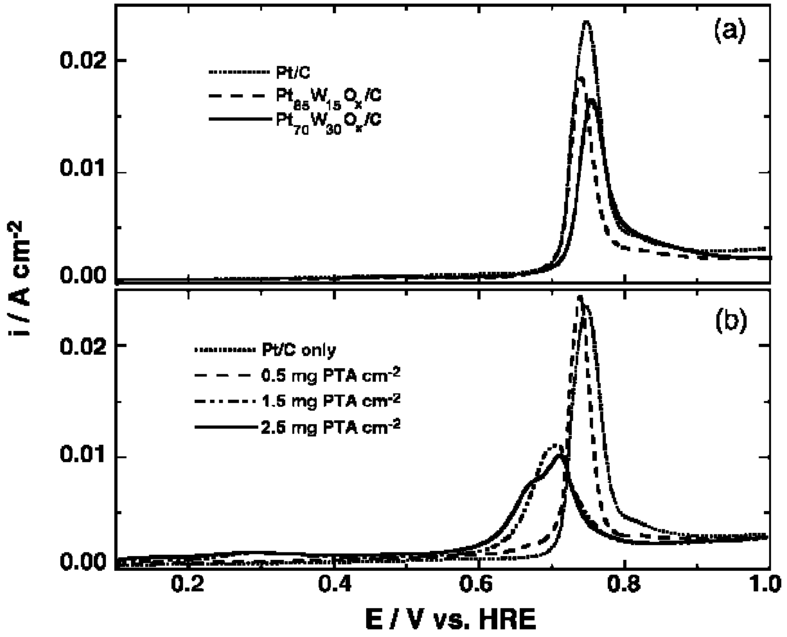

Figure 5. CO stripping scans, T = 27 °C, sweep rate = 10 mV/s. Reproduced from (36).

Downloaded by STANFORD UNIV GREEN LIBR on June 21, 2012 | http://pubs.acs.org
Publication Date (Web): April 30, 2010 | doi: 10.1021/bk-2010-1040.ch011

Cyclic voltammetry and linear sweep CO stripping experiments were also performed on the gas diffusion electrodes, using a potentiostat. In this setup, the anode acted as the working electrode, while the cathode acted as both the counter and reference electrodes when fed H_2. From CO stripping experiments, it was seen that the onset potential for CO oxidation was lower for the HPW impregnated Pt/C electrodes. These results can be seen in Figure 5.

As seen in Figure 5, for the electrodes impregnated with HPW, the onset potential for CO oxidation was at least 100 mV lower than for all other electrodes tested. Also, the onset potential moved to lower values as the loading of HPW was increased. For the $PtWO_x/C$ catalysts there was no change in the CO desorption peak compared to the Pt/C control MEA. Steady state cell polarization curves were also measured, in both pure hydrogen and in hydrogen with 100 ppm of CO, and can be seen in Figure 6.

In Figure 6, η represents the overpotential for CO oxidation, and was calculated from the difference between the potential obtained under pure hydrogen and H_2/CO, at a specific current density. In Figure 6, Pt/C-WO_x/C is an MEA with a Pt/C catalyst between the gas diffusion layer and the membrane, with WO_x/C layer on the other side of the gas diffusion layer (facing the flow fields). Thus, for this MEA, the WO_3 was not in contact with electrochemical three-phase boundary. As expected, the cell polarization results show a considerable drop in performance when CO-containing H_2 was introduced into the cell. However, the $Pt_{70}W_{30}O_x/C$, HPW impregnated Pt/C and Pt/C-WO_x/C electrodes all produce higher currents than the non-impregnated Pt/C control. It is also noteworthy that, in the absence of CO, all electrodes have similar performance profiles, with polarization losses dominated by the activation overpotential for the oxygen reduction reaction. The CO tolerance of the Pt/C-WO_x/C electrode is interesting, since the tungsten oxide could not take place in any electrochemistry. The authors attribute this CO tolerance to the lowering of CO content in the gas phase via the water-gas-shift reaction, as has been previously reported for these materials (*37*, *38*). Finally, these experiments were performed over a period of three days; no drop in cell polarization currents was seen during this time period. This is significant for the HPW impregnated Pt/C electrodes, as the HPW is soluble in water, and was simply mixed into an ink and sprayed on the gas diffusion electrodes.

Taking advantage of Pt/MoO_x/C catalysts, a paper was published in 2003 by Ioroi *et al.* (*39*) where fuel cell tests were performed using 100 ppm CO in H_2. To better understand the electrochemical processes involved, solution electrochemical tests were also performed, using a rotating disc electrode (RDE). To make these catalysts, MoO_x was deposited on the Vulcan XC-72 carbon support, before Pt deposition. Pt/C and PtRu/C catalyst were also fabricated, to serve as a comparison for electrochemical properties. The noble metal loading of Pt and PtRu was 30 wt% for these control electrodes. For the RDE study, catalyst inks were made containing the desired catalyst and ethanol, and then applied to glassy carbon electrodes. Following solvent evaporation, the surface was covered with a 1 % Nafion® solution. CO stripping experiments were then performed with CO dissolved in a 0.5 M sulfuric acid electrolyte. For fuel cell tests, MEAs were built using Nafion® 112 as the electrolyte. Catalyst inks were made using a 5 wt% Nafion® solution, and this slurry was applied to a clean PTFE sheet by the doctor blade technique (*40*). Loadings were 0.2 – 0.3 mg/cm^2 of Pt or PtRu in these MEAs. Hot pressing was performed at 150 °C to construct the membrane electrode assemblies, which were tested in a 2 cm^2 cell at 80 °C and atmospheric pressure. CO concentration in the anode exhaust gas was monitored by gas chromatography.

From RDE measurements, the Pt/MoO_x/C catalyst showed peak potential for CO stripping of 40 mV less than did the Pt/C catalyst. However, the PtRu/C catalyst had a peak potential of 270 mV less than Pt/C. For the onset potential for CO stripping, Pt/MoO_x/C was 150 mV less than Pt/C, while PtRu/C was 230 mV less than the Pt/C electrode. These results suggest that Pt/MoO_x/C has a better CO tolerance than Pt/C, but less of a CO tolerance than PtRu/C. From fuel cell anodic polarizations with 100 ppm CO/H_2, the Pt/MoO_x/C catalyst showed an enhanced CO tolerance compared to Pt/C. Fuel cell tests with PtRu/C electrodes were not performed in this study. Anodic polarizations for Pt/MoO_x/C catalysts and Pt/C catalysts can be seen in Figure 7.

As shown above, the Pt/MoO_x/C catalyst shows an enhanced CO tolerance compared to the Pt/C MEAs. For the Pt/C MEAs, differing amounts of oxygen, fed to the cathode, affect the electrochemical oxidation of CO/H_2 on the anode. The authors suggested this was due to oxygen crossover from cathode to anode. The unusually high CO tolerance of the Pt/MoO_x/C catalyst was unexpected from CO stripping results obtained in solution. The authors claimed that this was due to Pt/MoO_x/C catalysts taking part in non-electrochemical processes to oxidize CO. This claim is backed up from GC measurements (*39*). As stated previously, it is possible that molybdenum oxide catalysts promote non-electrochemical oxidation of CO via the water-gas-shift reaction. This study provides an example of how results from solution electrochemical measurements do not necessarily correlate to results obtained in a fuel cell environment.

In a follow up study by the same research group, Pt/MoO_x/C catalysts were again tested in a fuel cell environment, and compared against Pt/C and PtRu/C electrodes (*41*). Experimental conditions were very similar to the previous study described above (*39*). Here, varying amounts of CO_2 were also fed to the fuel cell with H_2, and also with CO/H_2 to emulate a reformate feed. The authors found that Pt/MoO_x/C showed higher CO tolerance than Pt/C and PtRu/C for CO/H_2 mixtures. This was attributed to the higher electrocatalytic activity for CO oxidation, and also to a high catalytic activity of Pt/MoO_x/C for the water-gas-shift reaction. In contrast, the CO_2 tolerance of the PEMFC electrodes was lower for Pt/MoO_x/C catalysts and PtRu/C. Similar severe CO_2 poisoning has been observed in the past for PtMo alloy catalysts, and poisoning was ascribed to CO-like adsorbate species formed from the reduction of CO_2 (*42*). This study was a good follow up to the previous work; comparison of Pt/MoO_x/C catalyst to the PtRu/C electrode verified the CO tolerance characteristics of molybdenum oxide materials.

Continuing with examples molybdenum oxide catalysts being tested in PEM fuel cells, Song *et al.* (*43*) contributed a paper testing Mo oxide catalysts, in combination with Pt black and/or PtRu black, in direct methanol, formaldehyde, and formic acid fuel cells. Mo oxide catalysts were applied to gas diffusion electrodes (GDEs) already containing Pt or PtRu. These GDEs were coated

Downloaded by STANFORD UNIV GREEN LIBR on June 21, 2012 | http://pubs.acs.org
Publication Date (Web): April 30, 2010 | doi: 10.1021/bk-2010-1040.ch011

Downloaded by STANFORD UNIV GREEN LIBR on June 21, 2012 | http://pubs.acs.org
Publication Date (Web): April 30, 2010 | doi: 10.1021/bk-2010-1040.ch011

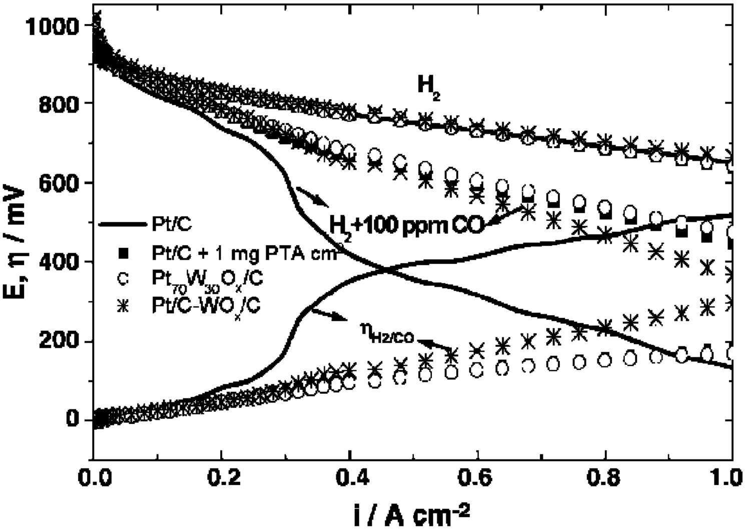

Figure 6. Steady state polarization curves. Reproduced from (36).

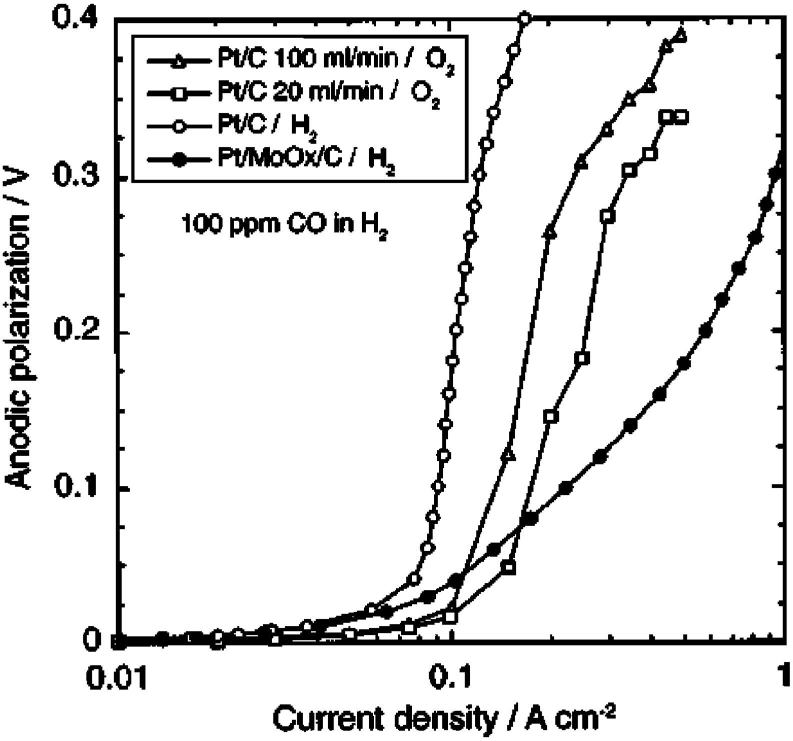

Figure 7. Anodic polarization curves obtained with either H_2 or O_2 on the cathode. Reproduced from (39).

Downloaded by STANFORD UNIV GREEN LIBR on June 21, 2012 | http://pubs.acs.org
Publication Date (Web): April 30, 2010 | doi: 10.1021/bk-2010-1040.ch011

with Mo oxide by electrodeposition from 1 mM Na_2MoO_4 in 3.7 M H_2SO_4. An alternate deposition method of Mo oxide was performed via spraying 1 % aqueous solution of Na_2MoO_4 onto the GDE surface, followed by air-drying. Nafion® 115 membranes were used, and the electrodes and membrane were placed in a 5 cm^2cell without prior pressing. For the DMFC, it was found that none of the Mo modified electrodes performed any better than the unmodified Pt black MEA. In addition, it was seen that Mo, if not reduced before use, can actually poison the Pt catalyst. For a direct formaldehyde fuel cell, presence of Mo species greatly increased the performance at current densities less than 20 mA/cm^2. For example, at 10 mA/cm^2, the potential of the cell with the Pt/MoO_x catalyst is ~ 800 mV, while that of the Pt control MEA is ~ 400 mV. Anodic polarizations were also performed on this formaldehyde fuel cell, and they showed that the presence of Mo species greatly decreased the overpotential required to electrochemically oxidize formaldehyde. Overall, the best performance for the direct formaldehyde fuel cell was seen with Mo oxide modified PtRu/C catalyst.

A similar effect was seen for the direct formic acid fuel cell, with Mo species resulting in increased current densities in the activation region. Again, from anodic polarizations, it was seen that the Mo oxide species decreased the overpotential for formic acid electrooxidation at low currents. Compared to formaldehyde, the effect from Mo incorporation was not as significant for formic acid fuel cells (*43*). This is a significant contribution in showing that DMFC performance dropped with the addition of Mo oxide species. However, the Mo oxide species were not characterized, therefore, it could be that the precursor materials are present, and not actually Mo oxide.

The Use of Heteropoly Acids in Direct Methanol Fuel Cell Anodes

There have been several studies where heteropoly acids (HPAs) have been used in the catalyst layer for PEMFCs (*44–46*). HPAs are desirable in the catalyst layer not only because they have been shown to have catalytic activity for the necessary redox reactions, but also because they have a high protonic conductivity. Thus it may be possible to fabricate electrode structures where no ionomer is required in the catalyst layer. While most studies involved incorporation of HPAs into catalyst layers for PEMFCs, we recently published a paper focusing on the effect of HPAs in the anode catalyst layer of a DMFC (*47*).

Polarization and electrochemical impedance spectroscopy experiments were performed on a direct methanol fuel cell (DMFC) incorporating the heteropoly acids (HPAs) phosphomolybdic acid, $H_3PMo_{12}O_{40}$, (HPMo) or phosphotungstic acid, $H_3PW_{12}O_{40}$, (HPW) in the anode Pt/C catalyst layer (*47*). Both HPW-Pt and HPMo-Pt showed higher performance than the Pt control at 30 psig of backpressure and at ambient pressure. The polarizations curves at 30 psig of backpressure can be seen in Figure 8.

Anodic polarizations were also performed, and Tafel slopes were extracted from the data between 0.25 V and 0.5 V. At 30 psig, Tafel slopes of 133 mV/

Downloaded by STANFORD UNIV GREEN LIBR on June 21, 2012 | http://pubs.acs.org
Publication Date (Web): April 30, 2010 | doi: 10.1021/bk-2010-1040.ch011

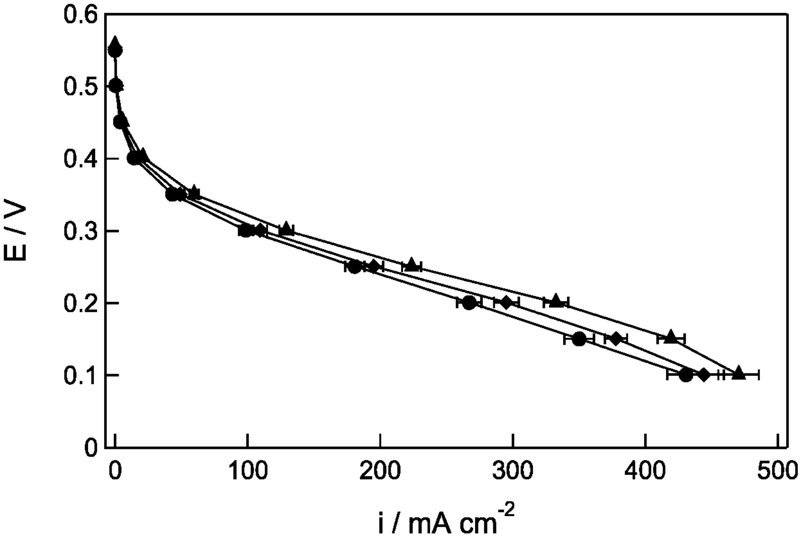

Figure 8. DMFC polarization curves at 30 psig of backpressure. Pt Control (-●-), HPMo-Pt (-♦-), and HPW-Pt (-▲-). Reproduced from (47).

dec, 146 mV/dec, and 161 mV/dec were found for HPW-Pt, HPMo-Pt and the Pt control, respectively. At 0 psig, the Tafel slopes were 172 mV/dec, 178 mV/dec, and 188 mV/dec for HPW-Pt, HPMo-Pt and the Pt control. An equivalent circuit model which incorporated constant phase elements (CPEs) was used to model the impedance data. A sample impedance spectrum is shown in Figure 9.

As shown in Figure 9, the points are the experimental data and the lines are the fit obtained from the equivalent circuit model. From the impedance model it was found that the incorporation of HPAs into the catalyst layer resulted in a reduction in the resistances to charge transfer. This showed that these two heteropoly acids did act as co-catalysts with platinum for methanol electrooxidation.

The Use of Heteropoly Acids in Dimethyl Ether PEM Fuel Cell Anodes

While the use of heteropoly acids and metal oxides have been investigated heavily for methanol, these materials have not seen nearly as much attention for dimethyl ether (DME). Compared to methanol, DME has some desirable physical properties. DME has a vapor pressure between butane and propane, making storage as a liquid simple with existing technology. In this manner, DME combines the ease of delivery of hydrogen (i.e. no pumps required) with the high energy density of a liquid fuel such as methanol. DME also has a low toxicity; it is not toxic upon skin contact as is methanol. We have recently reported using heteropoly acids in the anode catalyst layer, in combination with platinum, of a direct dimethyl ether PEM fuel cell (DMEFC) (*48*).

Downloaded by STANFORD UNIV GREEN LIBR on June 21, 2012 | http://pubs.acs.org
Publication Date (Web): April 30, 2010 | doi: 10.1021/bk-2010-1040.ch011

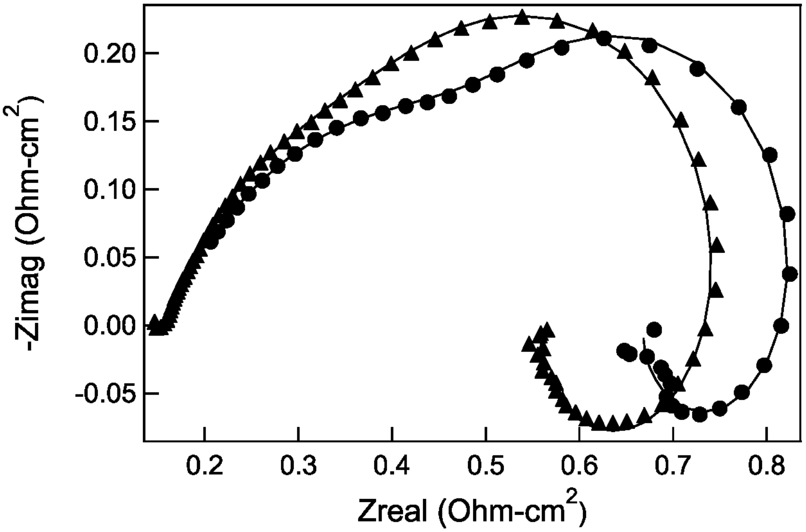

Figure 9. Impedance at 182 mA/cm^2 and 30 psig backpressure. Platinum Control (-●-), and HPW-Pt (-▲-).

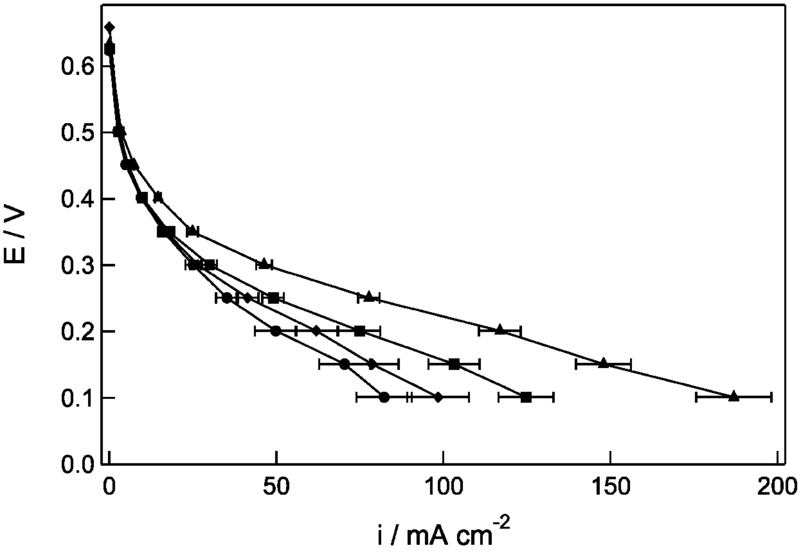

Figure 10. DMEFC Cell Polarization. Cell Temperature: 100 °C, 30 psig backpressure, DME flow rate: 100 sccm, water flow rate: 1.2 ml/min. Pt Control (-●-), HPMo-Pt (-♦-), HSiW-Pt (-■-), and HPW-Pt (-▲-).

Polarization and impedance experiments were performed on a direct dimethyl ether fuel cell (DMEFC). The experimental setup allowed for independent control of water and DME flow rates. The DME flow rate, backpressure, and water flow rate were optimized. Three heteropolyacids, phosphomolybdic acid, $H_3PMo_{12}O_{40}$. (HPMo), phosphotungstic acid, $H_3PW_{12}O_{40}$, (HPW), and silicotungstic acid, $H_4SiW_{12}O_{40}$, (HSiW) were incorporated into the anode catalyst layer in combination with Pt/C. Both HPW-Pt and HSiW-Pt showed higher performance than the Pt control (*48*). The polarization curves at 30 psig can be seen above.

As seen in Figure 10, the incorporation of phosphotungstic acid resulted in a more than doubling of current density, when compared to the platinum control. Anodic polarizations were also performed, and Tafel slopes were extracted from the data. At 30 psig, Tafel slopes of 67 mV/dec, 72 mV/dec, and 79 mV/dec were found for HPW-Pt, HSiW-Pt and the Pt control, respectively. At 0 psig, the Tafel slopes were 56 mV/dec, 58 mV/dec, and 65 mV/dec for HPW-Pt, HSiW-Pt and the Pt control. The trends in the Tafel slope values were in agreement with the polarization data. The electrochemical impedance spectroscopy results were also in agreement with the polarization trends. The addition of phosphotungstic acid more than doubled the power density of the fuel cell, compared to the Pt control. When the maximum power density obtained using the HPW-Pt MEA is normalized by the mass of Pt used, these results are the highest seen to date in terms of mW/mg Pt (*48*). While the DMEFC is still in early days, this study has shown that heteropoly acids can greatly enhance the anodic electrocatalysis.

Downloaded by STANFORD UNIV GREEN LIBR on June 21, 2012 | http://pubs.acs.org
Publication Date (Web): April 30, 2010 | doi: 10.1021/bk-2010-1040.ch011

Conclusions

In this chapter, the development of various metal oxides and heteropoly acids for use as electrocatalysts in direct PEM fuel cells was reviewed. First the development of hydrogen-tungsten-bronze materials, and the hydrogen spillover effect was discussed. The discovery of the hydrogen spillover effect lead to more research involving many other metal oxides. The use of Pt and PtRu supported on WO_3 for methanol electrooxidation was reviewed; most of these studies were performed in solution. Other oxides containing Sn, Mo, and Os, and combinations thereof, were also reviewed in the context of methanol electrooxidation. The use of metal oxides, in the anode catalyst layer of direct PEM fuel cells, was also reviewed. These studies often used a small amount of CO in hydrogen fed to the anode of the fuel cell. Finally, the use of heteropoly acids in direct methanol and direct dimethyl ether PEM fuel cells was presented. The majority of the work reviewed here was performed in solution; there are still many studies needed in the fuel cell environment. In some cases, the metal oxide under study, often in combination with Pt, has shown higher activity than PtRu electrodes. This is promising, as PtRu is often regarded as the state of the art electrocatalyst for methanol.

References

1. Niedrach, L. W.; Weinstock, I. B. *Electrochem. Technol.* **1965**, *3*, 270.

2. Benson, J. E.; Kohn, H. W.; Boudart, M. *J. Catal.* **1966**, *5*, 307.
3. Glemser, O.; Naumann, K. *Z. Anorg. Allg. Chem* **1951**, *256*, 288.
4. Hobbs, B. S.; Tseung, A. C. C. *Nature* **1969**, *222*, 556.
5. Hobbs, B. S.; Tseung, A. C. C. *J. Electrochem. Soc.* **1973**, *120*, 766.
6. Hobbs, B. S.; Tseung, A. C. C. *J. Electrochem. Soc.* **1972**, *119*, 580.
7. Tseung, A. C. C.; Chen, K. Y. *Catal. Today* **1997**, *38*, 439.
8. Shen, P. K.; Syed-Bokhari, J.; Tseung, A. C. C. *J. Electrochem. Soc.* **1991**, *138*, 2778.
9. Waszczuk, P.; Solla-Gullon, J.; Kim, H. S.; Tong, Y. Y.; Montiel, V.; Aldaz, A.; Wieckowski, A. *J. Catal.* **2001**, *203*, 1.
10. Shen, P. K.; Tseung, A. C. C. *J. Electrochem. Soc.* **1994**, *141*, 3082.
11. Hamnett, A. *Catal. Today* **1997**, *38*, 445.
12. Lu, G. Q.; Chrzanowski, W.; Wieckowski, A. *J. Phys. Chem. B* **2000**, *104*, 5566.
13. Shukla, A. K.; Ravikumar, M. K.; Arico, A. S.; Candiano, G.; Antonucci, V.; Giordano, N.; Hamnett, A. *J. Appl. Electrochem.* **1995**, *25*, 528.
14. Park, K. W.; Ahn, K. S.; Nah, Y. C.; Choi, J. H.; Sung, Y. E. *J. Phys. Chem. B* **2003**, *107*, 4352.
15. Park, K.-W.; Ahn, K.-S.; Choi, J.-H.; Nah, Y.-C.; Sung, Y.-E. *Appl. Phys. Lett.* **2003**, *82*, 1090.
16. Chen, K. Y.; Shen, P. K.; Tseung, A. C. C. *J. Electrochem. Soc.* **1995**, *142*, L54.
17. McLeod, E. J.; Birss, V. I. *Electrochim. Acta* **2005**, *51*, 684.
18. Ganesan, R.; Lee, J. S. *J. Power Sources* **2006**, *157*, 217.
19. Cui, X. Z.; Shi, J. L.; Chen, H. R.; Zhang, L. X.; Guo, L. M.; Gao, J. H.; Li, J. B. *J. Phys. Chem. B* **2008**, *112*, 12024.
20. Maiyalagan, T.; Viswanathan, B. *J. Power Sources* **2008**, *175*, 789.
21. Park, K. W.; Choi, J. H.; Ahn, K. S.; Sung, Y. E. *J. Phys. Chem. B* **2004**, *108*, 5989.
22. Yang, L. X.; Bock, C.; MacDougall, B.; Park, J. *J. Appl. Electrochem.* **2004**, *34*, 427.
23. Jayaraman, S.; Jaramillo, T. F.; Baeck, S. H.; McFarland, E. W. *J. Phys. Chem. B* **2005**, *109*, 22958.
24. Green, C. L.; Kucernak, A. *J. Phys. Chem. B* **2002**, *106*, 1036.
25. de Oliveira, M. B.; Profeti, L. P. R.; Olivi, P. *Electrochem. Commun.* **2005**, *7*, 703.
26. Wang, Y.; Fachini, E. R.; Cruz, G.; Zhu, Y.; Ishikawa, Y.; Colucci, J. A.; Cabrera, C. R. *J. Electrochem. Soc.* **2001**, *148*, C222.
27. Martinez-Huerta, M. V.; Rodriguez, J. L.; Tsiouvaras, N.; Pena, M. A.; Fierro, J. L. G.; Pastor, E. *Chem. Mater.* **2008**, *20*, 4249.
28. Mukerjee, S.; Lee, S. J.; Ticianelli, E. A.; McBreen, J.; Grgur, B. N.; Markovic, N. M.; Ross, P. N.; Giallombardo, J. R.; De Castro, E. S. *Electrochem. Solid State Lett.* **1999**, *2*, 12.
29. Mukerjee, S.; Urian, R. C. *Electrochim. Acta* **2002**, *47*, 3219.
30. Mukerjee, S.; Urian, R. C.; Lee, S. J.; Ticianelli, E. A.; McBreen, J. *J. Electrochem. Soc.* **2004**, *151*, A1094.

Downloaded by STANFORD UNIV GREEN LIBR on June 21, 2012 | http://pubs.acs.org
Publication Date (Web): April 30, 2010 | doi: 10.1021/bk-2010-1040.ch011

31. Cao, D.; Lu, G. Q.; Wieckowski, A.; Wasileski, S. A.; Neurock, M. *J. Phys. Chem. B* **2005**, *109*, 11622.
32. Janik, M. J.; Neurock, M. *Electrochim. Acta* **2007**, *52*, 5517.
33. Janik, M. J.; Taylor, C. D.; Neurock, M. *Top. Catal.* **2007**, *46*, 306.
34. Wee, J. H.; Lee, K. Y. *J. Power Sources* **2006**, *157*, 128.
35. Hou, Z.; Yi, B.; Yu, H.; Lin, Z.; Zhang, H. *J. Power Sources* **2003**, *123*, 116.
36. Pereira, L. G. S.; dos Santos, F. R.; Pereira, M. E.; Paganin, V. A.; Ticianelli, E. A. *Electrochim. Acta* **2006**, *51*, 4061.
37. Santiago, E. I.; Camara, G. A.; Ticianelli, E. A. *Electrochim. Acta* **2003**, *48*, 3527.
38. Santiago, E. I.; Batista, M. S.; Assaf, E. M.; Ticianelli, E. A. *J. Electrochem. Soc.* **2004**, *151*, A944.
39. Ioroi, T.; Yasuda, K.; Siroma, Z.; Fujiwara, N.; Miyazaki, Y. *J. Electrochem. Soc.* **2003**, *150*, A1225.
40. Ioroi, T.; Fujiwara, N.; Siroma, Z.; Yasuda, K.; Miyazaki, Y. *Electrochem. Commun.* **2002**, *4*, 442.
41. Ioroi, T.; Akita, T.; Yamazaki, S.-i.; Siroma, Z.; Fujiwara, N.; Yasuda, K. *Electrochim. Acta* **2006**, *52*, 491.
42. Lebedeva, N. P.; Janssen, G. J. M. *Electrochim. Acta* **2005**, *51*, 29.
43. Song, C. J.; Khanfar, M.; Pickup, P. G. *J. Appl. Electrochem.* **2006**, *36*, 339.
44. Kuo, M.; Stanis, R.; Ferrell, J.; Turner, J.; Herring, A. M. *Electrochim. Acta* **2007**, *52*, 2051.
45. Limoges, B.; Stanis, R.; Turner, J.; Herring, A. M. *Electrochim. Acta* **2005**, *50*, 1169.
46. Stanis, R.; Kuo, M.; Turner, J.; Herring, A. M. *J. Electrochem. Soc.* **2007**, *155*, B155.
47. Ferrell, J. R., III; Kuo, M.-C.; Turner, J. A.; Herring, A. M. *Electrochim. Acta* **2008**, *53*, 4927.
48. Ferrell, J. R., III; Kuo, M.-C.; Herring, A. M. *Electrochim. Acta* **2009**, submitted.

Downloaded by STANFORD UNIV GREEN LIBR on June 21, 2012 | http://pubs.acs.org
Publication Date (Web): April 30, 2010 | doi: 10.1021/bk-2010-1040.ch011

Subject Index

A

AMC. *See* Aromatic model compounds
Aromatic model compounds
  illustration of, 133, 135*f*
  preliminary Fenton's degradation results with, 133, 135*f*
ATR. *See* Attenuated total reflectance
Attenuated total reflectance
  absorbance of Nafion® films using, 116
  and FTIR difference spectra (Nafion/silicate-dry unfilled Nafion)
    for sample with 34% silica loading, 116, 118*f*

B

β relaxation
  curves spaced at 10°C increments from onset of
    up to 200°, 116, 119*f*
  involving chain segmental motions, 120
  with onset at 0°C, 116
  peak maxima for 6 and 10% silica increased
    by small amount to higher frequencies with silica insertion, 117
Biphenyl
  non-polar moieties with PBPDSA, 51
  using "mole %" of grafted group (equiv. wt.), 52*t*
BPSH. *See* Poly(arylene ether sulfone)
Broadband dielectric spectroscopic, studies of Nafion®/silicate membranes, 113

C

Carbon monoxide
  oxidation on WO_3 surface, 163
  stripping scans, 168*f*, 169
  tolerance effect of, 154, 166, 169
Catalyst
  FeCo/C-polypyrrole
    MEA performance of LANL for, 5, 7*f*
  $PtAuNi_5$ core-shell
    in comparison with Pt/C, 5, 6*f*
Cathode, anodic polarization curves obtained with H_2 or O_2 on, 171*f*
Conductivity, 56
  as function of
    EW for membranes
      measured at given relative humidities, 20, 21*f*
    relative humidity for similar range of EW membranes, 17, 20*f*
    RH for PBPDSA and PPDSA compared with Nafion 117, 57, 57*f*
    temperature for 3M ionomer membrane series at constant dew point, 17, 19*f*
  of rigid rod liquid crystalline polymers
    at various relative humidities, 7, 10*f*
  vs. temperature
    for 600 EW membrane at constant 80°C dew point, 26, 28*f*
    for crosslinked ionomer and two controls, 27, 28*f*
    and relative humidity, 7, 10*f*
Constant phase elements, with equivalent circuit model used to model impedance data, 172, 173, 174*f*
CPEs. *See* Constant phase elements
Cross-link, ionomers
  generalized reaction scheme of

Downloaded by 89.163.35.42 on June 21, 2012 | http://pubs.acs.org
Publication Date (Web): April 30, 2010 | doi: 10.1021/bk-2010-1040.ix002

Downloaded by 89.163.35.42 on June 21, 2012 | http://pubs.acs.org
Publication Date (Web): April 30, 2010 | doi: 10.1021/bk-2010-1040.ix002

- using cure site monomer and multifunctional crosslinker, 25, 26*f*
- performance implications of, 26
- strategies for, 24
- x-y swelling data for, and uncrosslinked ionomers, 25, 27*t*

D

- Degrees of substitution
  - di-t-butyl phenol and t-butyl benzene grafted samples after drying at 175°C for
    - equivalent weights determined by titration of, 51
  - t-butyl substituted moieties
    - for water insoluble PEMs at lower, 51
- Dielectric relaxation
  - spectral behavior of film samples, 116
    - α relaxation with onset at 80°C, 116
    - β relaxation with onset at 0°C, 116
    - ε″ vs. *f* at 60°C for films with different silica loading, 117, 119*f*
- Dimensional stability, 52
  - PBPDSA grafted/cast films equilibrated at RH, 51, 52, 52*t*
- Dimethyl ether fuel cell
  - cell polarization, 174*f*, 175
  - HPAs used in, 173
- Direct methanol fuel cell, 160, 166
  - polarization curves, 172, 173*f*
  - PtRu as state-of-the-art anode electrocatalyst for, 156
- Di-t-butyl phenol
  - equivalent weights determined by titration of, 51
  - graft on PBPDSA
    - comparison of λ as function of RH for, 56, 56*f*
    - relative weight loss of, 55*f*, 56
  - non-polar moieties with PBPDSA, 51
  - using "mole %" of grafted group (equiv. wt.), 52*t*
- DMEFC. *See* Dimethyl ether fuel cell

E

- Electrocatalysts
  - metal oxides and heteropoly acids as
    - in direct PEM fuel cells, 153
  - as anode for state-of-the-art PtRu DMFC, 156
- Electrochemical methanol oxidation, using Pt/WO_3 catalysts for, 156
- Equivalent circuit model, with CPEs used to model impedance data, 172, 173, 174*f*
- Equivalent weight, acid content
  - as function of
    - water solubility of 3M ionomer membranes, 22, 24*f*
  - length change vs. time for
    - membrane series, 22, 23*f*
    - dimensional changes with relative humidity, 22, 23*f*
  - ultra low path of, 17, 21
    - physical side of, 22
- Ethanol, 160

F

- 6F-bisphenol. *See* 4,4’-Hexafluoroisopropylidene diphenol
- Fenton’s degradation
  - preliminary results of
    - with AMC, 133, 135*f*
  - results of
    - for 3M ionomer, 134*f*
    - for Nafion® ionomer, 134*f*
- Fluoride release rate
  - as function of
    - anode catalyst geometric surface area for catalyst range, 139*f*, 143

Downloaded by 89.163.35.42 on June 21, 2012 | http://pubs.acs.org
Publication Date (Web): April 30, 2010 | doi: 10.1021/bk-2010-1040.ix002

    - fuel and oxidant concentration ratio, 141*f*, 146
    - MEA constructions, 139*f*, 142
    - multiple PEM MEAs, 147, 149*f*
    - time for different Mn loadings in 3M 825ew polymer, 146, 146*f*
  - ratio of anode to cathode effluent of
    - as function of fuel ratio to oxidant partial pressures, 141*f*, 146
- Fourier transform infrared spectroscopy
  - and ATR difference spectra (Nafion®/silicate-dry unfilled Nafion®)
    - for sample with 34% silica loading, 116, 118*f*
  - degree of intramolecular connectivity in
    - silicate, metal oxide and organically-modified silicate nanophases, 116
- Frozen-in free volume
  - determination using eq. 1, 60*f*, 61
  - effect of, 56
    - calculated polymer density as function of λ, 60*f*, 61
  - estimation of, 57, 59
  - rigid rod polyelectrolytes with
    - in high conductivity at low RH, 49
- 6FSH. *See* 4,4’-Hexafluoroisopropylidene diphenol
- FTIR. *See* Fourier transform infrared spectroscopy
- Fuel cells
  - anodic polarization
    - for Pt/MoO_x/C catalysts and Pt/C catalysts, 170, 171*f*
  - cost of, 3, 4
  - durability testing of open circuit voltage, 3, 9
    - using multiple PEM MEAs, 137
  - metal oxides and heteropoly acids as
    - anodic electrocatalysts in direct PEM, 153
  - recent advances of, 4
  - status and challenges of, 1, 3

H

- Havriliak-Negami equation, 117, 121*t*
- Heteropoly acids
  - for dimethyl ether PEMFC anodes, 173
  - and metal oxides as anodic electrocatalysts
    - in direct PEM fuel cells, 153
  - used in direct methanol fuel cell anodes, 172
- 4,4’-Hexafluoroisopropylidene diphenol
  - 6FSH32
    - AFM phase images of, 70, 71*f*
    - chemical structure of, 66, 67*f*
    - membrane properties of, 70, 72*t*
    - storage modulus and tan delta curves for, 71, 75*f*
    - three-dimensional tapping mode AFM height images for, 70, 74*f*
- Homopolymers, 51
  - larger than expected equivalent weight found for, 52
  - PBPDSA and PPDSA films
    - heated for 1 hour at specified temperatures, 53
    - heated under vacuum at 90°C for 24 hrs and weighed, 53
- Hydrogen spillover, 154
  - takes advantage of
    - hydrogen-tungsten-bronzes formation, 155
- Hydrogen-tungsten-bronze
  - materials, 154
  - function as intermediates in
    - anodic oxidation of
    - H on Pt/tungsten trioxide electrodes, 154
  - general formula, 154
  - by H-atom migration from Pt site to oxide, 155

Downloaded by 89.163.35.42 on June 21, 2012 | http://pubs.acs.org
Publication Date (Web): April 30, 2010 | doi: 10.1021/bk-2010-1040.ix002

- other characteristics, 154
- oxidized electrochemically
  - regenerate original WO_3 surface, 157

I

- Indium tin oxide, as substrate, 158
- Ionomers
  - DuPont's Nafion®
    - chemical structure for, 17, 18*f*
    - Fenton's degradation results for, 134*f*
    - major decomposition of, 132
    - potential sites of radical attack on, 127, 127*f*
    - weight percent TFE against equivalent weight for, 17, 18*f*
    - wide angle X-ray diffraction for, 17, 19*f*
  - 3M
    - approach of, 17
    - basics of, 17
    - calculated performance loss for series of, 18, 19, 20*f*, 26
    - chemical structure for, 17, 18*f*
    - Fenton's degradation results for, 134*f*
    - major decomposition of, 132
    - water solubility of, 22, 24*f*
    - weight percent TFE against equivalent weight for, 17, 18*f*
    - wide angle X-ray diffraction for, 17, 19*f*

L

- LCMS. *See* Liquid chromatography/mass spectroscopy
- Liquid chromatography/mass spectroscopy
  - results of
    - for MC4, 128, 130*f*
    - for MC7, 131*f*
    - for MC8, 131*f*

M

- Membrane electrode assembly
  - in combination with PEM
    - Pt concentration as measured by ICP for, 143*f*, 146, 147, 147*f*
    - representative tensile measurements made for, 140*f*, 145
    - tensile measurement toughness measured at 25°C 50%RH for, 144*f*, 146, 147, 148*f*
    - use for durability testing of open circuit voltage fuel, 137
  - constructions
    - fluoride release rate as function of, 139*f*, 142
  - demonstrating activity of
    - University of South Carolina metal-free carbon and carbon composite catalyst, 5, 8*f*
  - 3M nano structured thin film
    - accelerated durability test results for, 9, 10*f*
  - performance of
    - for FeCo/C-polypyrrole catalyst, 5, 7*f*
- Metal oxides
  - and heteropoly acids as anodic electrocatalysts
    - in direct PEM fuel cells, 153
  - with Pt materials
    - in direct PEMFC anodes, 166
    - for methanol electrooxidation, 163
  - using Pt/WO_3, 158
- Methanol electrooxidation
  - Pt/metal oxide materials for, 163
  - PtRu/WO_3 materials for, 161
- Model compounds, perfluorinated
  - containing -COOH, 128
    - chain end degradation mechanism, 129
  - MC4
    - typical LCMS results for, 128, 130*f*
  - MC7
    - LCMS results for, 131*f*

- trapping experiment results for, 130, 133*f*
- MC8
  - LCMS results for, 131*f*
  - potential trapping products from, 130, 132*f*
  - trapping experiment results for, 130, 133*f*
- trapping of
  - during radical degradation
    - to support ether cleavage mechanism, 132
- without -COOH, 128

N

Nafion®
- acid film
  - ε″ - *f* - T surface for, 116, 119*f*
- broadband dielectric spectroscopy and conductivity mechanism of, 97
- in combination with [ZrO_2]
  - broadband dielectric spectroscopy and conductivity mechanism of, 97
  - pseudo-activation energies of σ_{dc} and f_k for, in dry state and wet state, 107, 108*t*, 109*t*
  - $\sigma_{dc,i}$ dependence on conductivity temperature values for, 102*t*, 103
  - SRC values for, 102*t*, 103
- comparison of λ as function of RH for, 54*f*, 55
- conductivities as function of RH for 2 homopolymers compared with, 57, 57*f*
- different silica loading compared to unmodified
  - calculated from HN eq. fitted spectra with subtraction of d.c. conductivity contribution, 120, 121*t*
  - dielectric storage permittivity vs. f at 60°C for films with, 117, 120*f*
  - ε″ vs. *f* at 60°C for films with, 117, 119*f*, 120, 121*f*
- fitted values of *N* plotted vs. temperature for, 121, 123*f*
- pseudo-activation energies of σ_{dc} and f_k for
  - in dry state, 107, 108*t*
  - in wet state, 109*t*
- pure sol-gel-generated silicate nanophases in, 116
- $\sigma_{dc,i}$ dependence on conductivity temperature values for, 102*t*, 103
- with silicate membranes
  - BDS studies of, 113
- SRC values for, 102*t*, 103

P

PBPDSA. *See* Poly(p-biphenylene 3, 3’-disulfonic acid)

PEMFC. *See* Proton exchange membrane fuel cells

Perfluorinated sulfonic acid
- chemical durability studies of, 125
- membranes
  - chain end attack mechanism for, 127, 127*f*, 128, 129*f*
- model compounds of, 128, 129*f*
- model studies of, 127
- small molecule model compounds of
  - to degrade via ether cleavage, 130

Perfluorosulfonic acid, ionomer/polymer based
- with reactive cure site, 24, 25, 26*f*
- short-side-chain
  - average radius of water domains, 92, 93*f*
  - Bragg spacing of water domains, 93, 93*f*
  - contour plots of water density as two dimensional cross section for, 90*f*, 91
  - hydrated morphology of, 83, 89, 89*f*, 91

Downloaded by 89.163.35.42 on June 21, 2012 | http://pubs.acs.org
Publication Date (Web): April 30, 2010 | doi: 10.1021/bk-2010-1040.ix002

        - radial distribution functions of C beads for, 92, 92*f*
        - structural analysis of phase segregated morphologies, 91
        - water particles radial distribution functions for, 90*f*, 91
    - torque vs. time for
        - in sulfonyl fluoride form compounded with peroxide and crosslinker, 25, 27*f*
    - way to add additional acid groups (R) to, 21, 22*f*
- PFSA. *See* Perfluorosulfonic acid, ionomer/polymer based
- Phosphotungstic acid
    - dissolved in ethanol and incorporated in KIT-6 structure
        - by incipient wetness impregnation technique, 160
    - incorporation of, 175
    - suspension in methanol infiltrated into alumina disc under vacuum, 161
    - used as tungsten source, 160
- Platinum
    - combination with WO_3 catalysts used for electrochemical methanol oxidation, 156
    - concentration gradient of
        - as function of time operation, 148, 149*f*
    - with metal oxide materials
        - in direct PEMFC anodes, 166
        - for methanol electrooxidation, 163
    - Ru
        - as state-of-the-art anode electrocatalyst for DMFC, 156
        - with WO_3 materials for methanol electrooxidation, 161
    - WO_3 aided methanol oxidation for, 156
- Poly(arylene ether sulfone)
    - BPSH35
        - AFM phase images of, 70, 71*f*
        - chemical structure of, 66, 67*f*
        - membrane properties of, 70, 72*t*
        - three-dimensional tapping mode AFM height images for, 70, 73*f*
    - BPSH100x-PBPy
        - AFM phase images of, 72, 74, 76*f*
        - chemical structure of, 66, 67*f*, 72
        - TEM micrographs of, 74, 78*f*
        - three-dimensional tapping mode AFM height images for, 73, 77*f*
        - water uptake and proton conductivities of, 72, 77*t*
    - BPSH100x-PIy
        - AFM phase images of, 72, 74, 75*f*, 78, 79*f*
        - chemical structure of, 66, 67*f*, 72
        - storage modulus and tan delta curves for, 75, 77, 78*f*
        - TEM micrographs of, 74, 78*f*
        - three-dimensional tapping mode AFM height images for, 73, 77*f*
        - water uptake and proton conductivities of, 72, 76*t*
    - molecular weight effects on, 65
- Polymer electrolyte membrane, nonfluorinated
    - chemical durability studies of, 125
    - illustration of, 133, 135*f*
    - materials of
        - preliminary model studies, 133
- Polymer synthesis, 50
    - method using
        - Suzuki reaction, 50
        - Ullman reaction, 50
- Poly(p-biphenylene 3, 3'-disulfonic acid)
    - comparison of λ as function of RH for, 54*f*, 55
    - conductivity as function of RH for

Downloaded by 89.163.35.42 on June 21, 2012 | http://pubs.acs.org
Publication Date (Web): April 30, 2010 | doi: 10.1021/bk-2010-1040.ix002

    - compared with Nafion 117, 57, 57*f*
  - grafted/cast films equilibrated at RH
    - dimensional stability of, 51, 52, 52*t*
  - ^{1}H NMR measurements of λ for, 54
  - molecular weight obtained for
    - 10-15K Daltons, 50
  - non-polar moieties with
    - 2, 6-di-t-butyl phenol, 51
    - biphenyl, 51
    - t-butyl benzene, 51
  - TGA measurements of water absorption of, 53
- Poly(p-phenylene 2, 5-disulfonic acid)
  - as function of RH for
    - comparison of λ, 54*f*, 55
    - conductivity, compared with Nafion 117, 57, 57*f*
    - WAXD transmission spectra, 58, 58*f*
  - molecular weight obtained for
    - 40-50K Daltons, 50
  - water absorption for
    - measured by equilibrating dried films at given RH, 53
- Poly(vinylidene fluoride)-*g*-polystyrene
  - graft copolymers
    - DSC curve with different mole ratio and graft density of, 38*f*, 39*f*, 40, 41
    - experimental results summary of, 35*t*, 36*t*
    - thermal properties and morphologies of, 40
- Poly(vinylidene fluoride)-*g*-sulfonated polystyrene
  - graft copolymers
    - DSC curve with different mole ratio and graft density of, 39*f*, 41
    - experimental results summary of, 35*t*, 36*t*
    - preparation of, 33*s*, 38
    - proton conductivity of, 44
    - thermal properties and morphologies of, 40
    - transmission electron microscopy micrographs of, 40*f*, 41, 42, 43, 44, 46
    - water uptake (wt%) and water content λ vs. IEC, 41*f*, 42, 43, 43*f*
  - synthesis and characterization of
    - for proton exchange membrane, 31, 38
- Potassium acetate, dissolved in D_2O to make a calibrated solvent for further measurements, 54
- PPDSA. *See* Poly(p-phenylene 2, 5-disulfonic acid)
- Proton conductivity
  - comparison of
    - between several pairs of PVDF-g-SPS graft copolymers, 46, 47*t*
  - of PVDF-g-SPS
    - vs. graft density, 44*f*, 45
    - vs. relative humidity, 43*f*, 44
- Proton exchange membrane fuel cells
  - in combination with MEA
    - Pt concentration as measured by ICP for, 143*f*, 146, 147, 147*f*
    - representative tensile measurements made for, 140*f*, 145
    - tensile measurement toughness measured at 25°C 50%RH for, 144*f*, 146, 147, 148*f*
    - use for durability testing of open circuit voltage, 137
  - dimensionally stable, 51
  - HPAs used in dimethyl ether, 173
  - membranes for, 15
  - metal oxides and heteropoly acids as
    - anodic electrocatalysts in, 153
  - Pt/metal oxide materials in, 166
    - steady state polarization curves, 169, 171*f*
  - single cell performance, 164*f*, 167, 168*f*
  - strain as function of, 140*f*, 145
  - synthesis and characterization
    - of PVDF-g-SPS, 31, 38

Downloaded by 89.163.35.42 on June 21, 2012 | http://pubs.acs.org
Publication Date (Web): April 30, 2010 | doi: 10.1021/bk-2010-1040.ix002

water insoluble
  from t-butyl substituted moieties at lower degrees of substitution, 51
PVDF-g-PS. *See* Poly(vinylidene fluoride)-g-polystyrene
PVDF-g-SPS. *See* Poly(vinylidene fluoride)-g-sulfonated polystyrene

R

Relative humidity
  comparison of λ as function of
    for PBPDSA, PPDSA and Nafion 117®, 53*t*, 54, 54*f*, 55
    for PBPDSA and di-t-butyl phenol graft, 56, 56*f*
  dimensional changes from 22 to 100%
    on grafted PBPDSA films, 51, 52, 52*t*
  effect on Pt particle size during potential cycling, 9, 11*f*
  high conductivity at low, 49
  vs. conductivity, of rigid rod liquid crystalline polymers, 7, 10*f*
  WAXD transmission spectra of PPDSA films as function of, 58, 58*f*
RH. *See* Relative humidity
Rigid rod polyelectrolytes, with frozen-in free volume in high conductivity at low RH, 49
Rotating disc electrode
  demonstrating activity of University of South Carolina metal-free carbon and carbon composite catalyst, 5, 8*f*
  results of
    from Argonne National Laboratory for 3M PtNiFe alloy over polycrystalline Pt, 4, 6*f*

S

SRC. *See* Stability range of conductivity
Stability range of conductivity values for
    Nafion 117, 102*t*, 103
    Nafion/[ZrO_2], 102*t*, 103
Suzuki reaction, 50

T

T-butyl benzene
  equivalent weights determined by titration of, 51
  non-polar moieties with PBPDSA, 51
  using "mole %" of grafted group (equiv. wt.), 52*t*
Temperature
  vs. conductivity
    for 600 EW membrane at constant dew point, 26, 28*f*
    for crosslinked ionomer and two controls, 27, 28*f*
TEMPO. *See* 2,2,6,6-Tetramethylpiperidine-1-oxyl
2,2,6,6-Tetramethylpiperidine-1-oxyl, 130
Titration
  of dried films, 52*t*
  equivalent weights determined by
    of di-t-butyl phenol and t-butyl benzene, 51

U

Ullman reaction, polymerization of, 50, 51*s*

W

Water absorption, 52
  graft polymer, 56
  methods used

Downloaded by 89.163.35.42 on June 21, 2012 | http://pubs.acs.org
Publication Date (Web): April 30, 2010 | doi: 10.1021/bk-2010-1040.ix002

        exposing it to RH atmosphere
            and reweighing until
            weight stabilization, 52
        vacuum drying film, 52
        weighing it, 52
    for PPDSA
        measured by equilibrating
            dried films at given RH, 53

WAXD. *See* Wide-angle X-ray
    diffraction
Wide-angle X-ray diffraction
    molar volumes as function of RH
        calculated from, 58, 59*f*
    transmission and reflection
        on PPDSA films conditioned
            at different RH, 58, 58*f*

Downloaded by 89.163.35.42 on June 21, 2012 | http://pubs.acs.org
Publication Date (Web): April 30, 2010 | doi: 10.1021/bk-2010-1040.ix002